

**UNIVERSITY OF SOUTHAMPTON**

FACULTY OF PHYSICAL SCIENCES AND ENGINEERING

School of Electronics and Computer Science

**A Study of Re-ignition Phenomena and Arc Modelling  
to Evaluate Switching Performance  
of Low-Voltage Switching Devices**

by

**Dongkyu Shin**

Thesis for the degree of Doctor of Philosophy

June 2018



UNIVERSITY OF SOUTHAMPTON

# **ABSTRACT**

FACULTY OF PHYSICAL SCIENCES AND ENGINEERING

School of Electronics and Computer Science

Thesis for the degree of Doctor of Philosophy

## **A STUDY OF RE-IGNITION PHENOMENA AND ARC MODELLING TO EVALUATE SWITCHING PERFORMANCE OF LOW-VOLTAGE SWITCHING DEVICES**

Dongkyu Shin

This thesis deals with the prediction, improvement and simulation of switching performance of low-voltage switching devices (LVSDs). A literature review of arc characteristics, interruption principle, switching performance and arc modelling of LVSDs has been conducted. The experimental investigations of switching tests, arc imaging measurement and arc spectra measurement are also discussed. Switching tests have been carried out with 10kA, 20kA, 55kA and 100kA test circuits using either miniature circuit breakers or moulded case circuit breakers to investigate re-ignition phenomena and re-ignition evaluators. It is found that the ratio of the recovery voltage to exit arc voltage, where the exit arc voltage is defined as the value of the arc voltage immediately prior to the current zero point, is a reliable evaluator for the prediction of re-ignition in the switching tests of LVSDs. It is also noted that there are no occurrences of instantaneous re-ignition where this voltage ratio lies in the range of 1.0 to -1.0 and there is a threshold of the voltage ratio at approximately -2.0, which can distinguish the successful interruption and instantaneous re-ignition. Arc imaging measurement has been conducted through an array of total 109 optical fibres to allow observation of the overall quenching chamber of the flexible test apparatus. This experiment reveals that arc motion fluctuation (repeat of back- and forwards-motion) in the splitter plate region leads to the instability of the arc voltage. Moreover, the arc moves further as well as more quickly in the case of the larger vent size. The well distributed vent contributes to an increase in an arc motion velocity and reduction in a total arc duration. Arc spectrum is captured by a spectrometer to calculate the arc temperature when the arc is ignited by copper wire in a narrow enclosed chamber. It is found that the arc light intensity measured by the arc imaging system is directly related to the arc temperature: the light intensity increases as the arc temperature rises. 3-D arc modelling has been implemented, based on the magnetohydrodynamics theory. Lorentz force, plasma properties depending on temperature as well as pressure, contact motion, radiation loss, arc root voltage, and external circuit are considered in this modelling. It is observed that the simulated results have a similar trend with the experimental data and it is able to predict current limitation and exit arc voltage, which are key features of switching performance.

This page is intentionally left blank.



# ACADEMIC THESIS: DECLARATION OF AUTHORSHIP

I, Dongkyu Shin, declare that this thesis and the work presented in it are my own and has been generated by me as the result of my own original research.

A Study of Re-ignition Phenomena and Arc Modelling to Evaluate Switching Performance of Low-Voltage Switching Devices

I confirm that:

1. This work was done wholly or mainly while in candidature for a research degree at this University;
2. Where any part of this thesis has previously been submitted for a degree or any other qualification at this University or any other institution, this has been clearly stated;
3. Where I have consulted the published work of others, this is always clearly attributed;
4. Where I have quoted from the work of others, the source is always given. With the exception of such quotations, this thesis is entirely my own work;
5. I have acknowledged all main sources of help;
6. Where the thesis is based on work done by myself jointly with others, I have made clear exactly what was done by others and what I have contributed myself;
7. Parts of this work have been published as: [1], [2], [3], [4], [5], [6], [7].

Signed: .....

Date: .....

This page is intentionally left blank.

## ACKNOWLEDGEMENTS

I would like to express my deepest thanks to my first supervisor, Prof. Igor Golosnoy and second supervisor, Prof. John McBride for their valuable guidance and encouragement that have substantially helped in my work.

I would like to extend my gratitude to technical supporters, Thomas Bull and Timothy Hartley who helped with the arc imaging measurement.

I also acknowledge HE (Hyundai Electric & Energy Systems Co., Ltd.) for funding my study.

I would especially like to thank my wife, Eunae Park, my son and daughter for their support and encouragement.

This page is intentionally left blank.

## LIST OF PUBLICATIONS

1. D. Shin, I. O. Golosnoy, and J. W. McBride, “Numerical analysis of switching performance evaluators in low-voltage switching devices” in *Proc. ISEF*, Spain, 2015.
2. D. Shin, I. O. Golosnoy, and J. W. McBride, “Arc modelling for switching performance evaluation in low-voltage switching devices,” in *Proc. ICEC*, UK, 2016, pp. 41–45.
3. J. W. McBride, D. Shin and T. Bull, “A study of the motion of high current arcs in splitter plates using an arc imaging system,” in *Proc. ICEC*, UK, 2016, pp. 175–180.
4. D. Shin, I. O. Golosnoy, and T. G. Bull, and J. W. McBride, “Experimental study on the influence of vent aperture size and distribution on arc motion and interruption in low-voltage switching devices” in *Proc. ICEPE-ST*, China, 2017, pp. 213 – 217.
5. D. Shin, I. O. Golosnoy, and J. W. McBride, “A study of arc modelling in low-voltage switching devices” in *Proc. COMPUMAG*, South Korea, 2017.
6. **D. Shin, I. O. Golosnoy, and J. W. McBride, “Experimental study of re-ignition evaluators in low voltage switching devices,” *IEEE Trans. Components Packag. Manuf. Technol.*, vol. PP, no. 99, 2018.**
7. **D. Shin, I. O. Golosnoy, and J. W. McBride, “Development of switching performance evaluator and arc modelling tool for low-voltage switching devices,” *COMPEL-Int. J. Comput. Math. Elect. Electron. Eng.*, to be published.**

This page is intentionally left blank.

# CONTENTS

ACADEMIC THESIS: DECLARATION OF AUTHORSHIP.....	III
ACKNOWLEDGEMENTS .....	V
LIST OF PUBLICATIONS .....	VII
CONTENTS .....	IX
ABBREVIATIONS.....	XIII
1 CHAPTER 1: INTRODUCTION.....	1
1.1 Overview .....	1
1.2 Research Motivation .....	3
1.3 Research Objectives.....	5
1.4 Thesis Summary .....	5
2 CHAPTER 2: LITERATURE REVIEW .....	6
2.1 Types of Low-Voltage Switching Devices .....	6
2.1.1 Magnetic Contactors.....	7
2.1.2 Miniature Circuit Breakers.....	8
2.1.3 Moulded Case Circuit Breakers.....	8
2.1.4 Air Circuit Breakers.....	9
2.2 Arcs in Low-Voltage Switching Devices .....	10
2.2.1 Arc Ignition .....	10
2.2.2 Ionisation .....	11
2.2.3 Arc Structure .....	14
2.2.4 Arc Voltage and Current Characteristics .....	19
2.2.5 Arc Temperature obtained by Spectroscopic Analysis.....	21
2.3 Interruption Principles.....	23
2.3.1 Interruption for DC Circuits .....	23
2.3.2 Interruption for AC Circuits .....	25
2.4 Switching Performance of Low-Voltage Switching Devices .....	28
2.4.1 Current Limitation .....	28

2.4.2	<i>Re-ignition Phenomena</i> .....	36
2.5	<i>Arc Modelling in Low-Voltage Switching Devices</i> .....	45
2.5.1	<i>Assumptions and Simplifications for Arc Modelling</i> .....	45
2.5.2	<i>Arc Column Modelling</i> .....	46
2.5.3	<i>Arc Root Modelling</i> .....	53
2.5.4	<i>Arc Modelling Example</i> .....	58
2.6	<i>Summary</i> .....	61
3	CHAPTER 3: EXPERIMENTAL METHODS .....	63
3.1	<i>Purposes of Experiments</i> .....	63
3.2	<i>Switching Tests for Re-ignition Evaluators</i> .....	63
3.2.1	<i>Switching Test Circuits and Conditions</i> .....	63
3.2.2	<i>Waveform Analysis</i> .....	66
3.3	<i>Arc Imaging Measurement</i> .....	73
3.3.1	<i>Overall Set-up</i> .....	73
3.3.2	<i>Flexible Test Apparatus</i> .....	73
3.3.3	<i>Capacitor Discharge System</i> .....	75
3.3.4	<i>Arc Image System</i> .....	76
3.4	<i>Arc Spectra Measurement</i> .....	83
3.4.1	<i>Overall Set-up</i> .....	83
3.4.2	<i>Flexible Test Apparatus</i> .....	84
3.4.3	<i>Spectrometer</i> .....	85
3.5	<i>Summary</i> .....	87
4	CHAPTER 4: EXPERIMENTAL RESULTS AND DISCUSSIONS .....	88
4.1	<i>Re-ignition Evaluators</i> .....	88
4.1.1	<i>Exit Arc Voltage</i> .....	88
4.1.2	<i>Voltage Ratio</i> .....	90
4.1.3	<i>Discussion</i> .....	91
4.2	<i>Arc Motion</i> .....	94



4.2.1	<i>Correlation between Arc Motion and Arc Voltage .....</i>	<i>94</i>
4.2.2	<i>Effect of Vent Size and Distribution.....</i>	<i>101</i>
4.2.3	<i>Discussion.....</i>	<i>106</i>
4.3	<i>Arc Temperature .....</i>	<i>108</i>
4.3.1	<i>Cu I Lines of Emission Spectra.....</i>	<i>108</i>
4.3.2	<i>Calculation of Arc Temperature .....</i>	<i>110</i>
4.3.3	<i>Discussion.....</i>	<i>115</i>
4.4	<i>Summary .....</i>	<i>120</i>
5	CHAPTER 5: ARC MODELLING .....	121
5.1	<i>Methodology of Arc Modelling .....</i>	<i>121</i>
5.1.1	<i>Geometry and Boundary Condition of Arc Modelling.....</i>	<i>121</i>
5.1.2	<i>Lorentz Force.....</i>	<i>123</i>
5.1.3	<i>Current Limitation .....</i>	<i>129</i>
5.1.4	<i>Contact Motion .....</i>	<i>132</i>
5.1.5	<i>Arc Root Formation.....</i>	<i>135</i>
5.1.6	<i>Radiation Losses.....</i>	<i>138</i>
5.1.7	<i>Effect of the V-J Curve on the Arc Voltage at Arc Extinction (Low current Region) ...</i>	<i>141</i>
5.1.8	<i>Flow Chart of Arc Modelling.....</i>	<i>147</i>
5.2	<i>Verification of Arc Modelling .....</i>	<i>148</i>
5.2.1	<i>Temperature Comparison .....</i>	<i>148</i>
5.2.2	<i>Simulation Results without Current Limitation.....</i>	<i>151</i>
5.2.3	<i>Simulation Results with Current Limitation.....</i>	<i>156</i>
5.2.4	<i>Effect of Vent Distribution on Arc Motion.....</i>	<i>159</i>
5.3	<i>Summary .....</i>	<i>163</i>
6	CHAPTER 6: CONCLUSION .....	164
6.1	<i>Summary of Main Findings and Results .....</i>	<i>164</i>
6.2	<i>Future Work.....</i>	<i>166</i>
7	REFERENCES.....	167

APPENDIX A: DETAILS OF ARC IMAGING MEASUREMENT ..... 175

*A1 Experiment Process*..... 175

*A1.1 Resetting FTA*..... 175

*A1.2 Starting Computer Program*..... 177

*A1.3 Charging Voltage in CDS* ..... 177

*A1.4 Setting AIS for Trigger Signal*..... 179

*A1.5 Running Test*..... 180

*A1.6 Discharging Voltage from CDS* ..... 181

*A1.7 Saving Experimental Data* ..... 181

*A2 Preparations for FTA*..... 182

*A2.1 Splitter Plates*..... 182

*A2.2 Filter and Glasses for Optical Fibres* ..... 184

*A3 Rearrangement of FTA after Switching Test*..... 185

*A3.1 Cleaning Window Glasses*..... 185

*A3.2 Adjusting Fixed Contact and Arc Runner* ..... 185

APPENDIX B: ARC IMAGES WITH CONSIDERATION OF CURRENT LIMITATION ..... 186

APPENDIX C: PUBLISHED JOURNAL PAPER ..... 189

## ABBREVIATIONS

AC	Alternating Current
ACB	Air Circuit Breaker
AIS	Arc Imaging System
CDS	Capacitor Discharge System
Cu I	Neutral Copper
DC	Direct Current
DSO	Digital Storage Oscilloscope
FEM	Finite Element Method
FTA	Flexible Test Apparatus
IEC	The International Electro-technical Commission
LVSD	Low Voltage Switching Device
LTE	Local Thermal Equilibrium
MC	Magnetic Contactor
MCB	Miniature Circuit Breaker
MCCB	Moulded Case Circuit Breaker
MHD	MagnetoHydroDynamics
ND	Natural Density
NEC	Net Emission Coefficient
PC	Personal Computer
V-I	Voltage and Current
V-J	Voltage and Current Density
3-D	Three Dimension



# CHAPTER 1: INTRODUCTION

## 1.1 OVERVIEW

An electrical power network is an interconnected grid system for delivering electricity from suppliers to consumers. It is basically composed of power plants that generate the electrical power, transmission lines that transfer high voltage power from transmission substations to distribution ones and distribution lines that connect individual end users (see Figure 1). In order to operate and protect the power network, it is essential to insert switching devices in every line from power stations to final loads. In general, each switching device varies with the location and electrical rating such as high, medium and low voltage devices [8].

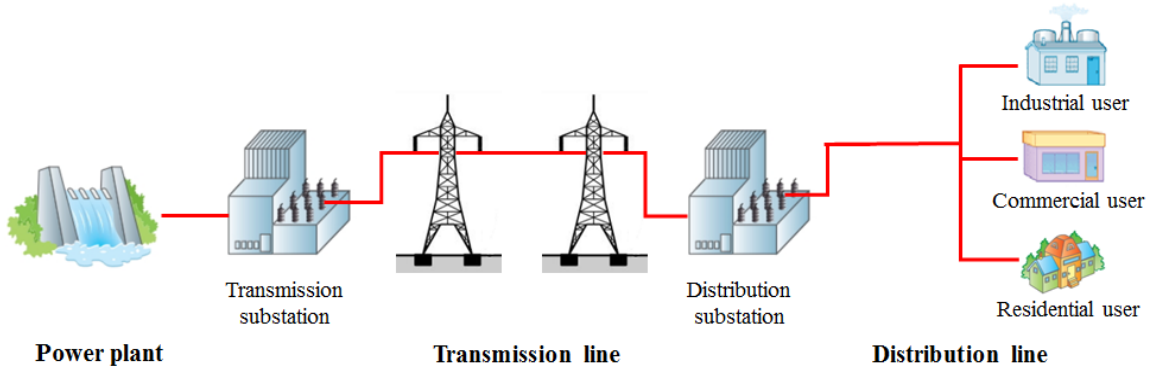


Figure 1 Electrical power network.

Low-voltage switching devices (LVSDs) are usually utilized to turn on and off AC or DC current in the distribution power network by industrial, commercial and residential users. The primary functions of LVSDs are to carry, make and break the current under normal circuit conditions as well as to clear fault currents and to ensure safety for both humans and other connected equipment against overload or short circuit accidents. They are essential for end users as switching and protective devices.

In general, a LVSD consists of three main parts, namely, a trip unit, an operating mechanism and a quenching chamber as shown in Figure 2. The trip unit is a current sensing and triggering element that drives the operating mechanism to break the current in the event of short circuit or prolonged overload current. The operating mechanism moves the movable contact towards the opening or closing direction either manually or automatically. The quenching chamber is an interruption volume where the arc is established, elongated, and finally extinguished after contact separation.

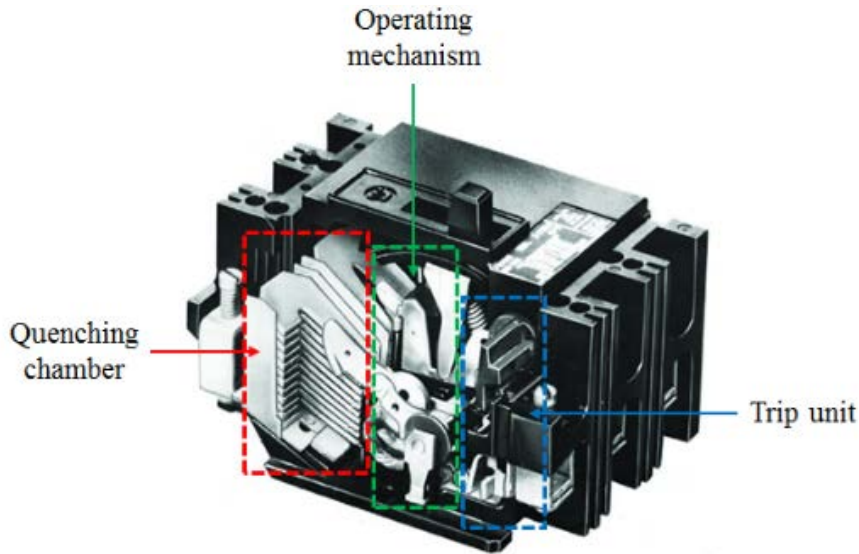


Figure 2 Basic structure of LVSDs [9].

The quenching chamber of a LVSD is the main volume to interrupt the current and consists of a movable and fixed contact, splitter plate, side plate, magnetic yoke and vent as shown in Figure 3. When the movable contact separates from the fixed contact, an arc is established in the contact gap which then moves towards the splitter plates by the combination of gas flow and Lorentz forces. After the arc enters the splitter plates, there is an increase in the arc voltage resulting from the multiple anodic and cathodic potential drops associated with the surface interactions with the splitter plates. In the case of AC system, the arc is ideally extinguished at the first current zero moment, however the arc can re-ignite beyond this point. During the interruption process described above, the arc behaviour inside the quenching chamber is a main factor to guarantee the successful arc interruption without re-ignition; therefore, investigating arc behaviour is fundamental in prediction of a LVSD performance.

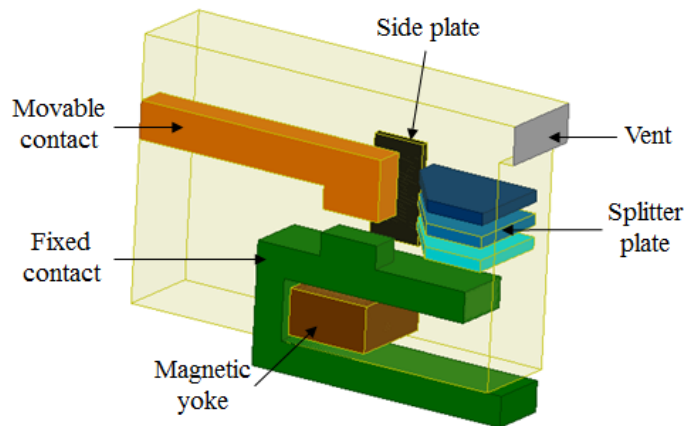


Figure 3 Basic structure of quenching chamber.

## 1.2 RESEARCH MOTIVATION

A LVSD (AC or DC switching devices) should have a good reliability since its switching failure under fault current can lead to the loss of human lives and properties. Apart from this top priority of a LVSD, there are two main present trends in the LVSD market. Customers demand a more compact product with higher breaking capacity. Secondly, the need of DC switching devices has gradually increased as the installation of DC network steadily increases; for example in a sector of photovoltaic power generation and data centres. Normally, higher breaking capacity requires a larger chamber space due to the greater arc energy and DC switching is more difficult than AC switching due to no natural current zero point in DC system. It is a challenging work to design a compact AC LVSD with high breaking capacity and a DC LVSD. In order to design a reliable LVSD meeting present trends, effectively, it is essential to predict switching performance and to improve a LVSD prior to manufacturing a real device. Without prediction and improvement of switching performance, it will take much more cost and time to develop a reliable compact AC or DC LVSD.

There are two main factors to determine LVSD's switching performance; current limitation and re-ignition. The device improvement can be achieved by enhancing current limitation without re-ignition phenomenon during the switching process. Numerous empirical studies have been carried out in an attempt to improve the switching performance based on current limitation, for example [10], [11]. However, there has been little detailed investigation of re-ignition phenomena and an evaluator to predict re-ignition, even though avoiding re-ignition is a key goal when designing the quenching chamber. Numerical simulation has been widely used in improvement and prediction of switching performance of LVSDs, for example [12], [13]. Most of simulation work has focused on current limitation phenomenon and behaviour of the arc plasma prior to the current zero moment without evaluating re-ignition following the current zero point. Empirical investigation based on the wide range of switching data is necessary to confirm a reliable re-ignition evaluator. Also, the numerical simulation evaluating both re-ignition phenomena and current limitation is required to design a LVSD effectively.

It is known that arc motion has a significant influence on the arc voltage that is one of the main characteristics in the air arc. The effect of arc motion on the arc voltage has been investigated by comparing the arc trajectory with the arc voltage. However, there has been little empirical work about detailed arc motion in the splitter plate region and its effect on the arc voltage. The understanding of arc motion in the splitter plates region can benefit to design the quenching chamber.

The vent condition is one of the key factors to influence arc motion in the LVSD chamber; in general, the wider vent helps to increase the arc motion velocity. Practically, the size of vent area is limited to

prevent the chamber contamination from the outside matter like dust. The distribution of vent apertures (under the condition of the same overall vent size) can be the design parameter to improve arc motion; but, its effect has not been closely examined.

The arc imaging system has been used to investigate arc motion by capturing the arc light intensity. It is assumed that the light intensity is related to the arc temperature. But, there has been no detailed empirical study about the correlation between the light intensity and arc temperature. If we prove that the arc light intensity represents the arc temperature, arc modelling can be validated by comparing the simulated temperature distribution and measured light intensities.



### 1.3 RESEARCH OBJECTIVES

1. To investigate a re-ignition evaluator of LVSDs based on the switching data of various kinds of test conditions and to propose a reliable evaluator.
2. To develop a 3-D arc model evaluating switching performance (current limitation and re-ignition) of a LVSD and to validate the simulation results with experimental data, especially measured arc images.
3. To find the correlation between arc motion and arc voltage in the region of splitter pates.
4. To investigate the effect of vent condition, especially vent distribution, on the arc motion.
5. To prove that the light intensity measured by the arc imaging system (AIS) is related to the arc temperature.

### 1.4 THESIS SUMMARY

Chapter 1 deals with the overview of LVSDs, research motivation, objectives and thesis summary.

Chapter 2 describes literature reviews. The topics included here are: types of LVSDs, arc characteristics, interruption principles, switching performance and arc modelling in LVSDs.

In Chapter 3, a description of the experimental set-up is given. Switching tests of miniature circuit breakers (MCBs) and moulded case circuit breakers (MCCBs) are conducted for re-ignition investigation. The arc image measurement is carried out to record arc motion in the overall chamber. Arc spectra are measured with the aim of obtaining the arc temperature.

Chapter 4 tells the experimental results and discussions. The new evaluator for re-ignition prediction is proposed based on the switching data of various test conditions. The arc motion is investigated through the arc imaging measurement and the correlation between arc temperature and the arc light intensity is explained.

In Chapter 5, arc modelling based on the magnetohydrodynamics (MHD) theory is described. There are explanations about modelling methodology including improvement of arc voltage calculation in the low current region. In addition, the verification of arc modelling is presented by using experimental data.

Chapter 6 summarizes the overall conclusion and suggests further works.

## CHAPTER 2: LITERATURE REVIEW

### 2.1 TYPES OF LOW-VOLTAGE SWITCHING DEVICES

LVSDs are electro-mechanical devices that are inserted in circuits covering up to 1000 V AC or 1500 V DC (rating definition by IEC standard [14]) for the purpose of making, carrying and breaking current under normal circuit conditions and also making, carrying for a particular time and breaking currents under abnormal circuit conditions such as short circuit accidents (see Figure 4) [8], [15]. In general, LVSDs can be classified by type, as magnetic contactors (MCs), miniature circuit breakers (MCBs), moulded case circuit breakers (MCCBs) and air circuit breakers (ACBs) (see Figure 5).

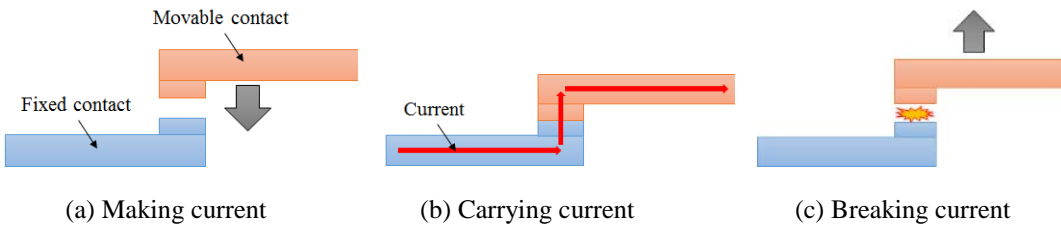


Figure 4 Functions of LVSDs.



(a) Magnetic Contactor



(b) Miniature Circuit Breaker



(c) Moulded Case Circuit Breaker



(d) Air Circuit Breaker

Figure 5 Types of LVSDs (Courtesy of Hyundai Electric & Energy Systems Co., Ltd. (HE)).

### 2.1.1 MAGNETIC CONTACTORS

The MC is a switching controller for motors, capacitor banks, lights and other electrical loads. Unlike other LVSDs, the MC is not capable of dealing with short-circuit currents. Its primary function is to switch on and off the normal circuit. The switching range is up to a 800A rated current under the AC 440V circuit condition [16]. Figure 6 shows a structure of the magnetic contactor comprising the quenching chamber and an electromagnet (which corresponds to the operating mechanism of other LVSDs). The electromagnet has a movable core, a fixed core, a main coil, shading coils and a return spring. The mechanism is energized by an external AC or DC power source connected to the main coil that provides the driving force for the movable contact. When an external control current flows through the main coil, an attractive magnetic force between the movable and fixed core is generated, and the movable contact travels towards the fixed contact along with the movable core. An electromagnet powered from a DC power source produces a constant magnetic force resulting in a stable closed state. However, an AC power source produces an alternating magnetic field resulting in null magnetic force on the movable core twice in each cycle. A shading coil helps prevent the magnetic force from dropping to zero [17]. When the main coil is de-energized, the movable contact separates from the fixed one by means of the driving force of the return spring, and then the electric circuit is switched off.

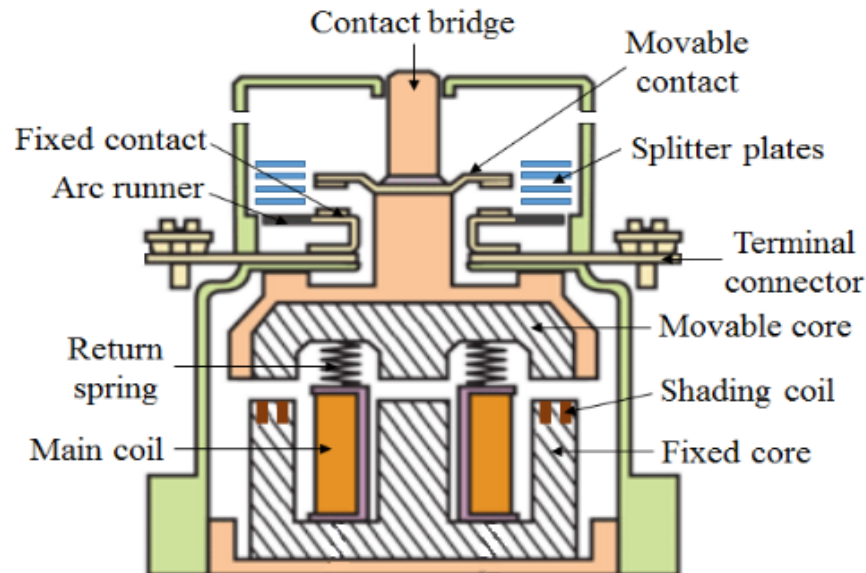


Figure 6 Structure of magnetic contactors [18]; 70mm(W) × 140mm(H) × 128mm(D) dimensions based on a 100A rated 3 pole MC made by HE.

### 2.1.2 MINIATURE CIRCUIT BREAKERS

The MCB is a small and compact switching device, which is widely used for protecting circuits against fault current in domestic and light industrial electrical installations. It has the range of up to a 125 A rated current and 15kA breaking capacity under the AC 460V circuit condition. Figure 7 illustrates the internal structure of an MCB. The current flows through conducting parts that are a line terminal, a bi-metal strip, a movable contact, a fixed contact, a solenoid, and a load terminal. The bi-metal strip, which is made of two metals of different thermal expansion coefficients, bends triggering the opening operation by the thermal effects of a long term overload current. In contrast, the solenoid is an instantaneous trip unit to release the operating mechanism by short-circuit currents. The operating mechanism can be manually activated by the user through a handle mechanism.

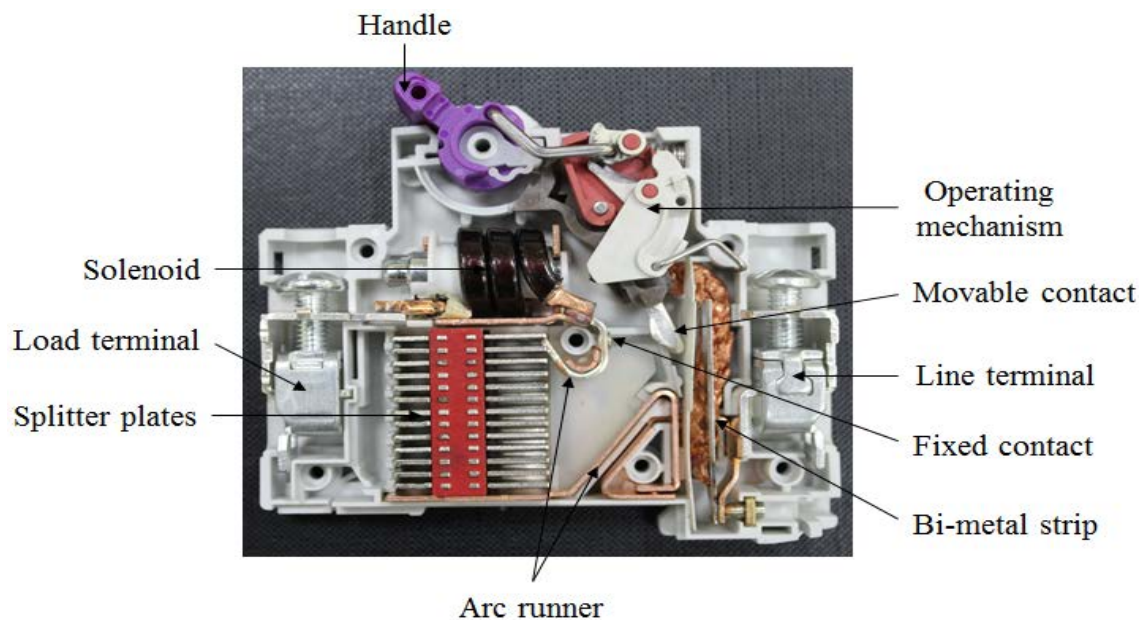


Figure 7 Structure of miniature circuit breakers (Courtesy of HE); 80mm(W) × 80mm(H) × 74mm(D) dimensions based on a 125A rated 3pole MCB made by HE.

### 2.1.3 MOULDED CASE CIRCUIT BREAKERS

The MCCB is entirely enclosed by a plastic housing and sometimes adopts dual quenching chambers to enhance the breaking performance like the model shown in Figure 8. The rated current covers up to 1600A and the breaking capacity is up to 150kA under the 460V AC circuit condition. The tripping operation of the MCCB is similar to that of the MCB. The movable contact of most MCCBs and

MCBs starts to open by means of the repulsion force (the Lorentz force which is derived from the current path through conductors and from the current constriction between contacts) before a trip unit releases the operating mechanism when short-circuit currents flow through the product [19]. This action, called ‘auto-protection’, is stronger in MCCBs than in MCBs because of higher currents. The auto-protection function influences the switching process of LVSDs as it normally determines the start of the arc ignition and the motion of the movable contact.

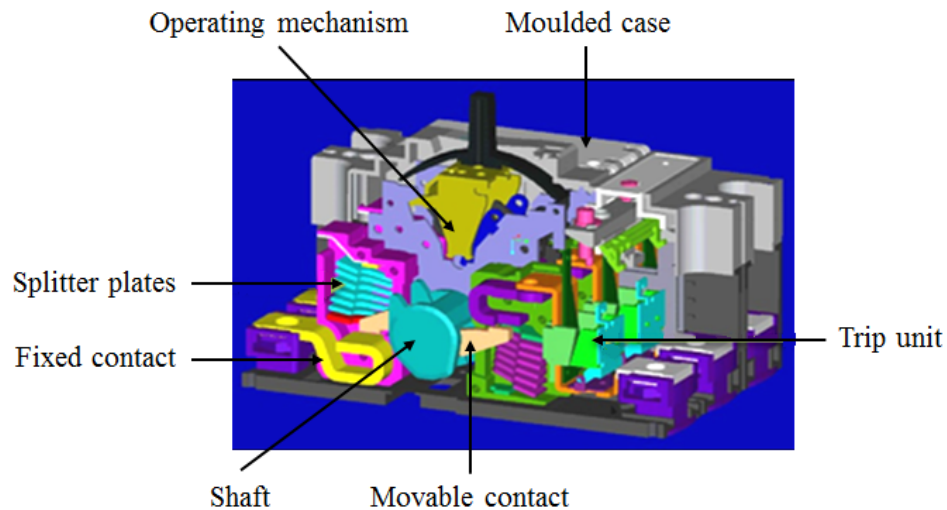


Figure 8 Structure of moulded cased circuit breakers (Courtesy of HE); 75mm(W)  $\times$  130mm(H)  $\times$  82mm(D) dimensions based a 100A rated current 3pole MCCB made by HE.

#### 2.1.4 AIR CIRCUIT BREAKERS

The ACB has a bigger and more complex structure than other LVSDs. The size is the dimension of 328mm(W)  $\times$  460mm(H)  $\times$  368mm(D) for a 2000A rated current 3pole ACB made by HE. It covers up to a 6300A rated current and a 100 kA breaking capacity under the 460V AC circuit condition. Although the inner structure of the ACB is similar to the MCCB, most of its components can be accessed for inspection and can be replaced in the event of their malfunction. In addition, the ACB has the specific task of withstanding large short-circuit currents for a while (normally one second), in order to allow smaller and faster switching devices, installed in the network immediately before the fault location to clear the fault currents prior to the operation of the ACB.

## 2.2 ARCS IN LOW-VOLTAGE SWITCHING DEVICES

Air at ambient conditions (300 K and 1 atm) is a good insulating medium which is enough to withstand the electric field under the low voltage condition. But, during the switching process of a LVSD, air is transformed into the conductive medium, the arc plasma, and the current flows through it.

In this section, the fundamental characteristics of the air arc (the process of an arc ignition, ionisation, the arc structure, voltage characteristics and arc temperature) are described.

### 2.2.1 ARC IGNITION

The arc ignites between contacts during the switching operation of a LVSD by the opening movement of a movable contact. In [20], Jeffery presented the arc ignition process in consecutive order by showing the change of the contacting area for the current flowing (see Figure 9).

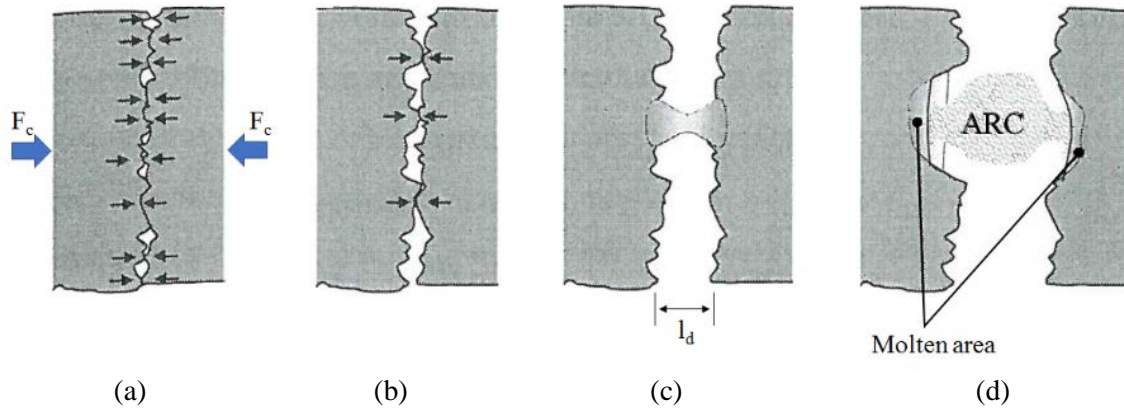


Figure 9 Process of the arc ignition between contacts [20]

Electric contacts can carry current through the physical connected contact area where the contact force,  $F_c$  is applied (see Figure 9 (a)). In general, the real contact area where current flows occupies the small fraction of area in the total apparent contact area due to practical surface roughness [21]. The contact resistance of the real area of contact is given by

$$R_c = \frac{\rho}{2a} = \frac{\rho}{2} \sqrt{\frac{\pi H}{F_c}}, \quad (1)$$

where  $a$  is the radius of the actual area of contact ( $m$ ),  $H$  is the hardness of contact material ( $N/m^2$ ),  $\rho$  is the resistivity ( $\Omega m$ ) and  $F_c$  is the normal contacted force ( $N$ ). As the movable contact begins to open, the contact force decreases resulting in reduced the real contact area and contact resistance increases (see Figure 9 (b)). The rise in the contact resistance results in a rise of temperature of the contact spot through the ohmic heating. When the temperature of the contact spot reaches the melting point of the contact material, the contact spot melts. As the movable contact continues to part from the fixed contact, a molten metal bridge is formed at the final contact point (see Figure 9 (c)). After formation of the molten bridge, it stretches and its diameter diminishes as the contacts separate. Hence, the temperature of the molten bridge rises by further increase in ohmic heating. Finally, the molten bridge reaches boiling temperature and ruptures, releasing metal vapour (see Figure 9 (d)). This metal vapour is the precursor of the arc between the contacts in the quenching chamber of a LVSD. As above, the process of an arc ignition in a LVSD is complicated and it is hard to simulate this process; normally, the simplified numerical technique is used for the arc ignition.

### 2.2.2 IONISATION

Ionisation is the process in which an atom or a molecule loses electrons resulting in a net positive charge called a positive ion. The ions and electrons transform air into a plasma which is a conductive medium. The thermal energy (heat) and electric field can be the main source of ionisation mechanism in the circuit breaker.

#### *Thermal ionisation*

The mean kinetic energy of molecules and atoms can be expressed as a function of the temperature,

$$\frac{1}{2}mv^2 = \frac{3}{2}kT \quad (2)$$

where  $m$  is the mass of molecules or atoms ( $kg$ ),  $v$  is the mean velocity ( $m/s$ ),  $k$  is Boltzmann's constant ( $J/K$ ) and  $T$  is the absolute temperature ( $K$ ). If heat is progressively applied to the molecular gas, the kinetic energy increases to a point where sufficient energy is available to overcome the binding energy of the molecules, which causes the molecules to dissociate into individual atoms. By heating further, the atoms lose their electrons and achieve an ionisation state. This phenomenon is called thermal ionisation.

In [21], Slade explained the ionisation process by showing the multiple ionisation of nitrogen and oxygen associated with the temperature. Figure 10 illustrates the relationship between the densities of nitrogen and oxygen particles as a function of the temperature under the 1 atm condition. If air is provided with sufficient energy, the oxygen and nitrogen molecules start to dissociate and change into O and N (electrically neutral atoms) at around 1500 K and 2500 K, respectively. Also, the recombination happens and both NO and NO<sub>2</sub> are generated from N<sub>2</sub> and O<sub>2</sub>. When the temperature exceeds about 6500 K, the oxygen and nitrogen atoms begin to ionize (N<sup>+</sup> and O<sup>+</sup> ions) releasing electrons. At much higher temperature, there is the second ionisation in the N<sup>+</sup> and O<sup>+</sup>, which leads to the creation of N<sup>++</sup> and O<sup>++</sup> ions and emission of additional electrons. If oxygen and nitrogen are ionized by creating positive ions and negative electrons as above, air becomes an electrical conductive state termed air plasma. This plasma is generally called an arc when it is formed between electrical contacts in switching devices or welding tools. Therefore, the air arc can be considered as a mixture of ions and electrons generated from the air, which has sufficient electrical conductivity for carrying current.

It is known that, in the LVSDs, thermal ionisation plays a significant role in sustaining the air arc because ohmic heat generates sufficient energy for ionisation when the arc current flows through the plasma [8].

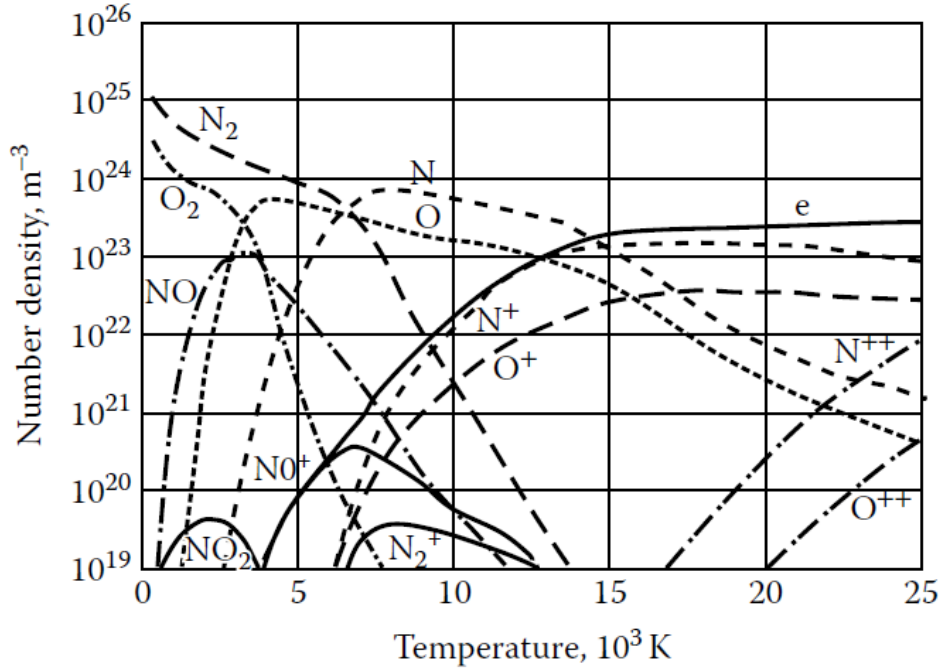


Figure 10 Ionisation of air plasma as a function of temperature at 1 atm [21].



### *Ionisation by Electric Field*

The high electric field can be another factor in air ionisation. When the electric field is applied across a gas that has some free electrons, the electrons can experience two types of collision with the gas molecules: elastic collision or inelastic collision. The electron preserves its kinetic energy after an elastic collision, because the mean energy loss is negligible owing to much less mass of the electron compared to that of heavy particles (ions, atoms or molecules). The electron gradually takes more energy from the electric field and eventually its energy can cause an inelastic collision with heavy particles leading to dissociation, excitation and ionisation. If the electron's kinetic energy is equal to or greater than the ionisation energy, the ionisation collision will occur and other electrons are released (additional positive ions and electrons are formed). Slade described the ionisation process by electric field by showing the collisions between an electron and a gas molecule or atom (see Figure 11) [21]. When a 30 kV voltage is applied across a 10 mm gap of the contact, the electron is accelerated and collides with heavy particles. If the electron mean free path  $\lambda_e$  (the average distance of the electron's travel between collisions) is 1  $\mu\text{m}$ , the electron gets 3 eV energy between collisions from  $eE\lambda_e$  ( $e \times 3 \times 10^6 \text{V m}^{-1} \times 10^{-6} \text{m}$ ). Ionisation (the electron release from an atom) takes place in the fifth collision while the electron accumulates the kinetic energy by travelling in the gas.

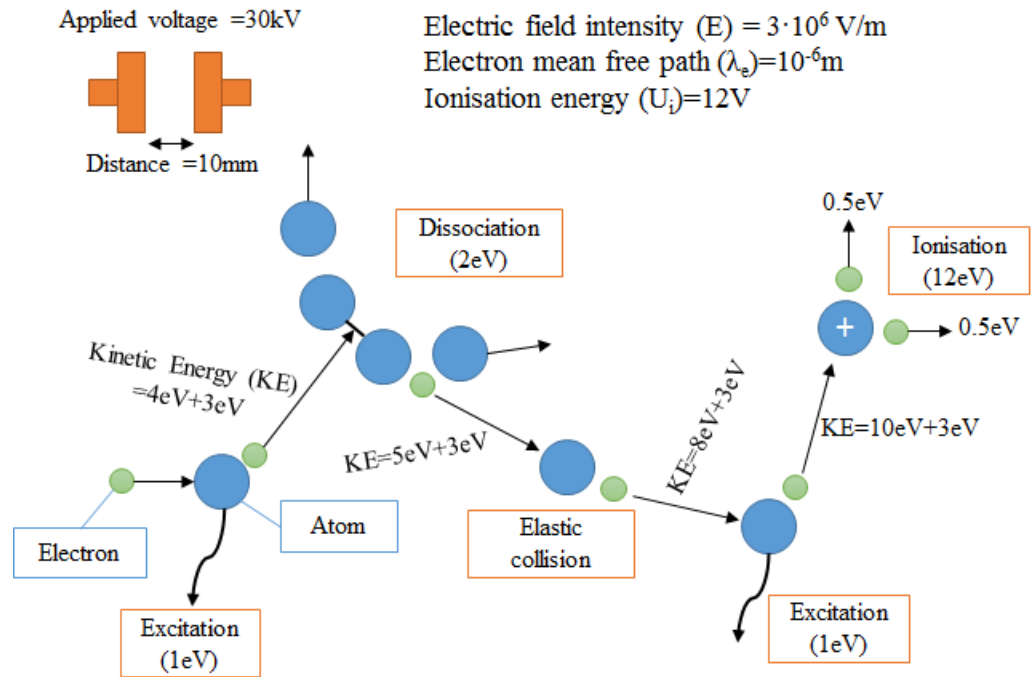


Figure 11 Possible interactions between heavy particles and electrons accelerated by an electric field; it is assumed that electron get 3 eV energy from the electric field and ionisation energy is 12 eV [21].

### 2.2.3 ARC STRUCTURE

The air arc is formed of three regions: an arc column, a cathode root and an anode root. Figure 12 shows an idealised structure of the air arc together with its voltage characteristic. It is seen that the voltage drop is not evenly distributed over the air arc. Most of voltage drop of the arc takes place in the cathode and anode roots near the contacts or splitter plates.

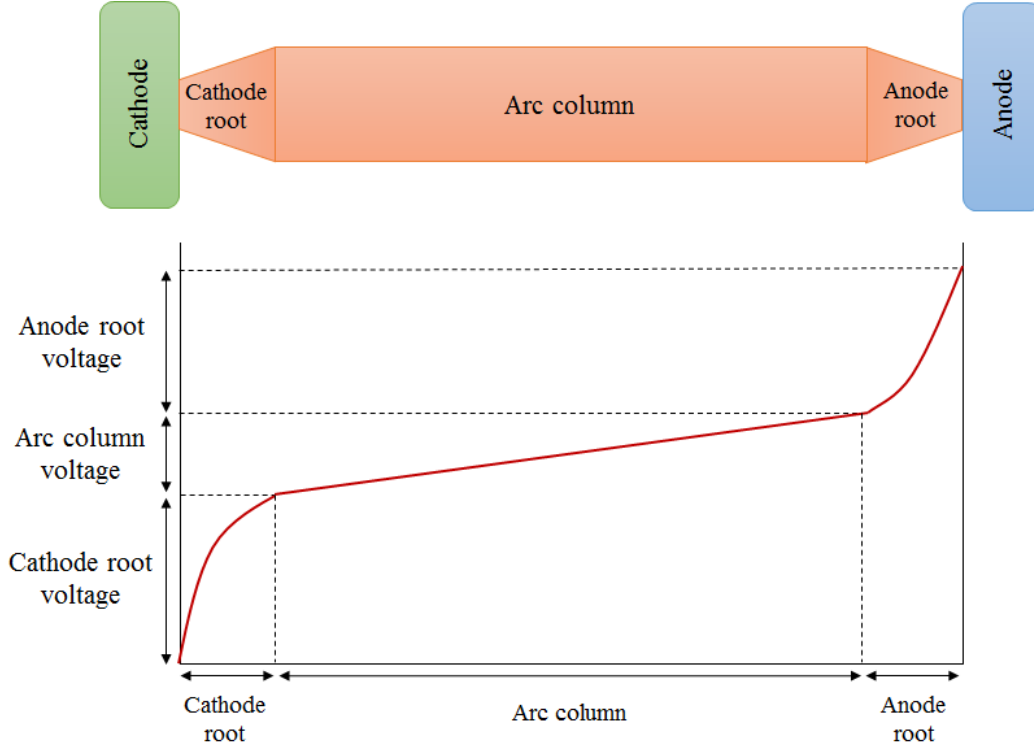


Figure 12 Schematic of the air arc with the corresponding voltage drops [21].

#### *Arc Column*

The arc column in a LVSD is regarded as the plasma. It consists of a hot mixture of ions, electrons and neutral gases, which allows a continuous thermal ionisation process via sufficient ohmic heating. Inside the arc column, the number density of the electrons is equal to that of the ions. It is regarded that all ions, electrons and gases have the same temperature, namely local thermal equilibrium (LTE). As a result of LTE, the arc column can be considered as a single hot gas, which satisfies the conservation equations for mass, momentum and energy. Based on the assumption of the LTE condition, it is possible to simulate the arc column by using the magnetohydrodynamics (MHD)

theory. The electrical conductivity is high enough to carry the large current with a small voltage drop in the arc column. The arc column has a uniform voltage gradient that varies with the arc current, temperature and pressure. From the arc simulation, we can calculate the voltage drop in the arc column based on the electrical conductivity of air.

### *Arc Roots*

The arc root is a thin region between an arc column and a contact or splitter plate. The arc root can be divided into two layers, the space charge layer and ionisation layer, as shown in Figure 13 [22]. They are also called sheath and presheath layers. The space charge layer is a region where quasi-neutrality and LTE conditions do not hold; whereas, quasi-neutrality holds in the ionisation zone under thermal non-equilibrium condition. The special treatment is required to consider the effect of the arc root into account in arc modelling since the LTE condition does not hold. There have been numerous theoretical studies of the arc root; however, the understanding of detailed physic is still limited due to the lack of measured data in the thin layer.

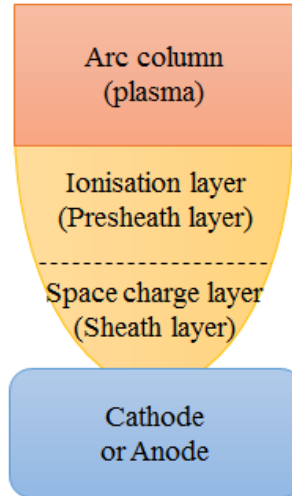


Figure 13 Structure of an air arc near a cathode or anode [22].

Macroscopic measured quantities can be used to identify the characteristics of the arc roots. Yokomizu *et al.* estimated the sum of the voltage drop in the cathode and anode roots of the four different gases including air at the pressure of 0.1 MPa by measuring the arc voltage between iron,

copper and titanium contacts [23]. Figure 14 shows the experimental set-up to measure the voltage drop of the arc roots (cathode and anode voltage drops). The arc is established from a 0.05 mm copper wire and a 60 Hz sinusoidal current of 330 A or 550 A (peak value) flows through it. The contact gap is adjusted to 0.2, 0.5, 1 and 3 mm at a given current.

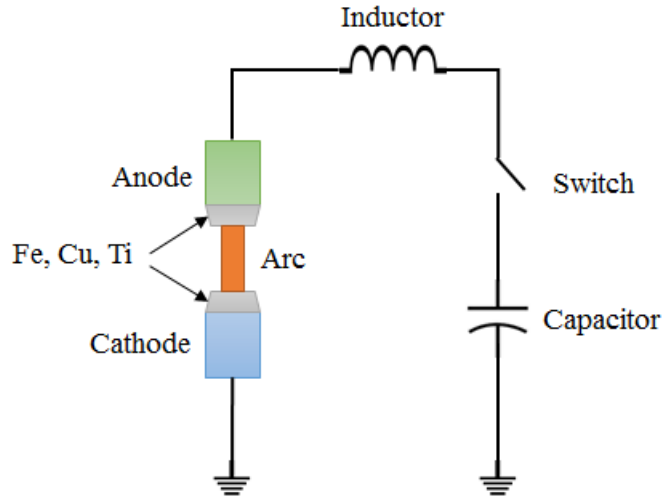


Figure 14 Experimental set-up to measure the arc root voltage of the air arc under the atmospheric condition [23].

Figure 15 shows the helium arc voltage measured between the Ti electrodes as a function of a contact gap at the peak current value of 330 A and 550 A. It is seen that the arc voltage decreases as the

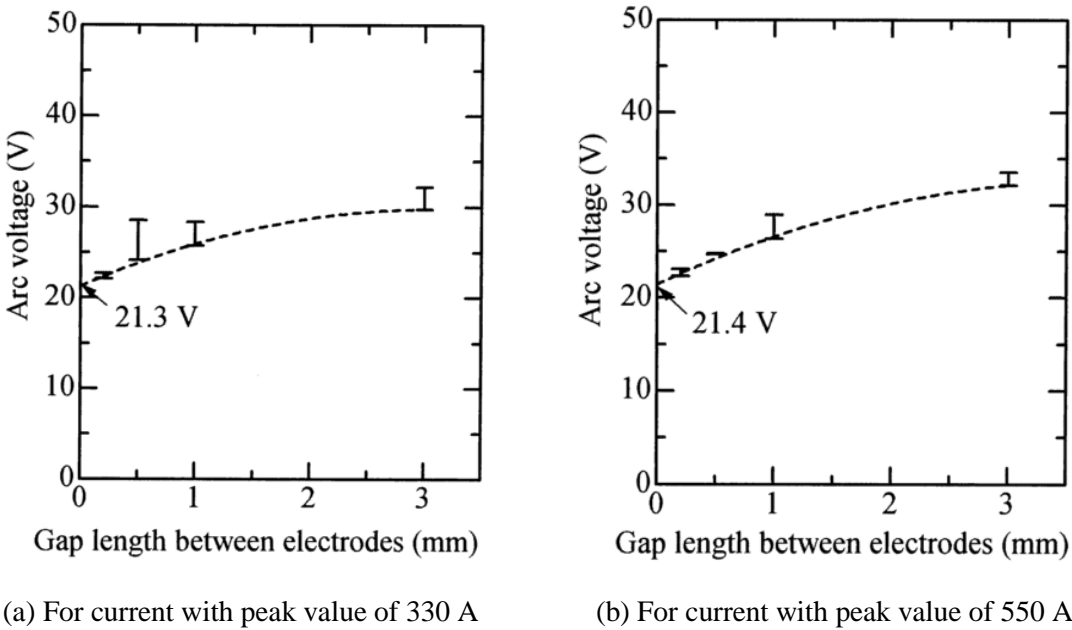


Figure 15 Voltage drop of helium arc as a function of gap length between Ti electrodes at a pressure of 0.1 MPa for AC currents with peak values of 330 A and 550 A [23].

contact gap decreases. The voltage at the zero contact gap is regarded as the sum of the voltage drops in the cathode and anode roots because the arc root region is extremely thin. It is obtained by extrapolating the curve. The voltage drop at the zero contact gap is independent of the arc current; 21.3 V for the peak current of 330 A and 21.4 V for the peak current of 550 A are observed.

Figure 16 shows the voltage drop at the zero contact gap of helium, SF<sub>6</sub>, argon and air arcs at a pressure of 0.1 MPa for Fe, Cu and Ti contacts. It is found that the sum of voltage drops in the cathode root and anode root of the air arc between the iron contacts and copper contacts is 16.6 V and 16.5 V in the air arc, respectively. In our research, 16.6 V is chosen for the arc root voltage on the surfaces of the splitter plates and copper electrodes since, normally, the number of the iron arc root is dominant in a LVSD.

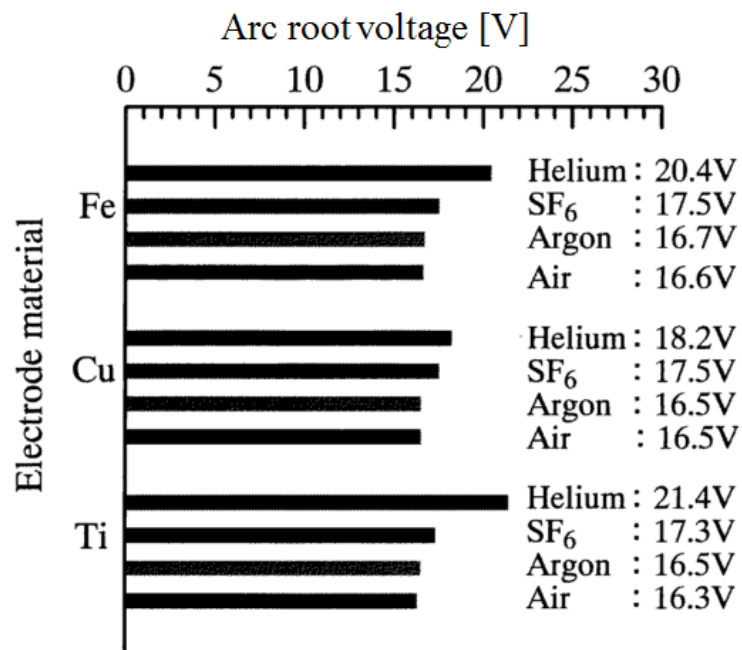


Figure 16 Voltage drop at the zero contact gap (arc root voltage) of helium, SF<sub>6</sub>, argon and air arcs at a pressure of 0.1 MPa for Fe, Cu and Ti contacts [23].

We do not know the specific values of each cathode and anode root in the air arc; however, the sum (16.6 V) of the voltage drops in the arc roots is useful to calculate the arc characteristics of a LVSD during the switching process through arc modelling.

### - Cathode Root

The cathode root is characterized by a strong electric field of  $10^8 - 10^9$  V/m, steep thermal gradient and high current density [21]. The cathode is the source of the electrons in the arc; hence, the arc extinguishes if the cathode does not provide these electrons. The emission of electrons requires to get more energy than the work function of a material. There are two primary emission mechanisms for the electrons: thermionic emission and field emission.

If the cathode is made of refractory materials that have high melting points such as tungsten, molybdenum and carbon, it can release electrons by cathode heating termed thermionic emission [9]. Heating at the cathode surface is caused by particle bombardment, thermal conduction and radiation from the arc column. The current density in the thermionic emission can be given by the Richardson-Dushman equation,

$$j_T = AT^2 \exp\left(\frac{-\Phi}{kT}\right), \quad (3)$$

where  $j_T$  is the current density (A/m<sup>2</sup>),  $A$  is the material constant (A/(m<sup>2</sup> K<sup>2</sup>)),  $T$  is the temperature of the cathode (K),  $\Phi$  is the work function of the material (eV or J) and  $k$  is Boltzmann constant (J/K). Thermionic emission takes place in refractory materials when their temperature does not reach the melting point.

In general, most of LVSDs have cold cathodes (non-refractory material) such as copper, silver or iron, which have lower melting points than those of the refractory materials. Thermionic emission cannot occur in the cold cathode. In order to explain the electron emission from the cold cathode, ‘non-thermionic’ theories have been suggested; however, there is no single theory which can fully explain the electron emission from the cold cathode [24]. The electric field can be one of the main parameters contributing to the cold cathode emission. The high electric field can increase the electron emission by decreasing the effective work function, known as the Schottky effect [25]. The current density in the field emission is determined by the electric field and the work function of the cathode material according to the Fowler-Nordheim equation,

$$j_F = 1.6 \times 10^{-2} \left( \frac{E^2}{\Phi} \right) \exp\left( -7 \times 10^9 \Phi^{\frac{2}{3}} \frac{F}{E} \right), \quad (4)$$

where  $j_F$  is the current density (A/m<sup>2</sup>),  $E$  is the electric field (V/m) and  $F$  is a numerical factor.

In general, it is known that the electron emission from the cold cathode is associated with a combination of ‘thermally enhanced field emission’ and the ion bombardment [21].

#### *- Anode Root*

The anode acts as an electron collector. The electrons emitted from the cathode pass through the arc column and enter the anode. There is a negative space charge layer in the anode root where the electrons can be accelerated to provide the necessary high current density at the anode surface [25]. When they hit the anode, they deliver their energy to the anode and heat the anode spot to a high temperature. A high temperature near the anode spot can contribute to the generation of positive ions in the anode root. Positive ions formed in the anode root are driven to the arc column.

In general, the anode root has a less voltage drop than the cathode root. This voltage drop in the anode root plays a role in adjusting the arrival rate of electrons at the anode surface in order that current continuity is achieved at the interface between the plasma column and metal [26].

#### *2.2.4 ARC VOLTAGE AND CURRENT CHARACTERISTICS*

The arc voltage including the voltage drops in the arc column and arc roots varies with the current for a fixed contact gap in the case of a free-burning arc. Figure 17 show the arc voltage as a function of

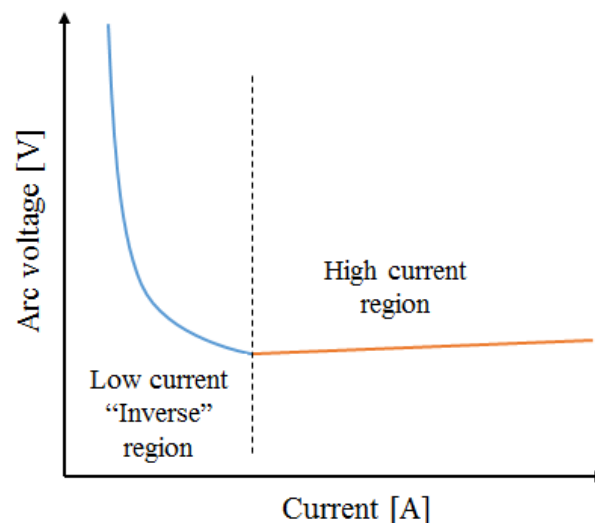


Figure 17 Arc voltage and current characteristic [27].

the current [27]. In the low current region (typically below 100A), there is the negative characteristics of the arc voltage (the arc voltage increases as the current decreases), called the negative V-I curve. For the high current, the arc voltage increases slightly with the current. This characteristics is varies with the contact material and pressure.

Mentel *et al.* carried out the empirical investigation about the voltage drops of the cathode and anode root in the range of 1 to 10 A current by using the Langmuir probes [28]. Figure 18 shows the comparison of total voltage, cathode voltage and anode voltage of an Ar arc under the condition of 0.26 MPa pressure. It is observed that the voltage drop in the cathode root strongly depends on the arc current whereas the anode voltage is almost constant. The total arc voltage increases as the current decreases; but its variation is determined by the change of the cathode root voltage.

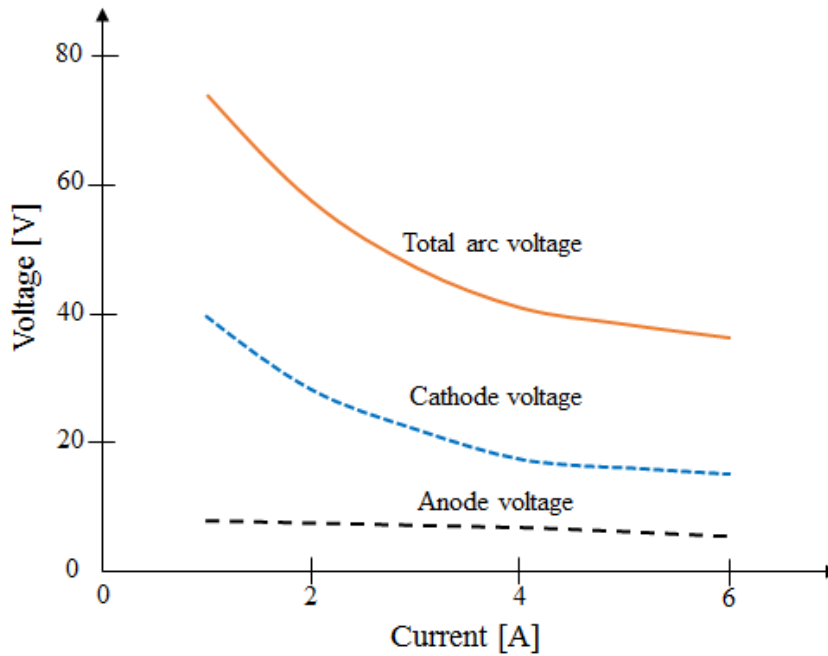


Figure 18 Comparison of total arc voltage, cathode voltage and anode voltage of an arc in 0.26 MPa Ar [28].

Wendelstorf explained that the increase of the cathode voltage is required to sustain the arc in the low current region [29]. Figure 15 shows the effect of the cathode voltage in the space charge layer on the electron emission and ionisation. Below a certain current, the thermal energy is not enough to sustain the arc. The increase in the cathode voltage can accelerate ions towards the cathode surface and increase the temperature of the surface by ion bombardment, enhancing thermionic emission. It



can also help improve the electron emission by the electric field and provide electrons with sufficient kinetic energy to achieve ionisation.

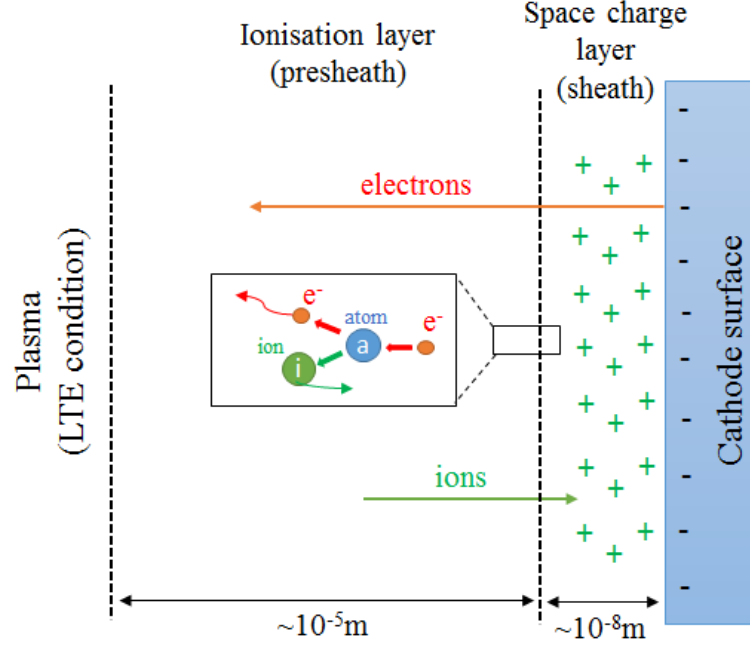


Figure 19 Ionisation and space charge layers of the cathode root [29].

The negative V-I characteristics contributes to the increase of the arc voltage near the current zero point during the switching process of a LVSD. It is essential to consider this phenomenon in order to evaluate the switching performance (especially re-ignition prediction) accurately. Based on the background physics of the negative V-I curve, the calculation method of the arc voltage near the current zero point is investigated in this research.

### 2.2.5 ARC TEMPERATURE OBTAINED BY SPECTROSCOPIC ANALYSIS

Temperature is one of the most important parameter in the arc plasma. There are some paper about the temperature measurement through the spectroscopic analysis. Slade *et al.* investigated the air arc temperature in a 9.6 mm gap through the absolute values of N II line spectra [30]. They found that the arc temperature is in the range of 20000 K to 23000 K when the 1100 A peak AC current flows through a free-burning arc. Li *et al.* analysed the arc temperature qualitatively associated with gassing

material (polymethylmethacrylate) inside a quenching chamber and investigated the effect of gassing material on the switching performance [31]. They found that the gassing material improves the switching performance since the arc can be cooled rapidly due to ablation of the gassing material. Takeuch *et al.* measured relative intensities of Ag I spectra from the air arc between Ag contacts and obtained the temperature of around 7000 K under the condition of a DC 50 V supply voltage and 3.3 A current [32].

Despite previous studies, there is little empirical work correlating the arc temperature and the light intensity measured by a photodiode (of the AIS), which is widely used to investigate the arc motion in a LVSD chamber. This thesis covers the study about the relationship between the arc temperature and the light intensity measured by the AIS. The arc temperature is estimated by the Boltzmann plot method. The Boltzmann plot method is widely used to evaluate arc temperature based on the relative intensities of the same species at a different wavelength. In the LTE state, the intensity ratio of two spectral lines can be given as follows,

$$\frac{I_1}{I_2} = \frac{g_1 A_1 \lambda_2}{g_2 A_2 \lambda_1} \exp\left(-\frac{E_1 - E_2}{kT}\right), \quad (5)$$

where,  $I_1$  and  $I_2$  are the intensities of the emission spectral lines,  $A_1$  and  $A_2$  are the transition probability (the probability per second that an electron de-excites from a specific upper state to a lower state, leading to photon emission),  $g_1$  and  $g_2$  are the statistical weights of the respective states,  $E_1$  and  $E_2$  are the energy levels,  $k$  is the Boltzmann constant, and  $T$  is the temperature in K. We can obtain (6) by taking the logarithm in both side of (5),

$$\ln\left(\frac{I_1 \lambda_1}{g_1 A_1}\right) - \ln\left(\frac{I_2 \lambda_2}{g_2 A_2}\right) = -\frac{E_1 - E_2}{kT} + C, \quad (6)$$

where,  $C$  is a constant. If we plot a straight line from  $E$  (energy level) in the horizontal axis and  $\ln(I\lambda/gA)$  in the vertical axis, the temperature is calculated from the slope of a line.

## 2.3 INTERRUPTION PRINCIPLES

Interruption refers to the stop of current flowing through the electric circuit. It is also called switching or breaking. Interruption is the fundamental function of a LVSD. In the DC system, reducing the current to zero is the main issue; whereas, clearing the current after the natural current zero point is generally focused in the AC system.

In this section, we describe the interruption principles of DC and AC LVSDs.

### 2.3.1 INTERRUPTION FOR DC CIRCUITS

There is no natural current zero point in a DC electrical system. This fact makes DC interruption much more challenging than AC interruption. It is a requirement to reduce the current to zero in order to break a DC arc. Fundamentally, there are two kinds of approaches to interrupt a DC arc as below.

#### *Avoiding the Stable Arcing Point*

Figure 20 and Equation (7) show an electrical circuit and circuit equation in a switching event, respectively. In addition, Figure 21 describes the condition for a failed interruption of a DC arc [9]. In Figure 21, the slope of the straight line (L1) represents the resistance  $R$  and the curved line (L2) indicates the voltage-current relationship of the arc, especially for the low current regime in LVSDs. In addition, the shadowed zone between the straight and curved line is the electromotive force (EMF) in the inductance  $L$ . There are two intersection points, P1 and P2, where  $di/dt = 0$ . The point P2 is a stable arcing point while the P1 point is not a real stable point: it is easy to converge on the P2 point

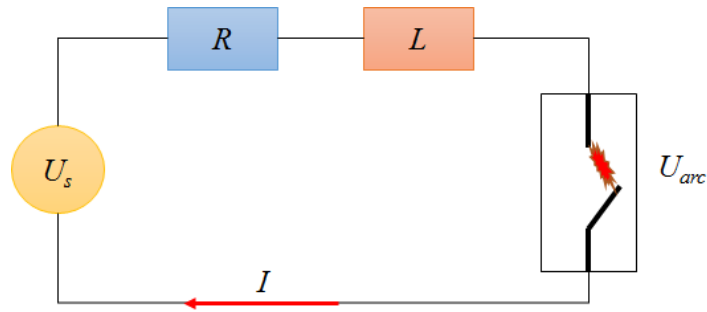


Figure 20 Equivalent electric circuit during interruption process;  $U_s$  is the system voltage,  $I$  is the current,  $R$  is the resistance,  $L$  is the inductance and  $U_{arc}$  is the arc voltage.

$$U_s(t) = I(t)R + L \frac{dI(t)}{dt} + U_{arc}(t) \quad (7)$$

whereas a small disturbance makes current increase or decrease further away from P1. A DC arc remains at the stable arcing point P2 as long as a power source supports it and the LVSD can withstand the strong thermal and mechanical effects of the arc.

For successful interruption of the DC arc, it is crucial to eliminate the stable arcing point, P2. There are two main strategies to avoid the stable point as shown in Figure 22; one is making a steeper slope

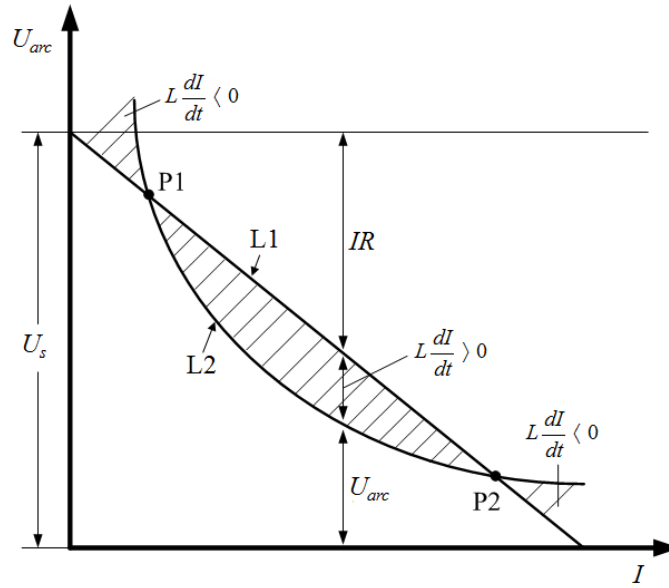


Figure 21 Current-voltage relationship in a DC circuit [9].

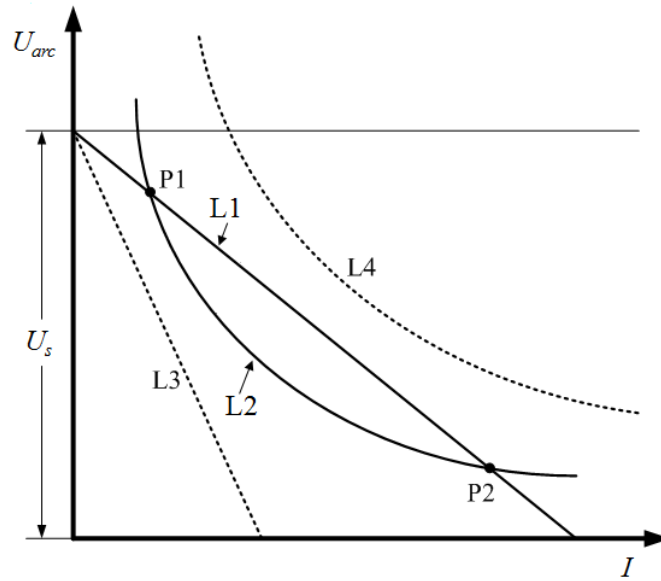


Figure 22 Principle of interrupting DC arc.

of the straight line like L3 and the other is raising the curve line such as L4 [9]. We can implement these, respectively by increasing the resistance and enhancing the arc voltage. If there is no stable arcing point, arc current goes to zero and the arc will be extinguished.

### *Current Injection*

Apart from the approach of arc instability, there is an alternative way to break a DC arc, which is the current injection method. Figure 23 shows a simplified circuit for implementing this method. When a fault current is detected, an injection switch is closed and the current generated by a capacitor flows through the Breaker1 in opposite direction to the system current [9]. This injected current results in an artificially created current zero point and Breaker1 interrupts the DC arc similar to an AC switching device. Normally, the current injection breaker is used in a high voltage DC system such as 500 kV [33].

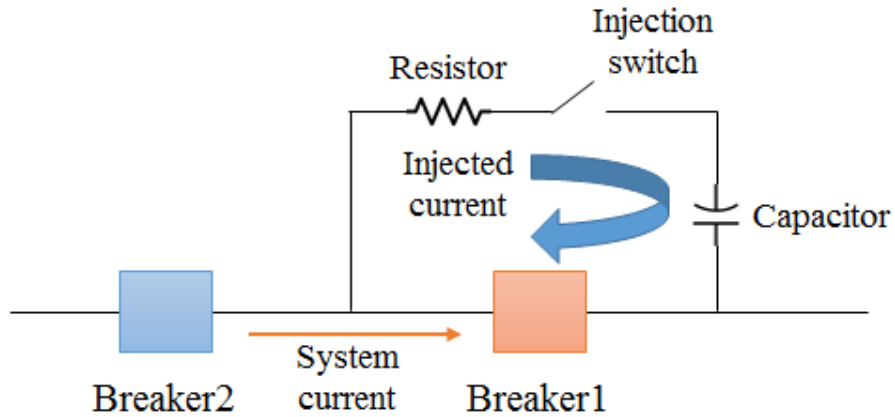


Figure 23 Simplified current injection circuit [9].

### *2.3.2 INTERRUPTION FOR AC CIRCUITS*

There are two natural current zero points each cycle in an AC system. Every AC switching device has a chance to interrupt an arc at the current zero point: as arc current falls to zero, electrical energy input to the arc also falls to zero. During this situation or close to the current zero point, the arc can be effectively transformed from a conductor into an insulator. Slepian explained the mechanism of the arc extinction in an AC circuit through the race theory [34], [35]. It is found that the extinction or re-

ignition of an AC arc depends on the outcome of race between the recovery voltage and the breakdown voltage. If the breakdown voltage is greater than the recovery voltage, the interruption will be successful and re-ignition will not occur. The recovery voltage is the voltage that appears across the contacts (terminals) after arc interruption. The recovery voltage is mainly dependent on a circuit conditions, i.e. the system voltage, resistance, inductance and capacitance of the circuit. The breakdown voltage is the maximum voltage that the air (the insulating medium) between contacts (terminals) can withstand without re-ignition of the arc. The breakdown voltage is affected by the residual arc that is associated with contact gap parameters, i.e. gap length, contact material, arc current, insulating medium and pressure.

Figure 24 shows the typical recovery process of the breakdown voltage between contacts after current zero where re-ignition does not occur [36], [37]. Stage 1 is the region where the breakdown voltage rapidly increases due to an electron depleted zone in front of a new cathode surface. In stage 2, the breakdown voltage slightly increases since the air (insulating medium) temperature near the contacts slowly decreases by the axial heat conduction through the relatively cool contact surfaces. After then, the breakdown voltage steadily increases because of an extension of the sheath layer and long-term cooling of the whole quenching chamber (stage 3). Finally, the breakdown voltage is saturated if the air is fully cooled (stage 4).

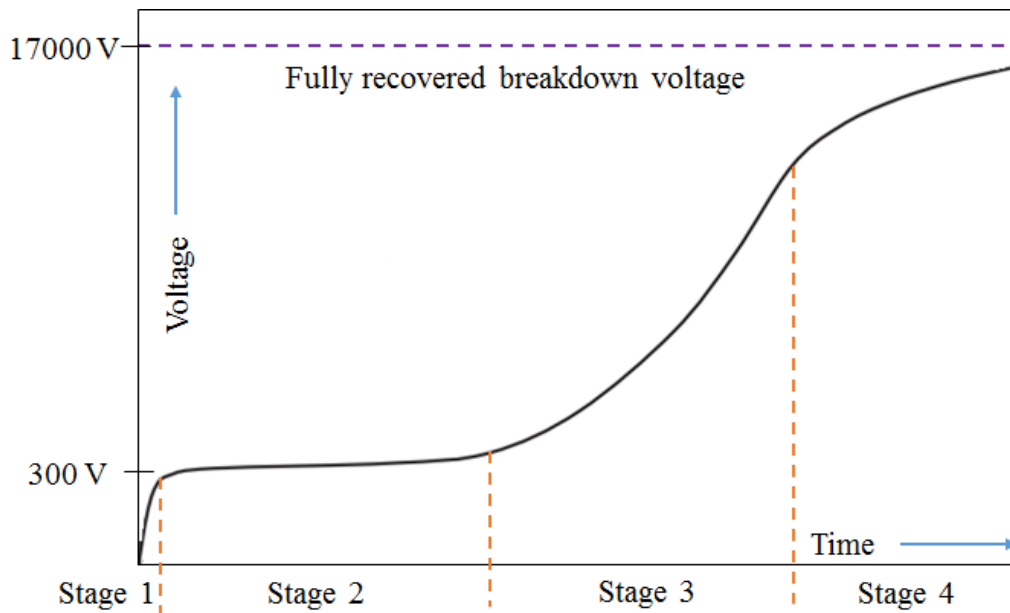


Figure 24 Recovery process of breakdown voltage of residual arc after the current zero point when there is no re-ignition; the breakdown voltage is measured between a 6.3 mm gap under the conditions of the 400 A peak current and 1 atm pressure [37].

Figure 25 shows how the breakdown voltage rapidly increases in the initial stage (stage 1 in Figure 24) after the arc interruption [21]. Since an ion is much heavier than an electron, ions may be regarded as stationary particles while electrons effectively move immediately after the current zero point. When the reverse voltage is applied across contacts after current zero, the electrons in front of the new cathode surface are propelled towards the anode, which leaves an electron depleted zone. This depleted zone is called a cathode sheath and results in a rapid increase of breakdown voltage immediately after the current zero point. The initial breakdown voltage is measured as approximately 300 V at 10  $\mu$ s after the current interruption under the condition of the 400 A peak current and 1 atm pressure, and this initial value (300 V) is sustained for 100  $\mu$ s [37].

In stages 2 and 3, the arc column cools and recombination of an ionized gas occurs. There is therefore a decrease in the gas temperature and an increase in the neutral particle density. In addition, this reduces the electric field in the cathode sheath since the voltage drop in the arc column increases, leading to diminishing the electron emission. If the arc column's temperature decreases below a critical value where thermal ionisation becomes negligible (air at atmospheric pressure: 2000 ~ 3000 K), the recovery voltage is applied to the whole contact gap because there is no good conduction path between contacts. If the gap length results in a dielectric sufficient to overcome the recovery voltage, there is no re-ignition and AC interruption is successful.

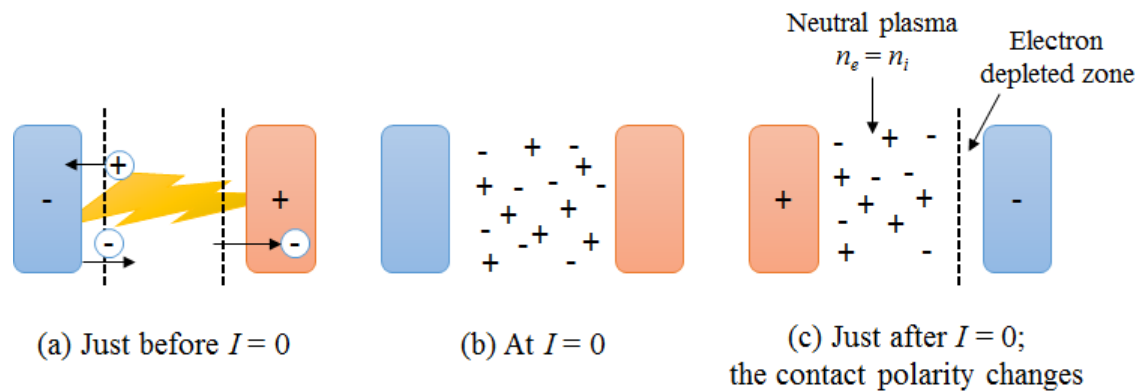


Figure 25 The initial rapid increase in breakdown voltage immediately after current zero by development of the cathode sheath (not to scale) in front of the new cathode when there is no re-ignition [21].

## 2.4 SWITCHING PERFORMANCE OF LOW-VOLTAGE SWITCHING DEVICES

In general, the switching performance of a LVSD is determined by current limitation and re-ignition phenomena. In this section, current limitation and re-ignition phenomena are explained based on the AC switching process.

### 2.4.1 CURRENT LIMITATION

Current limitation is one of the most important features in a switching operation of a LVSD since it reduces the mechanical and thermal stress on the switching devices and enhances the breaking capacity by limiting the arc current. When the arc enters the splitter plates in a quenching chamber, the arc voltage increases rapidly by multiple voltage drops in the arc roots and less current flows into the LVSD than the prospective value.

Figure 26 illustrates the detailed concept of current limitation when the system voltage, current, power factor and frequency are 240 V (RMS value), 55 kA (RMS value), 0.45, and 50Hz, respectively. It is

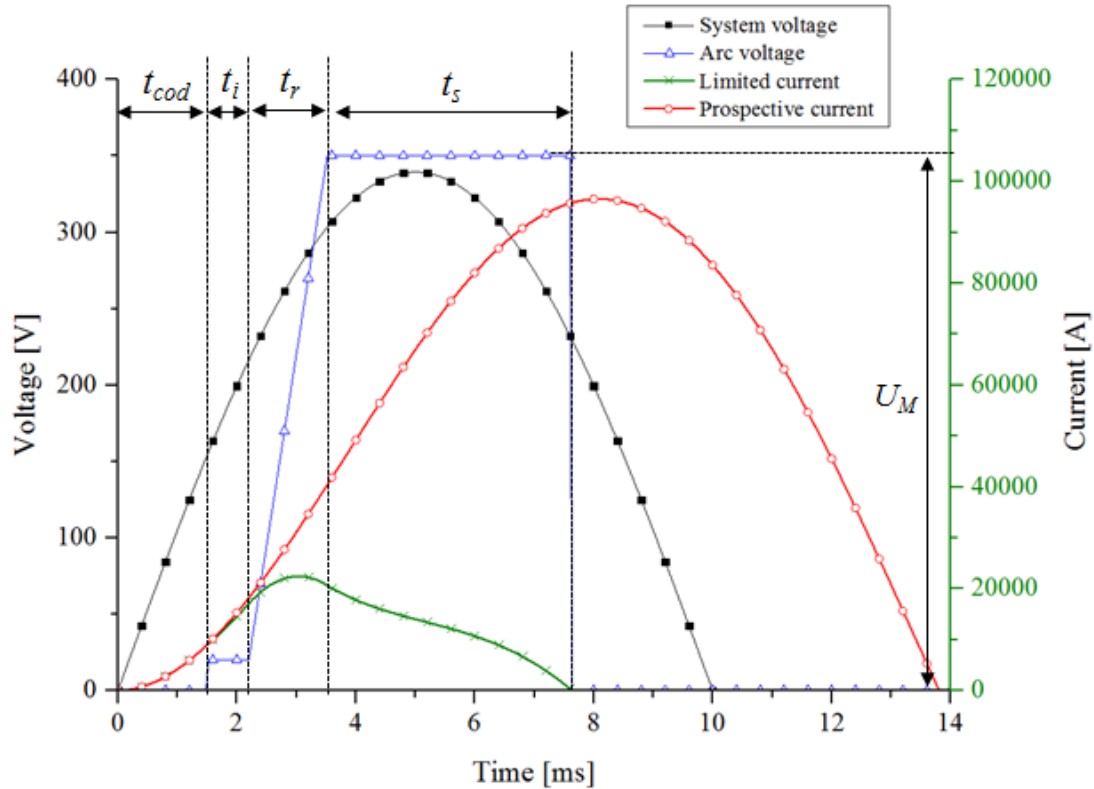


Figure 26 Effect of current limitation (calculated data);  $t_{cod}$ ,  $t_i$ ,  $t_r$ ,  $t_s$  and  $U_M$  refer to the contact opening delay time, immobility time, arc running time, splitter plate time and maximum arc voltage, respectively.



assumed there are the voltage step of 20 V (between 1.5 ms and 2.2 ms), the 1.3 ms rising duration (between 2.2 ms and 3.5 ms), and the constant voltage of 350 V (from 3.5 ms to the current zero point) in the arc voltage waveform. The currents (prospective and limited currents) are calculated based on Equation (7). If the system voltage with the zero phase angle is applied to the LVSD that keeps a closed circuit, the current reaches 96.5 kA (peak value) due to the DC component of the current during the transient situation. The current obtained from a closed circuit without the consideration of the arc voltage is called the prospective current. If we consider the arc voltage defined in Figure 26, the net current (22.4 kA peak value) is reduced considerably below its prospective value (96.5 kA peak value); this phenomenon is called current limitation.

The arc voltage varies with the arc position, length and current. This arc voltage greatly influences switching performance of LVSDs. Figure 26 shows the representative curve of the arc voltage during the switching operation. McBride *et al.* described the process of the arc development in a quenching chamber of LVSDs using the representative arc voltage curve [38]. The movable contact begins to separate from the fixed contact after the contact opening delay ( $t_{cod}$ ). At the same time, there is a step increase in the arc voltage between contacts due to the arc root formation in the contacts after an arc ignition. The arc tends to stay in the contact region after contact separation without moving out of it for the arc immobility time ( $t_i$ ). The arc then starts to move from the contact area towards the splitter plates during the arc running time ( $t_r$ ) by means of the magnetic force and the gas dynamic force. Finally, the arc is separated into multiple arcs by the splitter plates and the arc voltage remains at the maximum value ( $U_M$ ) during the splitter plate time ( $t_s$ ). The splitter plate time is defined as the period in which the arc stays in the splitter plates region.

There have been numerous studies on the four main parameters ( $t_{cod}$ ,  $t_i$ ,  $t_r$ , and  $U_M$ ) in an attempt to improve the switching performance of LVSDs by enhancing the effect of current limitation.

### *Contact Opening Delay Time*

With the exception of the ACB, the switching process in a LVSD normally begins with the magnetic repulsion force before the trip unit is activated. When a fault current flows in a LVSD, a repulsion force is generated on the movable contact, which is derived from the current path through conductors and from the current constriction between contacts. The repulsion force is proportional to the current squared and determines the contact opening delay time in the switching process. If the current is sufficient to produce a repulsion force on the movable contact exceeding the contact force, the movable contact starts to part from the fixed contact prior to any action of the trip unit. In order to

open the movable contact quickly and to rapidly increase the arc voltage, it is necessary to generate sufficient repulsion force. The repulsion force is mainly influenced by the current value, the current paths of conductors and the ferromagnetic material surrounding the conductors like the splitter plate [39], [40].

In our experimental research about arc motion, the opening time of the movable contact is determined by the solenoid action and the effect of the repulsion force on the switching performance is ignored.

### *Immobility Time and Arc Running Time*

When the arc is generated between contacts after contact separation, it tends to remain in the contact area until the driving force (Lorentz and gas dynamic force) is sufficient to move the arc. After the immobility period ( $t_i$ ), the arc is propelled towards the splitter plates by the magnetic force and the gas pressure gradient during the arc running time ( $t_r$ ). The immobility time and arc running time also play crucial roles in switching performance because it significantly affects the profile of the arc voltage. In order to reduce the contact damage caused by the arc and to improve the current limitation, the immobility time and the arc running time should therefore be minimized.

Previous investigations have been carried out to study arc motion in the quenching chamber and to identify the parameters that influence the immobility time and the arc running time by using a high-speed camera, magnetic sensors, or optical fibre imaging systems. Using high-speed camera requires the removal of a large section of the side wall to record the arc image within the quenching chamber [41]. This destructive modification of a quenching chamber may lead to a different result when compared with the original products. Sensing the magnetic field can provide the arc location and motion [42]; however, the calculated arc image is too simplistic and it is distorted by the ferromagnetic materials within the quenching chamber. An optical fibre imaging system may obtain detailed arc motion at a high scanning rate (up to 6 MHz) without significant modification to the quenching chamber [43], [44]. Optical fibres, which are placed in small apertures in the side wall of the quenching chamber, transmit the arc light intensity (associated with plasma temperature) to photodiodes as the arc propagates through the chamber. By capturing the light intensity, the imaging system enables the tracking of arc motion during the interruption process.

McBride's research group carried out an investigation on arc motion in the flexible test apparatus (FTA), designed to simplify the geometry of a MCB quenching chamber, with an optical fibre imaging system. The optical fibre imaging system used by McBride's research group is called the arc imaging system (AIS). They observed the influence of several parameters on arc motion as follows:

- Contact opening velocity,
- Contact material,
- Venting size,
- Arc current,
- Contact polarity,
- Gap behind the movable contact,
- Steel plates behind the arc runner.

Figure 27 shows details of the FTA chamber with the optical fibre positions that were used in their research. A set of optical fibres are placed in the quenching chamber with the exception of the splitter plate region (the arc stack).

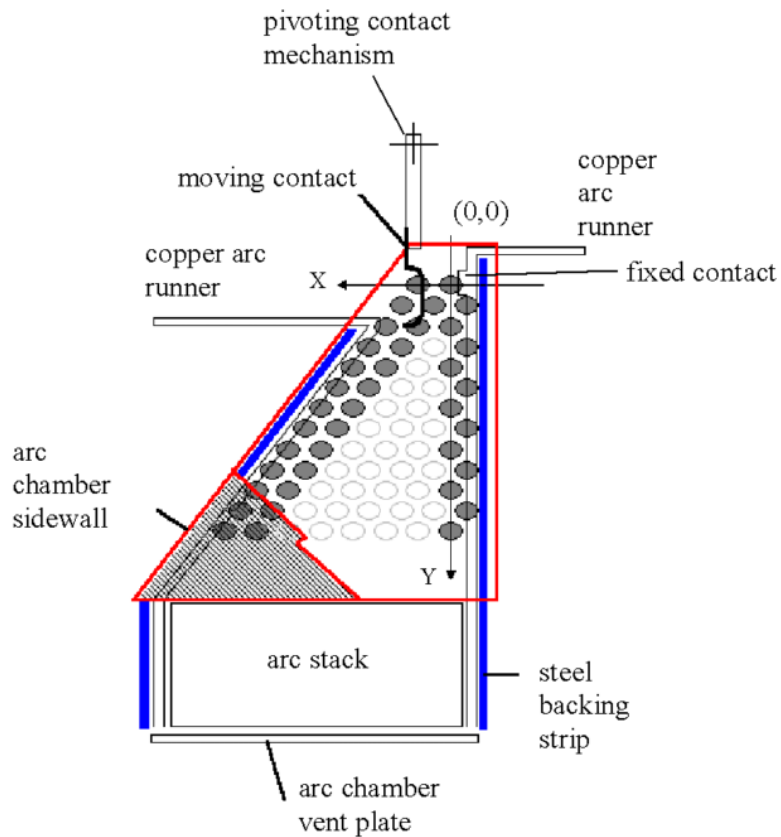


Figure 27 Quenching chamber with optical fibres and pressure devices [45].

In [46], McBride *et al.* measured the immobility time associated with the contact velocity, current and venting size by using the AIS. The immobility time is defined as the period during which the arc roots are fixed in the contact region. Figure 28 shows the immobility time varied with the moving contact velocity in the range of 4 to 10 m/s under the conditions of the 2000 A short-circuit current, partially open vent and ceramic chamber wall. It is observed that a high opening velocity leads to a decrease of the immobility time. As the contact velocity increases the peak current decreases due to enhanced current limitation. The reduction of the current can lead to a decrease of Lorentz force; however, the decreased immobility time is observed in the case of the increased contact velocity. This result may be related to the density of metallic vapour in the arc plasma [47]. The rupture of a molten bridge in an arc ignition process (see Figure 9) provides the high density of metallic vapour in the arc. The metallic arc is established in a short gap after the contact separation. If the contact gap increases and the ambient gas (air) enters the arc, it is transformed into the gaseous arc where the ambient gas becomes a dominant medium for ionisation [21]. There is a higher voltage drop in the gaseous arc and it has a higher pressure near the contact region when compared to the metallic arc. This higher pressure (the greater fluid dynamic force) may allow for the long arc to move earlier in the case of the high contact velocity.

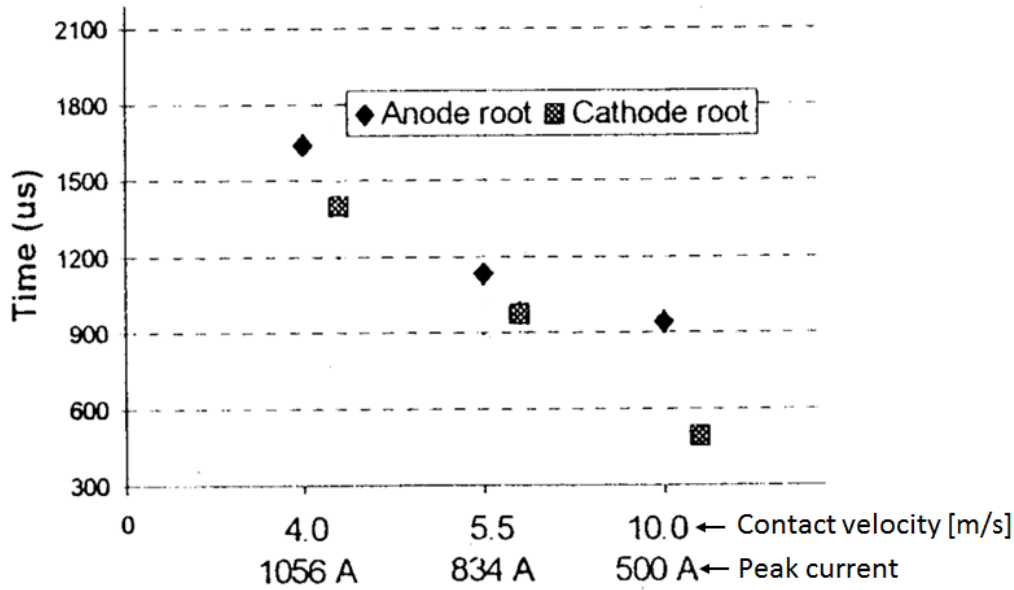


Figure 28 Immobility time as a function of contact opening velocity under the conditions of the 2000 A short-circuit current, partially open vent, ceramic chamber wall; the immobility time refers to the time period that each arc root remains in the contact region, the peak current represents the maximum current during each switching test [46].

It is also presented that the immobility time reduces as the vent area becomes wider in [46]. Figure 29 shows the effect of the vent area (closed, partially open and fully open vent) on the immobility time under the conditions of the 2000 A short-circuit current, 10 m/s contact velocity and ceramic chamber wall. The pressure gradient makes the fluid dynamic force on the arc. The narrow vent prevents the gas (air) from flowing out from the chamber; leading to a low pressure gradient between the contact region and the vent region (the place where the vent is located). This low pressure gradient, i.e. a low fluid dynamic force, keeps the arc remaining at the contact region longer.

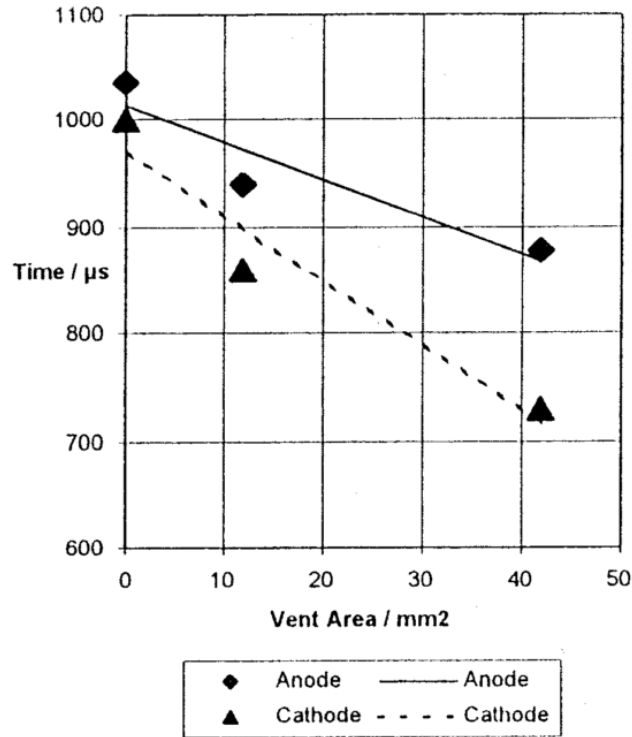


Figure 29 Immobility time as a function of vent area under the conditions of the 2000 A short-circuit current, 10 m/s contact velocity, ceramic chamber wall [46].

In [48], McBride *et al.* investigated the influence of gas flow around the movable contact on the immobility time. They found that the arc moves from the contact region approximately 20.5 % faster with the gap closed (see Figure 30 (b)) under the conditions of the 2000 A short-circuit current, 10 m/s contact velocity, partially open vent and ceramic chamber wall. Figure 30 illustrates the effect of the gap behind the movable contact on arc motion. There is a reduced pressure in the gap behind the movable contact, resulting in the adverse fluid flow near the contact region (see Figure 30 (a)). In the case of the closed gap, the fluid flow is improved and the arc can move smoothly from contact region to the arc runner (see Figure 30 (b)).

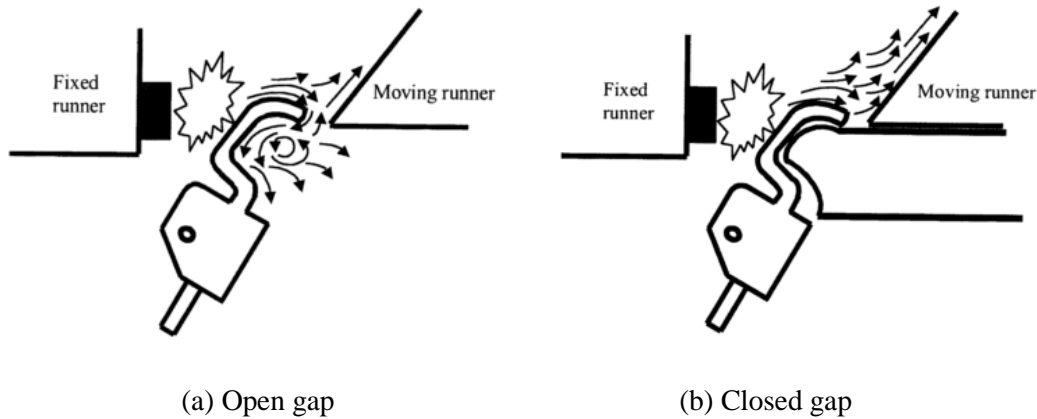


Figure 30 Effect of the gap behind the movable contact on arc motion in a contact region [48].

The effects of the short-circuit current and steel plates placed behind a runner on arc motion were also studied [46], [49]. Increasing the current results in a reduced delay of arc motion in the contact region. The arc velocity in the chamber with the steel plates is higher than that in the chamber without the steel plates. These results are attributed to increasing the Lorentz force on the arc; the higher current and the steel plates generate the greater Lorentz force.

The contact opening velocity, venting size, gap behind the movable contact, arc current, and steel plates behind the arc runner have a significant influence on arc motion. Conversely, the contact material and polarity have a minimal effect on arc motion [47].

As describe above, the AIS has been widely used to investigate arc motion and its characteristics in the LVSD chamber. It is assumed that the light intensity measured by the AIS is related to the arc temperature. But, there has been no detailed empirical study about the correlation between the light intensity and arc temperature; hence, this thesis covers the experimental investigation about the light intensity and arc temperature.

The vent distribution can be the design parameter of a quenching chamber. No previous study has investigated the effect of the vent aperture distribution on arc motion; it is worth to cover the vent distribution influence on arc behaviour.

Most of arc motion experiment has been carried out without capturing arc images in the splitter plate region (the region of the arc stack in Figure 27) in previous studies. In order to study the detailed arc motion in the splitter plate region and validate arc modelling (arc motion in the overall chamber), it

is necessary to measure the arc images in the overall quenching chamber including splitter plate region.

### *Maximum Arc Voltage*

The arc voltage plays a role as a resistor to prevent the arc current from increasing rapidly. Further, when the arc voltage is higher than the system voltage, the rate of change of the current ( $di/dt$ ) becomes negative, leading to the early current zero point. In order to achieve superior current limitation, it is necessary to increase the arc voltage itself. A double quenching chamber (see Figure 8) in each pole can be employed in a LVSD for higher breaking capacity. The LVSD with dual quenching chambers enables to stretch the arc longer and to split the arc into more segments, which generates a higher arc voltage.

Splitter plates made of the ferromagnetic material, like iron, are normally placed in the quenching chamber to raise the arc voltage during the interruption process. After the arc enters the splitter plates, there is an increase in the arc voltage resulting from multiple voltage drops in the arc roots associated with the surface interactions between the arc and splitter plates. Slepian proposed the arc quenching method using splitter plates and this method has been widely used in LVSDs [50].

Nakayama *et al.* investigated the empirical equation of the arc voltage associated with the number of splitter plates and arc current [51]. Figure 31 shows the experiment set-up and current generation circuit. The generating circuit is composed of a 1035  $\mu\text{F}$  capacitor, 3.98 mH inductor, 1 m $\Omega$  shunt resistor and transformer. A half cycle of a 50 Hz current flows through the experiment circuit after the main switch is closed. The anode and cathode contacts are coated with silver and a copper wire of a 0.05 mm diameter is connected in a contact gap of 30 mm for the arc ignition.

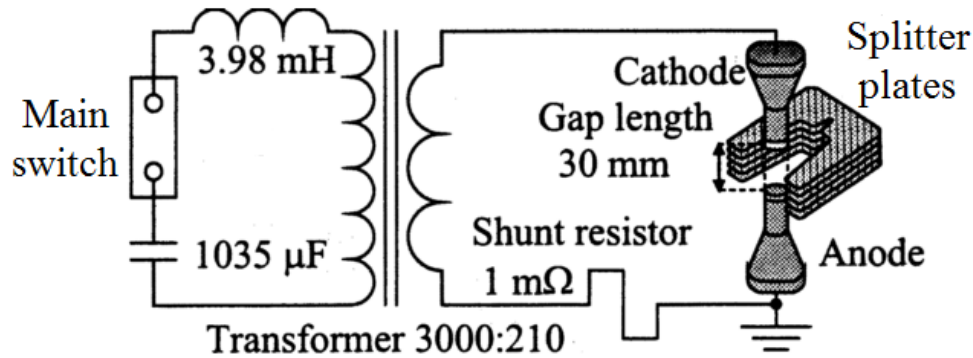


Figure 31 Experiment set-up and current generation circuit [51].

It is observed that the arc voltage is mainly a function of the number of plates. Equation (8) was proposed to calculate the total arc voltage after the arc enters the splitter plates,

$$\begin{aligned}
 U_{arc} &= \{23[V] + A \cdot L_{e-d} + (B + C \cdot L_{e-d})i\} + (D \cdot L_d + 24.5N_s), \\
 A &= 2.15 \times 10^3 [V / m], \\
 B &= 3.27 \times 10^{-3} [V / A], \\
 C &= 0.130 [V / (A \cdot m)], \\
 D &= 2.3 \times 10^3 [V / m], \\
 L_d &= (N - 1)l_d + (N - N_s)d,
 \end{aligned} \tag{8}$$

where  $U_{arc}$  is the arc voltage (V),  $L_{e-d}$  is the sum of lengths (m) between the contacts and splitter plates,  $i$  is the arc current (A),  $N$  is the total number of splitter plates,  $l_d$  is the distance (m) between splitter plates,  $d$  is the thickness (m) of the plate and  $N_s$  is the number of plates which have arc roots. This equation is useful to calculate the arc voltage roughly in a certain quenching chamber. If we assume the arc position with the time, we can estimate the arc voltage and evaluate current limitation. But, in order to calculate the arc voltage and current limitation accurately, it is essential to simulation arc motion affected by Lorentz force and fluid dynamic force.

#### 2.4.2 RE-IGNITION PHENOMENA

One of the main factors resulting in the deterioration of switching performance is re-ignition after the first current zero point. Re-ignition in a LVSD interruption process refers to the failure to achieve the arc interruption at the first current zero point; hence the current continues its flow after the current zero point. Re-ignition leads to longer arcing duration, severe contact erosion and side-wall damage of LVSDs during the interruption process. Avoiding re-ignition is therefore crucial when designing a quenching chamber. In practice, a reliable evaluator is required to predict the re-ignition phenomena and to improve the switching performance of a particular device prior to the costly empirical testing process for real products.



### *Re-ignition Mechanism*

The re-ignition mechanism can be classified by the process of electron emission and ionisation after the current zero point. There are three types of mechanism for re-ignition in switching devices: ‘thermionic’, ‘thermal’ and ‘dielectric’ re-ignition [21].

Thermionic re-ignition occurs when the cathodic surface is hot enough to release electrons under the recovery voltage. If after the current zero point, the electrons emitted from the hot cathode achieve sufficient kinetic energy from the recovery voltage, they reheat the arc column and maintain the arc current. Normally, this re-ignition takes place in refractory contact materials since they can support a high enough temperature for the electron emission.

Thermal re-ignition depends on maintaining a high temperature of an arc plasma, which keeps sufficient electrical conductivity of the residual plasma after the current zero event. If the arc column is still a good conductor, most of the recovery voltage appears across the cathode sheath (the electron depleted zone immediately after the current zero crossing). Re-ignition occurs in the sheath region when the recovery voltage exceeds the breakdown voltage, and then the arc column temperature increases to sustain the arc. Thermal re-ignition is also called ‘dielectric re-ignition with space charge’ as the electrons are released from the cathode due to the high electric field.

Even if thermionic and thermal effects are negligible due to the low temperature of the residual plasma and contact surface, the recovery voltage exceeding the breakdown voltage triggers breakdown and leads to re-ignition. In the case of the high electric field (the high recovery voltage), electrons emitted from the cathode are accelerated to gain enough kinetic energy for ionisation. This situation can happen in LVSDs when the system voltage is applied across a short contact gap, which is not sufficient to prevent breakdown from occurring.

### *Types of Re-ignition*

Hauer classified the re-ignition phenomena into two types based on the current and voltage waveforms; ‘instantaneous’ and ‘delayed’ re-ignition [52]. Figure 32 and Figure 33 show the examples of measured waveforms when instantaneous and delayed re-ignitions occur in the MCCB. In the case of instantaneous re-ignition, the arc re-ignites and the current continues to flow immediately following the current zero point; however, delayed re-ignition has a pause without current flowing prior to arc re-ignition. In LVSD interruption tests, delayed re-ignition occurs much less than instantaneous re-ignition. In Hauer’s experiment, only 8 delayed re-ignitions are observed while 31 instantaneous re-ignitions occur. Similarly, 6 delayed and 31 instantaneous re-ignitions are recorded among 110 switching tests in this thesis.

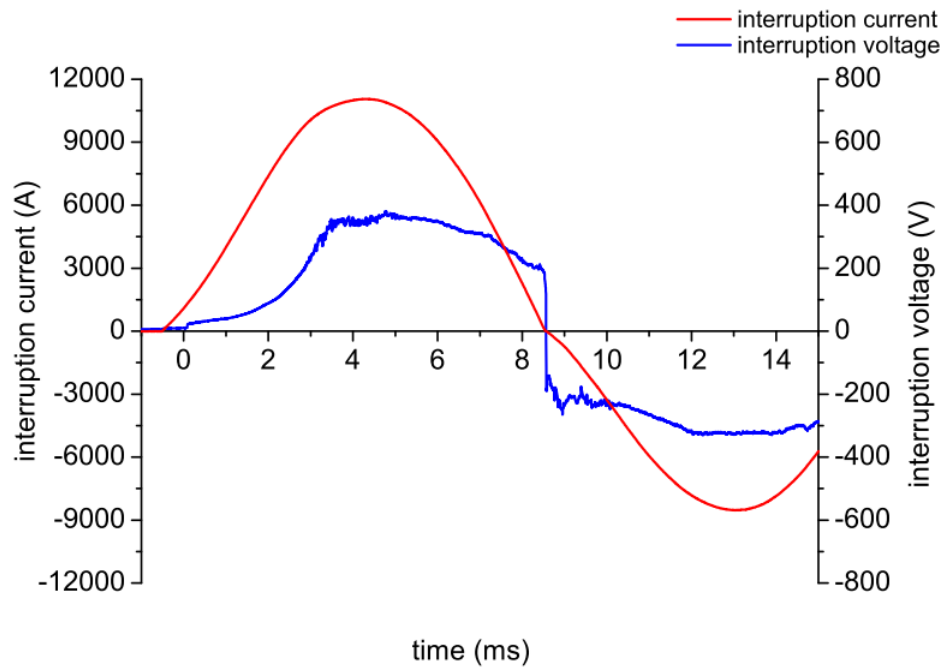


Figure 32 Voltage and current waveforms when instantaneous re-ignition occurs under the conditions of the 10 kA short-circuit current, 600V system voltage [52].

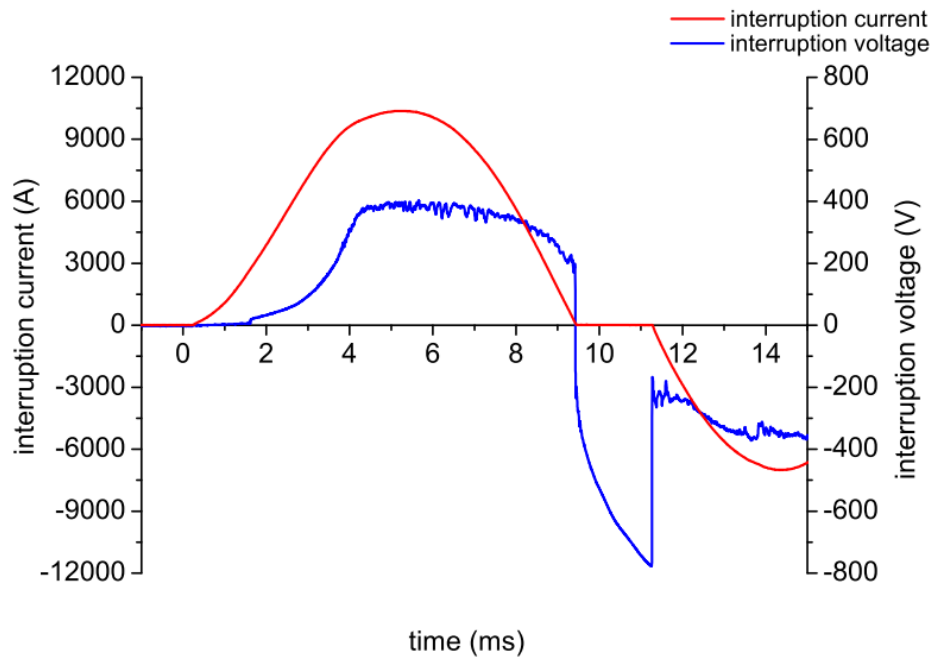


Figure 33 Voltage and current waveforms when delayed re-ignition occurs under the conditions of the 10 kA short-circuit current, 600V system voltage [52].

### *Evaluators of Re-ignition*

It has been suggested that if the breakdown voltage is greater than the recovery voltage, there will be a successful interruption without re-ignition [21], [34]; however, the problem of determining the breakdown voltage of the arc plasma after the current zero point has not been fully addressed. This is due to the difficulty of breakdown voltage measurement and the changes of the breakdown characteristics of the gas-plasma mixture by complex recombination and cooling processes in the breakers. Instead of investigating individual recovery voltage and breakdown voltage, experimental studies about a re-ignition evaluator have been undertaken. The re-ignition evaluator refers to the parameter to predict the re-ignition phenomena after the current zero point.

Chen *et al.* studied the correlation between arc motion and re-ignition in the MCs by using optical fibre arc imaging technology [53]. In the switching test, a 400 A current is provided by the capacitor bank charged as 808 V initially. The current oscillating frequency is 50 Hz and the copper wire is used for the arc ignition. They used 25 optical fibres, including 7 fibres in the splitter plate region, to detect the arc light in the chamber as shown in Figure 34.

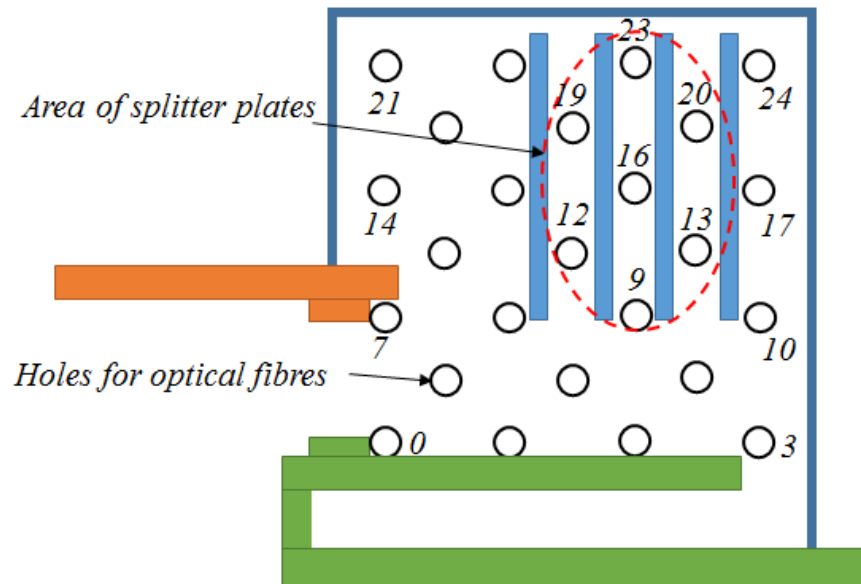


Figure 34 Optical fibre locations [53].

An index (K value) is defined to quantify how much of the arc enters the splitter plates. K is calculated from Equation (9),

$$K = \frac{\sum_{i=9,12,13,16,19,20,23} \int_0^T L_i dt}{\sum_{i=0}^{24} \int_0^T L_i dt} \quad (9)$$

where,  $T$  refers to the total switching duration and  $L$  represents the light intensity measured from the optical fibre. The numerator is the sum of light intensities from 7 optical fibres located in the splitter plate region whereas the denominator is the sum of light intensities from all 25 fibres. A larger  $K$  value means that the arc is more likely to enter the splitter plates and to stay there. Figure 35 shows four types of the chamber configurations used in the switching tests. Each chamber has a unique arrangement of splitter plates.

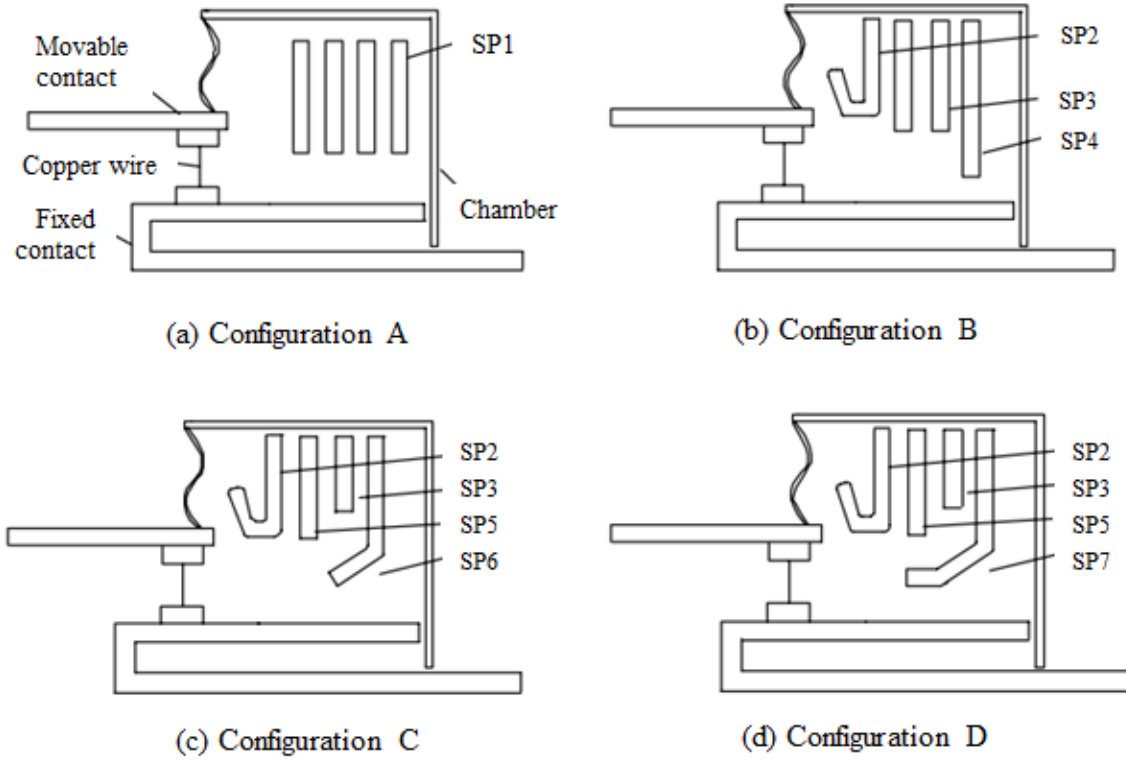


Figure 35 Four types of chamber configurations; each chamber has a different arrangement of splitter plates, SP1-7 refer to the types of the splitter plate [53].

It is found that there are different arc motions in four chambers and arc motion has a significant influence on the probability of re-ignition. The bended shape splitter plate in the chamber leads to enhanced arc motion towards the splitter plate region. The highest arc voltage is observed in the D

chamber, which has the bended shape plates in the first and last plat position, when compared to other chambers under the similar current condition (see Table 1).

Table 1 Experimental results associated with the chamber configurations [53].

Chamber configuration	Maximum current <sup>a</sup> [A]	Maximum voltage <sup>a</sup> [V]
A	532	151
B	533	188
C	536	202
D	535	225

<sup>a</sup> It is the average value over 25 experimental results.

Figure 36 shows K values and re-ignition probability associated with the chamber configuration. It is seen that the higher arc voltage corresponds to the better the arc entry into the splitter plates and the better arc entry leads to the reduction in the re-ignition probability. Here, the re-ignition probability defined as the ratio of the re-ignition number to the total switching number (25 tests).

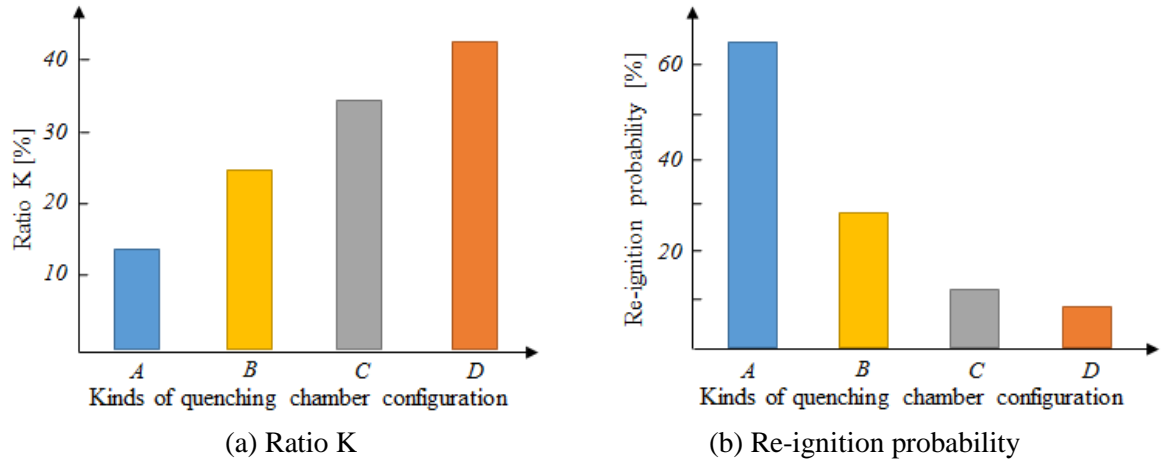


Figure 36 K value ratio and re-ignition probability [53]: re-ignition probability (%) = total re-ignition number / 25 tests \*100.

Hauer *et al.* studied about the evaluator of re-ignition based on the MCCB switching data under the conditions of the 606 V system voltage, 10.4 kA short-circuit current, 0.485 power factor and 60 Hz frequency [52], [54]. A 69 kV AC power line is used as the energy source and a 7.5 MVA three-phase

transformer is utilized to step down the voltage. The switching tests were conducted through only a single type of MCCB under a single test condition. Several candidates of the re-ignition evaluator were introduced; the arc energy in Equation (10), net-through energy in Equation (11), mean arc current in Equation (12) peak arc current in Equation (13) and exit arc voltage Equation (14). The exit arc voltage is defined as the arc voltage 20  $\mu$ s prior to the current zero point.

$$E_{arc} = \int_0^T U_{arc}(t) \cdot I(t) dt , \quad (10)$$

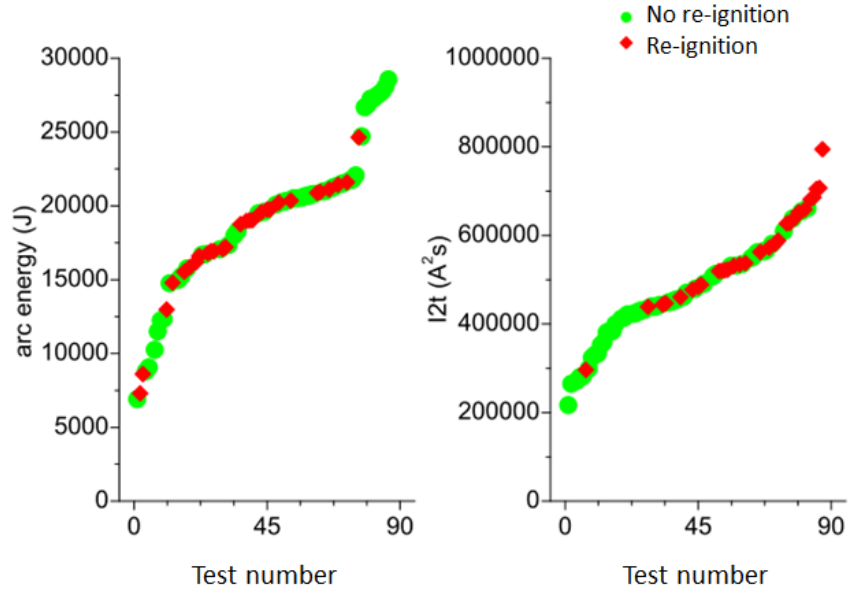
$$I^2 t = \int_0^T I^2(t) dt , \quad (11)$$

$$\bar{I} = \frac{1}{T} \int_0^T |I(t)| dt , \quad (12)$$

$$\hat{I} = \text{Max}_{0 < t < T} |I(t)| , \quad (13)$$

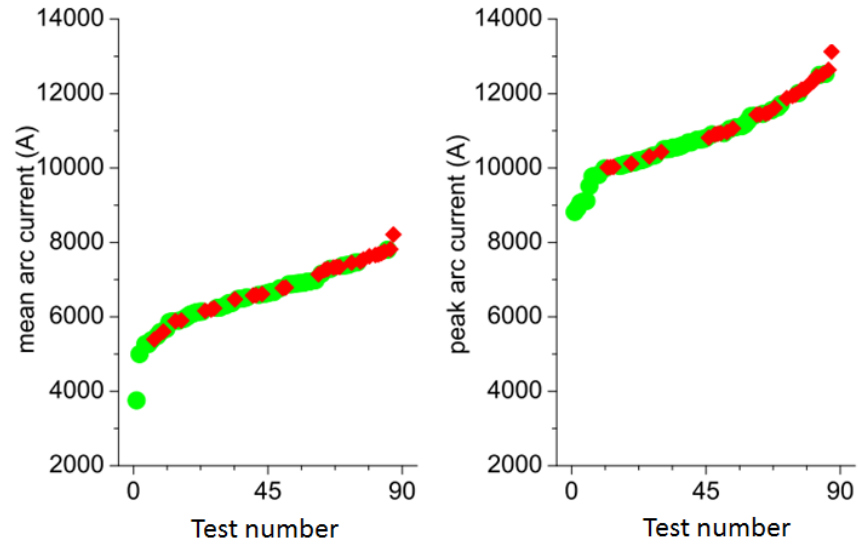
$$\text{Exit arc voltage} = U_{arc}(t) \Big|_{t=T-20\mu s} , \quad (14)$$

where,  $T$  refers to the total switching duration,  $U_{arc}$  is the arc voltage,  $I$  is the arc current. Figure 37 shows the correlation between instantaneous re-ignition and the evaluator candidates except the exit arc voltage. The green round dots represent the successful interruption without re-ignition whereas the red square dots refer to the failed interruption with instantaneous re-ignition. It is seen that there is no clear threshold in all figures between the successful and failed interruption. This implies none of those parameters has an influence on the re-ignition phenomena in the LVSD and they cannot be the re-ignition evaluator.



(a) Effect of arc energy

(b) Effect of net-through energy



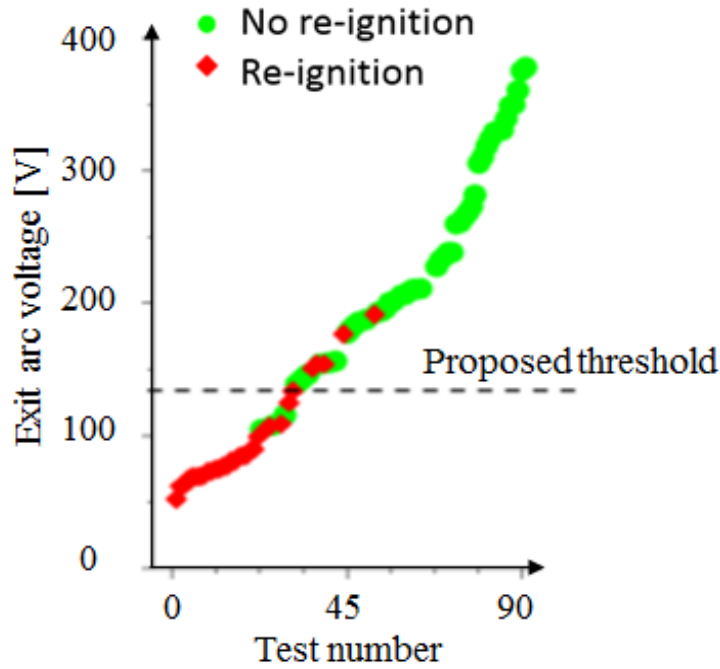
(c) Effect of mean arc current

(d) Effect of peak arc current

Figure 37 Correlation between the re-ignition and evaluator candidates (the arc energy, net-through energy, mean and peak arc current) [52].

Figure 38 shows the correlation between instantaneous re-ignition and the exit arc voltage. It is observed that the probability of re-ignition is strongly dependent on the exit arc voltage. If the exit

arc voltage is higher than a particular value, re-ignition probability significantly decreases and the probability of successful interruption increases. For example, the probability of the successful interruption without re-ignition is 90% in cases where the exit voltage is above 134V.





## 2.5 ARC MODELLING IN LOW-VOLTAGE SWITCHING DEVICES

An arc simulation is one of the most effective tools in evaluating the switching performance of a LVSD without testing of a real product since it can predict arc behaviour that is fundamental in determining LVSD performance. Arc behaviour in a LVSD is very complex and influenced by multiple interactions; fluid dynamics, electromagnetic phenomenon, heat conduction, and charge carrier generation. Despite the complexity of the arc, the rapid progress of modern computer science has allowed users to model arc phenomenon in a LVSD and to get useful information for product design.

In this section, we deal with the assumptions for arc modelling, methodology of arc column as well as arc root modelling and arc modelling example.

### 2.5.1 ASSUMPTIONS AND SIMPLIFICATIONS FOR ARC MODELLING

In order to reduce the complexity of modelling the air arc in a LVSD, several assumptions and simplifications are adopted in the arc simulation.

#### *Local Thermal Equilibrium*

It is regarded that the arc column under the 1 atm pressure is electrically quasi-neutral and thermally equilibrium mixture of electrons and heavy particles (ions, atoms and molecules) at the high temperature, which is called a state of local thermal equilibrium (LTE). However, the LTE condition does not hold in the cathode and anode roots due to the significant temperature difference of electrons and heavy particles. In spite of thermal non-equilibrium in the arc root, it is possible and necessary to model the whole arc including the arc column, the cathode and the anode roots at the macroscopic scale with the assumption of LTE. If the whole of the arc is regarded to be in a state of LTE, the arc can be treated as a single fluid, with a single temperature and a single average velocity field in the magnetohydrodynamics (MHD) theory [55]. Based on the LTE assumption, the arc in the LVSD can be modelled and the switching performance can be predicted through an MHD approach.

### *Arc Ignition*

Since the phenomenon of arc ignition by the molten bridge between contacts is too complicated to be considered in the arc simulation, the arc initial state is modelled as a hot channel in a small gap between contacts, which has a homogeneous temperature distribution. For example, a 15000 K channel is modelled in a 2 mm contact gap for the arc ignition in the MCCB [56].

### *Laminar Flow*

The effect of the turbulence flow on the air arc in a LVSD can be negligible and the arc can be regarded as a laminar flow since Reynolds number is low. Most studies of arc simulation have been carried out with the assumption of laminar gas flow, for example [57], [58]. Thompson *et al.* calculated Reynolds number of 1000 in a MCB, which is much lower than the critical value of 2100 between laminar and turbulent flow [59].

## **2.5.2 ARC COLUMN MODELLING**

The modelling of the arc column is based on the MHD theory involving conservation equations for gas plasma dynamics, and Maxwell equations for the electromagnetic field.

### *Fluid Dynamics Equations*

The mass, momentum and energy conservation equations describe the relation between the velocity, pressure and temperature in the gas as given below,

$$\frac{\partial \rho}{\partial t} + \nabla \cdot (\rho \vec{V}) = 0, \quad (15)$$

$$\frac{\partial (\rho v_i)}{\partial t} + \nabla \cdot (\rho v_i \vec{V}) = -\nabla p + \nabla \cdot (\eta \nabla v_i) + (\vec{J} \times \vec{B})_i, \quad (16)$$

$$\frac{\partial (\rho H)}{\partial t} + \nabla \cdot (\rho H \vec{V}) = \nabla \cdot (\lambda \nabla T) + \frac{\partial p}{\partial t} + \sigma E^2 + S_{rad} + S_\eta, \quad (17)$$

where,  $\rho$  is the density ( $kg/m^3$ ),  $t$  is the time ( $s$ ),  $\vec{v}$  is the velocity ( $m/s$ ),  $v_i$  is the velocity component in  $i$  direction,  $p$  is pressure ( $Pa$ ),  $\eta$  is the dynamic viscosity ( $kg/(m \cdot s)$ ),  $\vec{J}$  is the current density ( $A/m^2$ ),  $\vec{B}$  is the magnetic flux density ( $T$  or  $Wb/m^2$ ),  $H$  is the dynamic enthalpy ( $J/kg$ ) expressed by  $h + \frac{1}{2}\vec{v}^2$ , and  $h$  is the static enthalpy ( $J/kg$ ) determined by  $\int c_p dT$ .  $\lambda$  is the thermal conductivity ( $W/(m \cdot K)$ ),  $T$  is the temperature ( $K$ ),  $\sigma$  is the electrical conductivity ( $S/m$ ),  $E$  is the electric field intensity ( $V/m$ ),  $S_{rad}$  the radiation energy source ( $W/m^3$ ) and  $S_\eta$  is the viscous dissipation ( $W/m^3$ ).

The mass conservation equation (15) indicates that net mass flow out of the control volume is equal to the time rate of a decrease of mass inside the control volume (the first term represents the change rate of the density in the control volume and the second one refers to the net difference between input and output mass flow in the control volume). The momentum equation (16) refers to Newton's second law applied to a moving fluid. The left hand side of the momentum equation represents the mass acceleration product of the gas per unit volume; whereas, the right hand side corresponds to the net force on the gas, which is composed of the body (Lorentz force) and surface forces (pressure gradient and viscous forces). The energy equation (17) states that the rate of change of energy inside a fluid element (a control volume) is equal to the sum of net heat flux (thermal conduction, radiation and ohmic heating) and the rate of work done by pressure and shear stress [60].

### *Electromagnetics Equations*

The electric field ( $\vec{E}$ ) associated with the ohmic heating source is calculated from Equations (18) and (19),

$$\nabla \cdot (\sigma \nabla \Phi) = 0, \quad (18)$$

$$\vec{E} = -\nabla \Phi, \quad (19)$$

where  $\Phi$  is the electric scalar potential ( $V$ ).

The current density and magnetic flux density ( $\vec{J}$  and  $\vec{B}$ ) related to Lorentz force are obtained from the next equations,

$$\nabla^2 \vec{A} = -\mu \vec{J}, \quad (20)$$

$$\vec{B} = \nabla \times \vec{A}, \quad (21)$$

$$\vec{J} = \sigma \vec{E}, \quad (22)$$

where  $A$  is the magnetic vector potential ( $Wb/m$ ) and  $\mu$  is the permeability ( $H/m$ ).

The above electromagnetic equations are applied to the source terms in the momentum and energy conservation equations.

### *Air Properties*

In the arc simulation, the arc plasmas is treated as a single fluid of air based on the LTE assumption. The air properties (arc column) have nonlinear characteristics varying with the temperature and pressure. In order to develop a reliable arc model, it is essential to use the accurate air properties (density, electrical conductivity, thermal conductivity, specific heat capacity and viscosity) associated with the temperature and pressure.

Murphy investigated the properties of the air plasma considering the temperature as well as pressure and validated the calculated values against the experimental data [61], [62]. Figure 39~Figure 43 show the modelled data of air density, electrical conductivity, thermal conductivity, specific heat capacity and viscosity as a function of the temperature (from 300 K to 30000 K) under the different pressures (0.5, 0.8, 1, 2, 5, 8, and 10 atm). These data are used to develop the arc model in this research.

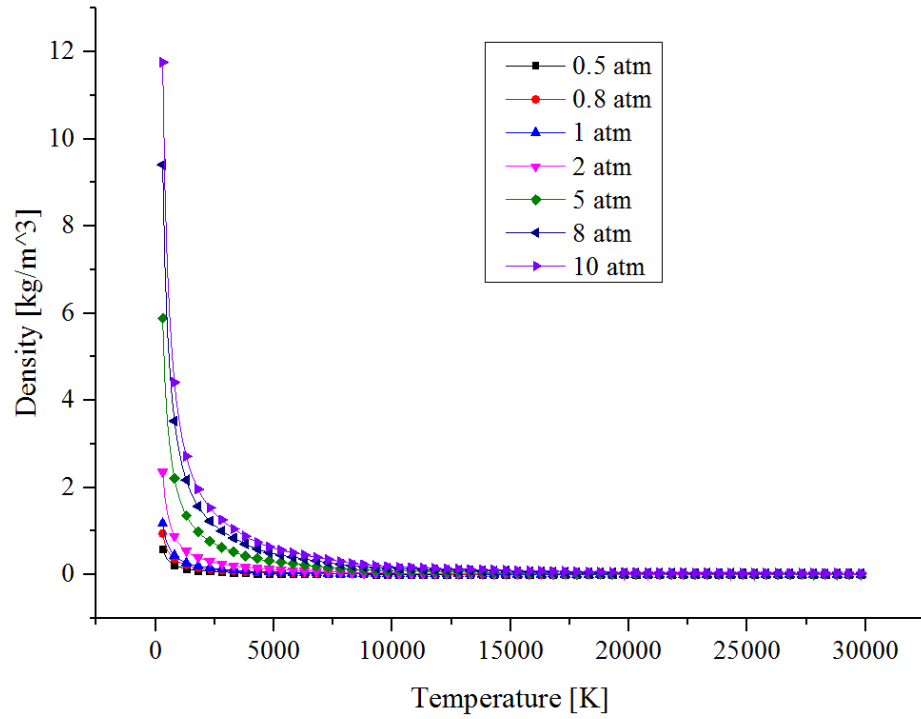


Figure 39 Air density as a function of the temperature under seven different pressure conditions [61], [62].

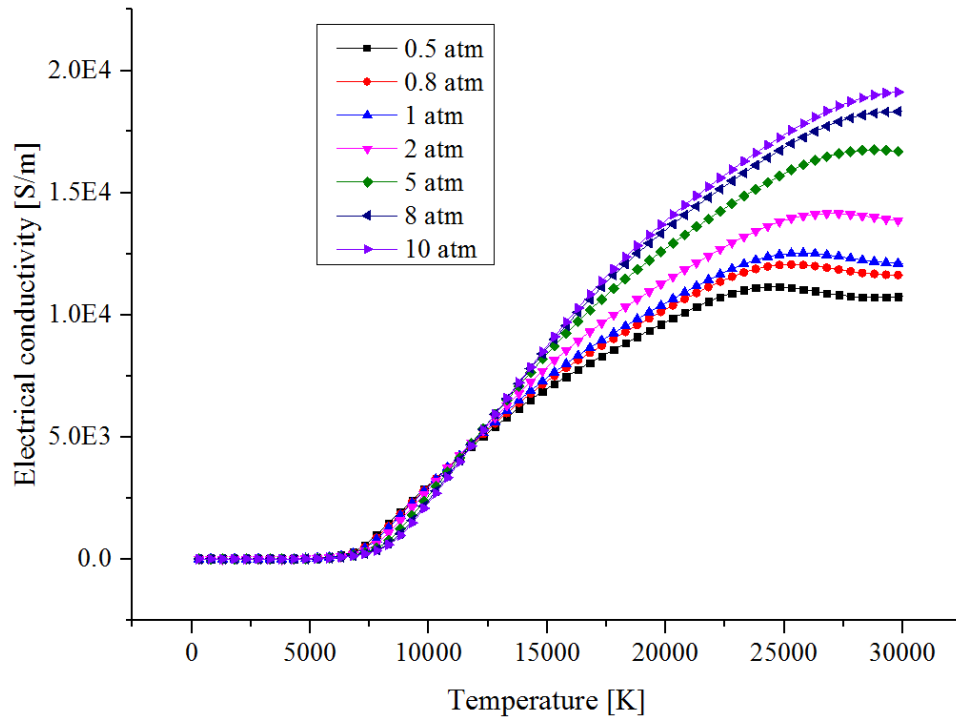


Figure 40 Air electrical conductivity as a function of the temperature under seven different pressure conditions [61], [62].

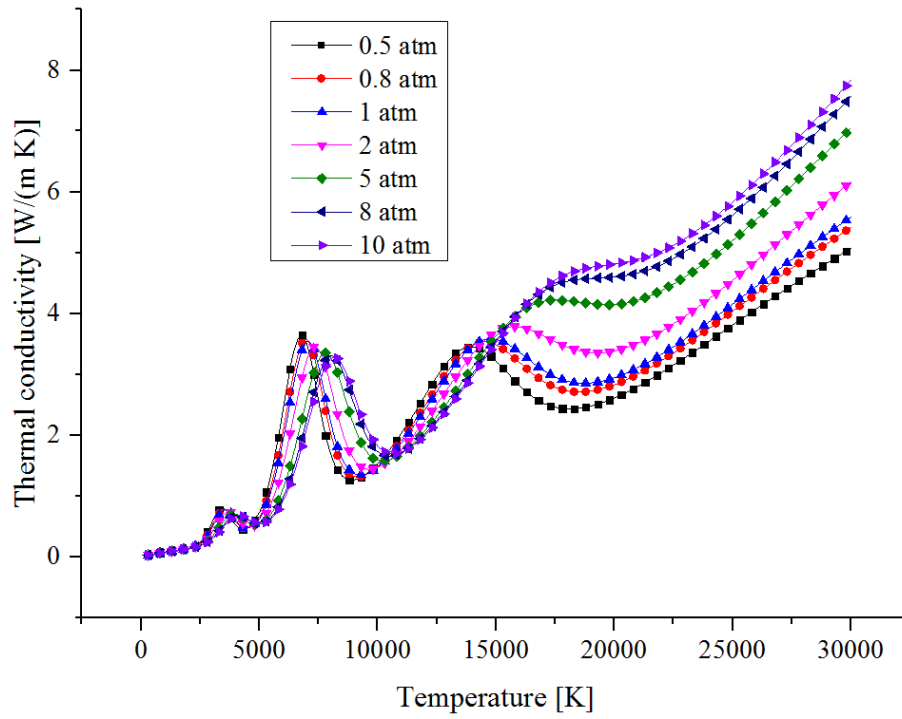


Figure 41 Air thermal conductivity as a function of the temperature under seven different pressure conditions [61], [62].

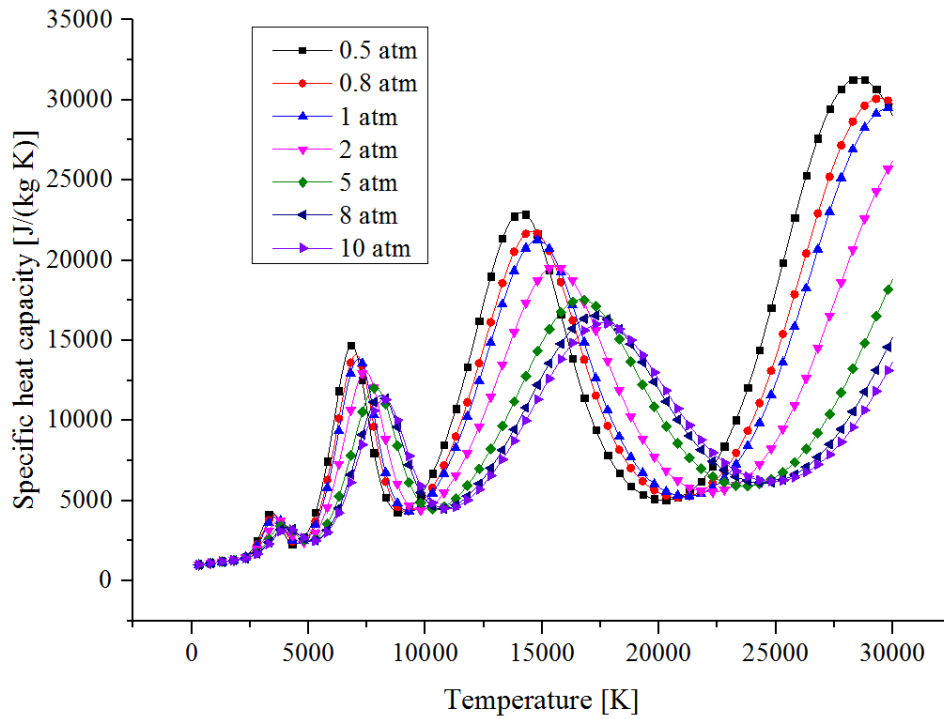


Figure 42 Air specific heat capacity as a function of the temperature under seven different pressure conditions [61], [62].

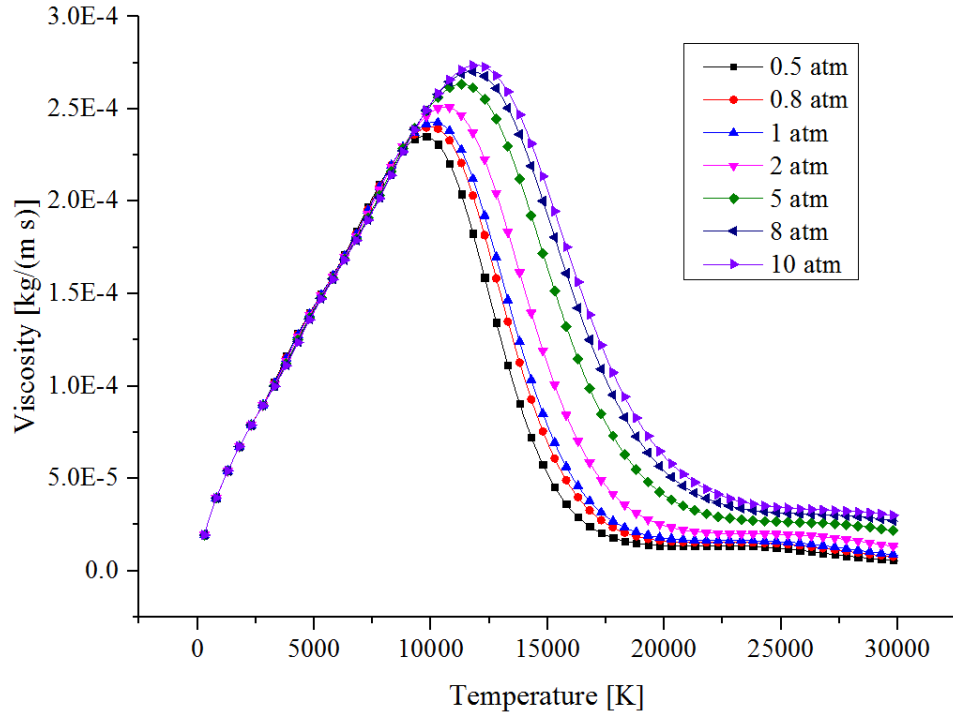


Figure 43 Air viscosity as a function of the temperature under seven different pressure conditions [61], [62].

### Radiation Loss

Radiation is the heat transfer mechanism via electromagnetic wave. It is the dominant mechanism of heat loss in the arc of the LVSD and has a significant influence on the temperature distribution and, consequently, plasma properties. Every local volume in the hot gas emits heat energy to the surrounding volume and, at the same time, absorbs the energy from the surroundings depending on temperature, frequency, geometry, *etc.*; therefore, it is difficult to calculate radiation loss in the arc modelling accurately.

Radiation loss has been often computed through the net emission coefficient (NEC) which can be easily tabulated versus temperature and simply used as a negative source term in the energy conservation equation. The NEC describes the difference between emission and absorption of radiation power associated with temperature, pressure and arc radius. Peyrou *et al.* investigated the radiative properties of the air plasma in a wide range of temperature (300 K ~ 3500 K) under the conditions of several different pressures [63]. Figure 44 shows NEC data of the air arc depending on temperature and pressure with an assumption of a 10 mm radius arc (it is observed that radius of free-burning arcs is around 10 mm at 1 atm in the case of a 10000 A current [64]). It is seen that the NEC value increases with the temperature and pressure. Especially, the increase rate of the NEC below

15000 K is much higher than that over 15000 K. These NEC data are used in arc modelling of this research.

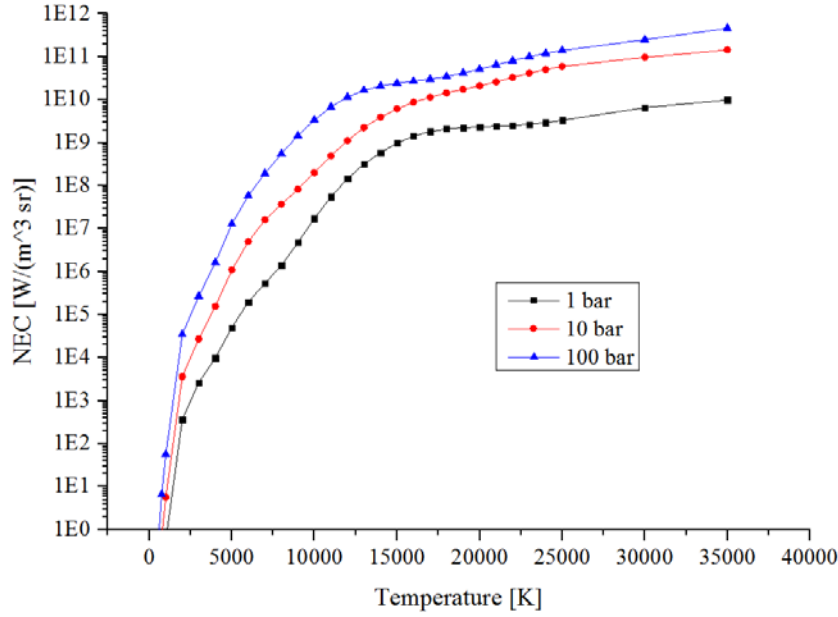


Figure 44 NEC of air plasma for a 10 mm radius [63].

### *Magnetohydrodynamic Process*

Arc behaviour in a LVSD is complex and it is influenced by several interactions; fluid dynamics, electromagnetic phenomenon and heat conduction. Karetta *et al.* studied the simulation about a LVSD arc with a 3-D MHD approach and showed the arc behaviour (arc displacement, voltage and pressure) in the simplified chamber consisting of only two parallel electrodes [65]. They presented the modelling process of an arc column as shown in Figure 45, which becomes the fundamental in the numerical approach of a LVSD arc. The current varied with the time is imposed at the boundary of the electrode. The current density distribution is calculated from the electrical conductivity and electric potential in the chamber. The current density is the main parameter to determine ohmic heating and Lorentz force. Based on ohmic heating, Lorentz force and plasma properties, the gas flow and energy transport are computed by conservation equations (Equations (15), (16) and (17)); and then the distributions of temperature and pressure are renewed leading to updating plasma properties (density, electrical conductivity, thermal conductivity, specific heat capacity and viscosity). The updated plasma properties are used to compute new electric potential and current density in the next



simulation time. This iteration continues until the termination condition. Basically, arc modelling of this research also follows Karetta's simulation process, but we include the effect of splitter plates, contact motion, current limitation and the negative V-I characteristics in the low current region.

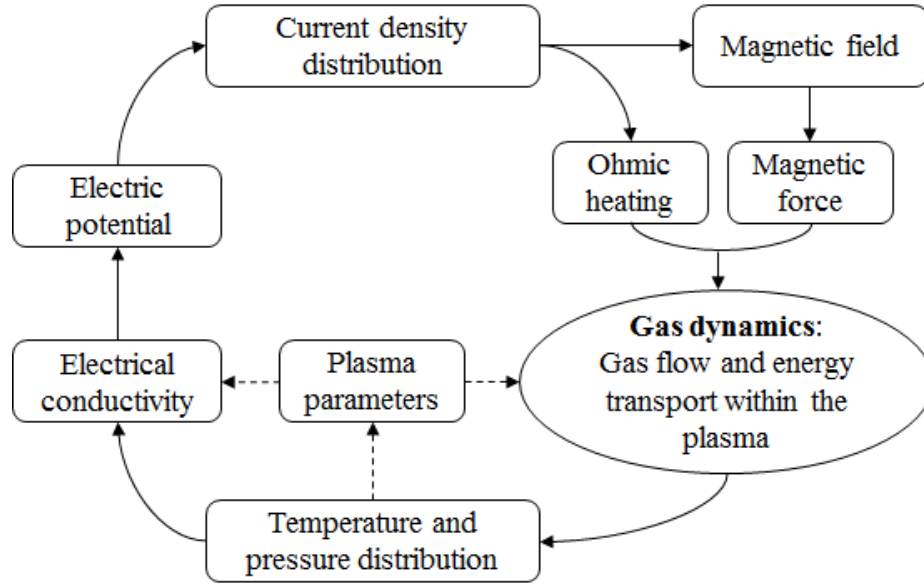


Figure 45 Process of arc modelling [65].

### 2.5.3 ARC ROOT MODELLING

The arc root is a thin layer between the arc column and the metal surface of the cathode or anode. It has a significant influence on arc motion near the splitter plates and the arc voltage. The special treatment is required to consider the effect of arc roots in arc modelling.

Lindmayer *et al.* empirically investigated the arc splitting process in the splitter plate and extended arc modelling by considering the effect of the arc root formation during the arc splitting process [66]. Figure 46 shows the test chamber for the investigation of arc splitting. It consists of two electrodes ( $1.5 \times 4$  mm) and a single splitter plate (3 mm total thickness). The splitter plate is divided into two steel plates (1 mm thickness) and there is a pressboard (1 mm thickness) between them. The arc ignites through a thin copper wire. In order to measure the current flowing through the plate, the shunt is connected with two steel plates. A high-speed camera is used to record arc motion at a 32000 frames/s rate.

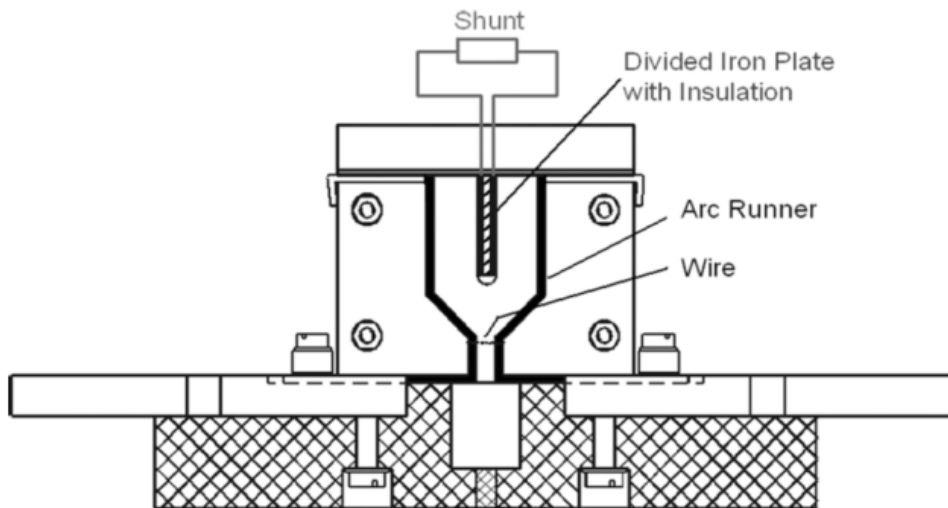


Figure 46 Test chamber for the investigation of arc splitting;  $1.5 \times 4$  mm arc runners (electrodes), a 12 mm width chamber, a 3 mm total thickness plate (two 1 mm steel plate and a 1 mm pressboard) [66].

Figure 47 shows the arc voltage, total current and current through the splitter plate under the conditions of the 1 kA (RMS value) prospective current, 20 % opening vent. Figure 48 presents the arc images captured by the high-speed camera, corresponding to Figure 47. After ignition by a wire explosion, the arc is forced towards the splitter plates by the pressure gradient and Lorentz force. From 1.35 ms, it is observed that the arc starts to bend and to stretch around the plates before a sufficient voltage arises for forming the arc root on the surface of the splitter plate. From 1.5 ms, the current through the plate increases and the arc roots are formed on the splitter plate between 1.59 ms and 1.72 ms. After arc root formation, two current paths are observed through and outside the plate. The current through the plate reaches the total current at 7 ms.

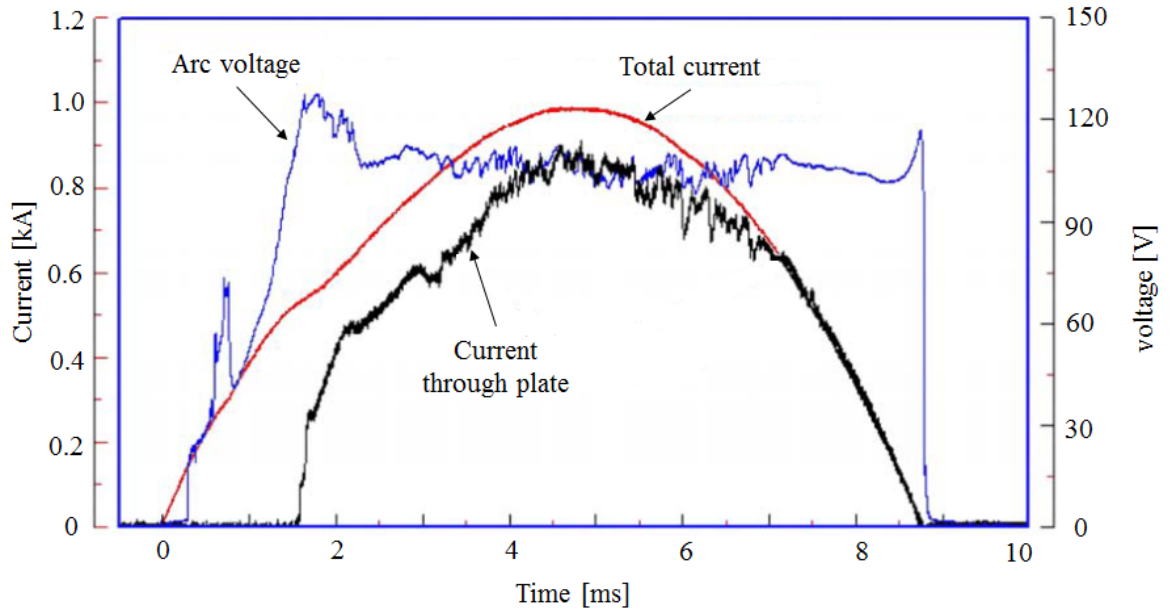


Figure 47 Arc voltage, total current and current through the splitter plate under the conditions of the 1 kA (RMS value) prospective current, 20 % opening vent [66].

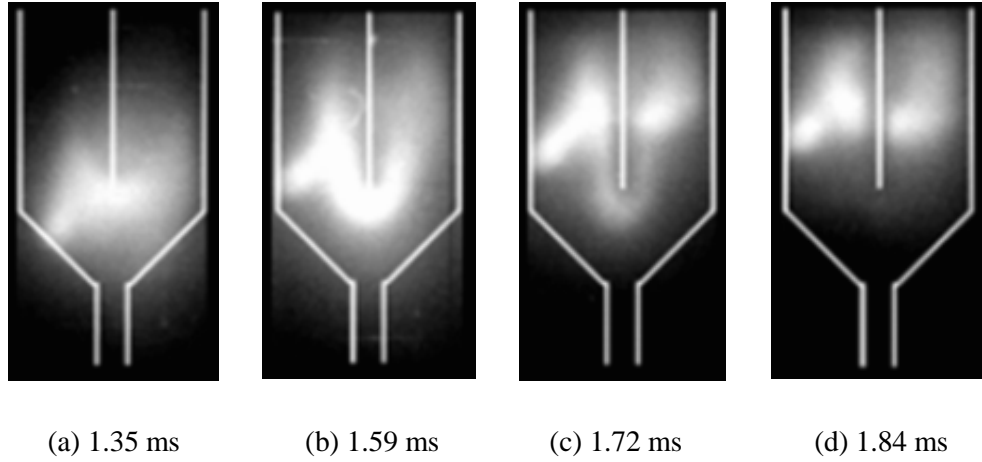


Figure 48 Arc images captured by high speed camera corresponding to Figure 47 [66].

It is thought that this phenomenon is the consequence of the arc roots between the arc column and splitter plate, where the LTE does not hold and there is a space charge region. In order to implement this phenomenon through arc modelling, Lindmayer's group chose the macroscopic approach instead of the microscopic scale analysis in the arc roots. They introduced the nonlinear relationship between the voltage drop and current density in the arc root region of the splitter plates as shown in Figure 49,

called V-J curve. The cathode and anode roots are treated equally. The voltage increases from 0 to 19.7 V in the range of the current density of 0 to 11000 A/m<sup>2</sup>; however, it decreases from a current density of 11000 A/m<sup>2</sup> and approaches 10 V above a certain threshold of the current density (10<sup>5</sup> A/m<sup>2</sup>). The peak voltage of 19.7 V is called the voltage hump. A thin layer (0.1 mm) is modelled in front of the splitter plates and its local electrical conductivity is determined according to the V-J curve (see Figure 49). The electrical conductivity in a thin mesh is calculated as below

$$\sigma_{il} = J_{ar} \frac{V_y}{V_{ar}}, \quad (23)$$

where,  $J_{ar}$  is the current density  $V_{ar}$  is the voltage drop in the arc root and  $\Delta y$  is the layer thickness (0.1 mm) [67].

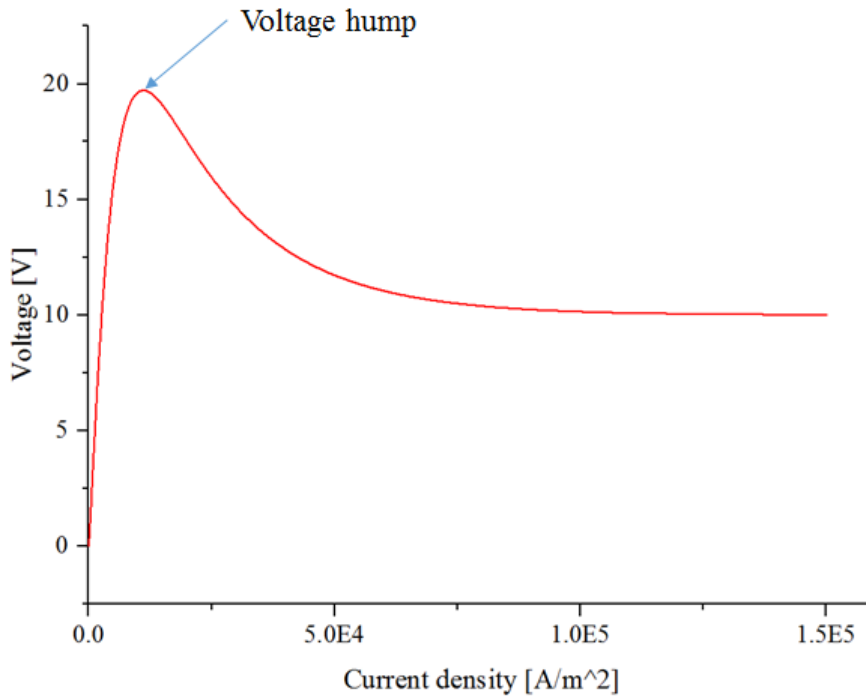


Figure 49 Nonlinear relationship between the voltage drop and current density in the arc root region (V-J curve) [68].

The preliminary simulation of the arc root formation was carried out by the commercial software, ANSYS CFX. The model has two parallel electrode ( $4.5 \times 1.5 \times 16$  mm), one copper plate ( $4.5 \times 2 \times 7$  mm) and a fully open vent. The arc current of 100 A DC is imposed to the electrode and the constant magnetic field (0.001 T) is applied in the chamber. Figure 50 shows the simulated results (current density) of arc splitting process. After ignition, the arc moves upwards and reaches the splitter plate at 0.24 ms. It starts to bend and the arc roots are visible at 0.48 ms. At 0.66 ms, two current paths are seen through and outside plate. At 0.72 ms, nearly the total current flow through the plate.

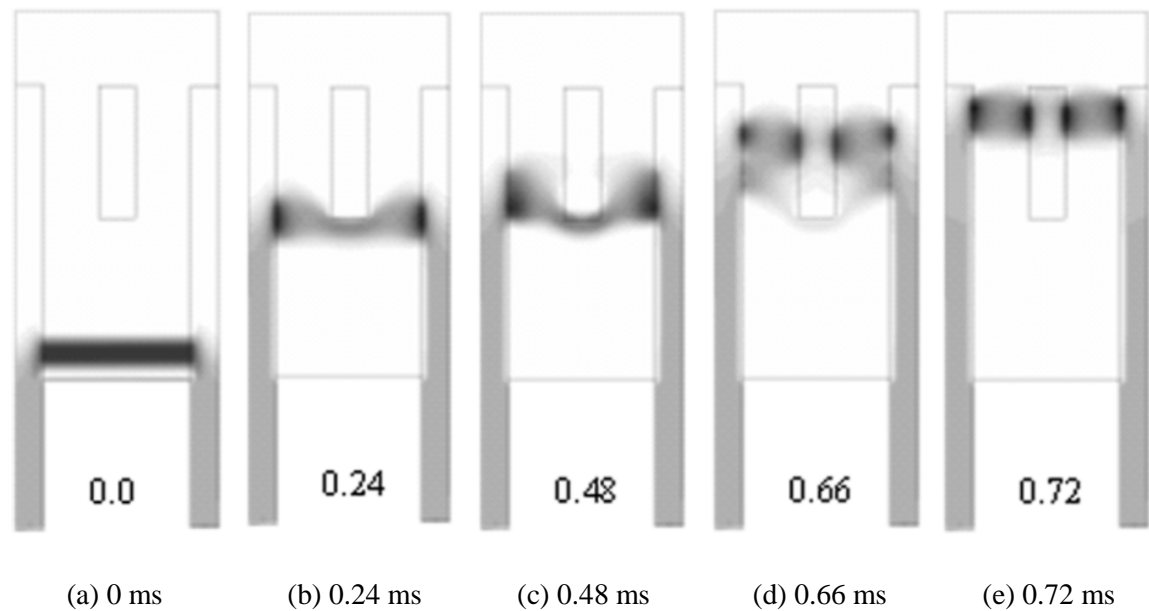


Figure 50 Simulated current density under the conditions of the 100 A DC current, 0.001 T magnetic field and fully open vent [66].

Lindmayer's arc root model (V-J curve in Figure 49) can simulate the arc behaviour when the arc enters the splitter plate region. It becomes the fundamental method to consider the arc root effect in arc modelling. But, there are few simulation studies that have investigated the negative V-I characteristics in the low current region as described in 2.2.4. Experimental results shows the arc voltage increases as the current decreases in the low current region, below approximately 100 A where the arc root voltages are the mainly contribution. It is essential to consider the negative V-I characteristics in order to obtain the accurate arc voltage near the current zero point. In this thesis, we will investigate the effect of Lindmayer's V-J curve on the arc voltage in the low current region and propose a modified V-J curve considering the negative V-I characteristics in the LVSD arc.

#### 2.5.4 ARC MODELLING EXAMPLE

Rong *et al.* carried out arc modelling based on the description above [67]. They modelled the MCB chamber that quite has a quite complex structure. Figure 51 shows the geometry of the MCB chamber consisting of 12 splitter plates, 2 vents, and side plates. The process of contact opening is not included and the simulation begins with a fully open contact gap. The NEC method is used for radiation loss and Lindmayer's idea is adopted to consider the arc root effect. The limited current is calculated based on the external circuit and arc voltage. A no slip wall condition is imposed on the interfaces between the fluid and solid part. All outside surfaces have the temperature of 300 K and zero magnetic vector potential is set on the outermost background surfaces.

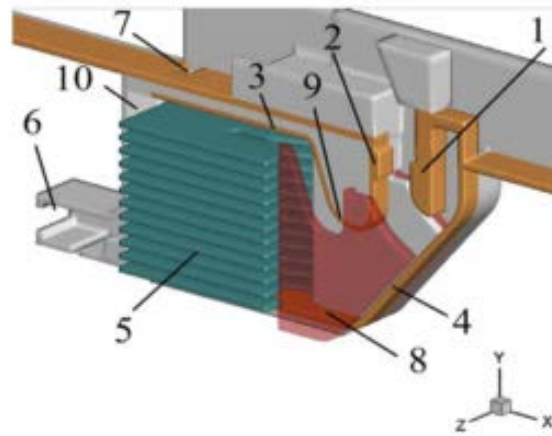


Figure 51 Geometry of the MCB; (1) Movable contact, (2) fixed contact, (3) upper runner, (4) lower runner, (5) splitter plate, (6) vent 1, (7) vent 2, (8) iron, (9) U-shape area of the upper runner, (10) air zone in chamber [67].

Figure 52 shows the simulated and measured results of current and arc voltage under the condition of the 2500 A (RMS value) prospective short-circuit current. The short-circuit current is provided from the capacitor bank. In the experiment, the switching process begins with contact opening, which is different from the simulation. Figure 53 presents the simulated temperature distribution in the MCB chamber, which corresponds to Figure 52. After ignition, the arc voltage increases until around 1.5 ms as the arc moves towards the splitter plates. Between 1.5 ms and 2.0 ms, the arc moves backwards since arc motion is blocked by the splitter plates, leading to a significant voltage drop. After then, the arc roots are formed on the splitter plates and the arc voltage increases up to 230 V. There are some discrepancies between measured and simulated results. The overall simulated arc voltage is lower than the measured one; hence, the simulated arcing time is longer by 0.7 ms. Several big drops of the

arc voltage are observed in the experimental results, which is related to arc back motions near the splitter plates; but, only a single voltage drop and arc back motion is simulated. But, it is worth mentioning that Rong's arc simulation is carried out with the real MCB considering current limitation and arc root formation.

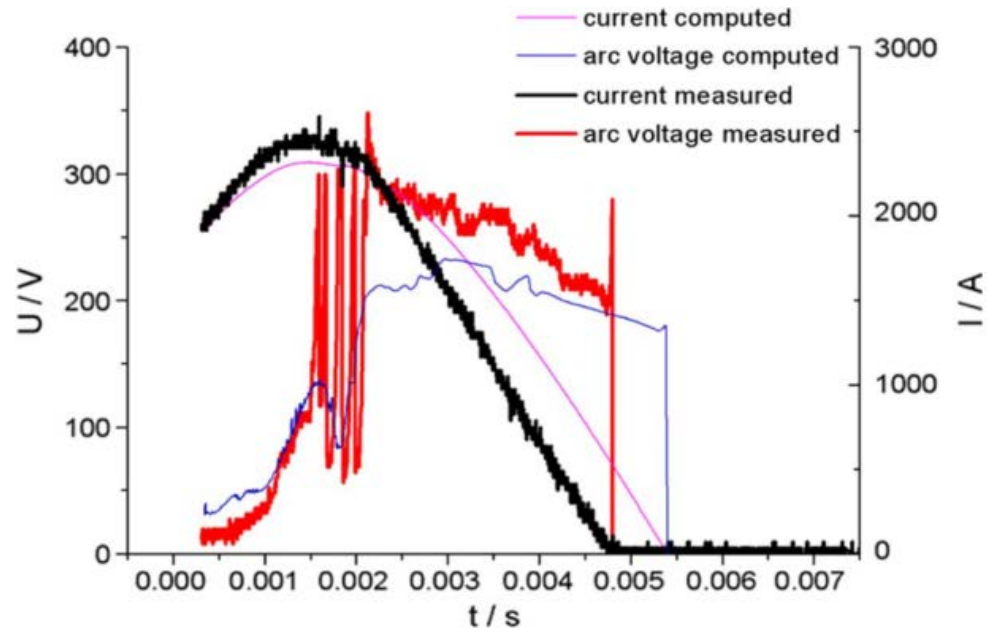


Figure 52 Simulated and measured results of current and arc voltage [67].

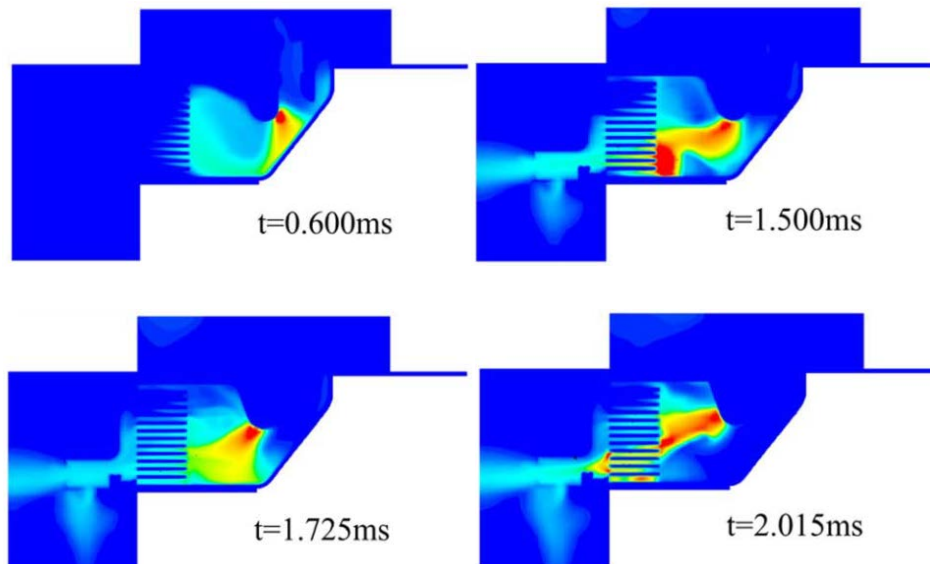


Figure 53 Simulated temperature distribution in the MCB chamber, which corresponds to Figure 52 [67].

In order to validate arc modelling, most of numerical studies compares only current and voltage waveforms like Figure 52; but, comparing arc motion is essential since arc motion is a fundamental characteristic of the LVSD arc, which determines the arc voltage and current limitation. In this thesis, we will compare the simulated arc motion (temperature distribution) with the arc images measured by the AIS for arc modelling validation.



## 2.6 SUMMARY

LVSDs can be classified into MCs, MCBs, MCCBs and ACBs. All of LVSDs switch the current in the quenching chamber which contains air. Air at ambient conditions is a good insulating medium which is sufficient to withstand the electric field under the low voltage condition. However, during the switching process of a LVSD, air is transformed into a conductive medium, the air arc, which is the ionized mixture of ions, electrons and neutral particles.

The air arc consists of three regions: an arc column, a cathode root and an anode root. The arc column is the plasma zone where the LTE condition holds. The arc column can be modelled through the MHD approach. The arc root (a cathode and an anode root) is a thin region between an arc column and the metal surface of the cathode or anode. The special treatment is required to simulate the effect of the arc root since the LTE condition does not hold in it.

The switching performance of a LVSD is determined by current limitation and re-ignition phenomena. Numerous empirical and numerical studies have been carried out in an attempt to predict and improve the switching performance; yet, there are some limitations in previous researches.

Firstly, there is little investigation of re-ignition phenomena and its evaluator based on a broad range of switching conditions (test circuit and type of LVSDs). In previous studies, the experimental investigations were carried out under the limited test condition (a single circuit condition using a single type of LVSD). Also, previously proposed evaluators do not consider the influence of the recovery voltage, which is the source of re-ignition. It is therefore necessary to investigate a more reliable evaluator including the effect of the recovery voltage, based on switching data obtained from a more varied range of test conditions.

Secondly, most of simulation work has focused on current limitation and behaviour of the arc plasma prior to the current zero moment without evaluating re-ignition following the current zero point. The numerical simulation calculating both current limitation and re-ignition phenomena is required to predict the whole switching performance.

Thirdly, it is known that arc motion has a significant influence on the arc voltage that is one of the main characteristics of the air arc. However, there has been little empirical work about detailed arc motion in the splitter plate region and its effect on the arc voltage. Most of arc motion experiment has been carried out without capturing arc images in the splitter plate region in previous studies.

Fourthly, the vent distribution can be the design parameter of a quenching chamber, which influences arc motion during the switching process. No previous study has investigated the effect of the vent

aperture distribution on arc motion; it is worth to study the influence of the vent distribution in an attempt to improve the switching performance.

Finally, the AIS has been widely used to investigate arc motion in the LVSD chamber by capturing the arc light intensity. It is assumed that the light intensity measured by the AIS is related to the arc temperature. Nonetheless, there has been no detailed empirical study about the correlation between the light intensity and arc temperature; hence, this thesis covers the experimental investigation about it.

## CHAPTER 3: EXPERIMENTAL METHODS

### 3.1 PURPOSES OF EXPERIMENTS

There are three kinds of experiments in this thesis; the switching tests, arc imaging measurement and arc spectrum measurement.

The switching tests are carried out with 10kA, 20kA, 55kA and 100kA test circuits using either MCBs or MCCBs. These various kinds of switching data are used to investigate a more accurate and reliable evaluator for the prediction of re-ignition phenomena.

The arc imaging measurement is conducted with the FTA and AIS. The measured data is used to study detailed arc motion in the splitter plate region and the effect of the vent aperture distribution on arc behaviour. Moreover, arc modelling is validated by comparing the simulated results with measured arc images.

The arc spectrum measurement is conducted by capturing the arc light intensity as well as arc spectra. The arc temperature is calculated from the arc spectra and its correlation with the light intensity is investigated. Based on the results of this experiment, we can prove that the light intensity measured by the AIS represents the arc temperature distribution, which is essential information to validate arc modelling.

### 3.2 SWITCHING TESTS FOR RE-IGNITION EVALUATORS

#### 3.2.1 SWITCHING TEST CIRCUITS AND CONDITIONS

The investigation for re-ignition phenomena and its evaluator has been carried out based on the switching data of various kinds of test conditions. Several kinds of LVSDs are used for the switching tests. Figure 54 shows diagrams of the interruption test circuits for single- and three-phase LVSDs. The short-circuit condition is adjusted by a transformer, resistor and reactor. Only R and T phases are utilized for the single-phase tests. A 13.8 kV commercial power line is used as the power source for the 10 kA and 20 kA switching tests, whereas a short-circuit generator provides the energy for the 55 kA and 100 kA tests. The current and voltage of each phase are recorded by an oscilloscope (10 MHz, Yokogawa DL750), a passive voltage probe (250MHz, Tektronix P5100) and a Rogowski current transducer (16MHz, PEM CWT).

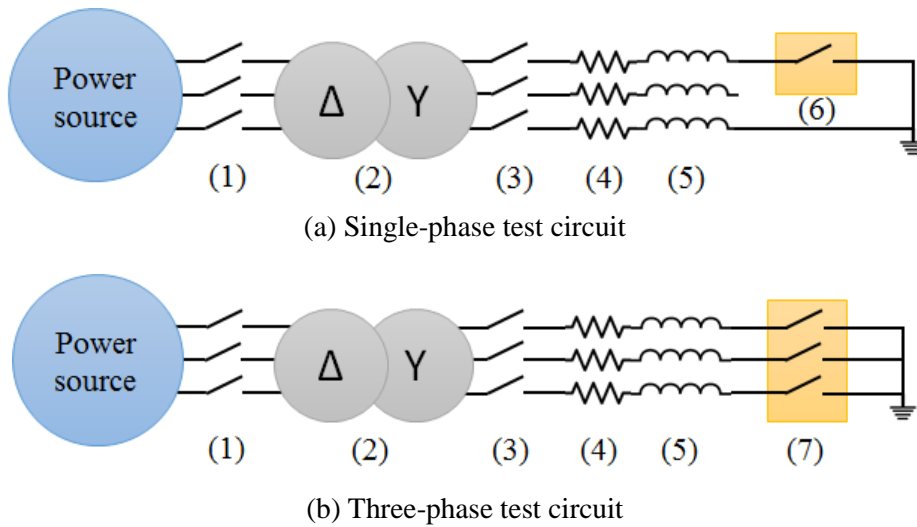


Figure 54 Test circuit diagrams for a single-phase and three-phase LVSD:  
 (1) back-up circuit breaker, (2) three-phase transformer, (3) making switch, (4) resistor,  
 (5) reactor, (6) single-phase MCB, (7) three-phase MCB or MCCB.

Table 2 shows the test condition of each switching case. All tests are carried out with the 60 Hz source. A total of 110 interruption tests are conducted with previously unused switching devices under five different test circuits. There is a single test circuit condition (voltage: 252 V, prospective current: 10 kA) in the single-phase tests. For three-phase tests, four kinds of test circuit conditions (voltage: 483 V, prospective current: 10, 20, 55, 100 kA) are used. The power factor is selected according to the test standard [14]. Table 3 shows the quenching chamber features of the LVSDs used for given switching tests. When the circuit condition is repeated for the tests on the same LVSD type (for example, the switching cases of test number 1 – 26 in Table 2), the venting condition varies or some components within the quenching chamber are replaced. This includes changing the geometry of the movable and fixed contact, splitter plate, side plate, magnetic yoke or gassing material. Therefore, there is no identical test condition among 110 switching cases presented in Table 2. Testing a variety of circuit conditions and chamber configurations provides the broad switching results for the thorough investigation of re-ignition evaluators.

Table 2 Switching test conditions.

Number of phase	Voltage <sup>a</sup> (RMS value)	Prospective current (RMS value)	Power Factor <sup>b</sup>	Kind of LVSDs	Test number <sup>c</sup>
1	252 V	10 kA	0.45 <sup>d</sup>	63AF <sup>e</sup> MCB	1 - 26
3	483 V	10 kA	0.45 <sup>d</sup>		27 - 28
		20 kA	0.3	100AF MCCB	29 - 41
				125AF MCCB	42 - 48
				250AF MCCB	49 - 52
				800AF MCCB	53 - 56
		55 kA	0.2	125AF MCCB	57 - 65
				160AF MCCB	66 - 67
				250AF MCCB	68 - 69
				400AF MCCB	70 - 73
				800AF MCCB	74 - 78
		100 kA	0.2	160AF MCCB	79 - 86
				250AF MCCB	87 - 88
				400AF MCCB	89 - 91
				630AF MCCB	92 - 99
				800AF MCCB	100 - 110

<sup>a</sup> The voltage value refers to the phase voltage in single-phase tests and line-to-line voltage in three-phase tests. It is a 60 Hz voltage.

<sup>b</sup> The power factor is selected according to IEC 60947-2 [14].

<sup>c</sup> The test number corresponds to the switching data in results section 4.1.

<sup>d</sup> According to IEC 60947-2, the power factor is 0.5 when short-circuit current is 10 kA.

<sup>e</sup> Ampere Frame(AF) represents the frame size rating of the LVSD. For example, a 800 AF MCCB has a rated current of 700 A or 800 A (r.m.s value). A different trip unit is adopted according to a rated current.

Table 3 Quenching chamber features of LVSDs.

Kind of LVSDs <sup>a</sup>	Type of chamber <sup>b</sup>	Quantity of splitter plates	Parameters <sup>c</sup>
63AF MCB	Single	13	- Venting condition - Geometry of movable and fixed contact - Geometry of splitter plate - Geometry of side plate - Geometry and kind of gassing material <sup>d</sup>
100AF MCCB	Single	10	- Venting condition - Geometry of splitter plate - Geometry of gassing material
125AF MCCB	Single	10	- Venting condition - Geometry of splitter plate - Geometry of gassing material
160AF MCCB	Double	16	- Venting condition - Geometry of magnetic yoke - Geometry of gassing material
250AF MCCB	Double	16	- Venting condition - Geometry of magnetic yoke <sup>e</sup> - Geometry of side plate <sup>e</sup>
400AF MCCB	Double	18	- Geometry of splitter plate - Geometry of magnetic yoke
630AF MCCB	Double	18	- Geometry of movable contact - Geometry of splitter plate - Geometry of magnetic yoke
800AF MCCB	Double	18	- Geometry of movable contact - Geometry of splitter plate - Geometry of magnetic yoke

<sup>a</sup> Each kind of LVSDs has a different configuration of the quenching chamber. In general, the quantity of splitter plates is larger and the volume of a quenching chamber is bigger as the ampere frame (AF) becomes higher.

<sup>b</sup> There are two types of quenching chambers in LVSDs: one is a single contact chamber and the other is a double contact chamber.

<sup>c</sup> When the circuit condition is fixed for the tests on the same kind of the LVSD (for example, the switching cases of test number 1 – 26 in Table 2), several design parameters (the venting condition and the geometry of a movable contact, fixed contact, splitter plate, side plate, magnetic yoke or gassing material) of the quenching chamber are changed.

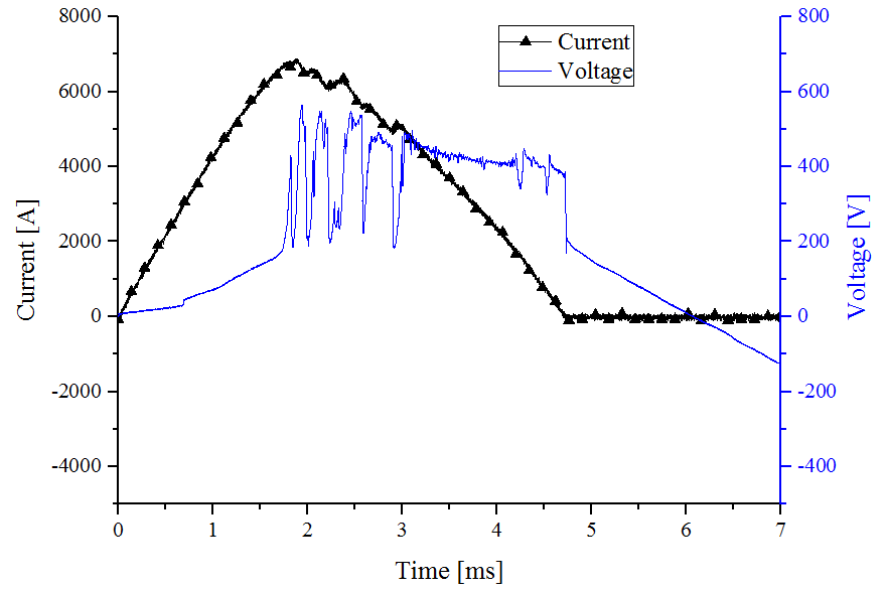
<sup>d</sup> The polymer can be placed inside the quenching chamber to improve the switching performance. This polymer is called the gassing material.

<sup>e</sup> The side plate and magnetic yoke (shown in Figure 3) influence the magnetic field in the chamber and they help to increase Lorentz force on the arc.

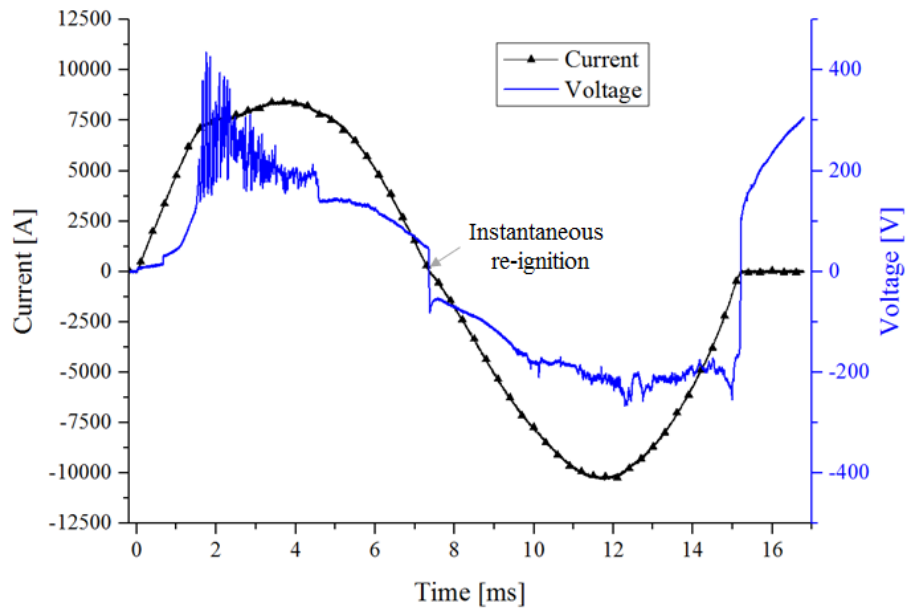
### 3.2.2 WAVEFORM ANALYSIS

There are three possible switching outcomes: 1) a successful interruption without re-ignition, 2) a failed interruption with instantaneous re-ignition or 3) a failed interruption with delayed re-ignition. All interruptions with re-ignition are regarded as failures in this thesis. Figure 55 shows the current and voltage waveforms of a successful interruption and two kinds of re-ignition in the switching test of LVSDs. In the successful interruption, the arc is extinguished at the first current zero point without

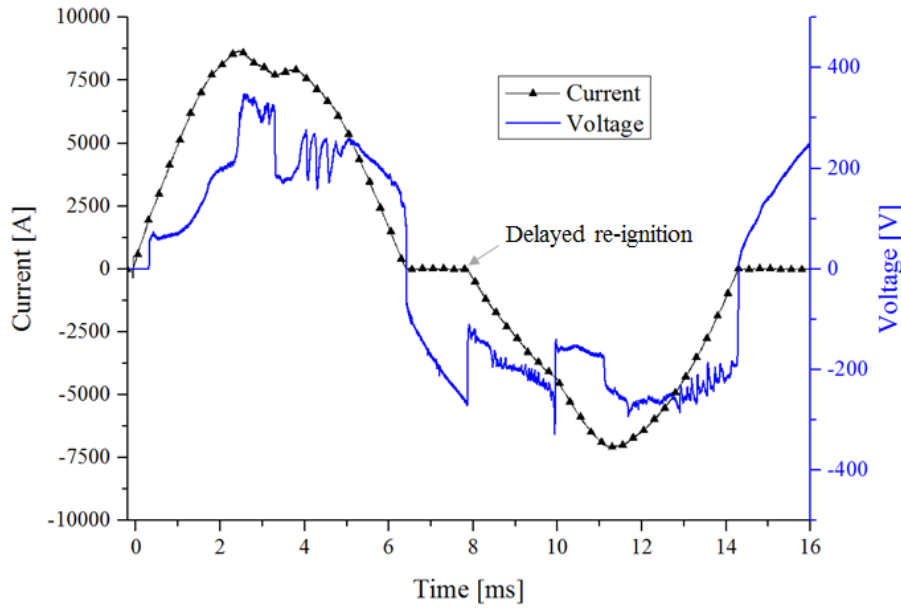
re-ignition (see Figure 55 (a)). In the case of instantaneous re-ignition, the arc re-ignites and the current continues to flow immediately following the current zero point (see Figure 55 (b)); however, delayed re-ignition has a pause without current flowing prior to arc re-ignition [52], [69] (see Figure 55 (c)).



(a) Waveforms of successful interruption



(b) Waveforms of instantaneous re-ignition



(c) Waveforms of delayed re-ignition

Figure 55 Current and voltage waveforms of a successful interruption and two kinds of re-ignition: these are the switching results of single-phase MCBs under 252 V and 10 kA condition.

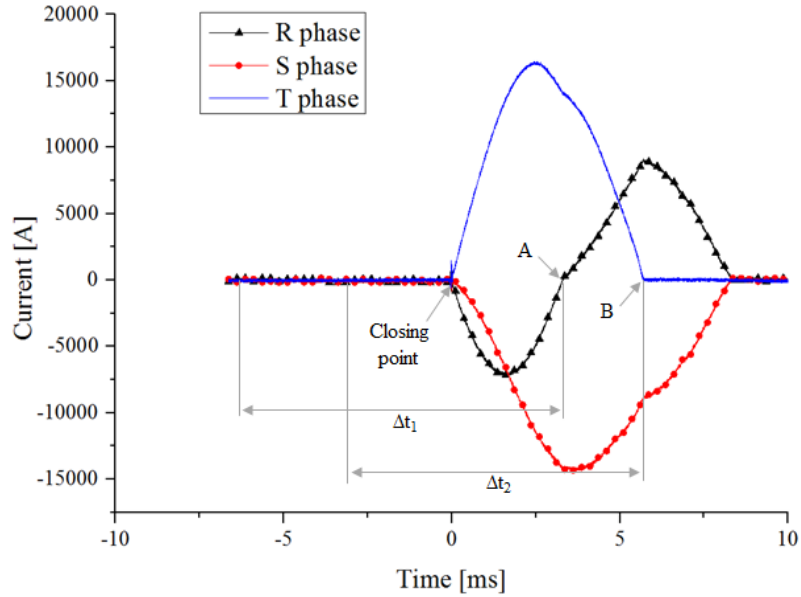
#### *Exit Arc Voltage, Re-ignition Arc Voltage and System Voltage at the Current Zero Point*

To investigate re-ignition evaluators the following parameters are derived from the switching waveforms: the exit arc voltage, re-ignition arc voltage and system voltage at the current zero point. The exit arc voltage is defined as the value of the arc voltage 20  $\mu$ s prior to the current zero point in either successful or failed interruptions, coinciding with the definition provided by Hauer *et al.* [52], [69]. The re-ignition arc voltage is the value of the arc voltage 20  $\mu$ s after the current zero point only when instantaneous re-ignition occurs. The system voltage at the current zero point is the value of the supplied voltage across a LVSD when the arc is extinguished or re-ignites.

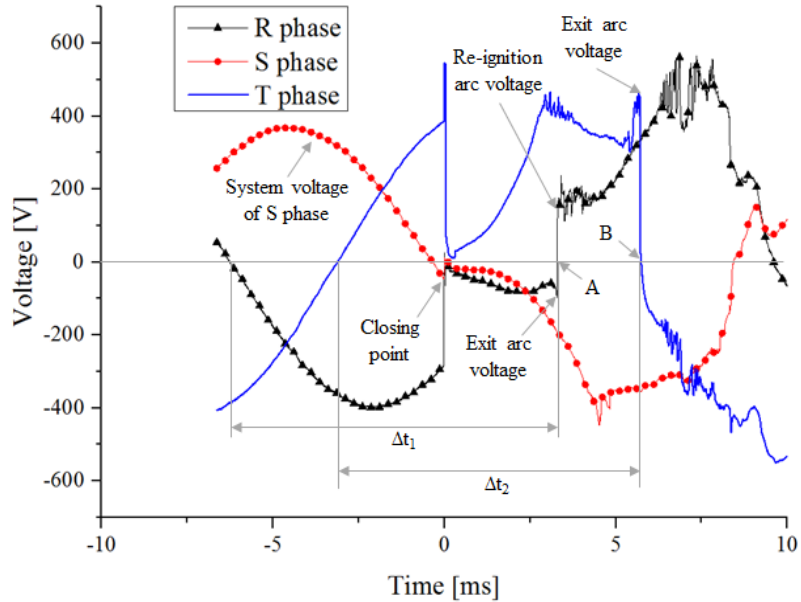
Figure 56 shows typical current (a) and voltage waveforms (b) during a three-phase interruption process of a MCCB where instantaneous re-ignition occurs in the R phase and the arc is first extinguished in the T phase. The movable contacts of the device are manually closed to the fixed contacts from the open state at 0 ms and instantaneously begin to separate automatically due to the repulsion force caused by short-circuit current. The arc voltage rises as the contact gap increases and the -93 V exit arc voltage is observed at the first current zero point (A) of the R phase. After passing the current zero point (A), the arc polarity reverses to match the current polarity in the R phase. After instantaneous re-ignition, the re-ignition arc voltage is recorded as 150 V immediately after the



current zero point. The first arc interruption takes place at the first current zero point (B) of the T phase where the 448 V exit arc voltage is observed. The exit and re-ignition arc voltage are directly measured from the arc voltage waveforms. The system voltages at the current zero points (A: 180 V and B: -80 V) are obtained through the extrapolation using the time period from the current zero point



(a) Current waveforms



(b) Voltage waveforms

Figure 56 Current and voltage waveforms of a three-phase MCCB switching test under 483 V and 20 kA condition: A is the first current zero point in R phase and B is the first current zero point in T phase.

to the last zero moment of the system voltage prior to the arc ignition ( $\Delta t_1$ : 9.58 ms and  $\Delta t_2$ : 8.84 ms). If instantaneous re-ignition occurs, the data of the next current zero event are measured.

### Definition of Voltage Ratio

The exit arc voltage, proposed by Hauer [52], [69], is the simplest evaluator to predict instantaneous re-ignition, which is easy to implement in an industrial design scenario; however, this evaluator does not consider the recovery voltage, which is the source of re-ignition. The voltage ratio is introduced as a new evaluator of re-ignition in order to consider the influence of the recovery voltage on the arc phenomena after the current zero point. It is defined as the ratio of the recovery voltage to the exit arc voltage. The recovery voltage is assumed as the system voltage in the single-phase system. Figure 55 shows that the recovery voltage is mainly determined by the system voltage. But, in the three-phase system, the voltage of the neutral point needs to be included to the recovery voltage.

In [70], Onchi *et al.* presented the calculation of the neutral point voltage in the three-phase LVSD test circuit. Figure 57 shows the equivalent circuit diagram of the three-phase switching test.

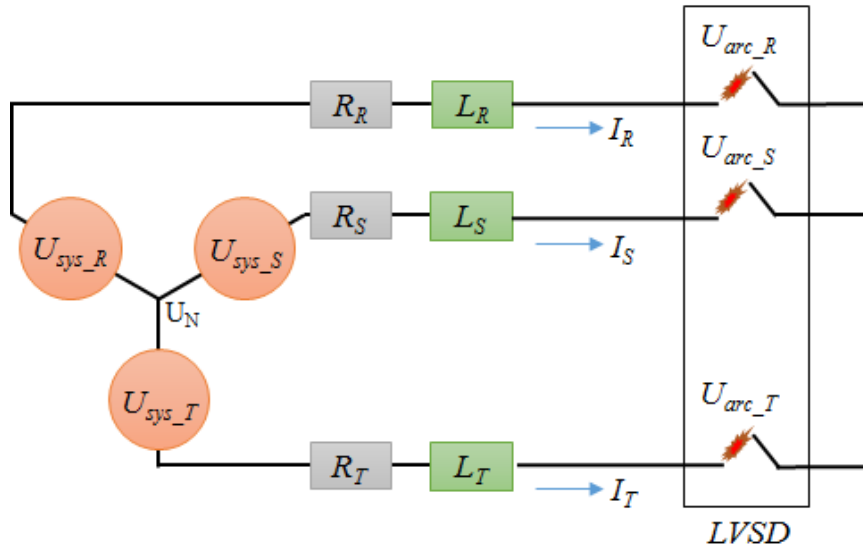


Figure 57 Equivalent circuit diagram of a three-phase switching test:  $U_{sys}$  is the system voltage,  $I$  is short-circuit current,  $U_{arc}$  is the arc voltage,  $U_N$  is the voltage at the neutral point,  $R$  is the resistance,  $L$  is the inductance and the subscripts ( $R$ ,  $S$  and  $T$ ) represent each phase of the circuit.

The circuit equation of the R-phase based on Kirchhoff's voltage law can be expressed as,

$$U_{sys\_R}(t) = I_R(t)R_R + L_R \frac{dI_R(t)}{dt} + U_{arc\_R}(t) + U_N, \quad (24)$$

where,  $U_{sys}$  is the system voltage,  $I$  is short-circuit current,  $U_{arc}$  is the arc voltage,  $U_N$  is the voltage at the neutral point,  $R$  is the resistance,  $L$  is the inductance and the subscripts ( $R$ ,  $S$  and  $T$ ) represent each phase of the circuit. We can get Equations (25), (26) and (27) since the three-phase power sources are synchronized.

$$U_{sys\_R}(t) + U_{sys\_S}(t) + U_{sys\_T}(t) = 0. \quad (25)$$

$$I_R(t) + I_S(t) + I_T(t) = 0. \quad (26)$$

$$\frac{dI_R(t)}{dt} + \frac{dI_S(t)}{dt} + \frac{dI_T(t)}{dt} = 0. \quad (27)$$

The voltage at the neutral point in the power source part can be calculated from Equation (28) by using the three circuit equations of each phase and Equations (25), (26) and (27).

$$U_N = -\frac{U_{arc\_R}(t) + U_{arc\_S}(t) + U_{arc\_T}(t)}{3}. \quad (28)$$

It is assumed that the recovery voltage applied across each phase of the LVSD is composed of the system voltage and the neutral point voltage. Since the arc voltage becomes zero at the current zero point, the recovery voltage across the R phase can be written as

$$U_{rec\_R} = U_{sys\_R}(t) + \frac{U_{arc\_S}(t) + U_{arc\_T}(t)}{3}. \quad (29)$$

For the three-phase and single-phase system, the voltage ratio can be formulated as Equations (30) and (31), respectively,

$$\text{Voltage ratio for three phase} = \frac{U_{rec\_j}}{U_{exit\_j}}, \quad (30)$$

$$\text{Voltage ratio for single phase} = \frac{U_{sys}}{U_{exit}}, \quad (31)$$

where  $U_{exit}$  is the exit arc voltage and  $j$  is the index of the phase.

#### *Polarity between the Recovery Voltage and Exit Arc Voltage*

When comparing the polarity of the recovery and exit arc voltage, there are two possible cases: the same polarity or opposing polarities. If there is a strong effect of current limitation and a high exit arc voltage during the interruption process, the current drops to zero prior to the zero point of the system voltage and the same polarity case is observed.

### 3.3 ARC IMAGING MEASUREMENT

#### 3.3.1 OVERALL SET-UP

Figure 58 shows the overall set-up of the arc imaging test which is able to detect the arc light intensity and to measure current and voltage waveforms during the interruption process. The arc image system (AIS) connected to optical fibres is used to detect light brightness associated with plasma temperature. The capacitor discharge system (CDS) generates a large current to demonstrate a short circuit condition for the interruption test. The flexible test apparatus (FTA) is designed as the quenching chamber for switching tests under controlled test conditions. The digital storage oscilloscope (DSO) is a data acquisition equipment to record the current and voltage waveforms. The personal computer (PC) is a management device to trigger the AIS, CDS, and FTA for the test. Details of the operation of arc image measurement is explained in Appendix A.

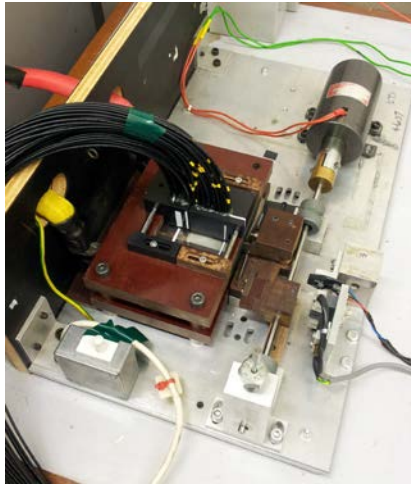


Figure 58 Overall set-up of the arc imaging test.

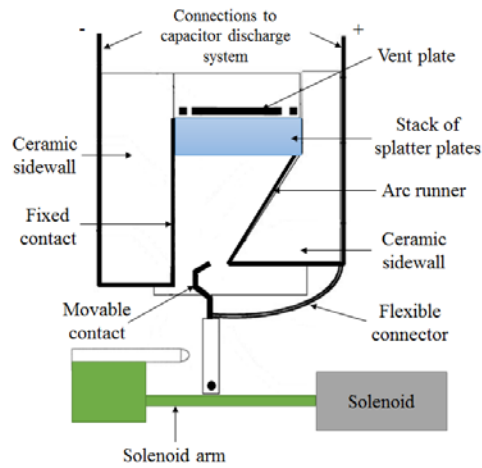
#### 3.3.2 FLEXIBLE TEST APPARATUS

The FTA is designed as the quenching chamber of a MCB [20]. We can change the configuration of the venting and splitter plate, chamber material, chamber geometry, contact material and the opening velocity of the movable contact; therefore, the test conditions can be controlled.

Figure 59 shows the external and internal configuration of the FTA. Optical fibres are put on the window of the chamber top plate and they are connected to the AIS to transmit the arc intensity. The solenoid makes the movable contact move at the beginning of interruption test. Although the total size of the FTA is bigger than that of a commercial MCB, the quenching chamber has a similar size with a commercial one. Figure 60 presents the dimension of the quenching chamber in the FTA.



(a) External configuration of FTA



(b) Internal configuration of FTA

Figure 59 Configuration of FTA.

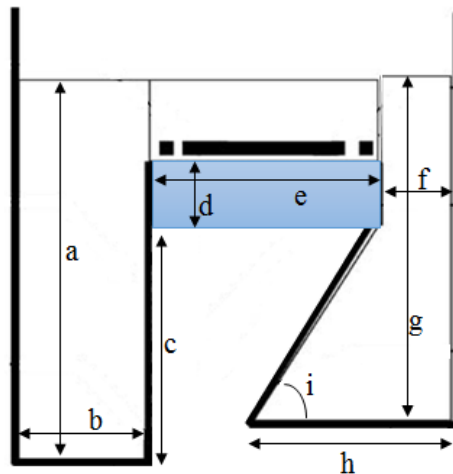


Figure 60 Dimension of quenching chamber in FTA:  $a = 87$  mm,  $b = 50$  mm,  $c = 45$  mm,  $d = 20$  mm,  $e = 32$  mm,  $f = 42$  mm,  $g = 80$  mm,  $h = 63$  mm,  $i = 60^\circ$ .

### 3.3.3 CAPACITOR DISCHARGE SYSTEM

The CDS provides the half cycle wave of the short-circuit current by discharging the electrical energy from a capacitor bank. The magnitude of current can be changed by adjusting the charging voltage of the capacitor bank. Figure 61 presents the schematic diagram of the basic parts in the CDS. The SCR (Silicon-Controlled Rectifier) thyristor is a switch to turn on and off the circuit of the CDS, which is controlled by the PC.

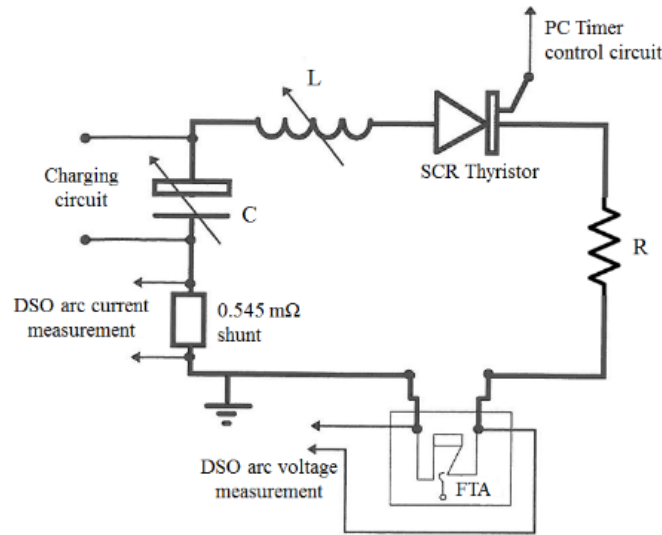


Figure 61 Schematic diagram of the capacitor discharge system [20].

Table 4 shows the specification of the CDS. Figure 62 illustrates the variation of the short-circuit current depending on the charging voltage. It is assumed that the arc is established at 1.9 ms and the arc voltage reaches 160 V after a 1.6 ms arc running time. The short-circuit current is calculated by (7) with the assumed arc voltage. As the charging voltage increases (100 V, 200 V and 300 V), the peak value of current increases (calculated current: 780 A, 1664 A, 2606 A).

Table 4 Specifications of CDS [20].

Component	Value
Capacitor	47.4 mF
Inductor	224 $\mu$ H
Resistor	30 m $\Omega$

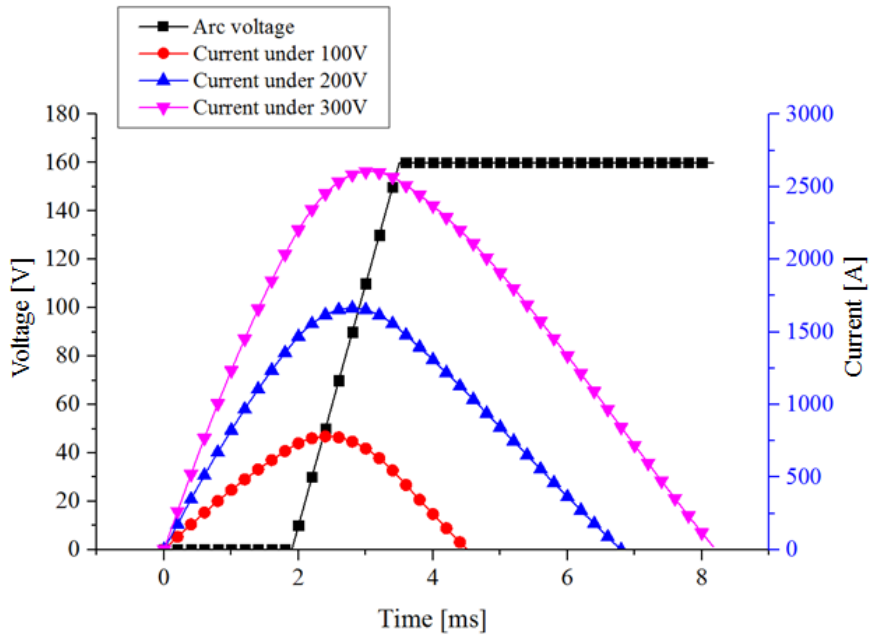


Figure 62 Short-circuit currents depending on the charging voltage.

### 3.3.4 ARC IMAGE SYSTEM

#### *Specification of AIS*

The arc images (light intensity) inside the quenching chamber are recorded by using the AIS linked to a flexible test apparatus (FTA). Figure 63 shows the AIS used in this research.



Figure 63 Commercial AIS made by Taicaan Technology Ltd [71].



Figure 64 shows the spectral characteristics of optical fibres used in the experiments. The fibres are connected to photodiode sensors in the AIS. The photodiode sensor has a spectral response range from 320 nm to 1060 nm. The AIS enables the tracking of the arc motion by capturing the arc light intensity inside the chamber during an interruption operation at 1 MHz sampling rate and 256 levels of intensity. Table 5 shows the specification of the AIS used in this study [71].

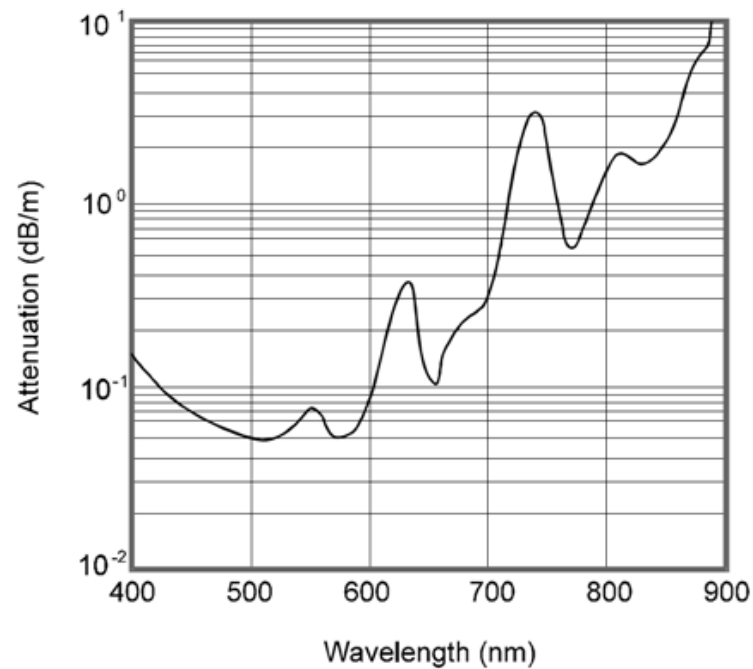


Figure 64 Spectral attenuation of optical fibre [72].

Table 5 Specification of AIS [71].

Item	Experimental value for this study
Sampling rate	1 MHz
Number of optical fibres	109
Light intensity resolution	8 bit (0-255)
Fibre length	2 m
Spectral sensitivity of photodiode	320 nm – 1060 nm

### Fibre array block

Optical fibres are slotted in the fibre array block that is placed on the quenching chamber window of the FTA. Figure 65 and Figure 66 show the fibre array block and fibre positions in the quenching chamber, respectively. The fibre array block is made of black delrin (engineering thermoplastic). It is possible that the fibres can detect the transmitted light from other arc positions instead of the positions just in front of fibres; however, the black block can prevent the arc light from transmitting through it and can record the clear arc images. An array of total 109 optical fibres is fitted into the holes of the fibre array block to allow observation of the overall quenching chamber including the splitter plate region of the FTA (see Figure 66). There are 32 fibres allocated in the region of the splitter plates (8 gaps with 4 fibres per gap).

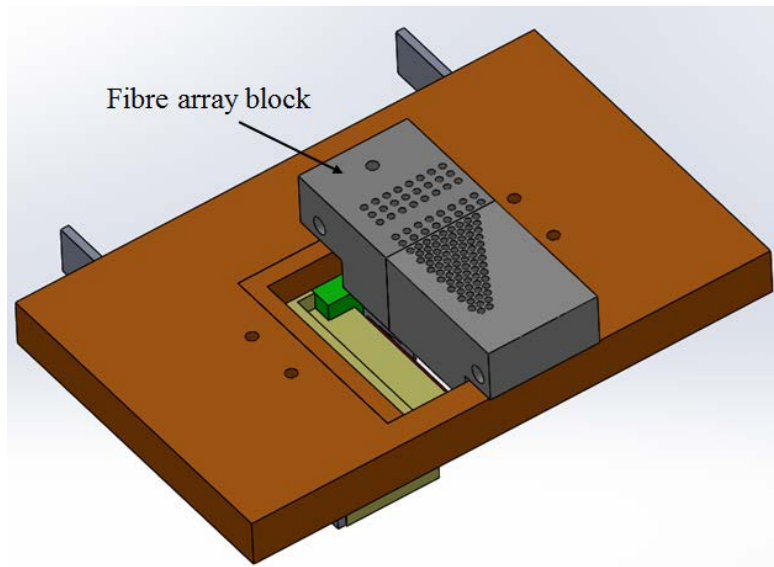


Figure 65 Fibre array block on FTA.

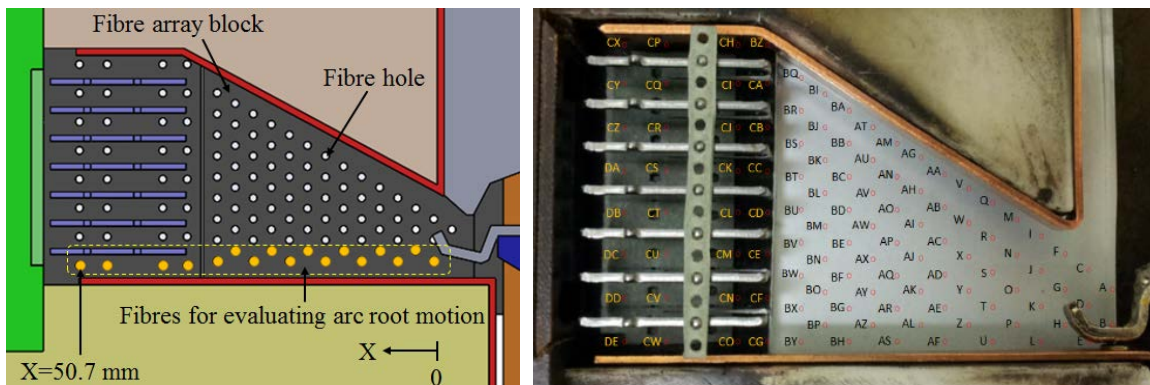


Figure 66 Fibre locations in a quenching chamber (horizontal sections view).

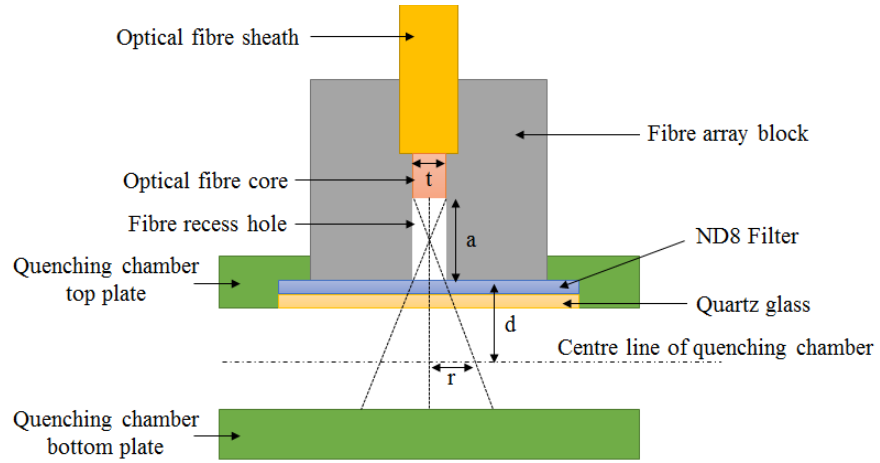


Figure 67 Cross-section of the fibre array block and quenching chamber.

Figure 67 shows a cross-section of the fibre array block and quenching chamber. Each optical fibre is slotted in the hole of the array block and it has a certain radius of view at the centre of the quenching chamber. This radius is calculated by Equation (32) [20],

$$r = t (0.5 + d/a), \quad (32)$$

where  $t$  is the diameter of the fibre (1 mm),  $d$  is the distance between the block and the centre of the chamber (15 mm) and  $a$  is the depth of the recess hole (20 mm). The viewing radius is computed as 1.25 mm.

In order to reduce the intensity of the arc light, ND (Natural Density) 8 filter is placed between the array block and the quartz glass (see Figure 67). Figure 68 shows the spectral transmission of the ND 8 filter. This filter allows only 12.5 % transmittance of the light and helps to avoid the saturation of the light level at each fibre; therefore, more clearer arc images can be measured.

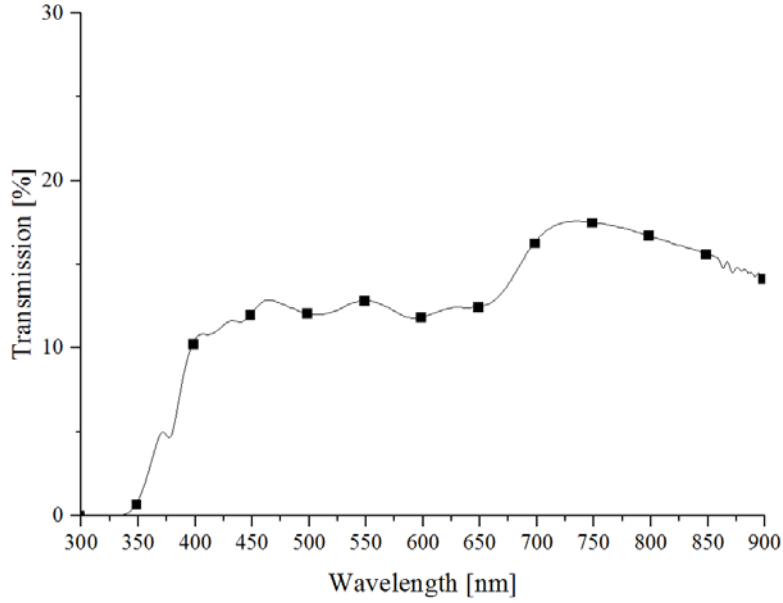


Figure 68 Spectral transmission of ND8 filter [73].

The main difference between the arc imaging measurement in this study and the previous one is observation of arc images in the splitter plate region. In previous studies, optical fibres were not placed in the splitter plate region and there were no detailed measurement of arc images in it. But, in this study, we can capture arc images from 32 fibres in the splitter plate region. These image data can allow to investigate detailed arc motion in the splitter plates and validate arc modelling including arc motion in the splitter plate region.

#### *Normalisation of Light Intensity and Arc Root Trajectory*

After setting optical fibres, we normalise the characteristic of each fibre by measuring the light intensity of the identical LED source. Through the normalisation process, each fibre's scaled factor is calculated, which can compensate the light loss from the connection between the fibre and the photodiode or array block. The fibre normalisation is essential to obtain proper light intensity distribution in the chamber.

Arc root motion is evaluated by the centre of intensity method,

$$x_{CR} = \frac{\sum I_i X_i}{\sum I_i}, \quad (33)$$

where,  $x_{CR}$  is the centre of light intensity,  $I_i$  is the light intensity at a time for the fibre at position  $X_i$  next to cathode surface [49]. The data from 17 fibres near the fixed contact (the cathode electrode) shown in Figure 66 are used for calculating the cathode arc trajectory in the X direction (from the ignition point to the region of the splitter plates). In order to get rid of the influence of low light levels, a filter value was applied to the calculation of arc trajectory in [43]. In this thesis, light levels below the filter value of 90 are set to zero as proposed in previous study.

### *Example of Arc Images*

There are two modes of arc imaging display: dynamic threshold mode and fixed threshold mode. In the dynamic threshold mode, the maximum light intensity across all the fibres at each frame is used as the highest value, so it is good at displaying the arc when light intensity is low. The fixed threshold mode uses the maximum light intensity for the whole data set and it is suitable for an overview of the arc process. There are 7 contour levels for displaying the arc images. We can edit these contour levels. In order to isolate the optimal visual position of the arc, a low range of intensity levels are used. Figure 69 shows the contour levels, which is set as [10 %, 13 %, 16 %, 19 %, 22 %, 25 %, 28 %]. In this thesis, the contour levels shown in Figure 69 are used to present arc motion.

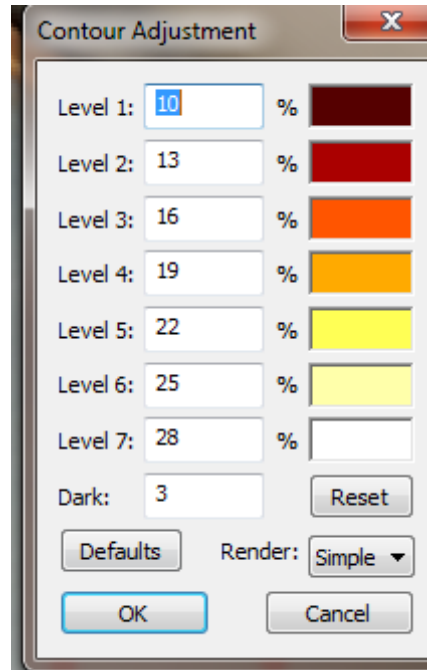


Figure 69 Contour level example; it is set as [10 %, 13 %, 16 %, 19 %, 22 %, 25 %, 28 %].

Figure 70 shows the typical arc motion in the quenching chamber during switching process. These arc images are recorded by the AIS and gives the detailed behaviour of the arc inside the chamber. They are displayed with the dynamic threshold mode and contour level of [10 %, 13 %, 16 %, 19 %, 22 %, 25 %, 28 %]. Basically, the arc develops with 6 steps; ignition between contacts, moving towards plates, entering plates, back motion (jump out of plates) and settlement in plates.

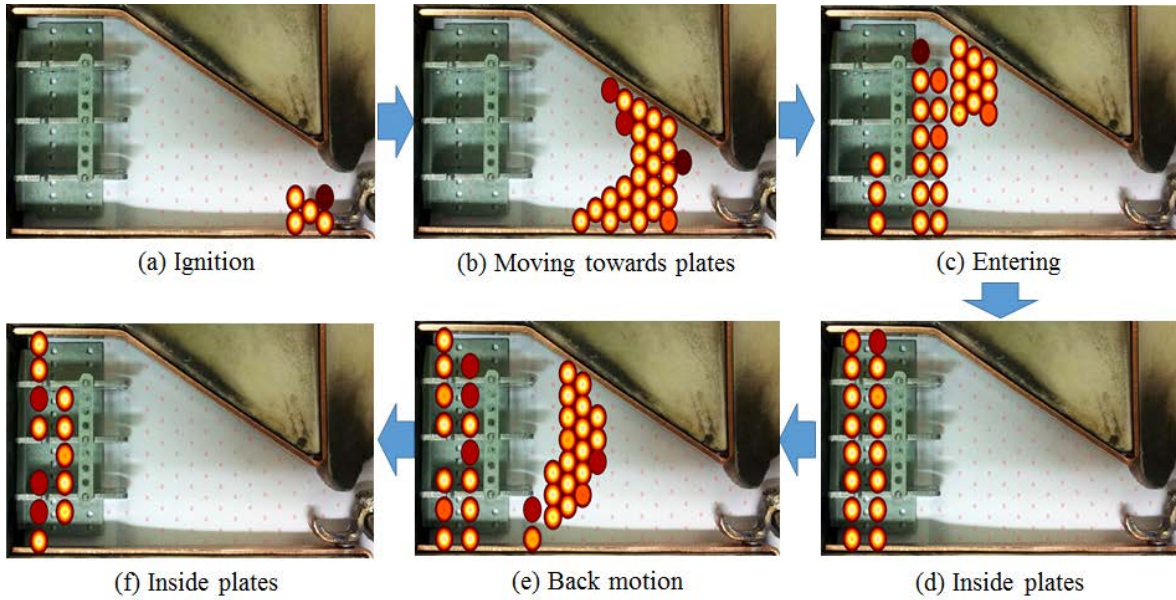


Figure 70 Typical arc motion during switching process; dynamic threshold mode and contour level of [10 %, 13 %, 16 %, 19 %, 22 %, 25 %, 28 %].

### 3.4 ARC SPECTRA MEASUREMENT

In a state of LTE, the arc temperature can be evaluated by the relative intensity of spectral lines as explained in 2.2.5. During the switching process, the arc spectrum at a single fibre location is measured and its temperature is calculated by the Boltzmann plot method. Based on the spectroscopy data, the relationship between the arc temperature and the light intensity measured by the AIS is investigated.

#### 3.4.1 OVERALL SET-UP

Figure 71 shows the set-up for the arc spectra measurement. The spectrometer, laptop and oscilloscope are included to capture the arc spectra: the FTA, CDS, DOS, PC and AIS are used as per the arc imaging measurement. A single fibre from the array of 109 optical fibres is connected to the spectrometer instead of the AIS. The optical emission radiated from the arc is transmitted to the spectrometer through this fibre during the switching operation of the FTA. Software (OceanView) is installed in the laptop to control the spectrometer and to download the spectrum data. The integration time (the time period that the detector of a spectrometer is allowed to collect photons [74]) and the measuring frequency can be adjusted through OceanView. While the spectrometer operates by OceanView, it generates a pulse signal synchronized to the starting moment for the spectrometer to collect photons from the arc. The pulse signals of the spectrometer and current, voltage waveforms are recorded by the oscilloscope at the same time.

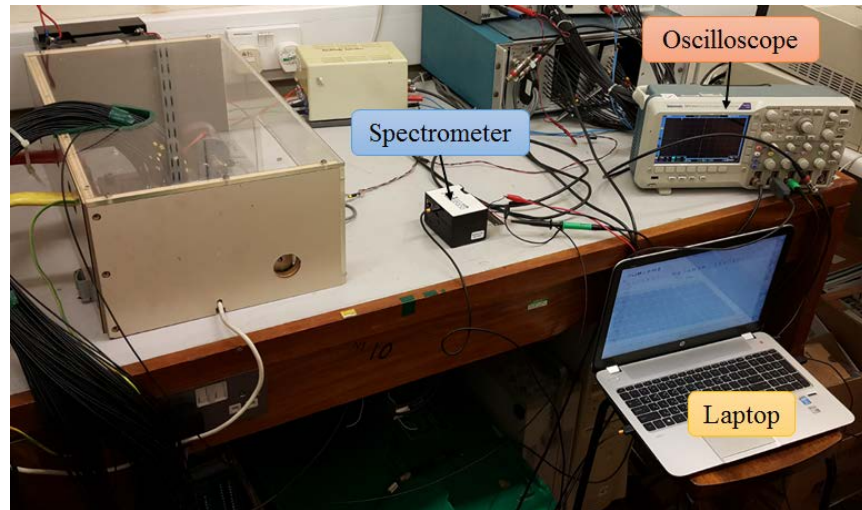


Figure 71 Overall set-up for arc spectra measurement.



### 3.4.2 FLEXIBLE TEST APPARATUS

During spectra measurement, the arc intensity at the same location of the spectrometer fibre cannot be measured by the AIS (since the spectrometer fibre is already occupied at that location). The arc intensity at the spectrometer fibre point can be interpolated from the neighbouring fibres. If the arc moves rapidly with a back- and forth-motion, it is difficult to estimate the arc intensity of the spectrometer fibre point. In order to keep the arc stable, the arc is ignited from a 0.2 mm diameter copper wire and the FTA is modified as shown in Figure 72. Two blocks of glass are placed in the quenching chamber to make a narrow, enclosed space (width 5 mm, depth 6 mm, length 30 mm) as an arc burning chamber. There are two copper wires connected between electrodes in the modified FTA. The capacitor bank is charged to 100 V for a switching, which provides a peak current of 450 A. Figure 73 shows the location of the spectrometer fibre; other fibres are connected to the AIS. The neighbouring BU and BW fibres are used to interpolate the arc intensity at the spectrometer fibre.

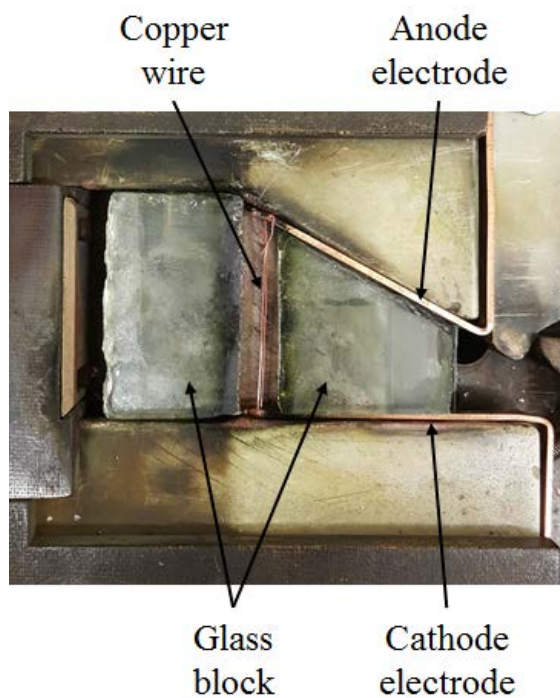


Figure 72 Modified FTA with thin copper wire for arc spectrum measurement.



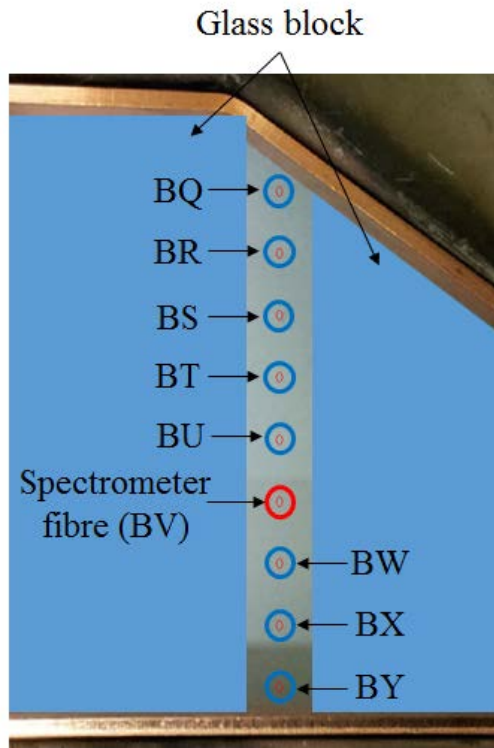


Figure 73 Fibre locations for arc spectrum measurement.

### 3.4.3 SPECTROMETER

An Ocean FX (the model name made by Ocean Optics) spectrometer is employed to obtain the spectrum data in this experiment. Table 6 shows its specifications for arc spectra measurement. The 600 lines/mm grating and the 25  $\mu\text{m}$  slit are used in the spectrometer with sensitivity in the wavelength range of 350 ~ 1000 nm. The integration time is 30  $\mu\text{s}$  and the acquisition rate is approximately 4000 frames/s.

Table 6 Specification of Ocean FX [75].

Grating	600 lines/mm
Entrance slit	25 $\mu\text{m}$
Spectral range	350 – 1000 nm
Integration time <sup>a</sup>	30 $\mu\text{s}$
Acquisition rate	About 4000 frames/s <sup>b</sup>

<sup>a</sup> Integration time is the time period that the detector is allowed to collect photons [74].

<sup>b</sup> Frame refers to a single data set of spectra intensities measured during a 30  $\mu\text{s}$  integration time.

Figure 74 shows the pulse signals generated from the spectrometer and the current and voltage waveforms during the arc spectra measurement. Before the current starts to flow through the FTA, the spectrometer is activated by OceanView software. It measures the arc spectrum from each rising edge of the pulse during a  $30\ \mu\text{s}$  integration period as shown in Figure 75 (the number of spectra measurement is controlled from OceanView software). The synchronized pulse signals and the integration time allow us to know when the spectrum is captured, thus to investigate the correlation between the spectroscopy and arc image with the current and voltage waveforms.

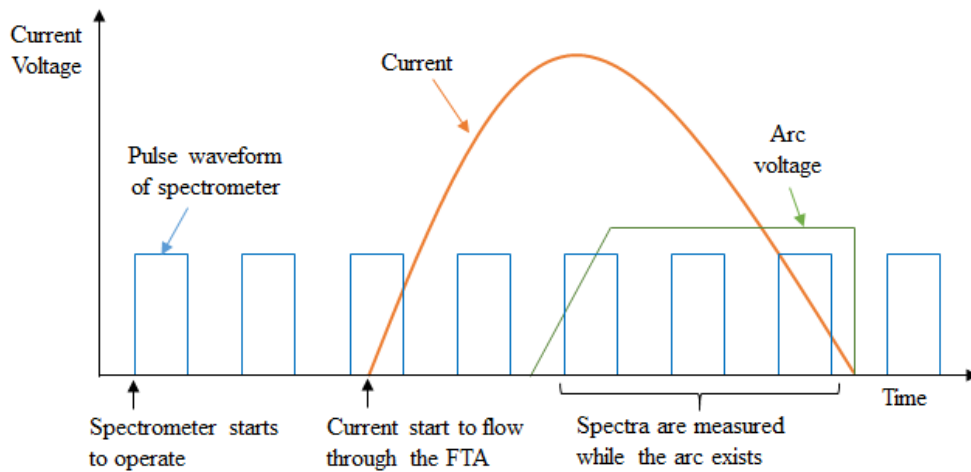


Figure 74 Pulse, current and arc voltage waveforms: the peak current is 450 A.

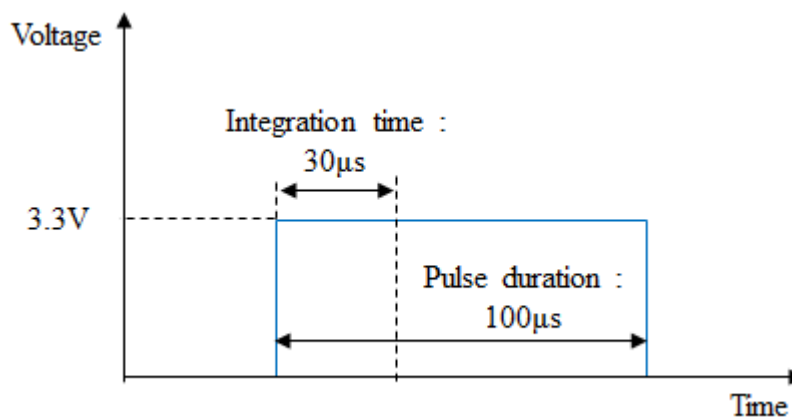


Figure 75 Pulse duration and integration time.

### 3.5 SUMMARY

We carry out three kinds of experiments; the switching tests, arc imaging measurement and arc spectrum measurement.

The switching tests are conducted by using a single- or three-phase circuits to investigate the re-ignition evaluator. The voltage ratio is found as a new evaluator, which is the ratio of the recovery voltage to the exit arc voltage. The recovery voltage in the three-phase system is calculated with the consideration of the voltage at the neutral point of the power source; whereas, for the single-phase system, the recovery voltage is regarded as the system voltage.

The arc imaging data is used to study detailed arc motion in the overall chamber and the influence of the vent aperture distribution on arc behaviour. The arc light intensity is recorded by using the AIS linked to the FTA. An array of total 109 optical fibres is placed in the overall quenching chamber to allow observation of the arc motion in the chamber including the splitter plate region.

We measure the arc spectrum and light intensity by using the spectrometer and AIS. The arc temperature is derived from the relative arc spectrum lines and its correlation with the light intensity is investigated. The result of this experiment is essential to prove that the arc light intensity measured by the AIS represents the temperature distribution in the chamber.

## CHAPTER 4: EXPERIMENTAL RESULTS AND DISCUSSIONS

### 4.1 RE-IGNITION EVALUATORS

The exit arc voltage is the simplest evaluator to predict instantaneous re-ignition, which is easy to implement in an industrial design scenario; however, this evaluator does not consider the recovery voltage and its limitation in predicting successful interruption is observed in the switching test data (see Figure 76). Firstly, there are some successful interruption cases where the exit arc voltage is too small to forecast the success and therefore a failed interruption is expected according to the exit arc voltage. Secondly, there is no clear threshold to distinguish a successful and failed interruption in the evaluator of the exit arc voltage. To overcome the limitations of the exit arc voltage as a sole evaluator and to predict re-ignition more accurately, the voltage ratio is introduced in this study, as in Equations (30) and (31).

The new evaluator, the voltage ratio, will be helpful for the LVSD designer when developing a new product or modifying an existing product. For example, in a new MCCB design process, we can evaluate the performance of a particular chamber and get the optimal design (the product which gives the best performance among design candidates) based on the simulation of the voltage ratio evaluator. The development time and cost will be reduced by the prediction of switching performance prior to real product tests.

#### 4.1.1 EXIT ARC VOLTAGE

Figure 76 presents the full data of the correlation between arc re-ignition occurrence and the absolute value of the exit arc voltage in 10 kA, 20kA, 55 kA and 100 kA switching tests. Since each point corresponds to a different test condition or device design, a large variation in exit arc voltage is observed as expected. It is thought the arc is still in the contact region due to not enough driving force on the arc in the case of a low exit arc voltage (below approximately 50 V). If the exit arc voltage exceeds 400V it is plotted as 400 V. There are 30 successful interruptions with the same polarities between the recovery and exit arc voltage, 74 successful ones with the opposing polarities, 31 instantaneous re-ignition events and 6 delayed re-ignition events in the switching data. In general, the absolute value of the exit arc voltage is low in the case of instantaneous re-ignition whereas a high value is observed in the successful interruption cases. But there are two limitations in the usage of the exit arc voltage as an evaluator for instantaneous re-ignition as presented in Figure 76. The average value of the exit arc voltage of all instantaneous re-ignition events is 47 V, however two successful

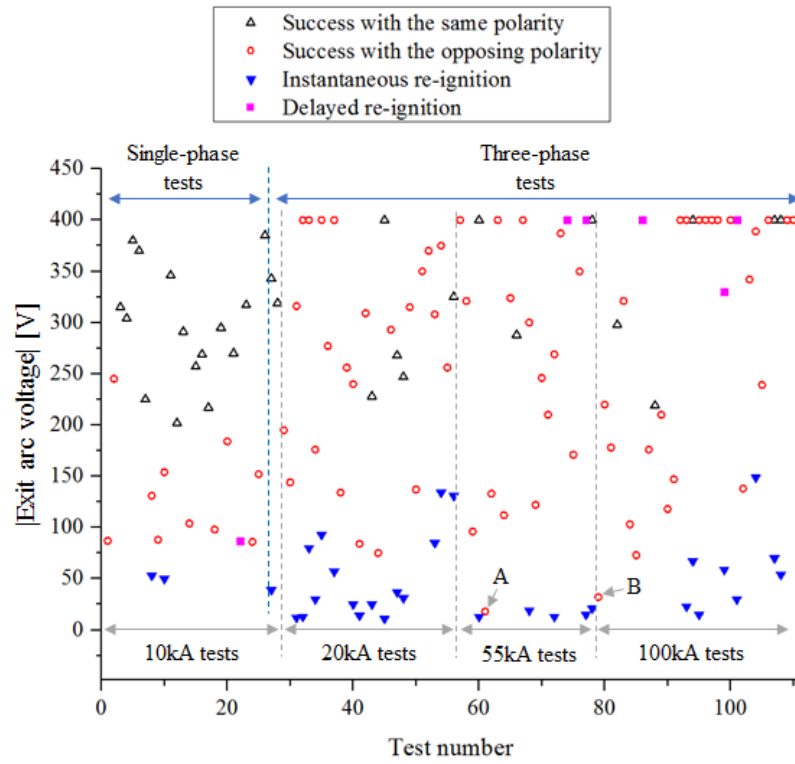


Figure 76 Re-ignition occurrences depending on the exit arc voltage: the exit arc voltage is plotted as 400 V if it is greater than 400 V.

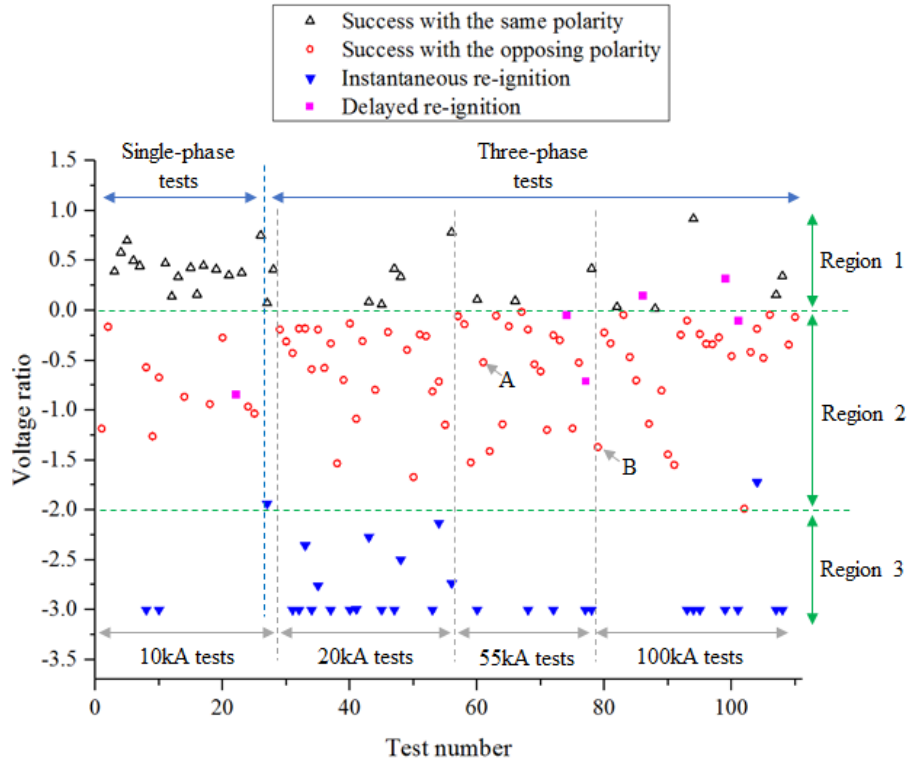


Figure 77 Re-ignition occurrences depending on the voltage ratio; the voltage ratio is plotted as -3.0 if it is lower than -3.0.

cases (A and B in Figure 76) are marked below this average, which is not explained by the evaluator of the exit arc voltage alone. Additionally, there is no clear threshold between successful and failed interruptions. Except A and B points, the minimum exit arc voltage in the case of the successful interruption is 73 V, whereas the maximum value in the instantaneous re-ignition case is 149 V. There are 20 successful cases and 6 instantaneous re-ignitions in this overlapping region between 73 V and 149 V, which are not predicted by the exit arc voltage, accurately.

The delayed re-ignition phenomena cannot be predicted by the exit arc voltage. This may be attributed to a fault in the LVSD operating mechanism detected during the post-test examination of the device. As an example of the post-test examination, if the movable contact is not locked by the operating mechanism after opening, it can rebound and the contact gap will reduce, causing a failure.

#### 4.1.2 VOLTAGE RATIO

Figure 77 uses the same test data as Figure 76, but now shows the dependence of the re-ignition occurrence on the voltage ratio defined in Equations (30) and (31). Values below a voltage ratio of -3.0 are plotted as -3.0. Three groups of the voltage ratio are observed: the first (region 1) is the positive ratio (in the case of the same polarity between the exit and system voltage), the second (region 2) is the range of 0 to -2.0 and the third (region 3) is less than -2.0. Omitting the cases of delayed re-ignition, all switching trials are successful in the range of the positive voltage ratio. There are 74 successful interruptions with the opposing polarity and 2 instantaneous re-ignition cases in the second region of 0 to -2.0 voltage ratio. Only instantaneous re-ignition events are seen in the range below -2.0. Particularly, both A and B successful interruptions are predicted by the voltage ratio, which is -0.52 and -1.37, respectively, but not by the exit arc voltage evaluator. Overall, it can be concluded that the voltage ratio is a more detailed and accurate evaluator to forecast the switching performance than the exit arc voltage.

Like the exit arc voltage, the voltage ratio evaluator cannot predict delayed re-ignition that is associated with the failure of the operating mechanism of the LVSD.

### 4.1.3 DISCUSSION

#### *Region of the Positive Voltage Ratio*

The successful operation with a positive voltage ratio can be explained by the inconsistency of the circuit equation near the current zero point. As the voltage drop across the external resistive load is negligible, the circuit equation near the current zero point in the single-phase test can be expressed as

$$U_{sys}(t) - U_{arc}(t) = L \frac{dI(t)}{dt} . \quad (34)$$

For the three-phase circuit, the voltage between the system voltage and the voltage at the neutral point is required in Equation (34). If instantaneous re-ignition occurs in the range of the positive voltage ratio with the decreasing current where both system voltage and exit arc voltage are initially positive, the value of the left hand side in Equation (34) prior to the current zero moment is negative due to a higher arc voltage compared to the system voltage. But it switches to positive immediately after the current zero moment due to a positive system voltage and the inversion of the arc voltage to negative if the current continues to flow after the zero point. However, the value of the right hand side is still negative because the current continues to decrease after the current zero point. It indicates that such situations are not possible and the only solution is an open circuit, i.e. successful interruption.

#### *Region of the Negative Voltage Ratio*

The situation of the negative voltage ratio can be explained with the aid of the race theory presented by Slepian [34]. Instantaneous re-ignition occurs in the case of the recovery voltage (which is effectively an open circuit voltage across the gap in the device) being higher than the breakdown voltage immediately after the current zero point. As the value of the arc voltage is determined by the power input required to sustain the arc [21], the breakdown voltage should be greater than the arc voltage.

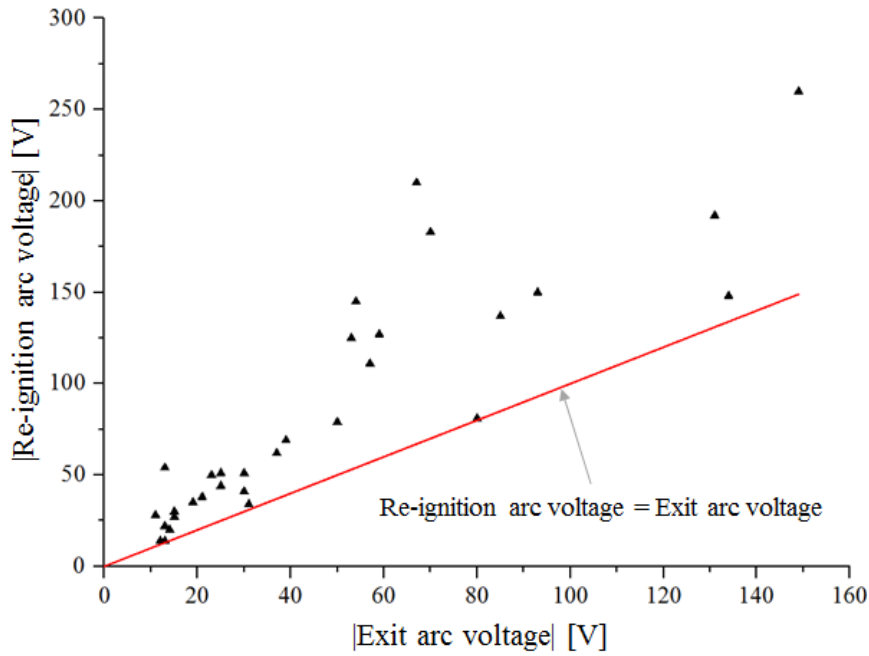


Figure 78 Relationship between the absolute values of the re-ignition arc voltage and exit arc voltage; the absolute value of the re-ignition arc voltage is higher than that of the exit arc voltage in all cases.

It can be observed in Figure 78 that the absolute value of the re-ignition arc voltage (the arc voltage immediately after the current zero point) is greater than that of the exit arc voltage in all instantaneous re-ignition cases. From this test result, it is apparent that the exit arc voltage has a significant influence on the arc characteristics immediately after the current zero point. Further, Figure 78 shows that a different test condition leads to very different re-ignition arc voltage which in turn indicates that the exit arc voltage itself is probably not the best evaluator.

It is in agreement with the theory, that there is no instantaneous re-ignition in the range of 0 to -1.0 voltage ratio, i.e. when the breakdown voltage is higher than the recovery voltage (note that the breakdown voltage is always higher than the exit arc voltage due to cooling effects). In practice, the threshold between successful and unsuccessful interruptions is observed at more relaxed conditions, when the voltage ratio of approximately -2.0 (see Figure 77). There are two possible explanations for the observed threshold. The increase in the breakdown voltage due to plasma cooling and reduction in plasma conductivity is possible; therefore, a higher than the exit arc voltage is needed to support a colder arc. The other explanation can be a switching of cathode and anode roots (especially, space charge layers) over the splitter plate surfaces. This switch takes place just before re-ignition when the sufficient recovery voltage is applied to 1) compensate the voltage drop (which corresponds to the exit arc voltage) in the existing sheaths (space charge layers) allowing electrons and ions to move in the opposite direction; 2) to create an additional voltage drop with opposite polarities accelerating



electrons and ions for the ions generation at the anode and the electron emission from the cathode. If we assume that situation (like the temperature) in the arc roots as well arc column immediately after the current zero is similar with that just prior to the zero point, the magnitude of the additional voltage with opposite polarities has a similar value of the exit arc voltage.

There are rare cases when re-ignition occurs at the ratio above -2.0. We believe that these cases correspond to situations when the arc is attached at the edges of some splitter plates prior to the current zero point and the arc re-ignites directly through an air gap skipping the edges. This re-ignition does not require the sheath switch as the arc is established through the hot gas region in front of the splitter plates without creating an additional voltage drop in the cathode and anode roots. In this case, the breakdown voltage can be less than 200% of the exit arc voltage, however, always greater than 100% of the exit arc voltage. The modelling can select the LVSD design to push the arc further towards splitter plates and this would allow to consider the relaxed re-ignition criterion, which is the voltage ratio  $> -2.0$ .

## 4.2 ARC MOTION

It is known that arc motion has a significant influence on the arc voltage that is one of the main arc characteristics to determine switching performance; however, there has been little empirical work about detailed arc motion in the splitter plate region and its effect on the arc voltage. In addition, no previous study has investigated the effect of the vent aperture distribution on arc motion, which can be the design parameter of a quenching chamber like the vent size.

In this section, the correlation between arc motion and arc voltage is investigated based on the arc voltage waveform and arc image data covering the overall quenching chamber including the splitter plate region. Also, the influence of the vent distribution (the distribution of vent apertures) on arc motion is experimentally investigated in an attempt to improve switching performance.

### 4.2.1 CORRELATION BETWEEN ARC MOTION AND ARC VOLTAGE

Figure 79 presents the arc voltage and the cathode arc root trajectory obtained by Equation (33) under 23 % open vent condition when the 1800 A peak current (see Figure 80) flows through the FTA. The CDS is charged to 200V and the flat Cu fixed contact is used. It is observed that there is synchronisation between the arc voltage drop and arc back-motion (back-jump); i.e. the arc voltage significantly falls when the arc root moves backwards (jumps towards the ignition region). Figure 81 shows the measured arc images with corresponding waveforms in Figure 79. They are displayed with the dynamic threshold mode and contour level of [10 %, 13 %, 16 %, 19 %, 22 %, 25 %, 28 %]. After ignition, the arc elongates as the movable contact parts from the fixed contact and the anode arc root jumps from the movable contact to the arc runner at around 4.0 ms. The arc gradually moves towards the splitter plates and the arc voltage rises; however, the cathode arc root suddenly moves backwards by 8 mm at 4.6 ms (see Figure 81 (d)) and there is another significant back-motion (back-jump) by 20mm at 4.85 ms (see Figure 81 (h)), leading to notable drops of the arc voltage. After then, the arc is forced again to enter the splitter plates by the gas flow and Lorentz force, but it is seen that the arc is not able to stay stably at the splitter plates because of arc back-motion (see Figure 81 (j), (l), (n) and (p)). Even though the arc fully enters the splitter plates, the reverse arc motion occurs afterwards as shown in Figure 81. (m) ~ (p).

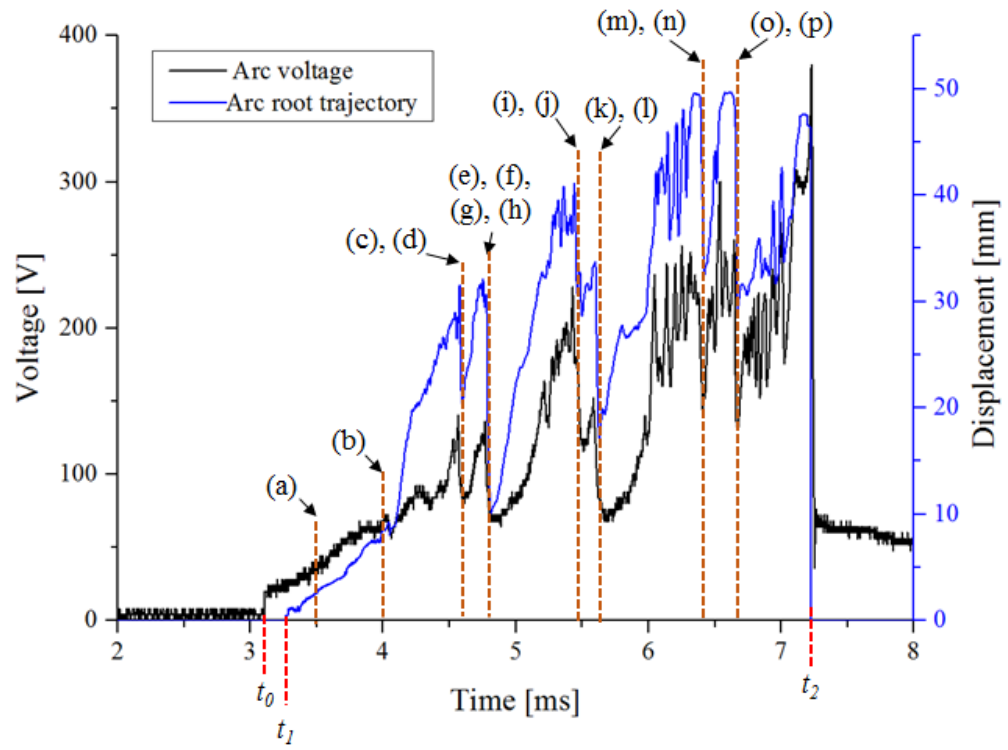


Figure 79 Arc voltage and cathode root trajectory waveforms;  $t_0$  is the arc ignition time (or the contact separation time),  $t_1$  is the starting time of the cathode root motion and  $t_2$  is the time when the arc extinguishes.

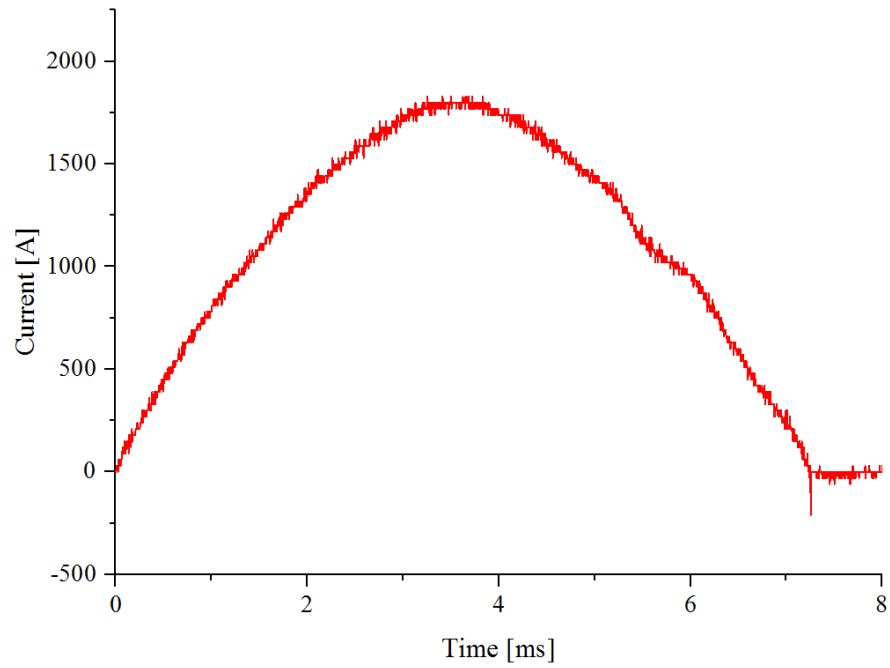
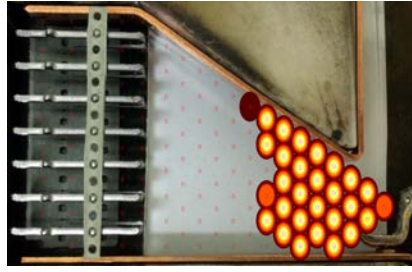


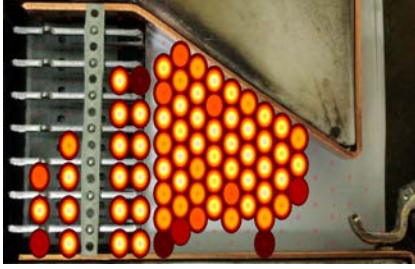
Figure 80 Current during switching process under 200 V charging voltage.



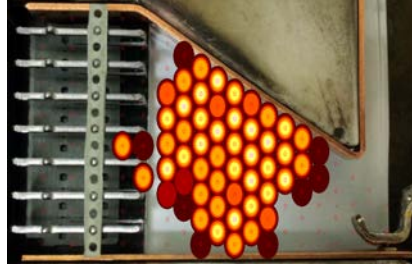
(a) 3.500 ms



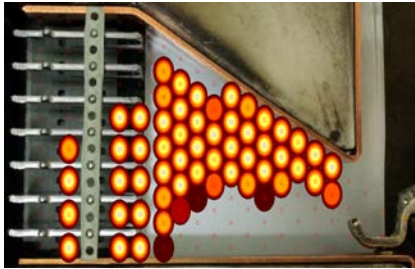
(b) 4.000 ms



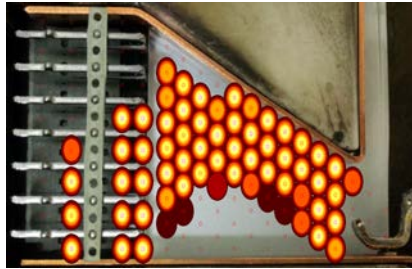
(c) 4.578 ms



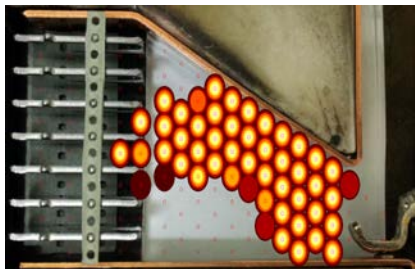
(d) 4.600 ms



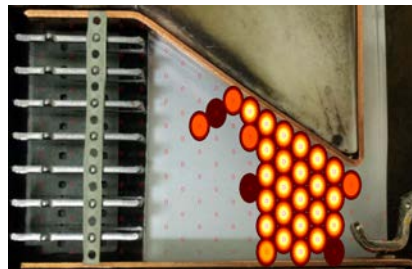
(e) 4.782 ms



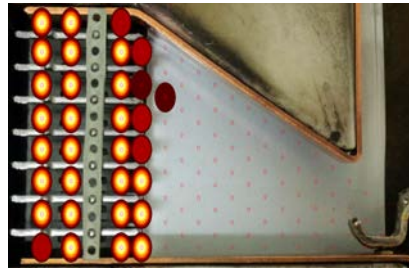
(f) 4.785 ms



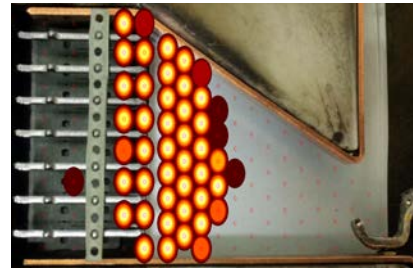
(g) 4.807 ms



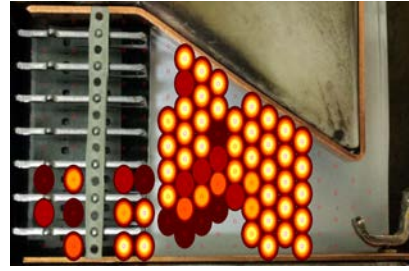
(h) 4.850 ms



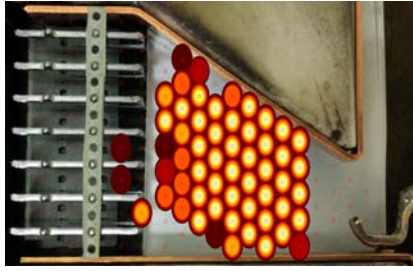
(i) 5.433 ms



(j) 5.500 ms



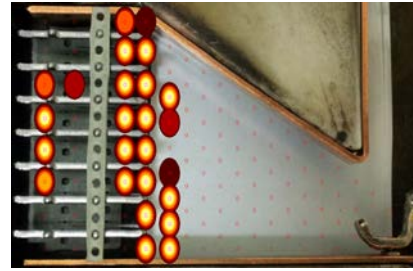
(k) 5.619 ms



(l) 5.632 ms



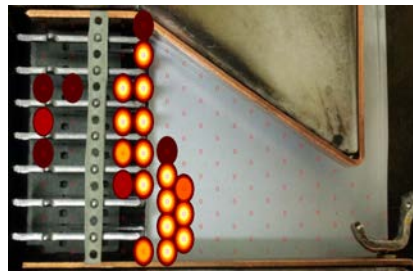
(m) 6.392 ms



(n) 6.418 ms



(o) 6.651 ms



(p) 6.671 ms

Figure 81 Arc images during interruption process: each image corresponds to (a) ~ (p) instants in Figure 79: dynamic threshold mode and contour level of [10 %, 13 %, 16 %, 19 %, 22 %, 25 %, 28 %].

Apart from a significant drop of the arc voltage as shown in Figure 79, there is a voltage fluctuation (instability of arc voltage) at a high frequency when the arc is near the splitter plates after 6.0 ms. In order to investigate the interaction between the arc motion and the voltage fluctuation, the arc voltage and cathode root trajectory waveforms are zoomed into as shown in Figure 82. It can be seen that the arc voltage fluctuation is dependent on the trajectory of arc cathode root: when arc root moves further to plates the arc voltage increases, whereas the voltage drops when the arc retreats away from plates. It is shown that the arc motion in the splitter plate region contributes to this voltage fluctuation.

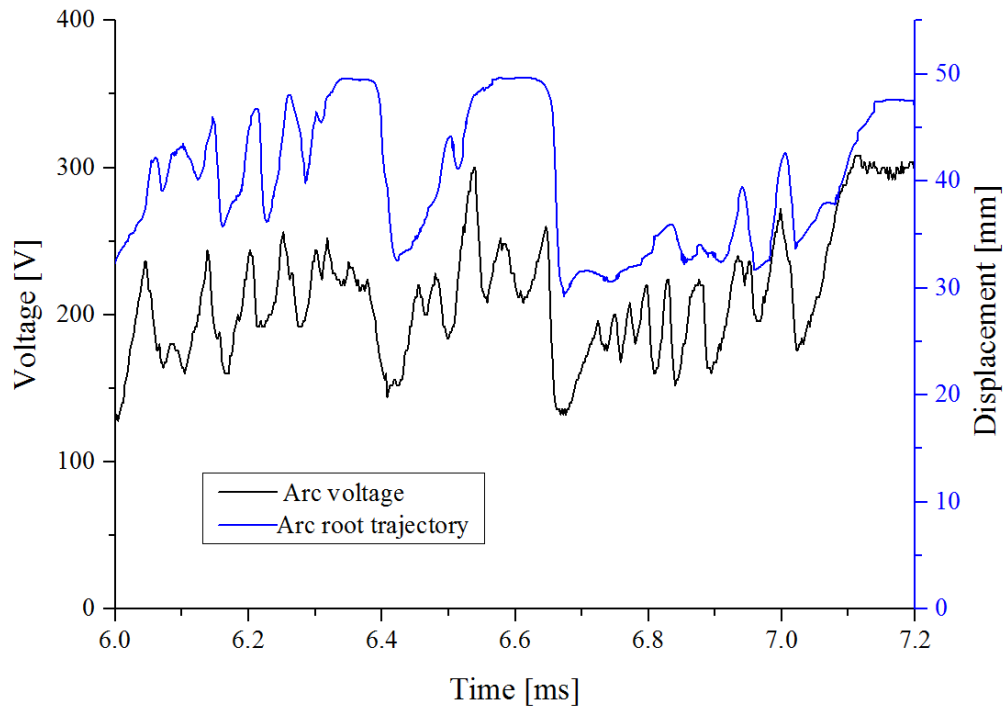


Figure 82 Arc voltage and cathode root trajectory waveforms from 6.0 ms to 7.2 ms.

The individual light intensity can show the evidence of the interaction between the arc motion and the fluctuation of arc voltage. The arc voltage and light intensity of the fibre CD (see Figure 83), at the front of the splitter plates, are presented in Figure 84. A clear correlation between the arc voltage and the light intensity at fibre CD is observed. In general, when the arc comes out from the splitter plates (when the fibre CD has the peak light intensity), the arc voltage drops coincidentally. A close inspection of the arc images shows that the arc suddenly jumps back (the arc comes out from the splitter plates), leading to creation of new current paths in front of splitter plates and enters again splitter plates. Figure 85 shows the arc images at (a) ~ (f) instance in Figure 84 where the arc voltage



and light intensity of fibre CD have the local peak point between 6.00 ms and 6.23 ms. The arc images are displayed with the fixed threshold mode and contour level of [10 %, 13 %, 16 %, 19 %, 22 %, 25 %, 28 %]. The arc almost fully enters the splitter plates at 6.052 ms with an arc voltage of 236 V (see Figure 84 (a)); however, shortly later the arc suddenly jumps backwards with a drop of arc voltage and it is established at the front of the splitter plates (see Figure 84 (b)). This forwards and backwards arc motion including a significant difference of arc voltage is also observed at (c), (d) and (e), (f) of Figure 84. This instability in the splitter plate's region repeats a number of times before the arc stabilises at around 7.15 ms, where the arc voltage remains relatively stable for the remainder of the event.

In Figure 84, there are some regions where the arc voltage is not correlated to the light intensity of the fibre CD. For example, there is no correlation between the arc voltage and intensity of the fibre CD at around 6.6 ms. It is due to limitation of a single fibre's data, which cannot represent the whole behaviour of the arc; but, the correlation at around 6.6ms is observed between the arc voltage and fibre DE intensity.

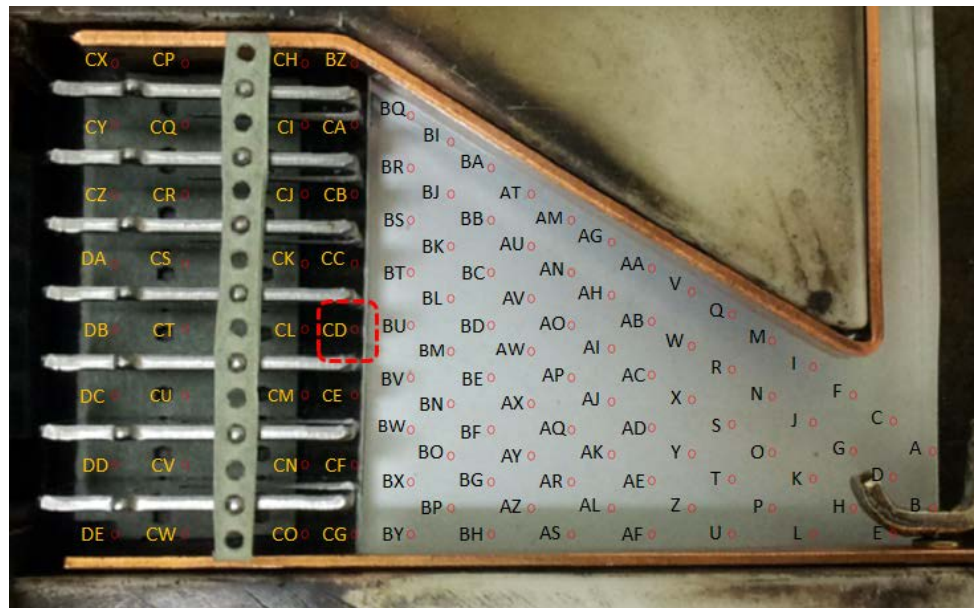


Figure 83 Location of fibre CD.

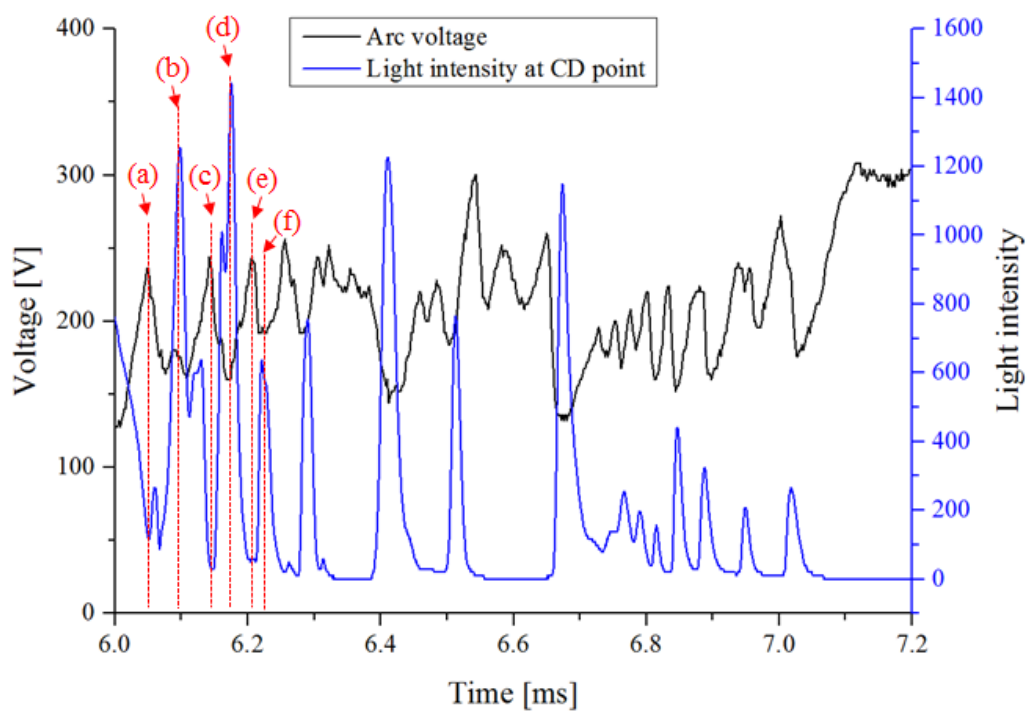


Figure 84 Arc voltage and light intensity on fibre CD.



(a) 6.052ms (236V)



(b) 6.095ms (176.0V)



(c) 6.145ms (244V)



(d) 6.177ms (160V)



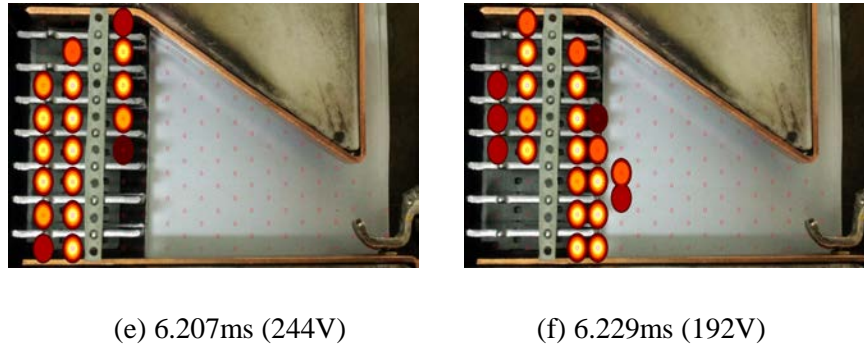


Figure 85 Arc images at (a) ~ (f) instants in Figure 84; fixed threshold mode and contour level of [10 %, 13 %, 16 %, 19 %, 22 %, 25 %, 28 %].

#### 4.2.2 EFFECT OF VENT SIZE AND DISTRIBUTION

Table 7 shows the vent conditions employed in the experiments. Three kinds of vents (closed, partially open and fully open) are used to investigate the effect of the vent size, whereas two kinds of vents (2 apertures and 12 apertures) are used for the study of the effect of the vent distribution. The identical size of vent area (23% open) is adopted in the experiments of the vent distribution; however, there are different distributions as shown in Figure 86.

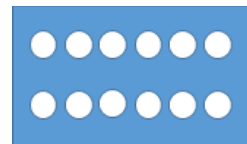
Table 7 Vent conditions.

Purpose of experiments	Vent conditions		
Effect of vent size on arc motion	Closed (0% open)	<sup>1</sup> Partially open (23% open)	Fully open (100% open)
Effect of vent distribution on arc motion	2 apertures (23% open)		12 apertures (23% open)

<sup>1</sup> The partially open vent is the same one with the 2 apertures vent used in the study of the effect of the vent distribution.



(a) 2 apertures vent



(b) 12 apertures vent

Figure 86 Two types of vent distribution.

To evaluate the effect of the vent condition on arc motion and switching performance, several parameters are introduced based on the cathode root motion and arc voltage as shown in Figure 79,

$$X_{aver} = \frac{\int_{t_1}^{t_2} x(t) dt}{t_2 - t_1} , \quad (35)$$

$$U_{aver} = \frac{\int_{t_0}^{t_2} U_{arc}(t) dt}{t_2 - t_0} , \quad (36)$$

$$t_{arcing} = t_2 - t_0 , \quad (37)$$

$$Vel_{aver} = \frac{X_{aver}}{t_{arcing}} , \quad (38)$$

$$I^2t = \int_{t_0}^{t_2} I^2(t) dt , \quad (39)$$

where  $X_{aver}$  is the average displacement of the cathode root,  $U_{aver}$  is the average arc voltage,  $t_{arcing}$  is the arcing time,  $Vel_{aver}$  is the average velocity of the arc,  $I^2t$  is the net-through energy,  $x$  is the cathode arc root trajectory (or the centre of light intensity),  $U_{arc}$  is the arc voltage,  $I$  is the current,  $t_0$  is the arc ignition time (or the contact separation time),  $t_1$  is the starting time of the cathode root motion and  $t_2$  is the time when the arc extinguishes.

### *Vent Size*

Table 8 shows the experimental results of the effect of the vent size on arc motion and switching performance. Each parameter value represents an average value from 3 repeated switching tests. In general, the arc moves further and more quickly towards the splitter plates and switching performance is improved as the vent size increases. A greater average displacement of the cathode root ( $X_{aver}$ ), higher average arc voltage ( $U_{aver}$ ), shorter arcing time ( $t_{arcing}$ ), higher average velocity ( $Vel_{aver}$ ) and less net-through energy ( $I^2t$ ) are measured in a wider vent, which benefit the switching process of a

LVSD. Figure 87 and Figure 88 present the comparison of the cathode root trajectories and arc voltage waveforms associated with the vent size. The waveform in Figure 87 and Figure 88 is not an average value but a single test result. The arc in the fully opened test initially reaches the splitter plates and there is a relatively high and stable arc voltage when compared to the partially open and closed cases. It is seen that there are significant fluctuations in the cathode root trajectory of the partially opened test, causing notable drops of the arc voltage. Also, the lowest velocity of the cathode arc root is observed in the closed case, which leads to the low arc voltage during the whole switching process.

Table 8 Results of effect of vent size.

	Closed (0% open)	Partially open (2 apertures, 23% open)	Fully open (100% open)
$X_{aver}$ [mm]	23.2	25.6	34.5
$U_{aver}$ [V]	95.3	124.6	143.3
$t_{arcing}$ [ms]	5.08	4.01	3.66
$Vel_{aver}$ [mm/s]	4.57	6.38	9.43
$I^2t$ [A <sup>2</sup> s]	7501	6974	5788

※ Each parameter is an average value from 3 repeated switching tests.

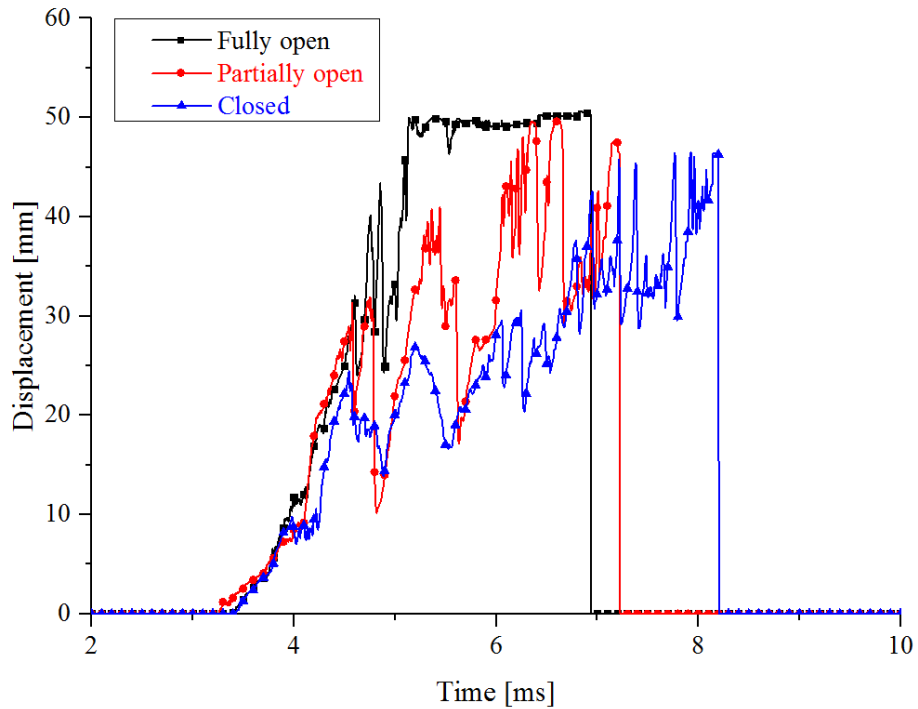


Figure 87 Cathode root trajectory waveforms depending on vent size; a single test result.

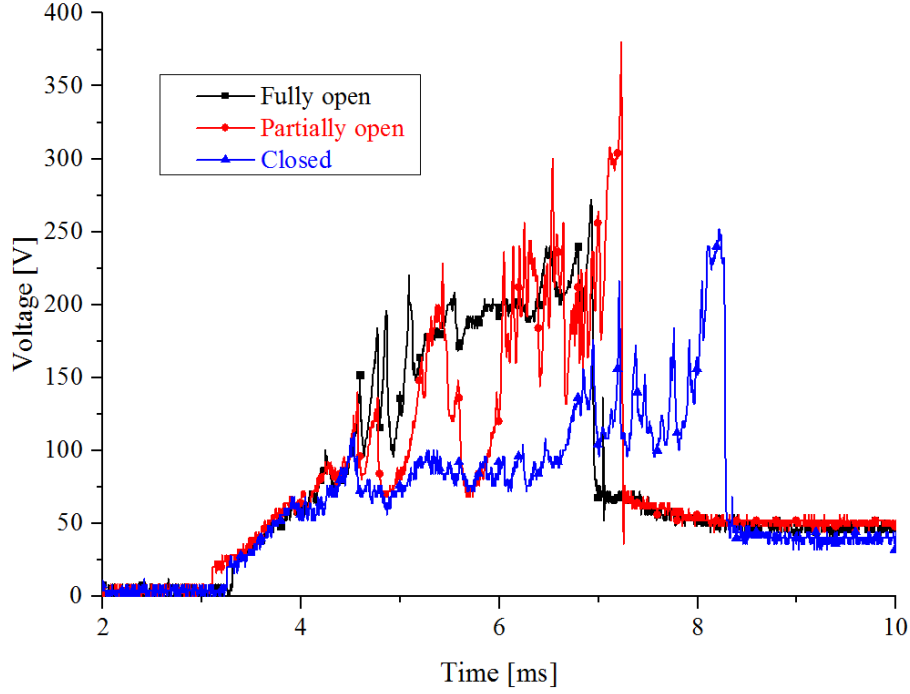


Figure 88 Arc voltage waveforms depending on vent size; a single test result.

#### Vent Distribution

Table 9 shows the effect of vent distribution on the LVSD switching process. It can be said that the well distributed vent achieves better switching performance due to decreased arc back-motion and fast arc motion towards the vent. Much less fluctuation and faster motion are observed in the cathode root trajectory of the 12 apertures vent test when compared to the 2 apertures case as shown in Figure 89. In addition, it is seen from Figure 90 that the arc voltage in the 12 apertures test is higher than that in the 2 apertures case, resulting in the better current limitation.

Table 9 Results of effect of vent distribution.

	2 apertures (23% open)	12 apertures (23% open)
$X_{aver}$ [mm]	25.6	28.9
$V_{aver}$ [V]	124.6	134.9
$t_{arcing}$ [ms]	4.01	3.74
$Vel_{aver}$ [mm/s]	6.38	7.73

$I^2t$ [A <sup>2</sup> s]	6974	6615
---------------------------	------	------

※ Each parameter is an average value from 3 repeated switching tests.

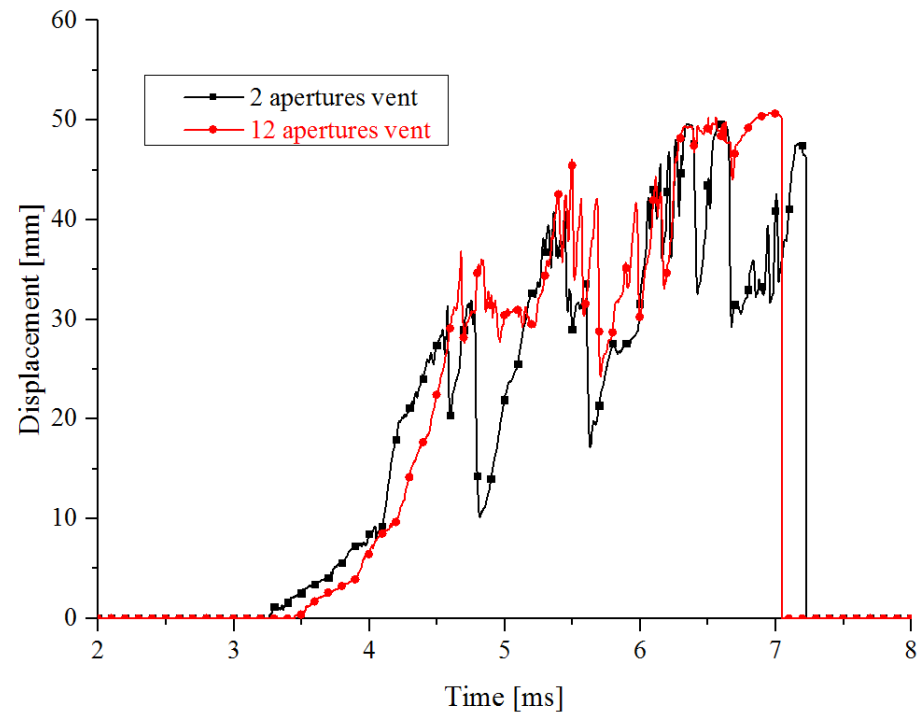


Figure 89 Cathode root trajectory waveforms depending on vent distribution; a single test result.

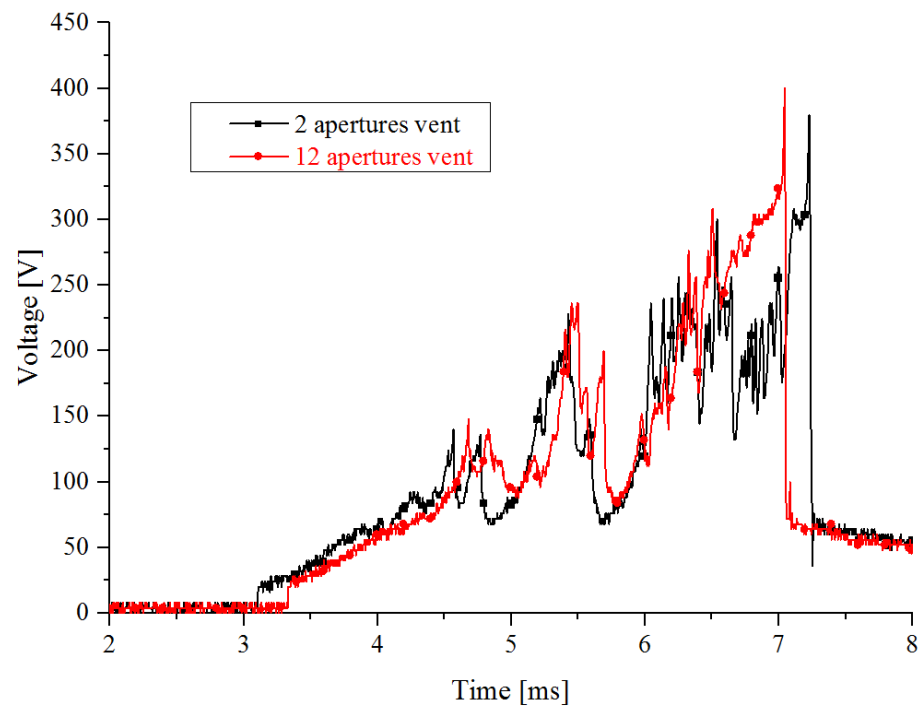


Figure 90 Arc voltage waveforms depending on vent distribution; a single test result.

#### 4.2.3 DISCUSSION

It is observed that arc back- and forth-motion in the splitter plate region leads to the instability of the arc voltage. Forming new arc roots on the surface of the splitter plate requires a certain amount of energy to emit electrons from the cathode and to generate ions at the anode. In a LVSD, the arc enters the splitter plates leading to new arc roots by stretching and bending near the splitter plate. During the arc splitting and root forming process in the plates, a new current path can be created in front of the splitter plates where there is a hot gas (low electrical resistance). This phenomena causes the instability of the arc position in the splitter plate region, which is related to the fluctuation of the arc voltage.

The cathode root trajectories have been obtained from AIS data and they are used to analyse the influence of vent size and distribution on the switching process. It is shown that the arc moves further and more quickly if there is a larger vent opening area in the quenching chamber. This is due to the wider vent providing better conditions for gas flow. Practical LVSDs do not have a fully open vent, but partially open vent. Fully open vents can cause the contamination of the quenching chamber and short-circuit between phases (R-S or S-T) of a LVSD during interruption operation. Additionally, partially open vents can generate a higher arc voltage than fully open vent due to achieving higher chamber pressure.

From AIS data, it is shown that the well distributed vents help increase the arc motion velocity and improve switching performance. It may be caused by the different gas flow due to the vent. Figure 91 shows a comparison of gas flows between the 12 apertures vent and 2 apertures vent.

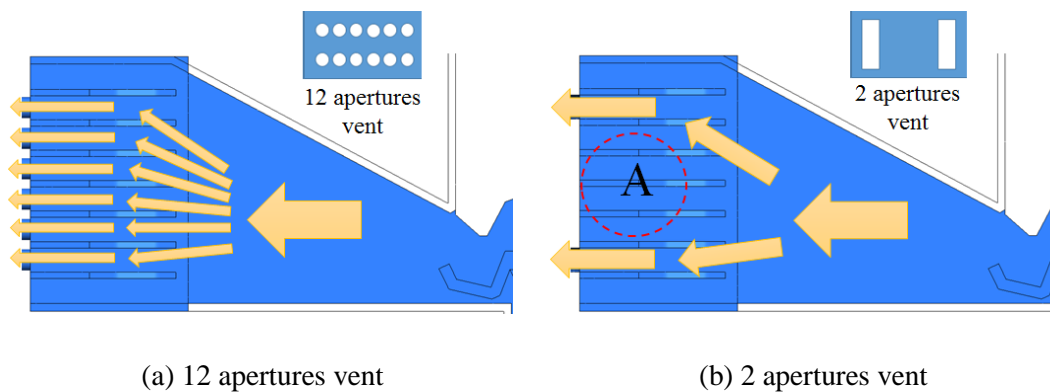


Figure 91 Comparison of gas flows in the case of 2 apertures and 12 apertures vent.

In the 12 apertures case, the gas uniformly flows out through 12 apertures and there is no blocking influence of vent distribution on the gas flow. However, in 2 apertures vent, the gas mainly flows through two path as shown in Figure 91 (b), and there is a relatively high pressure region between two apertures (A in Figure 91 (b)), which leads to blocking effect on gas flow. It prevents the gas from flowing smoothly inside the chamber. There are related simulation results in section 5.2.4.

### 4.3 ARC TEMPERATURE

Since the higher temperature leads to greater radiation (the higher energy of photon emission), it is assumed that the light intensity of the arc measured by the AIS is related to the arc temperature. However, there has been little study related to this. In this section, correlation between the arc intensity and arc temperature is investigated to determine the effect of temperature on the arc intensity.

#### 4.3.1 *CU I LINES OF EMISSION SPECTRA*

Figure 92 shows the current, arc voltage and spectra trigger pulse waveforms while a peak current of 450 A flows through the modified FTA. It is observed that the copper wire ruptures due to ohmic heating at 1.22 ms. During the arc existence period (between 1.22 ms and 9.69 ms), 36 frames of spectrum are measured by the spectrometer as shown in Figure 92; however 22 frames (from the 7th to 28th frame) are used to calculate the arc temperature since only these data have the distinct intensities of Cu I lines. It can be suggested that there is a period of burning of the Cu wire, from 1.22 ms when the arc starts to 2.53 ms (the position of the peak of arc voltage). With more Cu added as the wire is evaporated along its length. After 2.53 ms there is no wire remaining and the Cu gas is mixed with air.

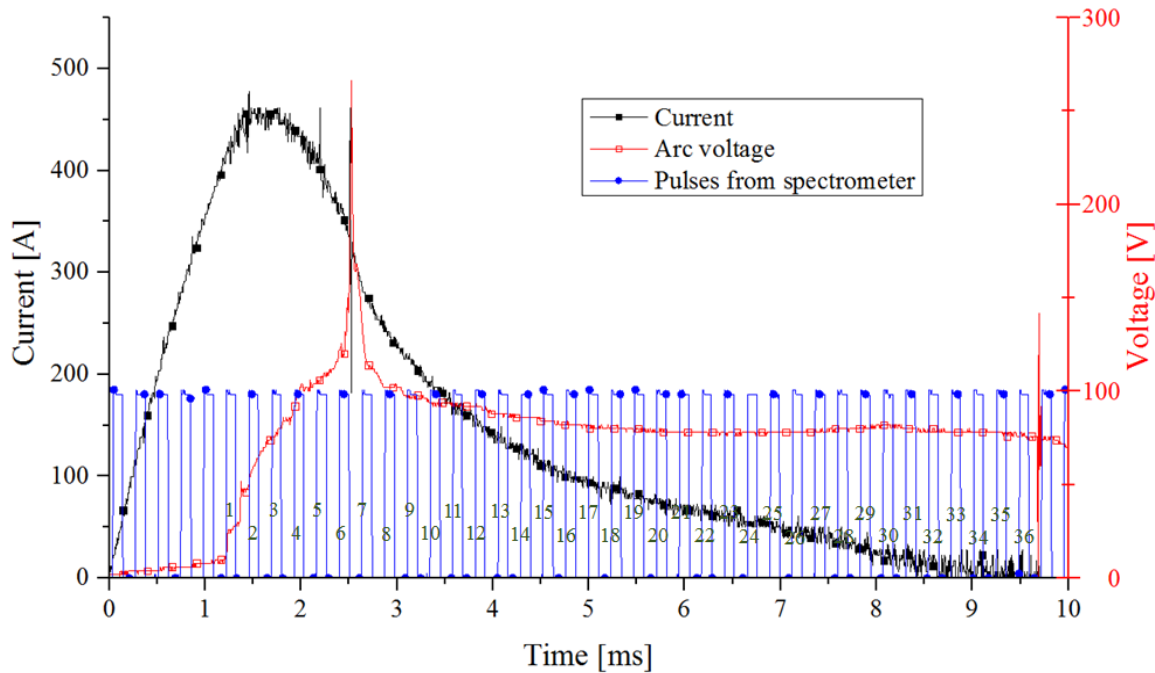


Figure 92 Current, arc voltage and pulse waveforms for arc spectra measurement; the voltage of spectrometer pulse is 3.3 V.



Figure 93 shows the spectra wavelengths between 500 nm and 600 nm, measured from the 7th to 28th frames which is used to calculate the arc temperature. It is seen that there are separate and distinct Cu I spectrum lines at 510.55 nm, 515.32 nm, 521.82 nm, 529.25 nm and 578.21 nm. Distinct spectrum lines are not observed in the 1st to 6th frames. This can be because the wire has not yet evaporated at the position of the spectrometer fibre. Also, from the 29th frame onwards, the peaks of Cu I spectrum lines are weak to evaluate the temperature.

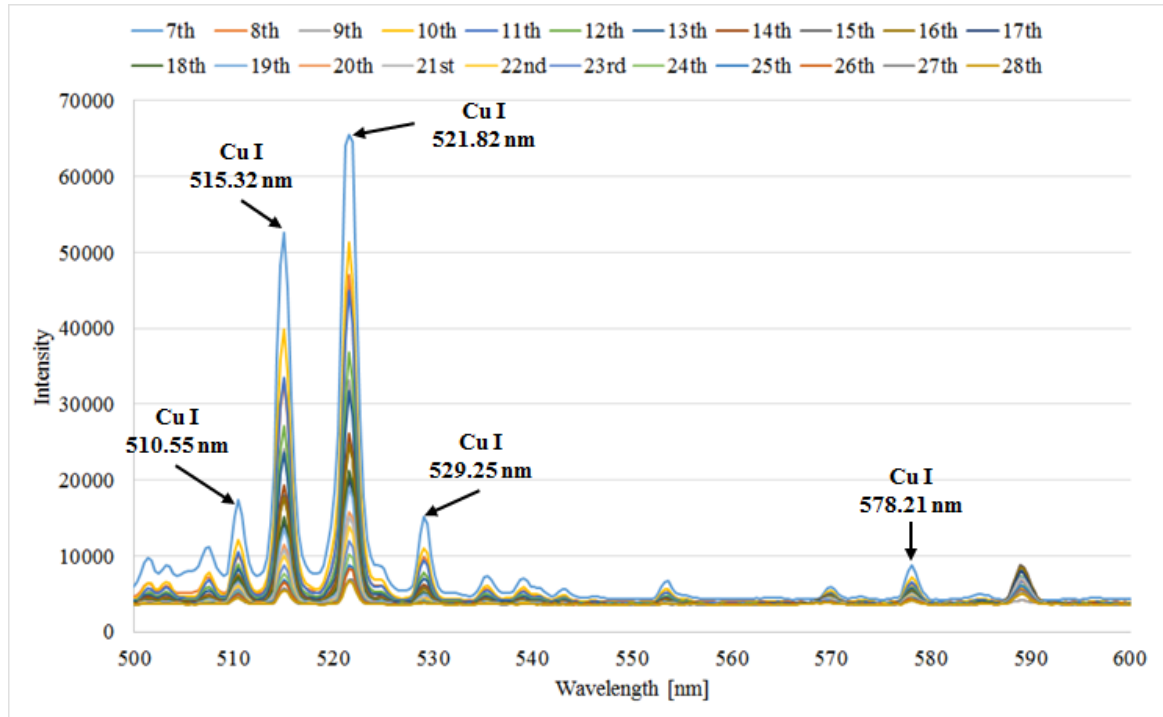


Figure 93 Cu I spectrum lines of arc plasma from 500 nm to 600 nm, measured at the frames of 7th to 28th in Figure 92; the spectrum intensity of the 7th frame reaches the saturated value of the spectrometer at 521.82 nm.

Figure 94 shows the intensity of 510.55 nm spectrum line measured at the frames of 1st to 28th. Just after the Cu wire rupture at 2.53 ms, the highest value of spectrum intensity is measured at the 7th frame and it drops by over 40 % at the 8th frame. Based on these data, we assume that the copper vapour from the fuse wire is attached on the wall just after the rupture and it disappears quickly.

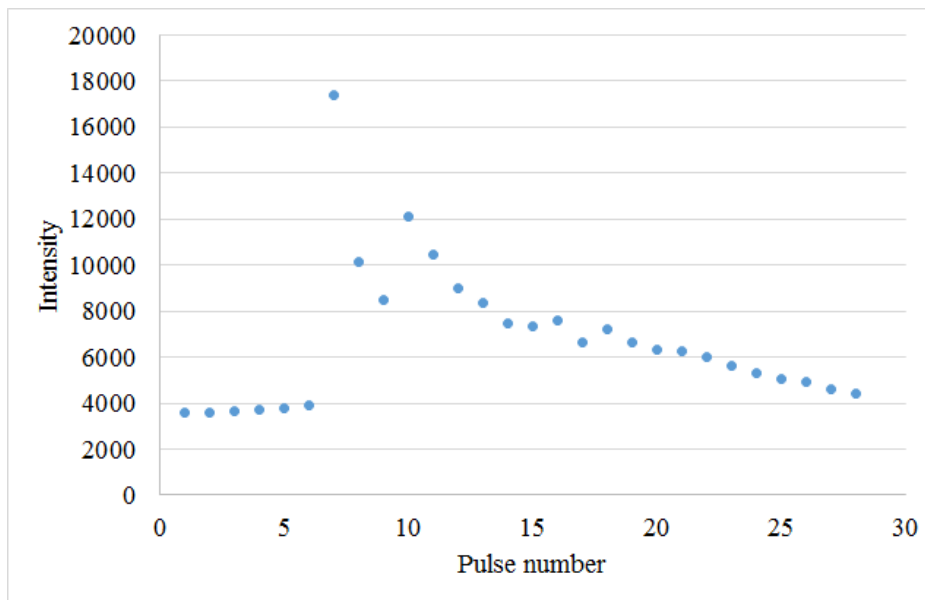


Figure 94 Cu I spectrum line at 510.55 nm measured at the frames of 1st to 28th in Figure 92.

Each spectrum line has own energy level, statistical weight and transition probability as shown in Table 10 [76] and these parameters are used to evaluate the arc temperature by the Boltzmann plot method. In the 7th frame, the spectrum intensity at 521.82 nm reaches saturation; therefore, only four intensities (510.55, 515.32, 529.25 and 578.21 nm) are used for the arc temperature calculation.

Table 10 Parameters of Cu I line spectrum [76].

Spectrum	Wavelength [nm]	Energy of upper state [eV]	$gA^a [10^8 \text{ s}^{-1}]$
Cu I	510.55	3.82	0.080
	515.32	6.19	2.4
	521.82	6.19	4.5
	529.25	7.74	0.87
	578.21	3.79	0.033

<sup>a</sup> g and A refer to the statistical weight and transition probability of the upper level, respectively.

#### 4.3.2 CALCULATION OF ARC TEMPERATURE

The effects of ND8 filter transmission, fibre attenuation and spectrometer efficiency are included to obtain accurate spectrum intensities. Figure 95, Figure 96 and Figure 97 show the data of ND8 filter

transmission, fibre attenuation and spectrometer efficiency in a range of 500 nm to 600 nm wavelength. The relative intensity of the arc is calculated based on the measured intensity data (see Figure 93) and the characteristics of the filter, fibre and spectrometer (see Figure 95, Figure 96 and Figure 97) as below

$$I = i_m \cdot f(filter, fibre, spectrometer), \quad (40)$$

where,  $I$  is the relative intensity,  $i_m$  is the measured spectrum intensity and  $f(filter, fibre, spectrometer)$  is the factor to consider the influence of the ND8 filter, fibre and spectrometer. Table 11 shows the relative intensity of Cu I spectrum lines,  $\ln(\lambda I/gA)$ , the linear trend line and calculated arc temperature at the 8th, 10th, 13th, 16th and 18th frames as shown in Figure 92.

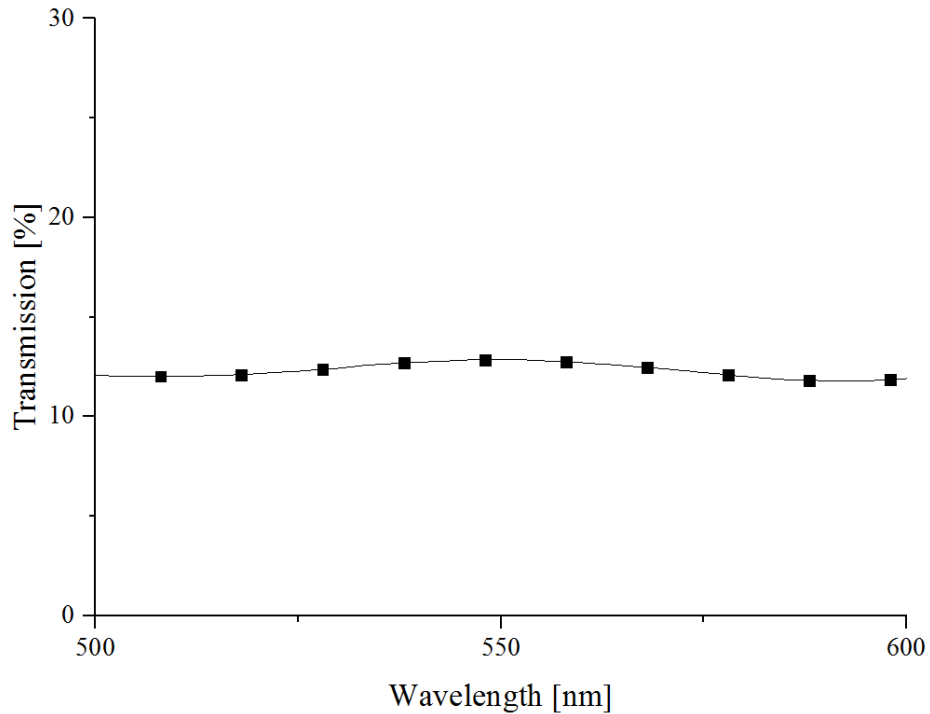


Figure 95 ND8 filter transmission in a range of 500 nm to 600 nm [73].

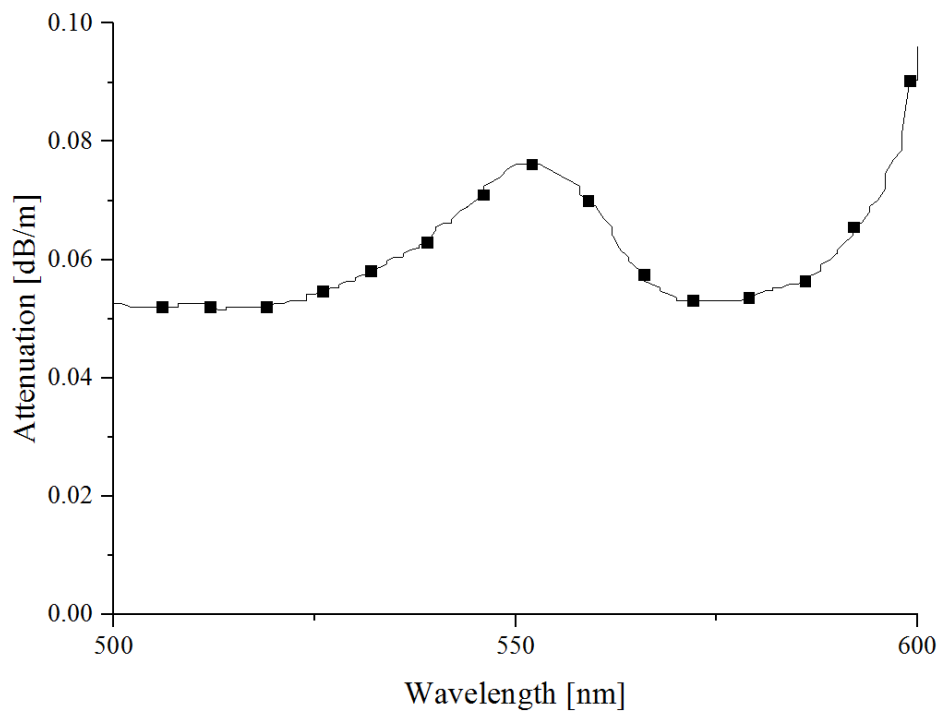


Figure 96 Fibre attenuation in a range of 500 nm to 600 nm [72].

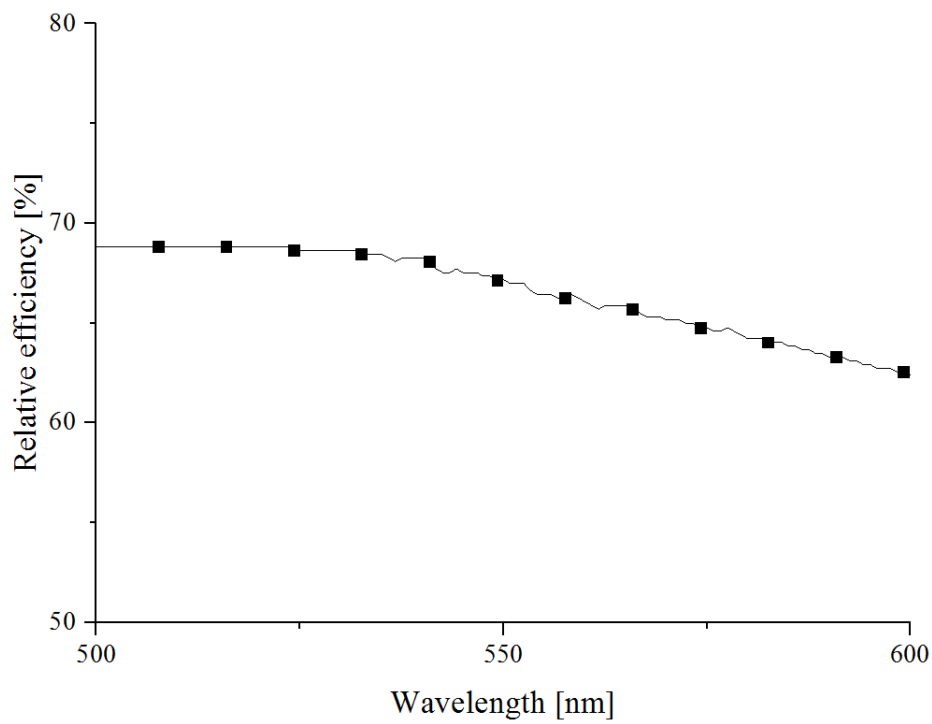


Figure 97 Spectrometer efficiency in a range of 500 nm to 600 nm [77].

Table 11 Relative intensity of Cu I lines and calculated temperature.

Frame <sup>a</sup> (Time <sup>b</sup> )	Wavelength ( $\lambda$ ) [nm]	Relative Intensity <sup>c</sup> (I) [a.u.]	$\ln(\lambda I/gA)$	Slope <sup>d</sup>	Temperature [K]
8th (2.88 ms)	510.55	79531	1.62	-0.69	16850
	515.32	437239	-0.063		
	521.82	636402	-0.30		
	529.25	81022	-0.71		
	578.21	41202	1.98		
10th (3.35 ms)	510.55	108242	1.93	-0.73	15832
	515.32	537798	0.14		
	521.82	694256	-0.22		
	529.25	95947	-0.54		
	578.21	56274	2.29		
13th (4.06 ms)	510.55	64499	1.42	-0.77	15005
	515.32	299084	-0.44		
	521.82	415341	-0.73		
	529.25	46438	-1.27		
	578.21	33067	1.76		
16th (4.77 ms)	510.55	56532	1.28	-0.84	13797
	515.32	213397	-0.78		
	521.82	314188	-1.01		
	529.25	27842	-1.78		
	578.21	29888	1.66		
18th (5.24 ms)	510.55	52982	1.22	-0.91	12792
	515.32	175999	-0.97		
	521.82	262434	-1.19		
	529.25	21985	-2.0		
	578.21	27844	1.58		

<sup>a</sup> The frame number corresponds with Figure 92.

<sup>b</sup> Time represents the starting instance of the integration time.

<sup>c</sup> The effects of filter transmission, fibre attenuation and spectrometer efficiency are considered to obtain the relative spectrum intensity.

<sup>d</sup> Slope refers to the slope of the linear trend line among five points as shown in Figure 98.

If we plot a straight line from E (upper energy level) in the horizontal axis and  $\ln(\lambda I/gA)$  in the vertical axis, the temperature is estimated from the slope of a linear fit trend line based on Equation (6). Figure 98 shows five points of each wavelength and the straight line at the 18th pulse. A slope of -0.91 relates to a temperature of 12792 K from the Boltzmann plot method according to Equation (6).

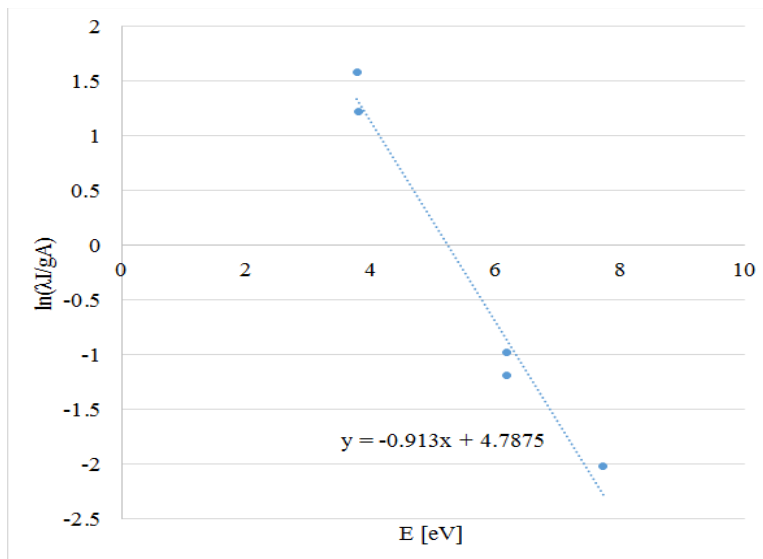


Figure 98 Boltzmann plot of Cu I spectrum lines at 510.55, 515.32, 521.82, 529.25 and 578.21 nm from the 18th frame in Figure 92 and Table 11.

Figure 99 shows the estimated arc temperature from all 22 frames (from the 7th frame to the 28th frame) and arc power obtained from the arc voltage and current. It is seen that the temperature drops as the arc power decreases; ohmic heating from arc power is regarded as the main factor related to the arc temperature.

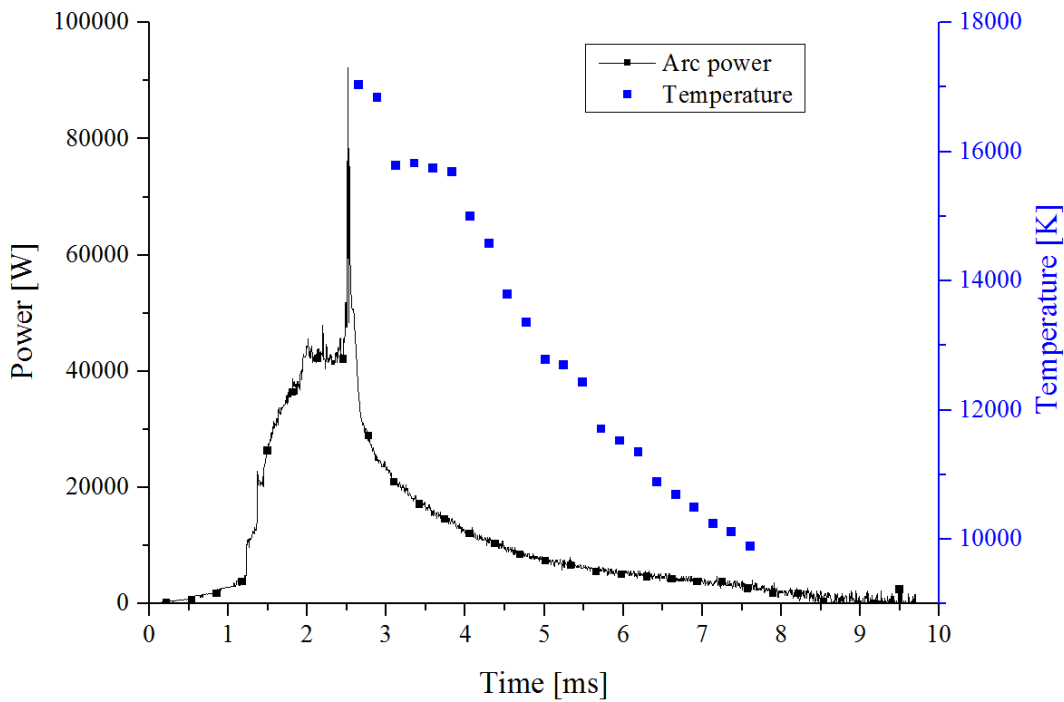


Figure 99 Arc power and estimated arc temperature.

### 4.3.3 DISCUSSION

The light intensity data from fibres BU and BW are used to derive the arc light intensity at the spectrometer fibre position (see Figure 73). Figure 100 shows the light intensities at fibres BU and BW. It is seen that the arc becomes stable from 3.5 ms since the patterns of light intensities at fibres BU and BW significantly fluctuate in the early stage of arcing period (until 3.5 ms). This may be related to the process of arc ignition by the copper wire within a narrow enclosed chamber.

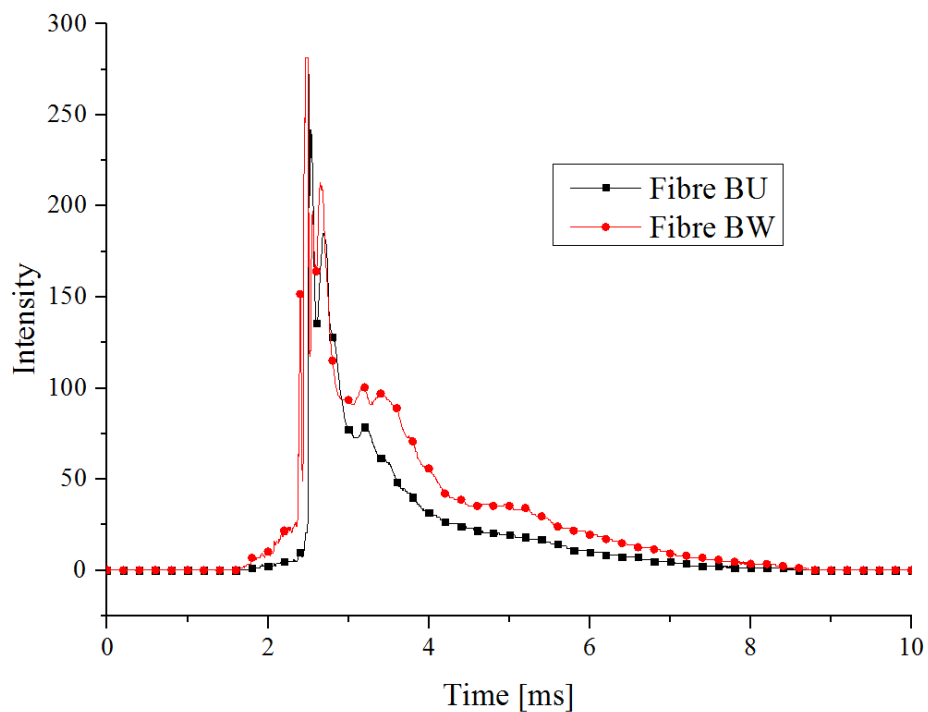


Figure 100 Light intensity at fibre BU and BW.

Figure 101 and Figure 102 show the arc voltage and light intensity data from all 8 AIS fibres between 1.0 ms and 4.0 ms. It is observed that the arc starts to ignite at the position of the fibre BY (the bottom region of the closed chamber) and the Cu wire is evaporated along its length (BY→BX→BW→BU). As the arc length increases, the arc voltage increases. After the gradual increase of the arc voltage, there is a peak of the arc voltage at 2.53 ms, which is almost synchronised with the peak intensity of fibre BQ, BR, BS, BT and BU. This can indicate that the Cu wire is fully ruptured at 2.53 ms.

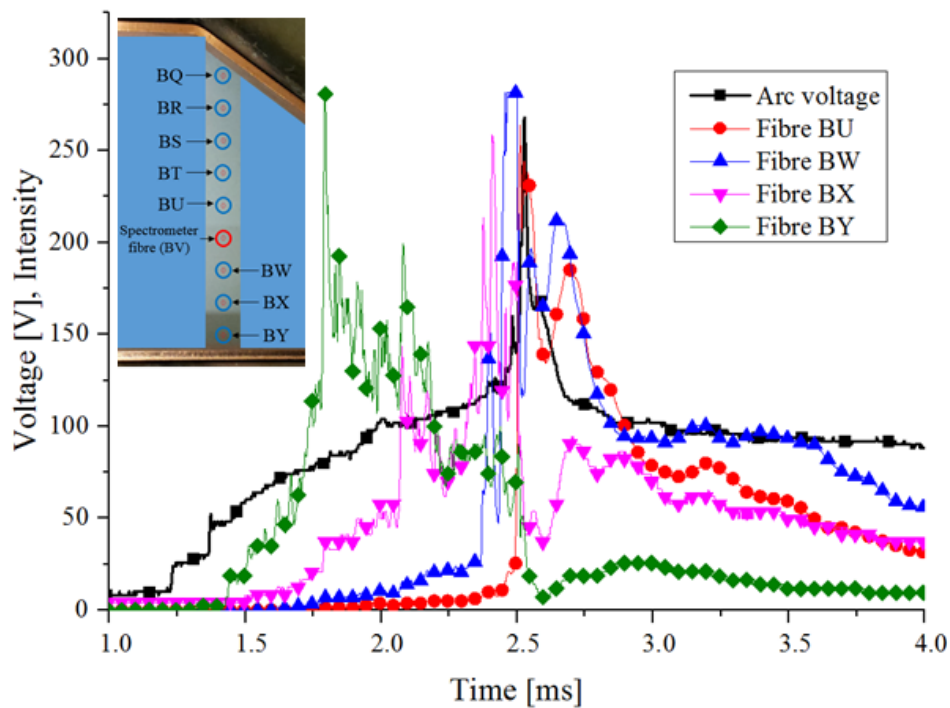


Figure 101 Arc voltage and light intensity at fibre BU, BW, BX and BY between 1.0 ms and 4.0 ms.

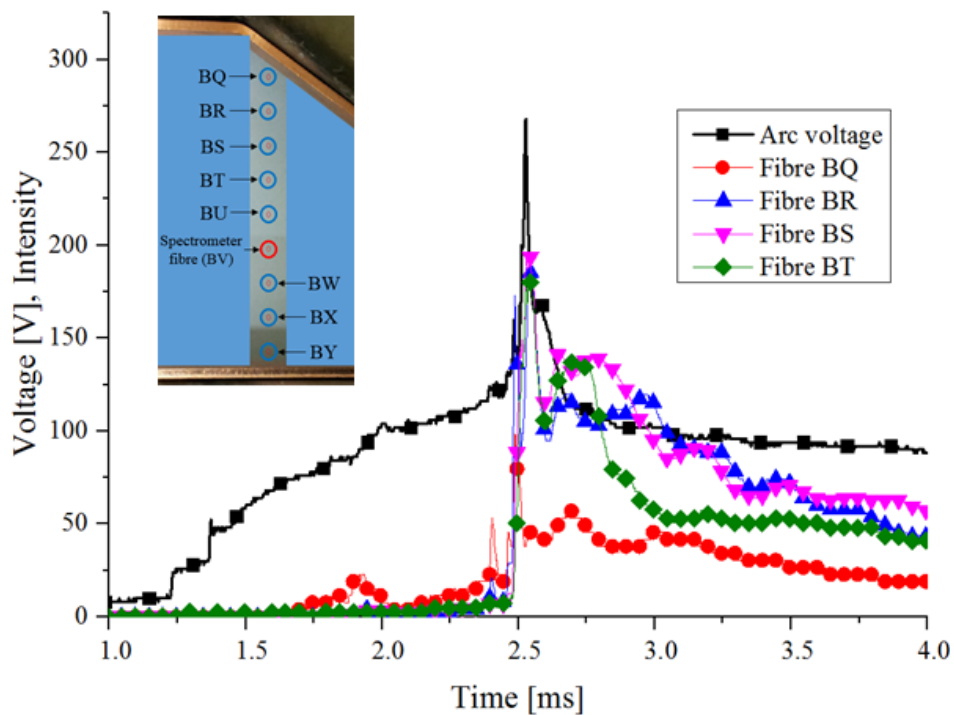


Figure 102 Arc voltage and light intensity at fibre BQ, BR, BS and BT between 1.0 ms and 4.0 ms.



Figure 103 shows the interpolated intensity at fibre BV with the calculated arc temperature. The intensity of fibre BV is an average value from two adjacent fibres (BU and BW). If we ignore the unstable transient period from ignition to 3.5 ms when the intensity of neighbouring fibre has significant fluctuation, it can be seen that the temperature decreases with light intensity.

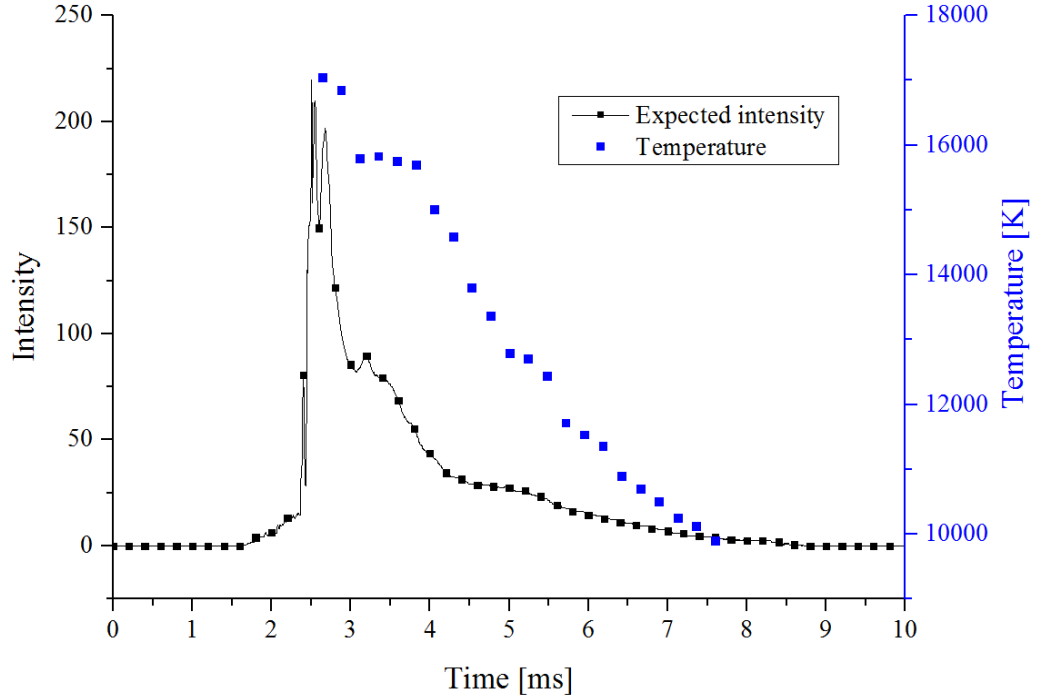


Figure 103 Expected light intensity at fibre BV with arc temperature: the intensity at BV is calculated as the average value of two neighbouring fibres (BU and BW).

Theoretically, the radiation power from the arc across all wavelength relates to the fourth power of temperature ( $T^4$ ) as below

$$P_r \propto \sigma_{SB} T^4 , \quad (41)$$

where,  $P_r$  is the radiation emissive power,  $\sigma_{SB}$  is the Stefan-Boltzmann constant and  $T$  is the temperature [78]. The photodiode provides the current which is proportional to the incident emissive power ( $P_r$ ). The value of the generated current implies the light intensity of the arc. The photodiode

used in the AIS has a 0.55 A/W photosensitivity under the conditions of 25 °C temperature and 780 nm wavelength [79].

Figure 104 shows the correlation between the fourth power of temperature and the light intensity measured by the AIS during the stable arc period (from 3.5 ms onwards). The fourth power of temperature represents the radiation power from the arc. In Figure 104, the intensity  $I$  refers to the maximum interpolated intensity at fibre BV during the 30  $\mu$ s integration time of the spectrometer. The light intensity strongly correlates with  $T^4$ . It can be seen that the relationship between the light intensity and  $T^4$  is a rough linear trend; the value of light intensity increases as the value of  $T^4$  increases. From this data, it is proved that the light intensity measured by the AIS indicates the arc temperature as expressed in Equation (41).

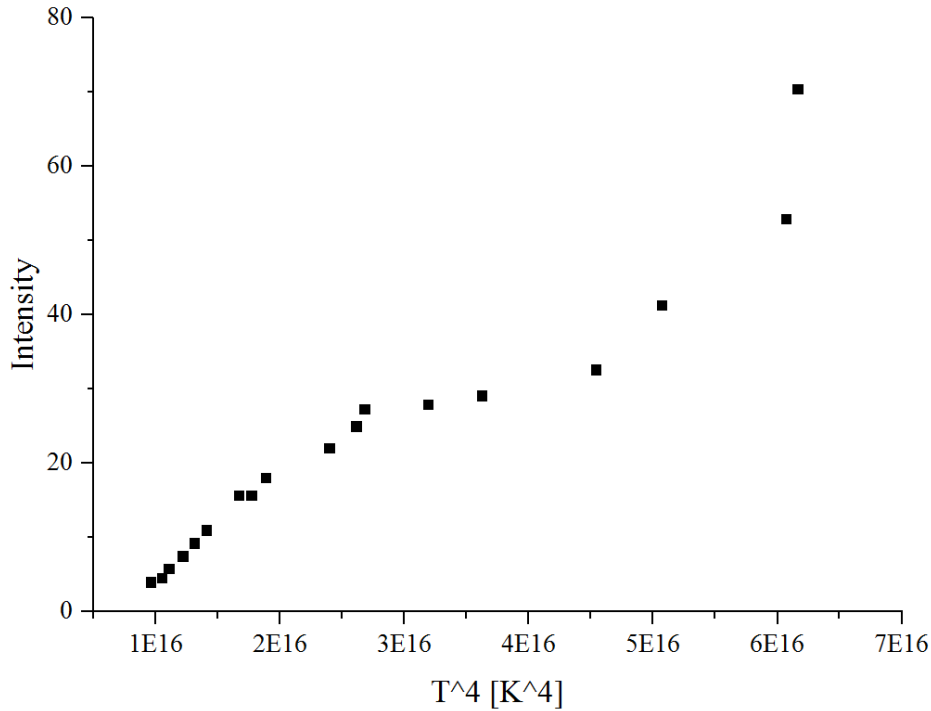


Figure 104 Correlation between arc temperature (the fourth power of temperature) and expected light intensity at fibre BV; the intensity  $I$  represents the maximum value of intensity during the 30  $\mu$ s integration time.

Figure 105 shows the relationship between the arc temperature and the measured current during the stable arc period after 3.5 ms. The current represents the maximum value of the current waveform in Figure 92 during the 30  $\mu$ s integration time. Black squares are the values of arc temperature derived

from spectrum lines at fibre BV and red rounds are the measured temperature for a 10 mm diameter arc in [80]. It can be seen that the temperature increases as the current increases. 11364 K and 13362 K of arc temperature are obtained at 61 A and 100 A current from spectroscopy measurement, respectively. The temperature of the cylindrical air arc of 10 mm diameter was measured at 12600 K at 60 A and 14200 K at 100 A current [80]; therefore, the calculated temperature from relative intensity of Cu I lines shows reasonable agreement with the experimentally obtained data in [80].

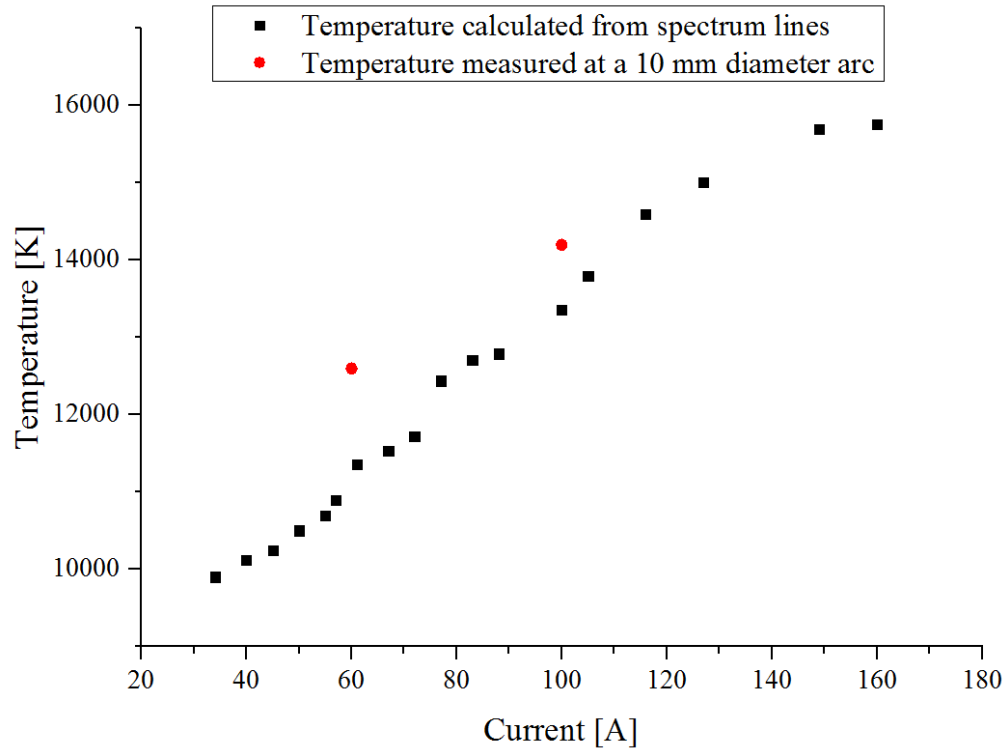


Figure 105 Arc temperature depending on current; the current represents the maximum value of the current waveform during the 30  $\mu$ s integration time, black squares are the values of arc temperature derived from spectrum lines at fibre BV, red rounds are the measured temperature at a 10 mm diameter in [80].

## 4.4 SUMMARY

We investigate the re-ignition phenomena based on the various switching data. It is found that the ratio of the recovery voltage to exit arc voltage is a reliable evaluator for the prediction of re-ignition in the switching tests of LVSDs. It is also observed that there are no occurrences of instantaneous re-ignition where this voltage ratio lies in the range of 1.0 to -1.0 and there is a threshold of the voltage ratio at approximately -2.0, which can distinguish the successful interruption and instantaneous re-ignition.

Arc imaging measurement has been conducted through an array of total 109 optical fibres to allow observation of the overall quenching chamber under the different vent condition. Experimental results show that arc motion instability (repeat of back- and forwards-motion) in the splitter plate region leads to the fluctuation of the arc voltage. The arc moves further as well as more quickly in the case of the wider vent. The well distributed vent contributes to an increase in an arc motion velocity and reduction in a total arc duration.

Arc spectrum is captured by a spectrometer when the arc is ignited by a copper wire in a narrow enclosed chamber. It is found that the arc light intensity measured by the arc imaging system (AIS) is directly related to the arc temperature: the light intensity increases as the arc temperature rises. This result shows that the arc image can represent the temperature distribution in the chamber.

## CHAPTER 5: ARC MODELLING

Most of simulation work has focused on current limitation phenomenon and behaviour of the arc plasma prior to the current zero moment without evaluating re-ignition following the current zero point. There has been little detailed numerical investigation of re-ignition phenomena even though avoiding re-ignition is a key goal when designing the quenching chamber.

Normally, the simulation has been validated by comparing calculated waveforms (current and voltage waveforms) with measured waveforms in previous works. The arc image data can be useful to validate arc modelling by showing the correlation between the measured light intensity and the simulated temperature distribution.

There are two objectives of arc modelling in this thesis; to calculate the exit arc voltage (the main parameter of the re-ignition evaluator) and to validate arc modelling with the measured arc images. The calculation of the exit arc voltage is improved by modifying the V-J relationship (original V-J curve is shown in Figure 49) in the arc root. In order to validate arc modelling, the simulated temperature distribution is compared with the arc images (light intensities).

### 5.1 METHODOLOGY OF ARC MODELLING

#### 5.1.1 GEOMETRY AND BOUNDARY CONDITION OF ARC MODELLING

Figure 106 shows the geometry for arc modelling, corresponding to the internal structure of the FTA. Arc modelling validation is achieved with this geometry. Table 11 shows boundary conditions used for arc modelling. The fluid domain is the volume of internal air in the FTA, which is modelled by MHD theory. The metal solid parts are considered as specific domains considering only the electric and heat transfer phenomena. The current density calculated from the circuit equation (7) is applied to the current-in boundary while there is a 0 V electric potential at the current-out surface. There are two opening boundaries; the front opening near the moving contact and the back opening near the vent. In the arc model, the back opening boundary is modelled closer to the vent than the real test condition after checking the effect of the opening boundary location in order to reduce the simulation time. The opening conditions are set as atmospheric pressure and temperature (1 atm, 300 K). There is the condition of no slip wall on the interfaces between the fluid and solid part. The simulation includes the temperature and pressure dependent properties of air (density, electrical conductivity, thermal conductivity, the specific heat capacity and viscosity) [61], [62].

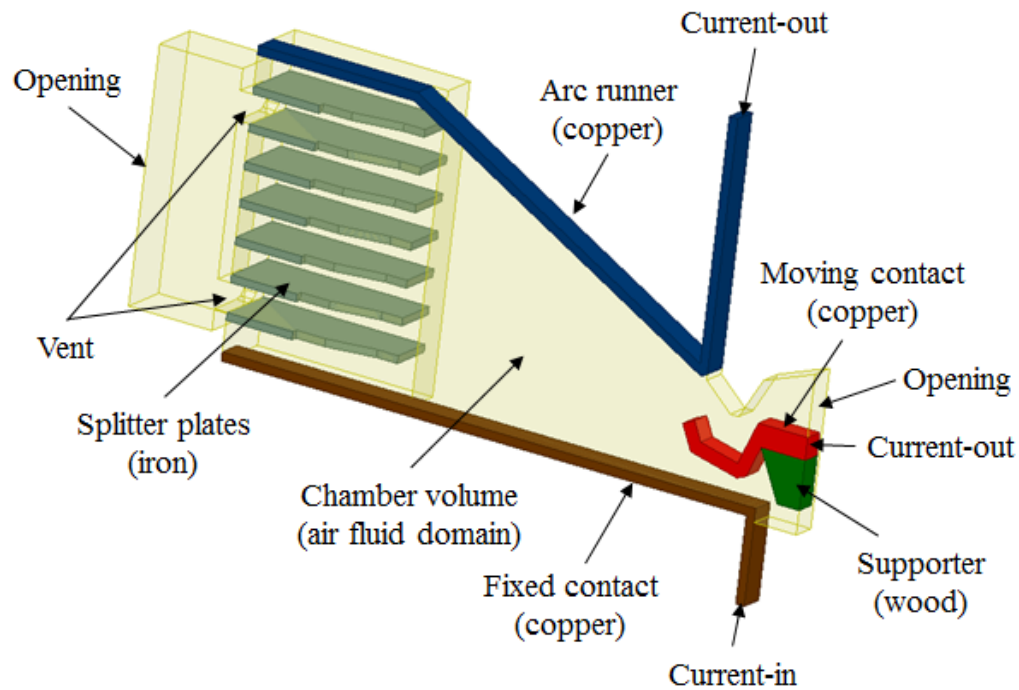


Figure 106 Geometry of LVSD used for arc modelling.

Table 12 Boundary condition for arc modelling.

Interface		Heat transfer	Mass/ momentum	Electric	Pressure
Fluid	Movable contact	CIF <sup>a</sup>	No slip wall	CIF	-
	Fixed contact				
	Splitter plates				
	Supporter	Adiabatic			
Fluid outermost surfaces		300 K [81]	-	Zero flux <sup>b</sup>	
Current-in		500 K [82]	-	- I= specific value - Zero flux	
Current-out		500 K [82]	-	- V= 0 V - Zero flux	
Opening		300 K	- Flow direction : normal to boundary	Zero flux	1 atm

<sup>a</sup> CIF (Conservative Interface Flux) implies that the quantity in question will “flow” between the current boundary and the boundary on the other side of the interface [83].

<sup>b</sup> Normal components of variables equal to zero.

### 5.1.2 LORENTZ FORCE

Lorentz force is one of the main factors to influence arc motion during the switching process. It is generated from the current flowing path and ferromagnetic material like the splitter plate in the LVSD's chamber. Volumetric Lorentz force on a hypothetical arc element is calculated by the finite element method (FEM) prior to the arc motion simulation by MHD theory. The external magnetic flux density is imported to the MHD arc simulation. The proposed method of arc modelling (using the look-up table for magnetic flux density) reduces the complexity and calculation time for the arc modelling.

Figure 107 shows the geometry for the Lorentz force calculation, which corresponds with the internal configuration of the FTA. Total Lorentz force on the arc column is calculated by FEM software (Maxwell 3D, a part of ANSYS Electronics Desktop 2016 [84]) depending on the current (0 A - 2000 A) and arc position (from the ignition point to the end point of the splitter plates). The nonlinear property (B/H curve) of iron splitter plates is considered in the Lorentz force calculations. There are two assumptions: the arc radius is independent of the current (assumed to be the same as the radius of a hot channel for arc ignition) and the arc column is perpendicular to the fixed contact.

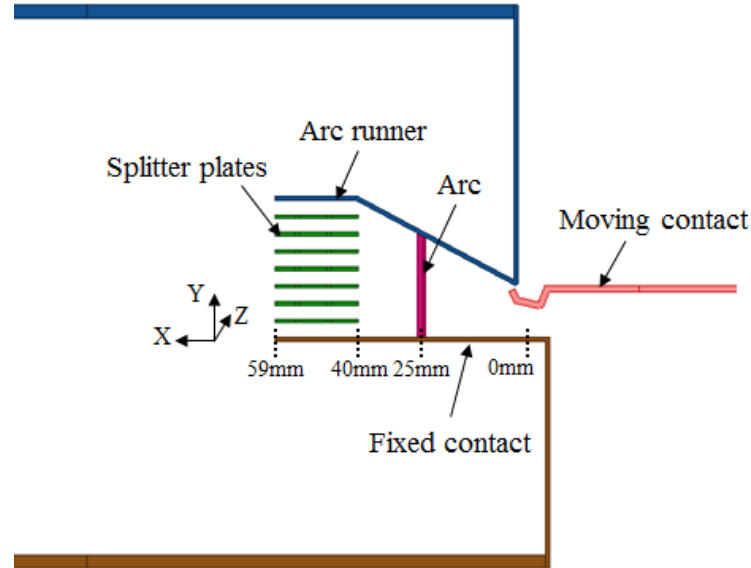


Figure 107 LVSD chamber geometry for Lorentz force calculation.

There are two factors to generate Lorentz force on the arc in the LVSD; one is the current path and the other is the splitter plate's effect. The effect of the splitter plate's on the Lorentz force is negligible

when the arc is near the ignition area; however, it becomes significant as the arc approaches the splitter plates. Table 13 shows the comparison of Lorentz force of models with and without splitter plates when a current of 1000 A flows. It is seen that Lorentz forces in both cases are very similar when the arc position is 20 mm or less. But, there is a significant difference in Lorentz force for the case of the 40 mm arc position; the Lorentz force with splitter plates is greater by over 5 times than that without plates. Figure 108 presents the magnetic flux density in the XY plane of the half symmetric FTA, computed by the FEM when the arc is at 0 mm, 20 mm and 40 mm position. The flux density on the right side of the arc column in the 40 mm arc position model is much greater than that of the left side when compared to the results of 0 mm and 20 mm cases. This is due to the influence of the high permeability of the ferromagnetic material (splitter plates).

Table 13 Comparison of Lorentz force between models with and without splitter plates under 1000 A input current.

Arc position [mm]	Lorentz force [N]	
	With splitter plates	Without splitter plates
0	0.22	0.22
20	0.42	0.41
40	2.90	0.51

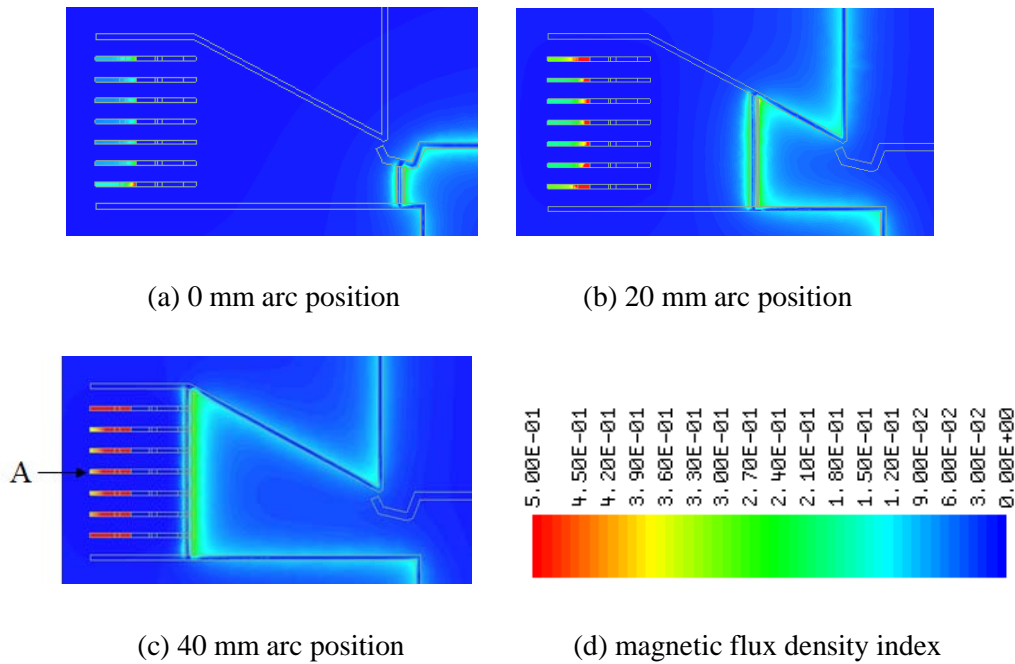


Figure 108 Magnetic flux density distribution in the XY plane of the half symmetric FTA.



The influence of the splitter plates is clearer in Figure 109 presenting the magnetic flux density in the XZ plane at the 'A' point in Figure 108 (c) (the middle position of the fourth plate from the bottom) when the arc is located at the 40 mm point. The left side of the arc (the region between the arc and the splitter plate) has much lower flux density than the right side since most of the magnetic flux penetrates into the more permeable splitter plate. This distortion of magnetic flux leads to large Lorentz force near splitter plate region.

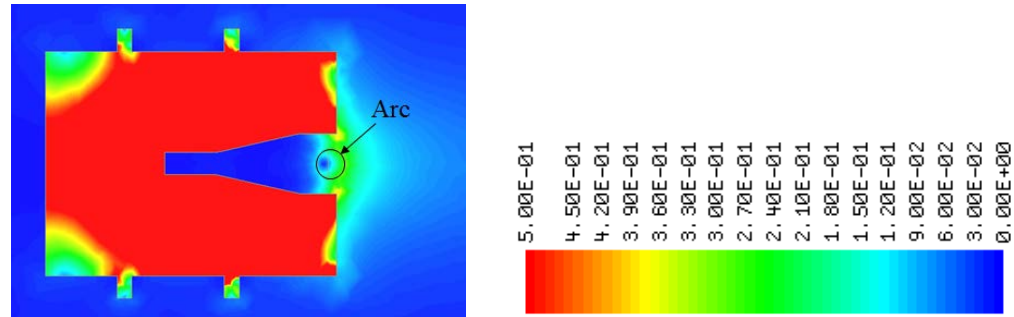
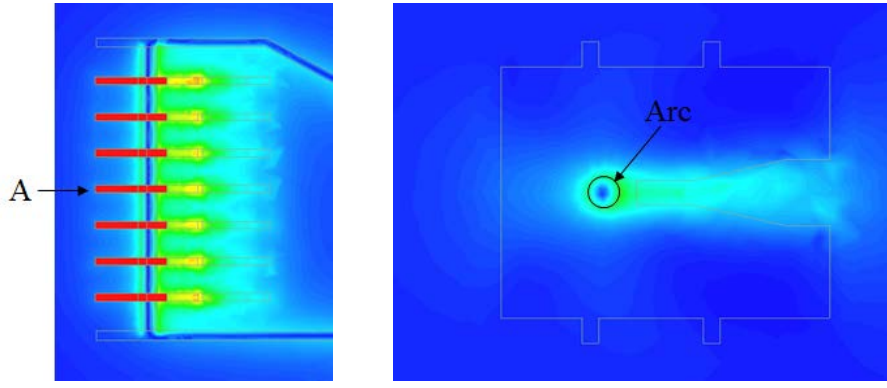
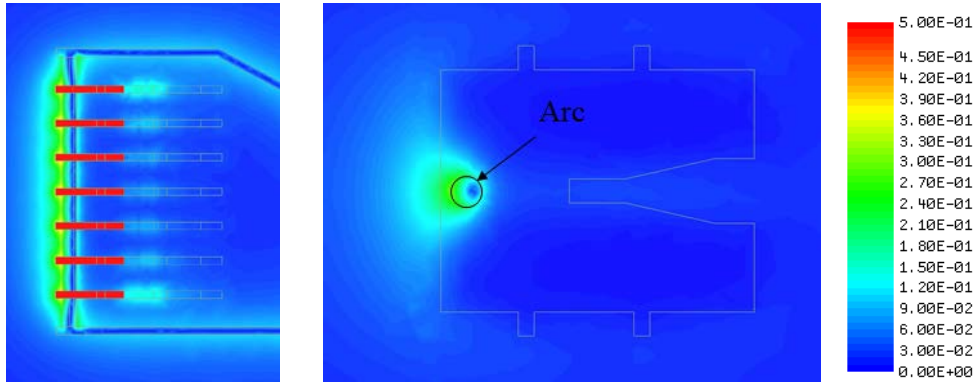


Figure 109 Magnetic flux density distribution in the XZ plane at the middle position of a plate (the fourth plate from bottom) when the arc position is 40 mm.

When the arc is divided into 8 segments by splitter plates, the Lorentz force of 8 small arcs is calculated. Lorentz force analysis shows that the arc tends to remain inside the splitter plates. After entering the splitter plates, the arc firstly experiences the Lorentz force acting towards the left side (the positive X direction as shown in Figure 107). As the arc further moves towards the left side, the Lorentz force decreases and there is net zero force on the arc at the 56 mm position. Figure 110 shows magnetic flux density distributions in the XY plane of the half symmetric FTA and in the XZ plane at the 'A' point Figure 110 (a) (the middle position of the arc segment between third and fourth plates from the bottom) when the arc is located at 53 mm and 57.5 mm from the ignition point. In the model of the 53 mm arc position, overall magnetic flux density on the right side of the arc is larger than that on the left side and then Lorentz force acts toward left side of the arc (X direction). However, this situation is reversed for the case of the 57.5 mm arc position. The balance point is observed at 56 mm.



(a) 53 mm arc position



(b) 57.5 mm arc position

Figure 110 Magnetic flux density distributions when the arc is located at 53 mm and 57.5mm: the left figure is the distribution in the XY plane of the half symmetric FTA and the right one is the distribution in the XZ plane at the 'A' point Figure 110 (a) (the middle position of the arc segment between the third and fourth plates from the bottom).

Figure 111 shows the Lorentz force on the arc towards the X direction associated with the current at several different arc locations; the arc is perpendicular to the fixed contact (X axis) and is located at the positions of 0 mm, 20 mm, 40 mm, 57.5 mm and 62.5 mm in the X axis. It is seen that the Lorentz force is significant different depending on the arc location and current. To consider the influence of the Lorentz force on the arc motion, the average apparent external magnetic flux density inside the chamber,  $B_{ex}$  is computed by Equation (42)

$$B_{ex} = F_{Lo} / (IL), \quad (42)$$

where  $F_{Lo}$  is the pre-calculated total Lorentz force on the arc column,  $I$  is the current and  $L$  is the arc length at the specific position.  $B_{ex}$  is the function of the current and the position in the X axis.

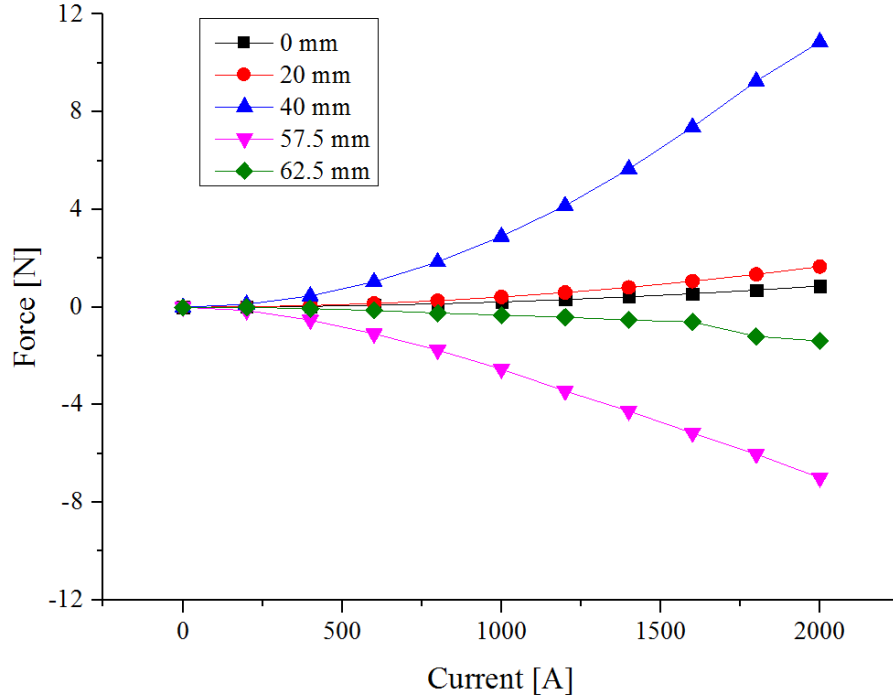


Figure 111 Lorentz force associated with current at different arc locations; the arc is perpendicular to the fixed contact (X axis) and is located at the positions of 0 mm, 20 mm, 40 mm, 57.5 mm and 62.5 mm in the X axis.

Figure 112 shows  $B_{ex}$  obtained from Equation (42), based on the results in Figure 111. It varies with the current as well as the position of the X axis. Figure 113 shows the example of the  $B_{ex}$  distribution in the overall chamber. It is calculated in the case of a 1000 A current. The position of the X axis represents the distance from an ignition point as shown in Figure 107. Before 35 mm,  $B_{ex}$  is stable at around 20 mT without the effect of splitter plates. When the arc is close to the splitter plates,  $B_{ex}$  increases up to 136 mT. After the arc enters the plates,  $B_{ex}$  decreases and it becomes a negative value (Lorentz force acts on the arc towards the negative direction of the X axis). If the arc comes out from the plates,  $B_{ex}$  increases again and it is still negative due to the splitter plates (Lorentz force acts on the arc towards the splitter plates which is the negative direction of the X axis).

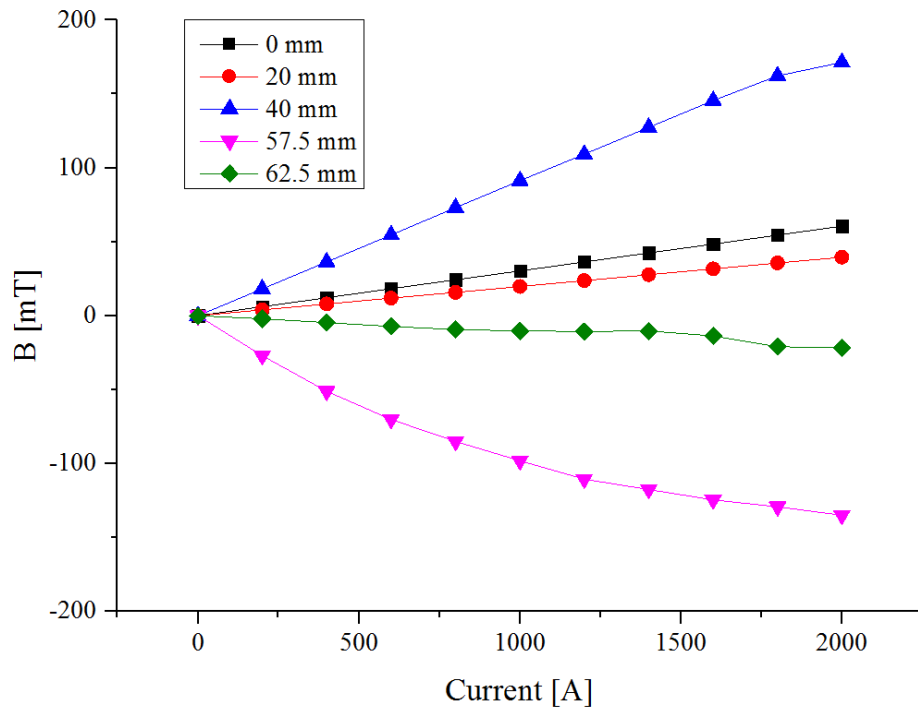


Figure 112 External magnetic flux density associated with the current in the cases of the 0 mm, 20 mm, 40 mm, 57.5 mm, 62.5 mm arc locations.

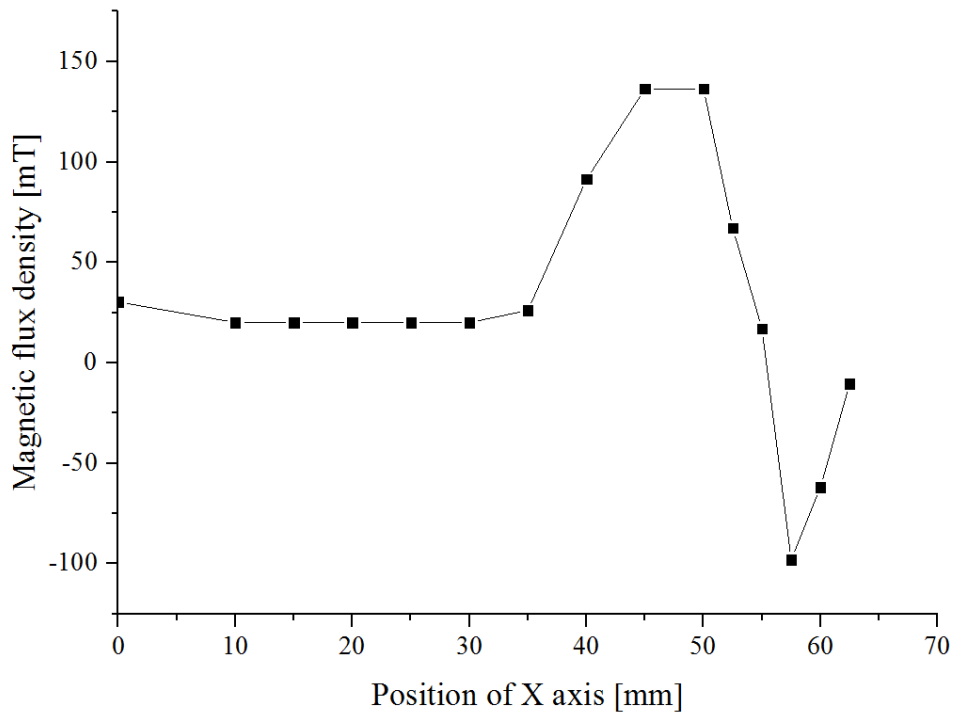


Figure 113 External magnetic flux density associated with the location in the chamber in the case of a 1000 A current; the position of the X axis represents the distance from an ignition point as shown in Figure 107.

In the MHD arc simulation,  $B_{ex}$ , which is a function of the current and position of the X axis, is used as an input parameter to generate the Lorentz force on the arc in the fluid domain. Local Lorentz force per unit volume is expressed as

$$f_{Lo} = J \times B_{ex} , \quad (43)$$

where  $f_{Lo}$  is the Lorentz force per unit volume and  $J$  is the current density. Local Lorentz force is calculated in the overall fluid domain and it affects the air fluid motion, which is regarded as the effect of Lorentz force.

### 5.1.3 CURRENT LIMITATION

Current limitation is one of the main factors in determining the switching performance of LVSDs. Normally, a high arc voltage is generated by multiple arc roots on the surfaces of the splitter plates during switching operation. This increase in the arc voltage achieves significant reduction of the arc current, leading to less damage to a LVSD when compared to the prospective current, if this phenomenon were not to occur.

Current limitation is implemented by using the forward Euler method. The forward Euler method is a step-by-step numerical procedure to solve an ordinary differential equation such as Equation (1) [85]. The current in the next iteration is calculated from the present current in the forward Euler method. Equation (1) can be changed into Equation (44)

$$\frac{dI(t)}{dt} = \frac{1}{L} [U_s(t) - I(t)R - U_{arc}(t)] , \quad (44)$$

where,  $U_s$  is the system voltage,  $I$  is the current,  $R$  is the resistance,  $L$  is the inductance and  $U_{arc}$  is the arc voltage (see Figure 20). If we apply a finite value of the time step ( $\Delta t$ ), the current variation Equation (44) can approximately be expressed as Equation (45)

$$\frac{dI(t)}{dt} \approx \frac{I(t_{n+1}) - I(t_n)}{\Delta t} = \frac{1}{L} [U_s(t_n) - I(t_n)R - U_{arc}(t_n)] , \quad (45)$$

where, the index  $n$  refers to the present simulation iteration,  $n+1$  indicates the next iteration, and  $\Delta t$  is the time step (period) between  $n$  and  $n+1$  step. The current in next iteration is obtained from Equation (46).

$$I(t_{n+1}) = I(t_n) + \Delta t \frac{1}{L} [U_s(t_n) - I(t_n)R - U_{arc}(t_n)] . \quad (46)$$

Figure 114 shows the current difference between the present and previous iteration (the second term of the right side in Equation (46)), calculated by the forward Euler method where the arc voltage is assumed zero, the time step is 5  $\mu$ s and other electrical parameters are as described by Figure 26 (the system voltage is 240 V, the current is 55 kA, the power factor is 0.45 and frequency is 50 Hz). To validate the forward Euler method, the solution of the forward Euler method is compared with the exact solution obtained by Equation (47) [86], as shown in Figure 115.

$$I(t) = -\frac{U_m}{\sqrt{R^2 + \omega^2 L^2}} \sin(-\theta) \exp(-\frac{R}{L}t) + \frac{U_m}{\sqrt{R^2 + \omega^2 L^2}} \sin(\omega t - \theta) . \quad (47)$$

In Equation (47),  $U_m$  and  $\omega$  were respectively defined by Equation (48) and (49)

$$U_s(t) = U_m \sin(\omega t) , \quad (48)$$

$$\omega = 2\pi f , \quad (49)$$

where,  $f$  is the frequency. It is observed that the solution of the forward Euler method is in close agreement with the exact solution.

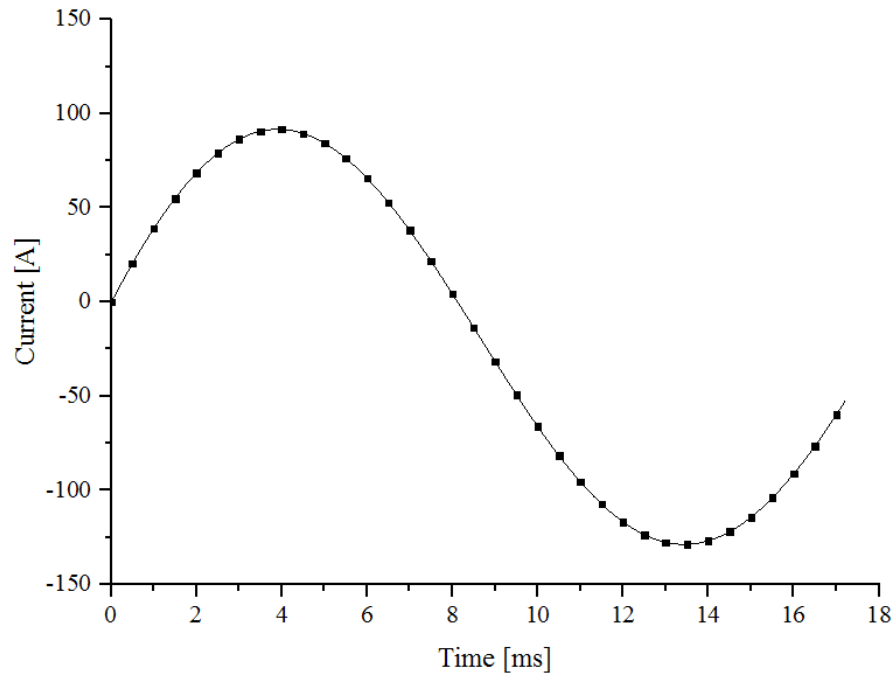


Figure 114 Current difference (between the present and previous iteration) calculated by the forward Euler method.

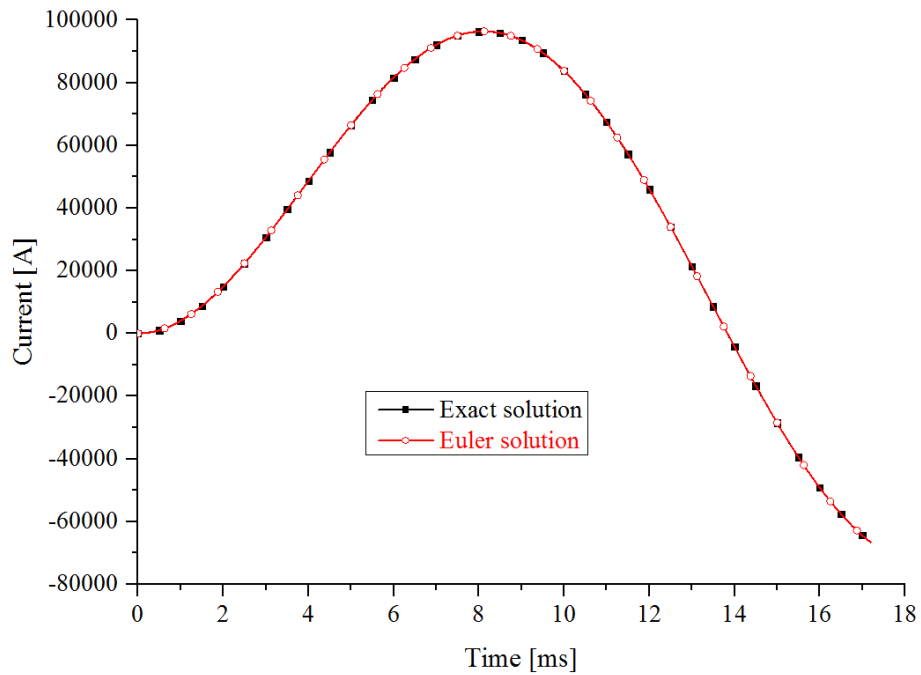


Figure 115 Comparison between the solution of the forward Euler method and exact solution: the arc voltage is 0 V, the system voltage is 240 V, the current is 55 kA, the power factor is 0.45 and frequency is 50 Hz.

#### 5.1.4 CONTACT MOTION

In [87], Rumpfer presented that comparison of simulated results with and without the consideration of contact motion; the model without contact motion overestimates the arc energy by 85 % when compared to the experimental result whereas there is a 13 % deviation from the test result in the model with contact motion. This implies the contact motion has a significant influence on the arc characteristics including arc motion and, for accurate arc modelling, the contact motion must be considered. In this research, the influence from the contact movement is modelled by the deformation and re-meshing technique introduced in [87]. We shows the voltage waveform and detailed arc motion associated with contact motion.

Table 14 shows the detail of the deformation and re-meshing process in the fluid domain as the contact gap increases (the movable contact parts from the fixed contact). To improve mesh quality, new meshes are generated after contact travel of 0.5 mm, 1 mm, 1.8 mm, 2.5 mm, 3.3 mm, 4 mm, 4.8 mm, and 5.5 mm.

Table 14 Mesh state associated with contact movement.

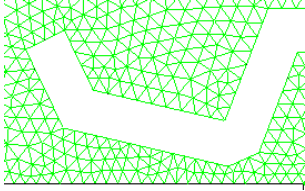
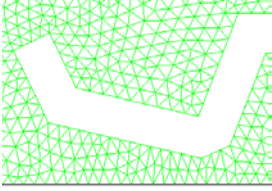
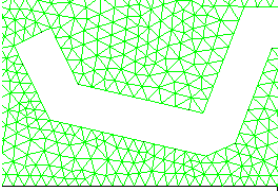
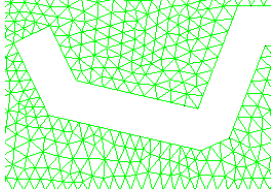
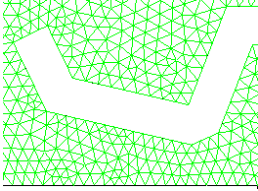
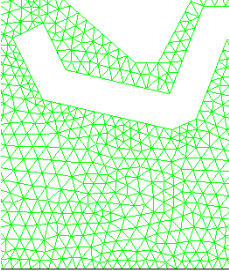
Displacement	Initial state (0.5 mm gap)	0.4 mm movement (0.9 mm gap)	0.5 mm movement (1.0 mm gap)
State of mesh	Initial state 	Deformation 	Re-meshing 
Displacement	0.9 mm movement (1.4 mm gap)	1.0 mm movement (1.5 mm gap)	Final state (6.0 mm gap)
State of mesh	Deformation 	Re-meshing 	Re-meshing 



Figure 116 and Figure 117 show the arc voltage waveform and the temperature distribution in the case of fully opened contact gap and opening movable contact. The current experimentally obtained data as shown in Figure 116 is applied to two models (fully opened gap and opening gap models). Since the model with the fully opened contact gap has a much longer arc column than that with the opening contact, there is a higher arc voltage in the case of fully opened gap at the early stage (from arc ignition to 0.75 ms) of simulation. From 0.5 ms to 0.75 ms, the arc moves backwards due to the large opening area behind the arc in the fully opened state. Figure 117 shows the comparison of opening condition behind the arc between two models. The arc back-motion affects the arc voltage and the voltage drops by 25 V in the case of the fully opened case. There is a similar value arc voltage (48 V) at 0.75 ms in both cases; however after this point, the arc rapidly moves towards the splitter plates and the voltage is higher in the case of the opening contact compared to the fully opened case. From this result, it is convinced that there is a significant difference between the models simulating fully opened and opening contact.

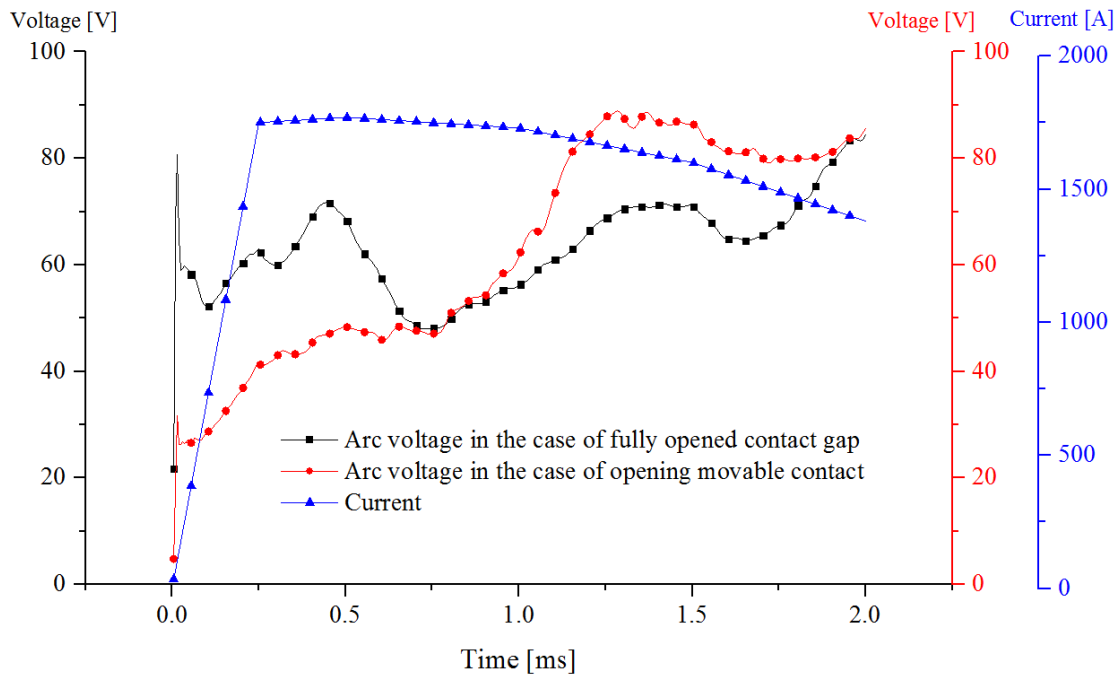


Figure 116 Comparison of arc voltage between the models simulating a fixed fully opened contact and opening contact.

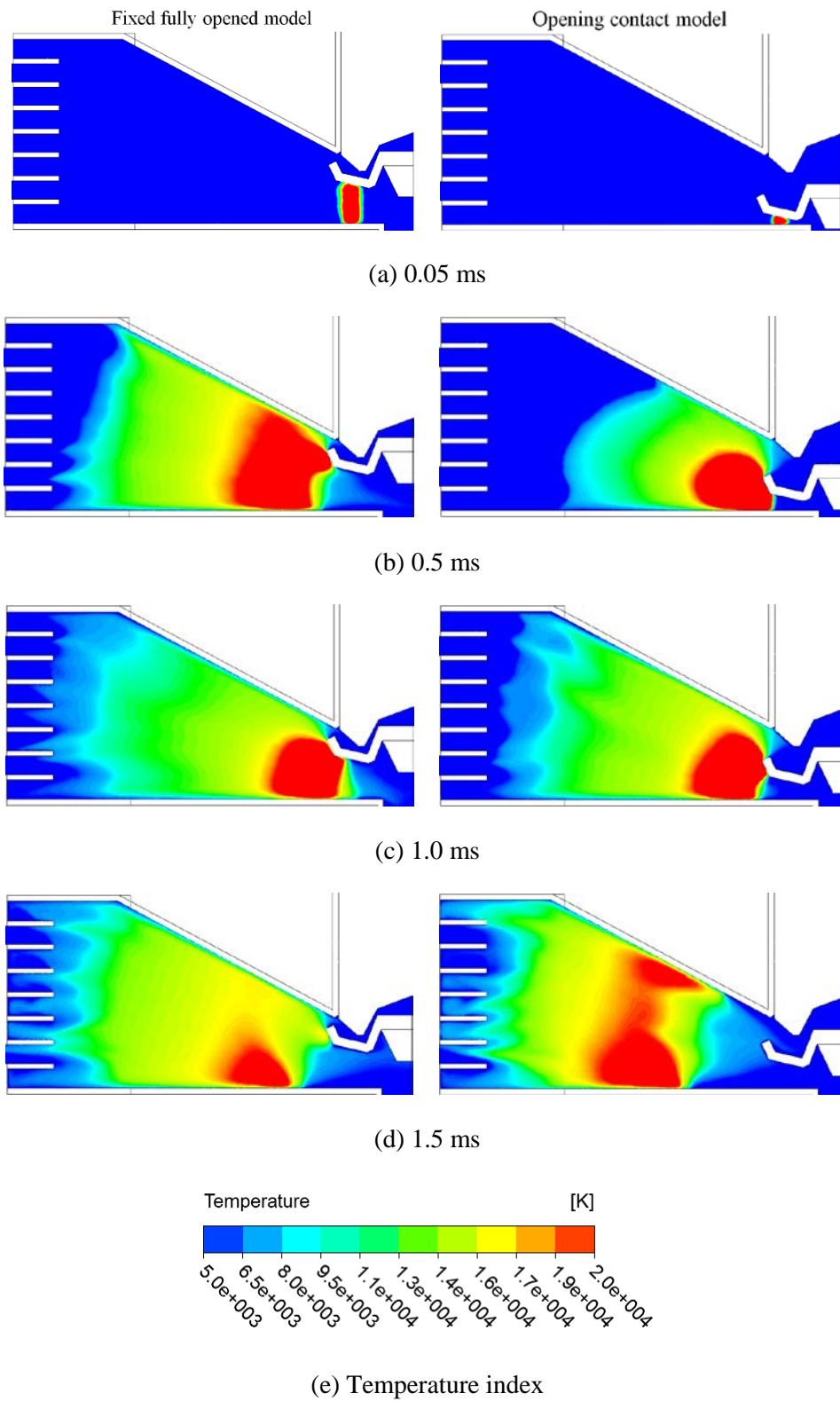
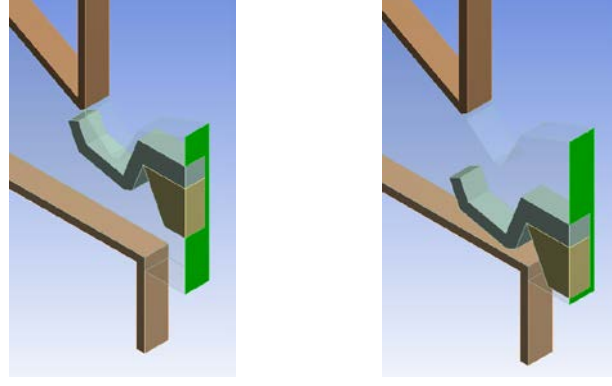


Figure 117 Comparison of temperature distributions between the fully opened contact and opening contact models; left figures are the temperature distributions for the opening movable contact whereas right ones are the temperatures for the fully opened contact gap.



(a) fully opened model      (b) opening movable contact model

Figure 118 Difference of the back opening condition between the fully opened model (a) and opening movable contact model (b): the green boundaries show the back opening area.

### 5.1.5 ARC ROOT FORMATION

The arc root formation process plays a key role in the arc motion and voltage increase during the switching operation of LVSDs. There are two methods to implement the arc root formation in arc modelling.

One is to build a thin mesh layer (0.1 mm) in front of the metal surface where the electrical conductivity is modified, based on the V-J curve like in Figure 49 [67]. The electrical conductivity in a thin mesh is calculated as below

$$\sigma_{il} = J_{ar} \frac{V_y}{V_{ar}}, \quad (50)$$

where,  $J_{ar}$  is the current density  $V_{ar}$  is the voltage drop in the arc root and  $\Delta y$  is the layer thickness (0.1 mm).

The other is to set the contact resistance on the interface between a fluid (air) and solid (splitter plate and electrode) also based on the V-J curve [82], [88]. The contact resistance ( $\rho_{cr}$ ) is expressed as below

$$\rho_{cr} = \frac{V_{ar}}{J_{ar}} . \quad (51)$$

In the case of contact motion, the contact resistance method is a simpler and more effective way. The mesh deformation and re-meshing process does not affect the contact resistance; however, the deformed mesh can influence the electrical conductivity in a thin mesh layer and the special treatment is required to calculate the thin layer's conductivity. In this research, the contact resistance method is adopted to model the arc root formation including the voltage drop in the arc root.

Figure 119 shows the simplified chamber that is composed of two electrodes, one splitter plate and two vents at the end of electrodes. The external magnetic field of 0.1T is applied in the fluid domain and 100 A DC current is provided as a boundary condition. The simulation geometry, condition and mesh quality are the same as described in [88]. Figure 120 and Figure 121 illustrate the arc splitting process with consideration of arc root formation. Following arc ignition, the arc moves towards the splitter place by the combination of Lorentz force and pressure gradient. At about 0.1 ms, the arc bends and stretches itself near the splitter plate; therefore, the corresponding arc voltage increases as shown in Figure 121. At about 0.17 ms, the arc roots are formed at a region 4 mm from the edge of the splitter plate. At 0.2 ms, the arc is totally divided into two segments. After the arc bends and stretches near the splitter plate, the arc voltage increases due to the contact resistance on the splitter plate's surface. If there is no resistance on the plate's surface, the arc penetrates the splitter plate and is easily divided as shown in Figure 122.

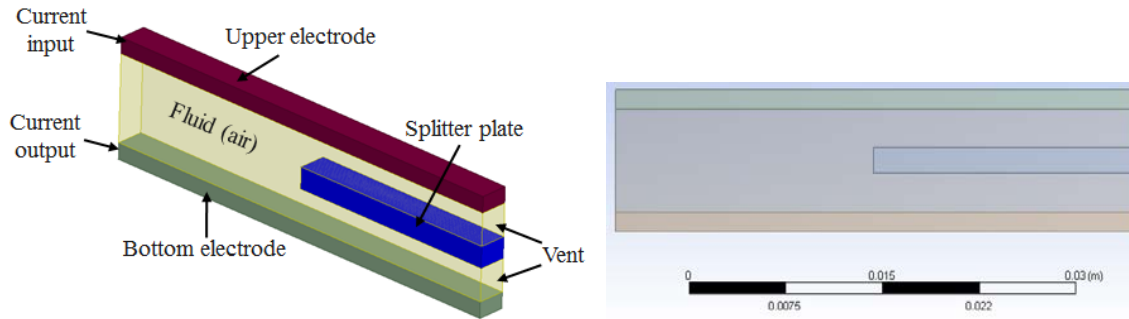


Figure 119 Simulation geometry.

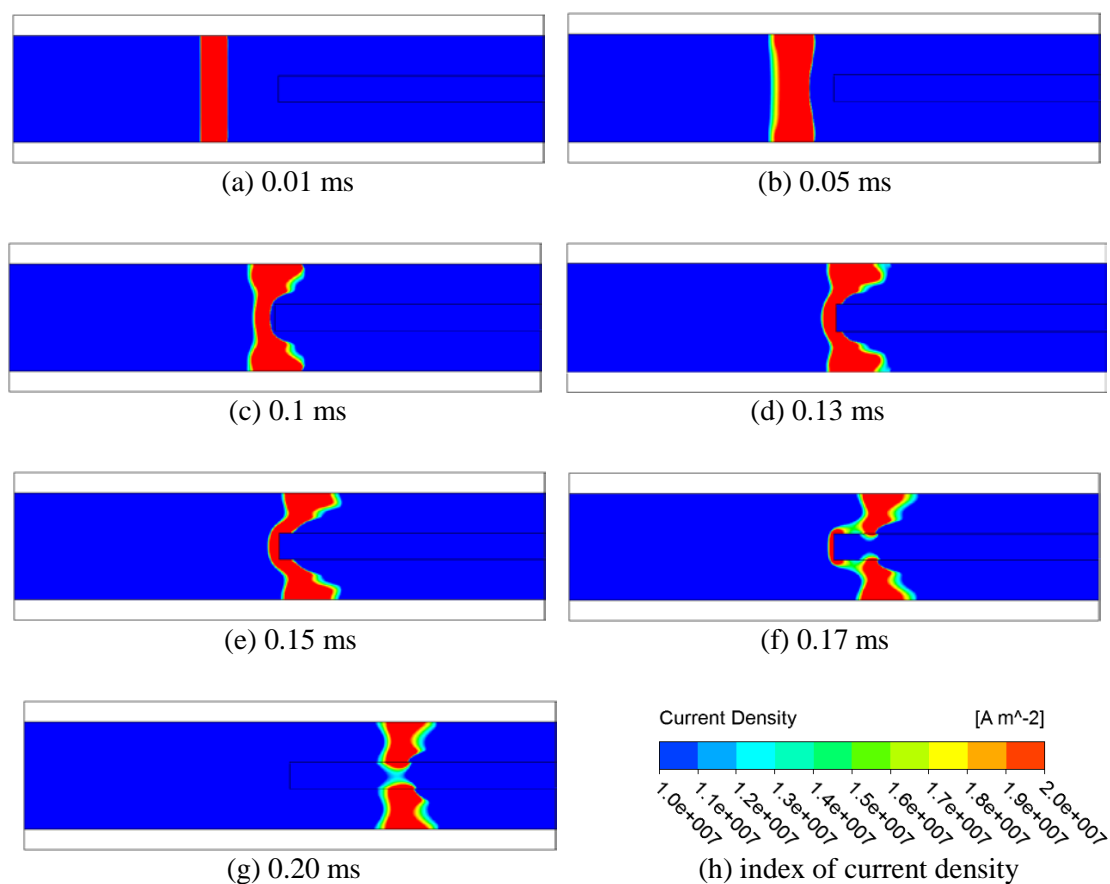


Figure 120 Distribution of arc current density during arc root formation.

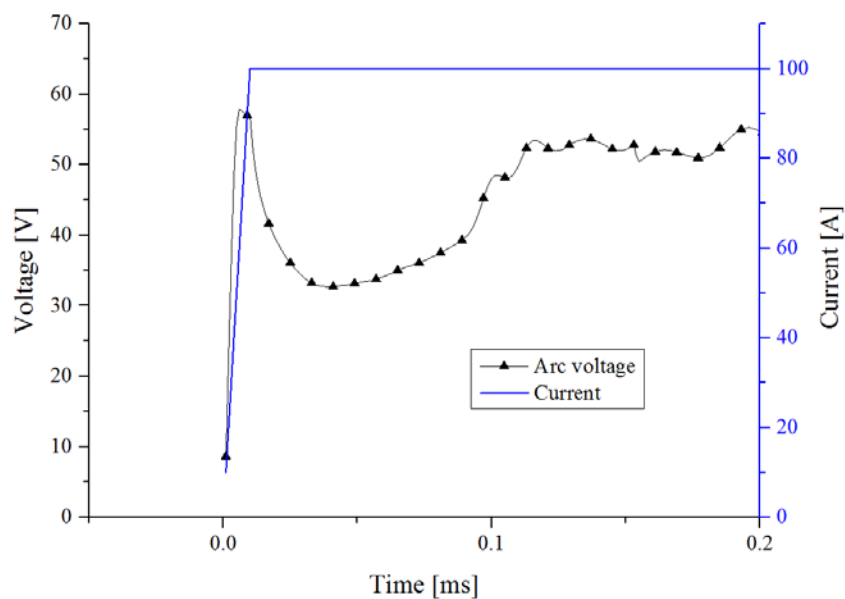


Figure 121 Arc voltage and current during arc root formation.

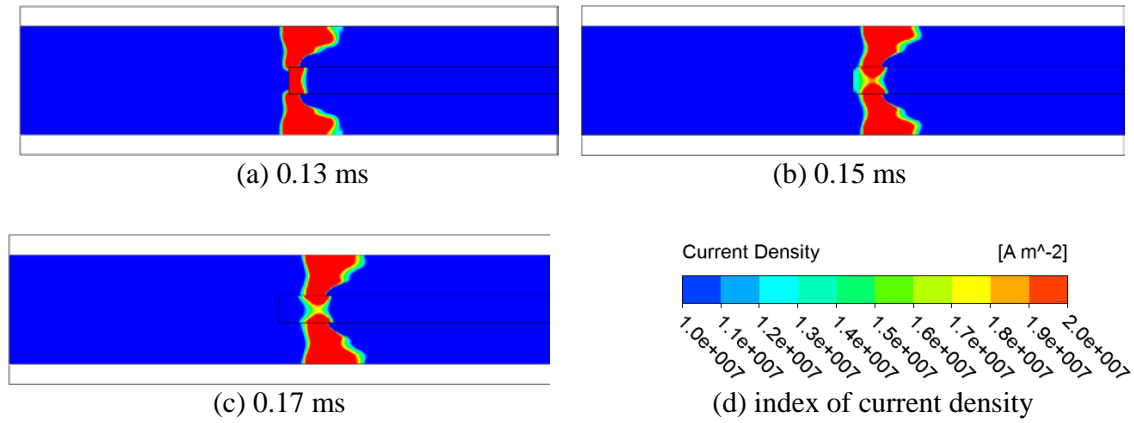


Figure 122 Distribution of arc current density when disregarding arc root formation.

### 5.1.6 RADIATION LOSSES

The high temperature arc in LVSDs has thermal losses primarily due to radiation. The prevalent method for the modelling radiation losses in previous work is the net emission coefficient (NEC) [21]. This arc modelling work also adopts the NEC method and NEC data varied with temperature and pressure (Figure 44) is used. We present the effect of radiation on the temperature, arc voltage and arc motion by comparing the results of arc simulation with and without radiation losses.

There is a significant difference between simulation results with and without radiation effect even though the identical current (current data in Figure 116) is applied to two models. Figure 123 shows the influence of radiation on the average temperature inside the quenching chamber. It is seen that radiation loss contributes to arc cooling. Due to the cooling effect, a higher arc voltage is obtained by simulating radiation loss as shown in Figure 124. Figure 125 shows a detailed comparison of chamber temperature distribution associated with radiation loss. As expected, the temperature is higher in the model without radiation than the model with radiation losses. Furthermore, in the case without radiation effect, the high temperature region above 20000 K spreads wider in the chamber. This difference in temperature distributions between models results in different plasma properties and leads to difference in arc motion.

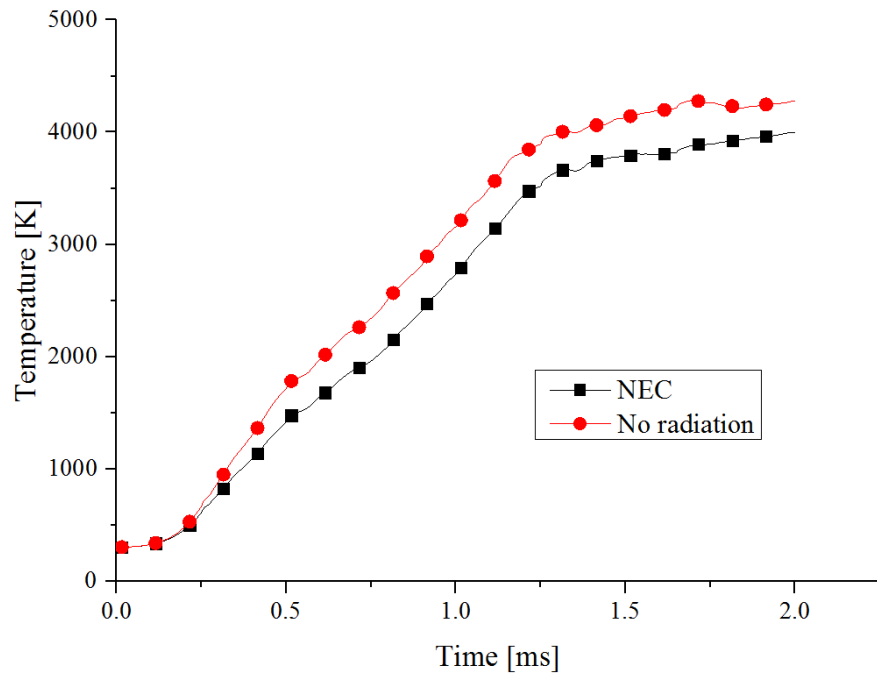


Figure 123 Comparison of average temperature in the chamber associated with radiation losses; the identical input current (current data shown in Figure 116) is applied to two models.

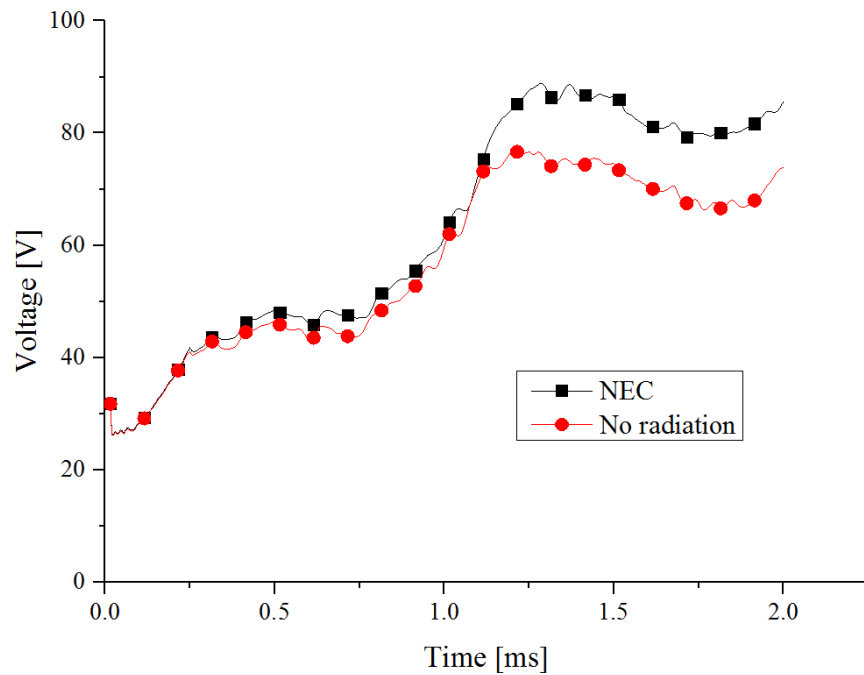


Figure 124 Comparison of arc voltage associated with radiation losses; the identical input current (current data shown in Figure 116) is applied to two models.

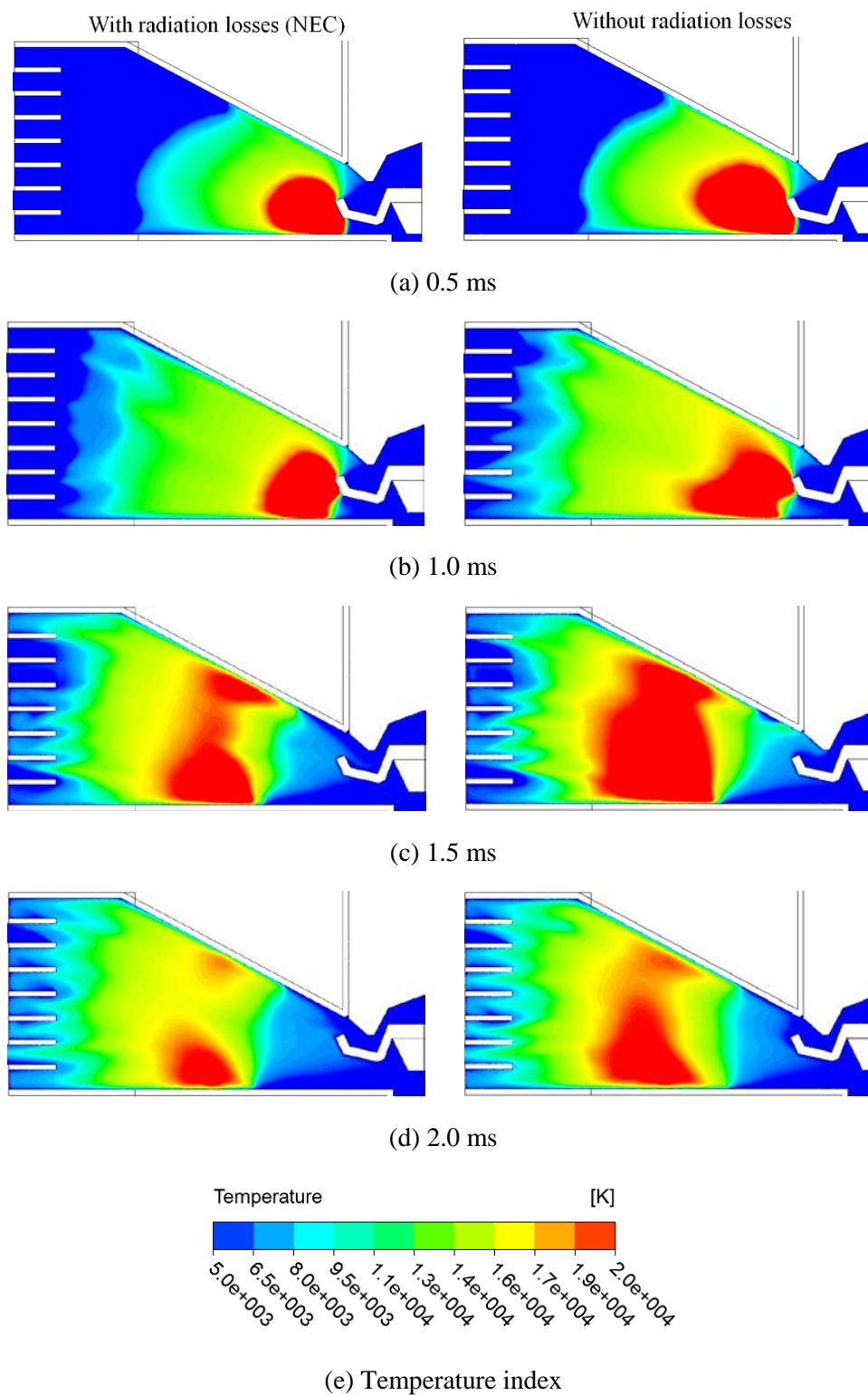


Figure 125 Comparison of temperature distributions associated with radiation losses; left figures are the temperature distributions from the simulation with radiation losses whereas right figures are the temperature distributions from the simulation without radiation losses.



### 5.1.7 EFFECT OF THE V-J CURVE ON THE ARC VOLTAGE AT ARC EXTINCTION (LOW CURRENT REGION)

The calculation of the exit arc voltage is important to predict re-ignition phenomena in LVSDs as described in 4.1. From the literature review (section 2.2.4), it is shown that the arc voltage increases as the current decreases in the low current region due the voltage increase in the arc root. We improve the calculation of the exit arc voltage by modifying the V-J curve of the arc root based on the measured arc voltage and simulated current density on the splitter plates.

The voltage and current waveforms measured by the AIS show the arc voltage significantly increases as the current decreases shortly before the current zero point. Figure 126 shows the measured and simulated arc voltage when the current in Figure 127 flows through the FTA. From the measured data, it is seen that the arc voltage is below 300 V prior to 3.95 ms; however, after this point the voltage increases and reaches 392 V immediately before the current zero point.

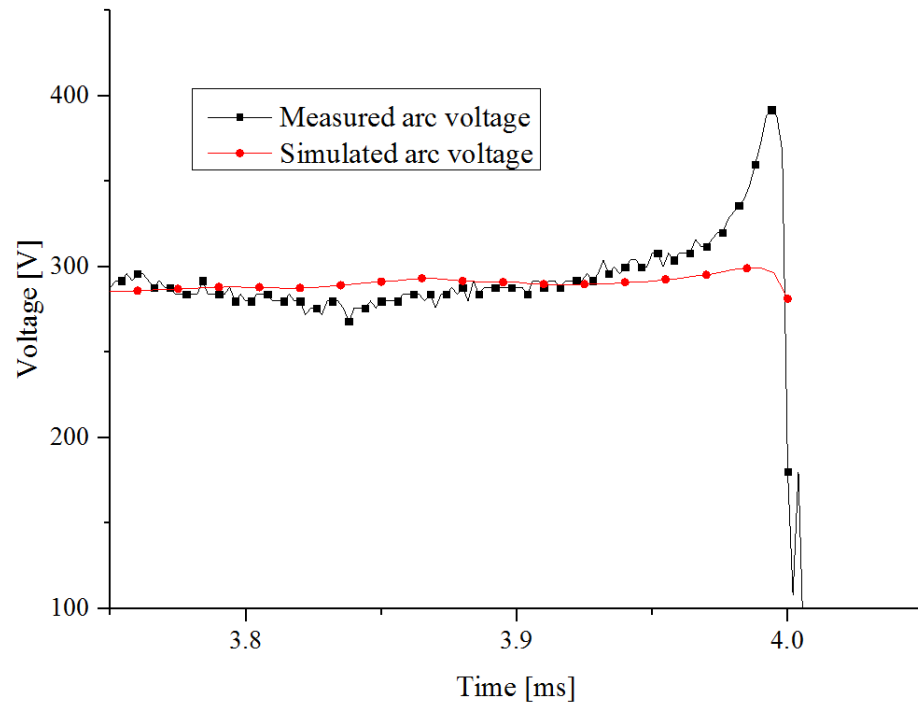


Figure 126 Measured and simulated arc voltage; arc voltage is calculated based on V-J relationship as shown in Figure 128.

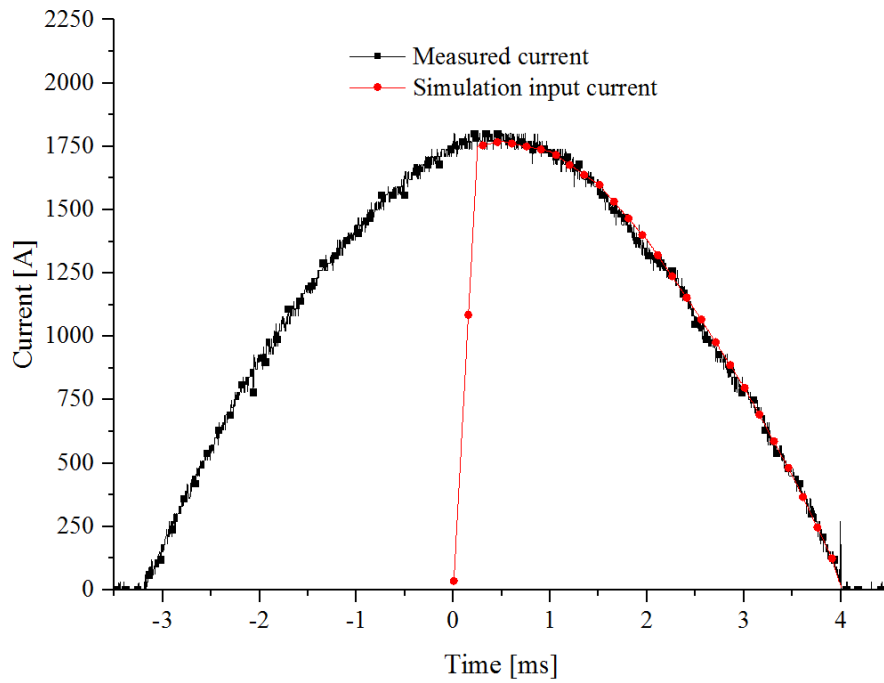


Figure 127 Measured and simulation input current; simulation input current is used for arc modelling.

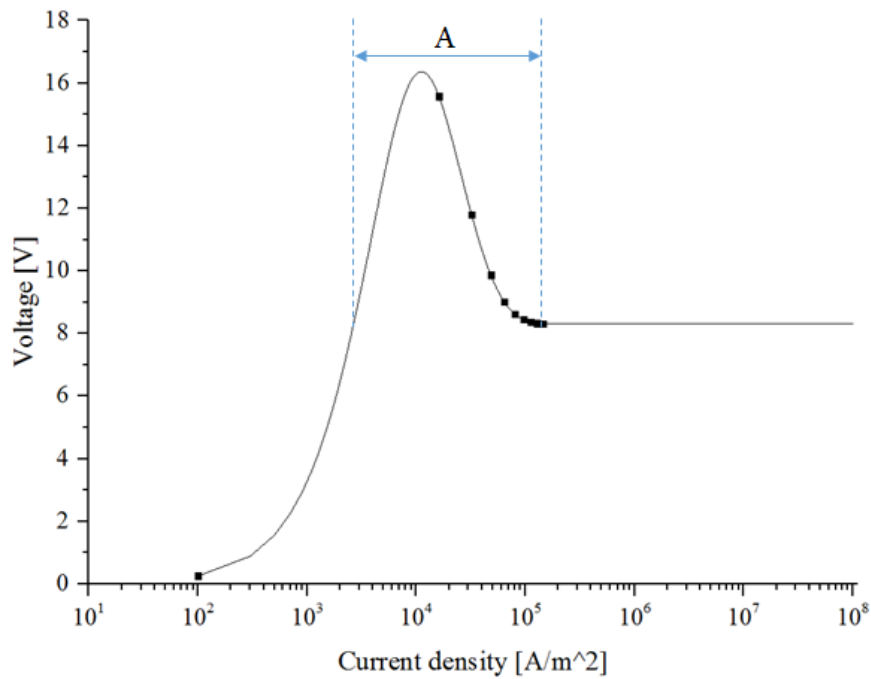


Figure 128 V-J relationship (relationship between voltage and current density): the sheath voltage (arc root voltage) is 8.3 V based on [23], 'A' is the hump region where the voltage is above 8.3 V.

Figure 128 shows the V-J relationship (relationship between the arc root voltage and current density) used in arc modelling for Figure 126. The graph in Figure 128 is based on Lindmayer's arc root model (see section 2.5.3); however, the value of voltage drop in the arc root is from Yokomizu's experimental results described in section 2.2.3. This V-J curve has the constant voltage of 8.3 V above  $1.2 \times 10^5 \text{ A/m}^2$  and the hump region in the range of  $2.7 \times 10^3 \text{ A/m}^2$  to  $1.2 \times 10^5 \text{ A/m}^2$ . The hump region is marked as 'A' in Figure 128 where the voltage is above 8.3 V. From the simulated data in Figure 126, it is seen that the arc voltage has no apparent influence by the low current region. The value of the arc voltage remains steady at approximately 290 V instead of increasing.

The increase in the arc voltage near the current zero point during LVSD's switching process can be explained by the negative V-I characteristic in the low current region as described in 2.2.4. Some experimental data shows the increase of the arc voltage in the low current region is mainly due to the increase in the voltage drop at the cathode root voltage. In this thesis, we treat the anode and cathode roots equally to reduce the complexity of arc modelling. It is assumed that the increase of the arc voltage near the current zero is due to the anode and cathode root effect, equally. If the voltage drop in the arc roots is modelled properly near the current zero point, we can get a more accurate exit arc voltage, which is the main parameter to predict the re-ignition phenomena. The calculation of the arc root voltage is improved by modifying V-J relationship, especially the hump region.

Figure 129 presents the current density on the splitter plates in the region of low current; it reveals that the current density in the arc root area decreases as the current approaches the zero point.

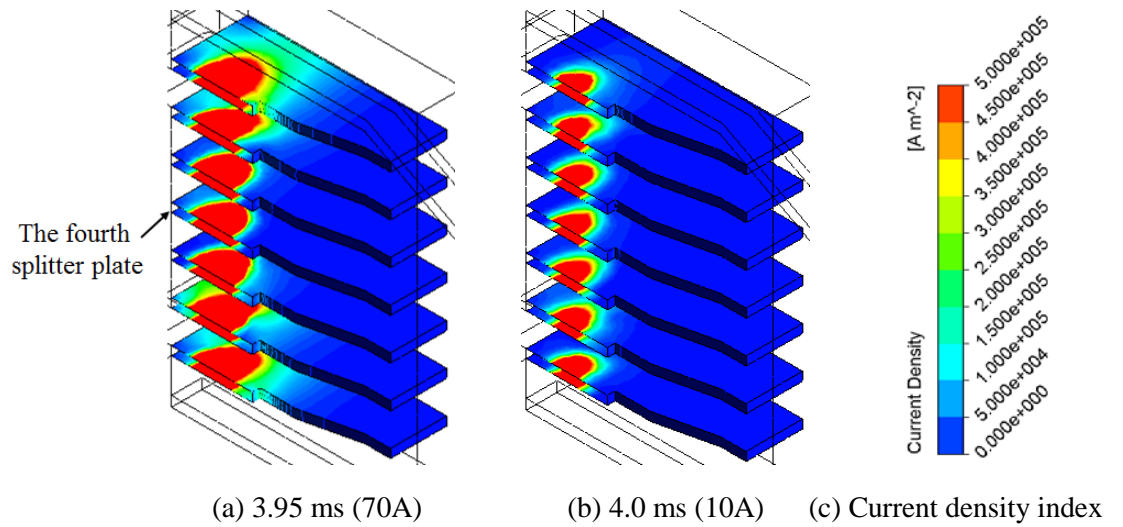


Figure 129 Current density on splitter plates near current zero point.

However, the value of the current density of the arc root spot on the splitter plate is still far away from the hump region in Figure 128. The hump region of Lindmayer's arc root model (see Figure 128) is in the range of  $2.7 \times 10^3 \text{ A/m}^2$  to  $1.2 \times 10^5 \text{ A/m}^2$ . In the simulation result, it is seen that there is the wide region of the arc root over  $5 \times 10^5 \text{ A/m}^2$  on the plate. We also calculate the arc voltage from the V-J relationship without the hump region and find that its result is the same to the simulated data considering the hump region. This supports that the hump region in Figure 128 has inconsequential influence on the arc voltage near the current zero point.

In order to modify the V-J curve, especially the hump region, we collect the current density, experimental arc voltage (A), simulated arc voltage (B) near the current zero point as shown in Table 15. The current density is the maximum value calculated at the surface of the fourth plate (see Figure 129). The current density decreases as the current lowers. The measured arc voltage increases as the current density decreases. However, it is seen that there is no significant variation in the simulated arc voltage associated with the current or current density.

We assume that the voltage increase in the low current region is mainly caused by the voltage of the arc roots. The experimental arc voltage represents the voltage drop including the negative V-I characteristics of the arc roots whereas the simulated arc voltage refers to the voltage drop without the consideration of the negative V-I curve. The difference between A and B can be considered as the effect of the negative V-I characteristics. When the arc stays at the splitter plates, there are 16 arc roots (anode and cathode roots). We can get the effect of the negative V-I relation in each arc root from Equation (52) and calculate the voltage drop in the arc root from Equation (53), which includes the effect of the negative V-I characteristics.

$$V_{NVI} = \frac{A(\text{experiment}) - B(\text{simulation})}{16} , \quad (52)$$

$$V_{mod} = V_{NVI} + 8.3 [\text{V}] , \quad (53)$$

where,  $V_{NVI}$  refers to the voltage increase in each arc root due to the negative V-I curve, A is the measured arc voltage, B is the simulated arc voltage,  $V_{mod}$  is the modified voltage in the arc root.  $V_{mod}$  is used as the basic data to modify the V-J curve for the arc root modelling.

Table 15 Simulated current density, measured arc voltage (A), simulated arc voltage (B),  $V_{NVI}$  from Equation(52) and  $V_{mod}$  from Equation (53) .

Time [ms]	Current [A]	Current density <sup>a</sup> [A/m <sup>2</sup> ]	Arc voltage [V]		$V_{NVI}$ <sup>b</sup> [V]	$V_{mod}$ <sup>c</sup> [V]
			Experiment (A)	Simulation (B)		
3.915	112	8638947.0	289.4	289.4	0.0	8.3
3.925	100	7968751.5	292.0	289.9	0.1	8.4
3.935	88	7379934.5	296.0	290.3	0.4	8.7
3.95	70	6401949.0	300.0	291.7	0.5	8.8
3.96	58	5593081.0	308.0	293.2	0.9	9.2
3.97	46	4687183.0	312.0	295.3	1.0	9.3
3.98	34	3488321.3	332.0	298.5	2.1	10.4
3.99	22	2042156.0	372.0	299.5	4.5	12.8

<sup>a</sup> The current density is the maximum value calculated at the surface of the fourth plate (see Figure 129).

<sup>b</sup>  $V_{NVI}$  is the increased voltage in each arc root due to the effect of negative V-I relation, which is calculated from Equation (52)

<sup>c</sup>  $V_{mod}$  is the modified voltage in the arc root, which is calculated from Equation (53). It includes the effect of the negative V-I characteristics.

Based on the calculated current density and the modified voltage in the arc root ( $V_{mod}$ ) in Table 15, several points (blue triangular points) of the new V-J relationship can be plotted as shown in Figure 130. The modified V-J curve is derived from new 8 points as shown in Figure 130. The modified V-J curve has a different voltage value from Lindmayer's V-J curve in the region of  $10^4$  A/m<sup>2</sup> to  $9 \times 10^6$  A/m<sup>2</sup>; the modified one has a much wider hump region ( $2.7 \times 10^3$  A/m<sup>2</sup> to  $1.0 \times 10^7$ ) than Lindmayer's one. Figure 131 shows the measured and simulated arc voltage by using the modified V-J relationship. It is observed that the simulated voltage increases as the current zero point approaches and there is a similar trend between the measure and simulated data. Furthermore, there is a good agreement in the exit arc voltages from the simulation and experiment (simulated value: 327 V, measured value: 332 V).

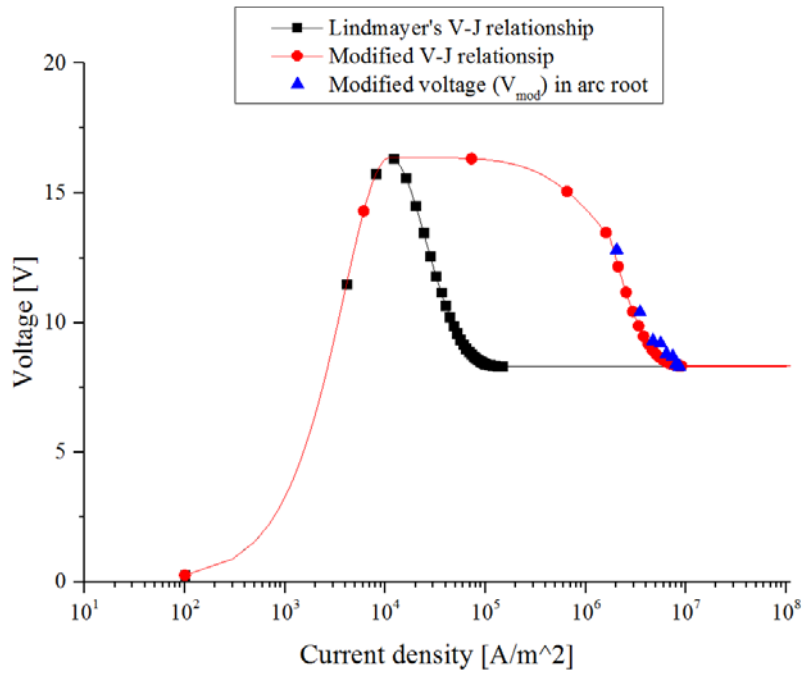


Figure 130 Modified voltage in the arc root (blue triangular points), modified V-J curve and Lindmayer's V-J curve.

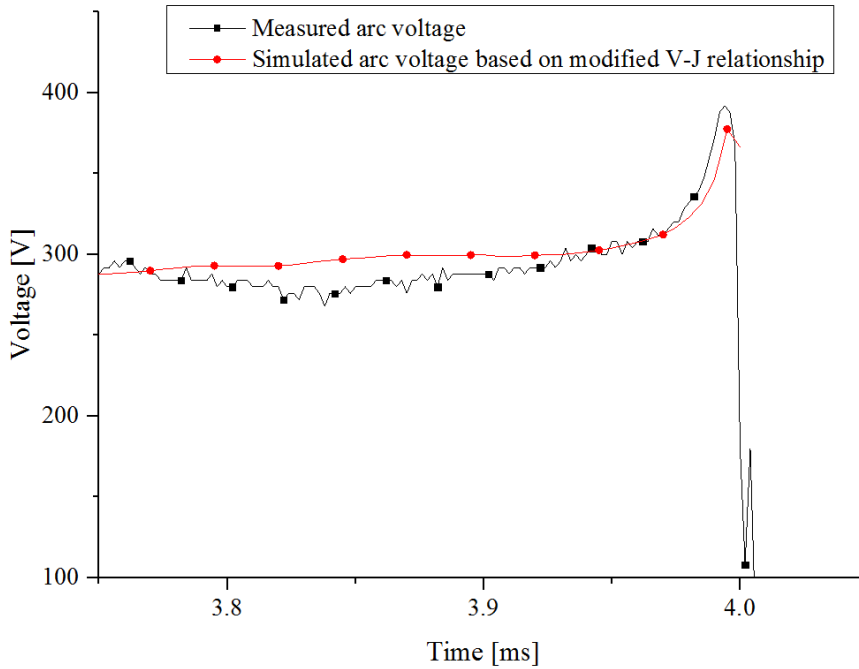


Figure 131 Measured and simulated arc voltage: the simulation is conducted based on the modified V-J relationship as shown in Figure 130.

### 5.1.8 FLOW CHART OF ARC MODELLING

Figure 132 shows a flow chart of the arc simulation process. Commercial software, ANSYS CFX, is used to build the arc model in this thesis. Arc modelling requires simulation of fluid dynamics, heat transfer and electromagnetic phenomena. An iterative approach is used to calculate simulation parameters with time. The RMS residual target (0.0005) is set as the convergence criteria.

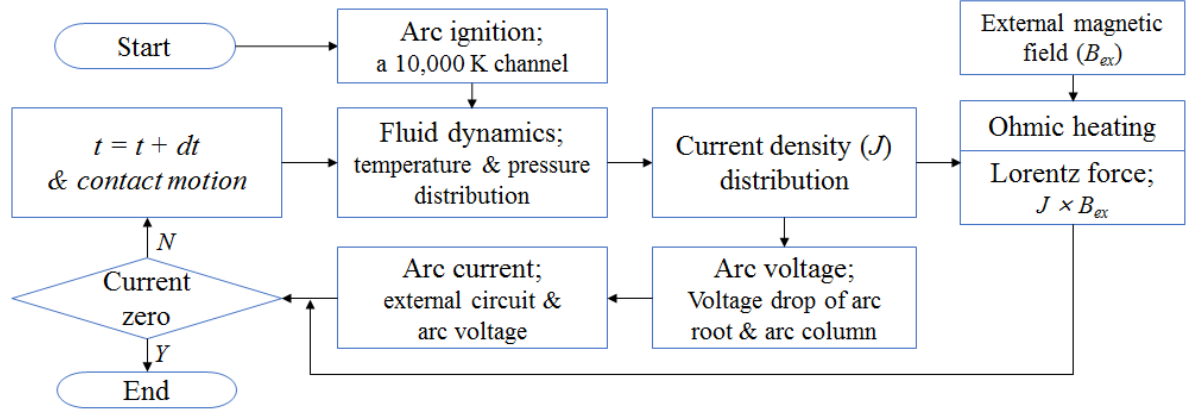


Figure 132 Flow chart of arc modelling.

The external magnetic flux density ( $B_{ex}$ ) is pre-calculated based on the arc position and current to account for Lorentz force within the arc simulation. The calculated  $B_{ex}$  is distributed in the fluid region and it is updated in each stimulation time based on the current value. After arc ignition from a hot channel between contacts, the current density distribution is calculated from the electrical conductivity of air and electric field strength in the quenching chamber. The current density is the main parameter used to determine ohmic heating, Lorentz force as well as arc voltage. The current is deduced from the external circuit after obtaining the arc voltage including voltage drops in arc column and arc root (sheath). Based on calculated ohmic heating, Lorentz force and current, a simulation of fluid dynamics is then carried out; and then the distributions of temperature and pressure are renewed and air properties updated (the density, electrical conductivity, thermal conductivity, specific heat capacity and viscosity). The current density, ohmic heating, Lorentz force, arc voltage as well as current are re-calculated from updated conditions. This iterative process continues until the current zero point.

## 5.2 VERIFICATION OF ARC MODELLING

We validate arc modelling by comparing the simulated arc temperature, arc motion and waveforms (current and voltage) with experimental data. Further, the effect of the vent distribution on arc motion is investigated through the simulation. Especially, the simulated temperature distribution is compared with the measured arc images in detail for the validation of arc motion.

### 5.2.1 TEMPERATURE COMPARISON

Temperature calculation is carried out through arc modelling and the simulated result is compared with measured temperature, which is evaluated from Cu I spectrum lines as described in section 4.3. Table 16 and Table 17 show the simulation and experimental conditions, respectively. The measured current in Figure 92 is used as the input source in the simulation. The effect of arc root formation and Lorentz force is not considered since the arc is established in the narrow enclosed chamber without moving. Figure 133 shows the geometry of arc modelling for temperature calculation, which represents the modified FTA for arc spectrum measurement (see Figure 72). The arc initiates through a 1 mm radius hot channel between electrodes. It is assumed that the developed arc diameter is the same to the chamber width (5 mm); hence, 2.5 mm radius NEC data is used in this modelling, which is derived from [63].

Table 16 Simulation condition for temperature calculation.

Item	Condition description
Input current	- The measured current is used as the input current. - The current between 3.5 ms and 8.0 ms in Figure 92 is imposed to the source boundary.
Geometry	- Figure 133 shows the geometry of temperature calculation. - The geometry is based on the modified FTA as shown in Figure 72.
Arc root formation (V-J curve)	- Not considered
Lorentz force	- Not considered
Radiation loss	- Using the NEC radiation loss as explained in 5.1.6



Table 17 Experiment condition for arc imaging measurement.

Item	Condition description
Vent	- No vent - Closed narrow chamber
Charging voltage	100 V
Current	- The 450 A peak current flows through the FTA. - Figure 92 shows the current waveform.
Filter	ND 8

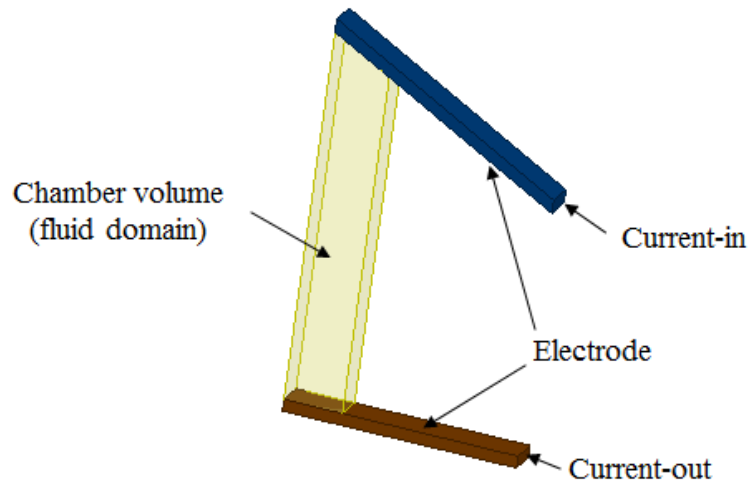


Figure 133 Geometry of arc modelling for temperature comparison

Figure 134 shows the simulated temperature distribution and Table 18 presents the comparison between measured and simulated temperature at four different frames linked to the spectrometer measuring time (see Table 18 for the time). The simulated temperature is obtained at the spectrometer fibre position. It is seen that the temperature decreases as the current decreases in both experimental and simulated results. The largest discrepancy is observed as 11.3 % at the 11th frame and the smallest difference (1.0 %) is seen at the 23th frame. Despite some discrepancies, overall, it can be said that there is a good agreement between measured and simulated temperature.

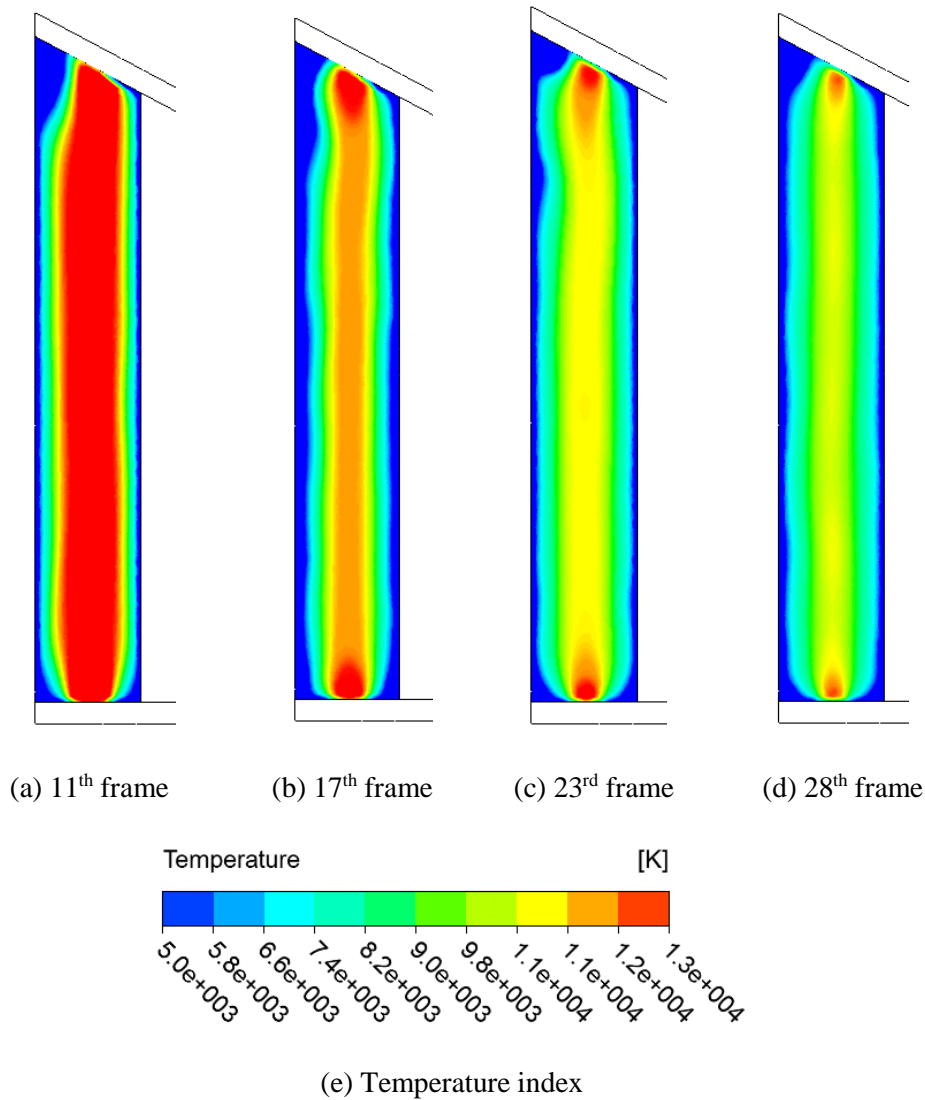


Figure 134 Simulated temperature distributions in the half model.

Table 18 Comparison between experimental data and simulation results.

Frame <sup>a</sup>	Time <sup>b</sup> [ms]	Current [A]	Temperature [K]		Remarks
			Experiment	Simulation	
11th	3.58	170	15755	13980	Figure 134 (a)
17th	5.00	88	12792	11999	Figure 134 (b)
23rd	6.42	57	10895	11000	Figure 134 (c)
28th	7.60	34	9901	10368	Figure 134 (d)

<sup>a</sup> The frame number corresponds with Figure 92.

<sup>b</sup> Time represents the starting instance of the integration time in each frame.

### 5.2.2 SIMULATION RESULTS WITHOUT CURRENT LIMITATION

In arc modelling without current limitation, the arc voltage and arc motion are computed by the given current without consideration of the external circuit. Table 19 and Table 20 show the simulation and experimental condition, respectively.

Table 19 Simulation condition for arc modelling without current limitation.

Item	Condition description
Current limitation	- Not considering the external circuit - The current is given as shown in Figure 127
Geometry	- Figure 106Figure 133 shows the geometry of temperature calculation. - The geometry is based on the FTA as shown in Figure 59.
Arc root formation (V-J curve)	- The modified V-J relationship is adopted as shown in Figure 130
Lorentz force	- Using the external magnetic field density to consider Lorentz force on the arc as explained in 5.1.2
Contact motion	- Using the method of deformation and re-meshing scheme as explained in 5.1.4
Radiation loss	- Using the NEC radiation loss as explained in 5.1.6

Table 20 Experiment condition for arc imaging measurement.

Item	Condition description
Vent	- Two apertures vent (23% open) - Figure 85 (a) shows the vent condition.
Charging voltage	200 V
Current	- The 1800 A peak current flows through the FTA. - Figure 127 shows the current waveform.
Filter	ND 8
Display mode	- Dynamic threshold mode - Contour level : [10 %, 13 %, 16 %, 19 %, 22 %, 25 %, 28 %]

The comparison between experimental and simulated arc voltage is presented in Figure 135 while the input current in Figure 127 is adopted as the boundary source condition. Figure 136 shows arc motion (light intensity) recorded by the AIS and the simulated arc temperature distribution in the quenching chamber of the FTA, with corresponding waveforms in Figure 135. The arc is established across the

contact gap after the contact separation and the arc voltage increases as the contact gap increases. And then, it is seen that the arc extends and the arc travels towards the splitter plates as seen in both measured and calculated data (see Figure 136 (a) ~ (d)). The experiment shows that the arc reaches the splitter plate and the voltage increases significantly at around 1.5 ms due to arc root formation at the plate surfaces. Furthermore, the arc voltage oscillates between 1.5 ms and 2.0 ms due to the instabilities of the arc attachment at the splitter plates. After then, it notably drops near 2.0 ms when the arc back motion is observed and the arc root is detaches from the plates (see measured data in Figure 136 (d) and (e)). The simulated arc voltage continuously increases until 1.3 ms, however it remains at about 85 V between 1.3 ms and 2.0 ms while the arc is located in the middle position between the ignition point and splitter plate region (see simulated data in Figure 136 (d) and (e)). This results in a less simulated arc voltage than the measured one between 1.3 ms and 2.0 ms. Both measured and simulated arc voltage start to increase again from 2.0 ms. It can be seen that there are more than 10 times of significant drops of the arc voltage in the experimental data from 2.0 ms, which are caused by arc back motions. For instance, it drops by 156 V and 176 V at 2.5ms and 3.3 ms, respectively. The voltage drop and arc back motion also can be seen in the simulated data but the modelled arc moves back only once slightly at 2.8 ms (see simulated data in Figure 136 (g) ~ (i)) and the drop of the calculated arc voltage is relatively small (74 V) compared to the measured data. The simulated arc stably stays in the splitter plates after entering them at approximately 3.0 ms (see simulated data in Figure 136 (j) ~ (m)). The measured data show that the arc does not remain in the splitter plate region until 3.7 ms. The stable arc in the splitter plates is observed after 3.7 ms (see measured data in Figure 136 (l) and (m)). The discrepancy between the simulation and experiment may be mainly due to the simplified model of Lorentz force.

In general, it can be said that the simulated waveforms and arc motion have similar trends with the measured data in spite of some discrepancies of the arc back motion, voltage drops and arc shape between experimental and modelled data. Furthermore, it is worth that the arc model gives the similar value of the exit arc voltage when compared to the measured one (simulated value: 327 V, measured value: 332 V)

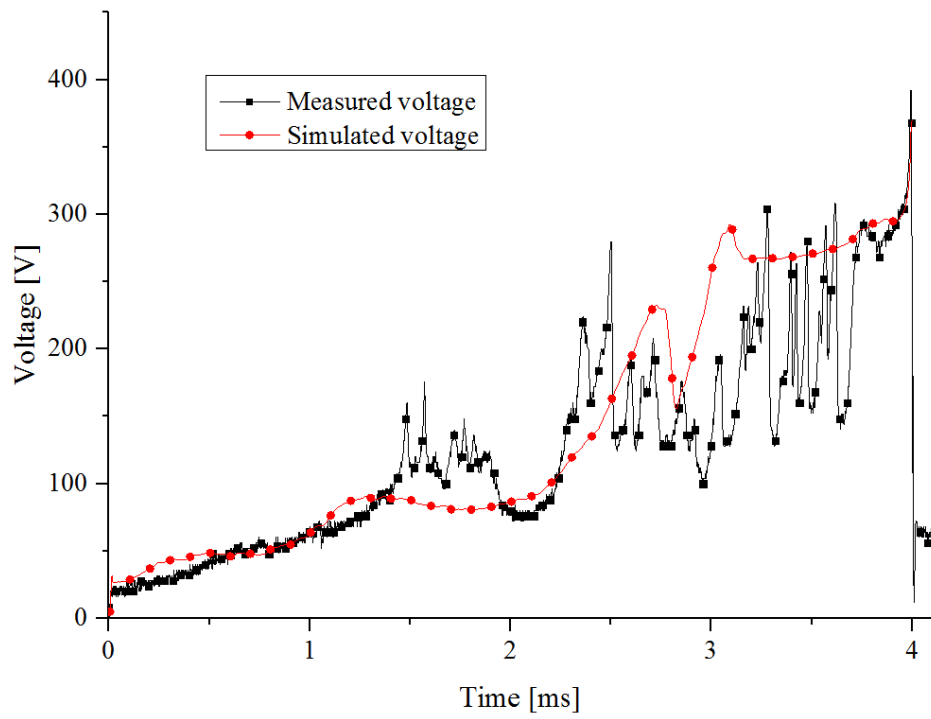
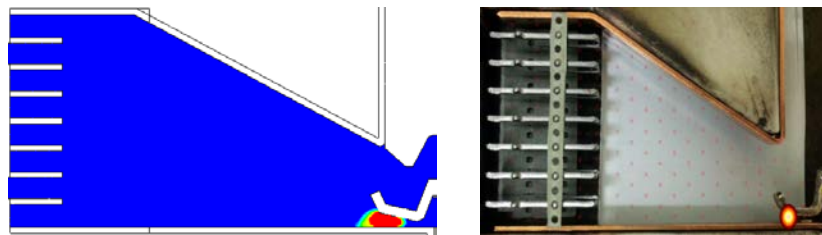
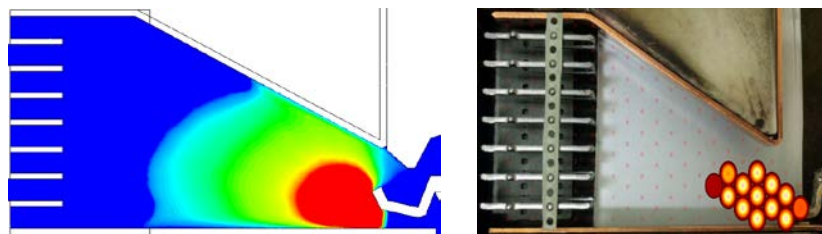


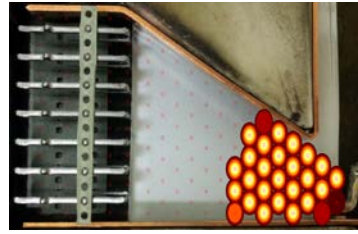
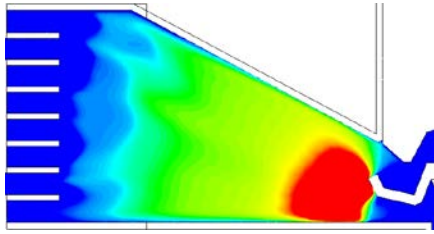
Figure 135 Measured and simulated arc voltage.



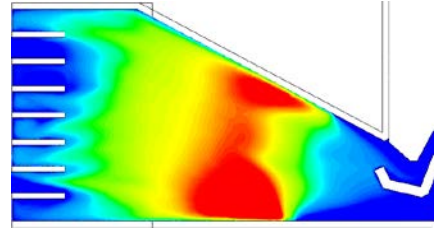
(a) 0.1 ms



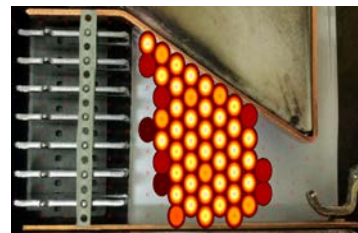
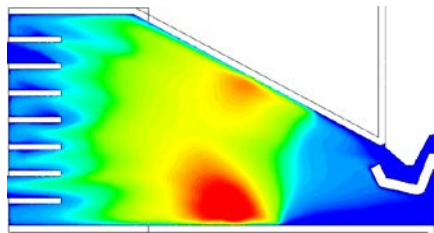
(b) 0.5 ms



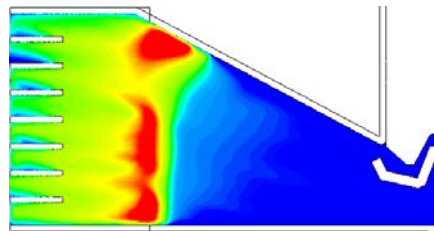
(c) 1.0 ms



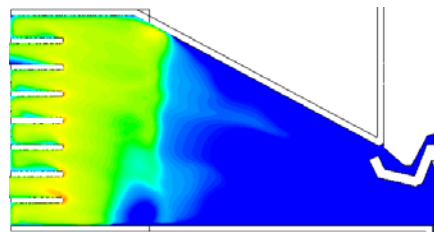
(d) 1.5 ms



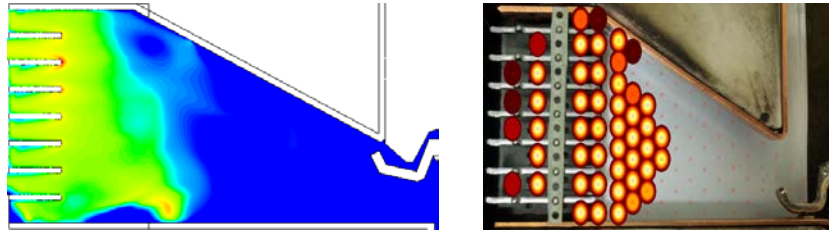
(e) 2.0 ms



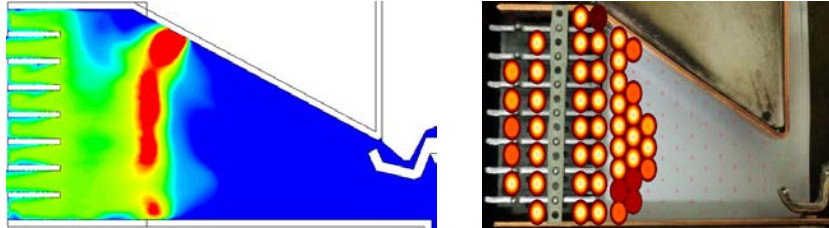
(f) 2.45 ms



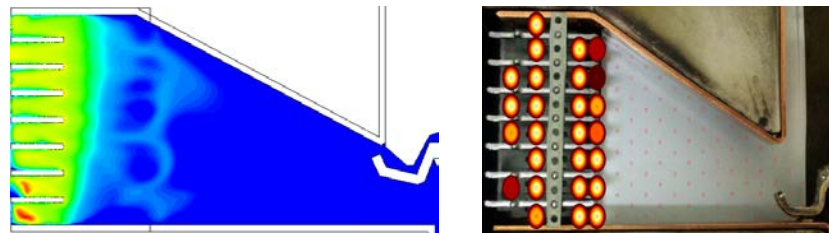
(g) 2.65 ms



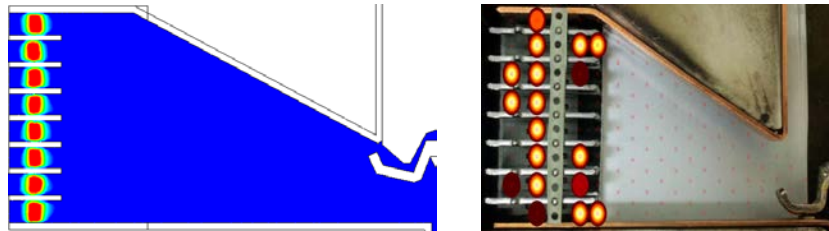
(h) 2.75 ms



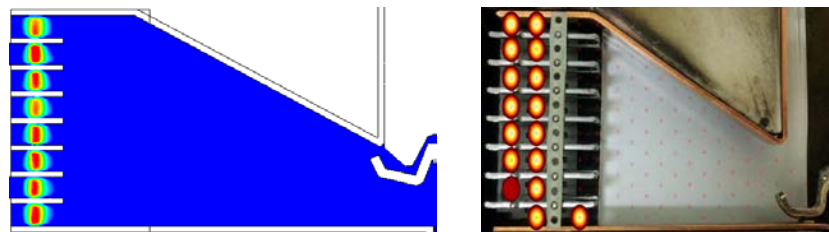
(i) 2.8 ms



(j) 3.0 ms



(k) 3.5 ms



(l) 3.7 ms

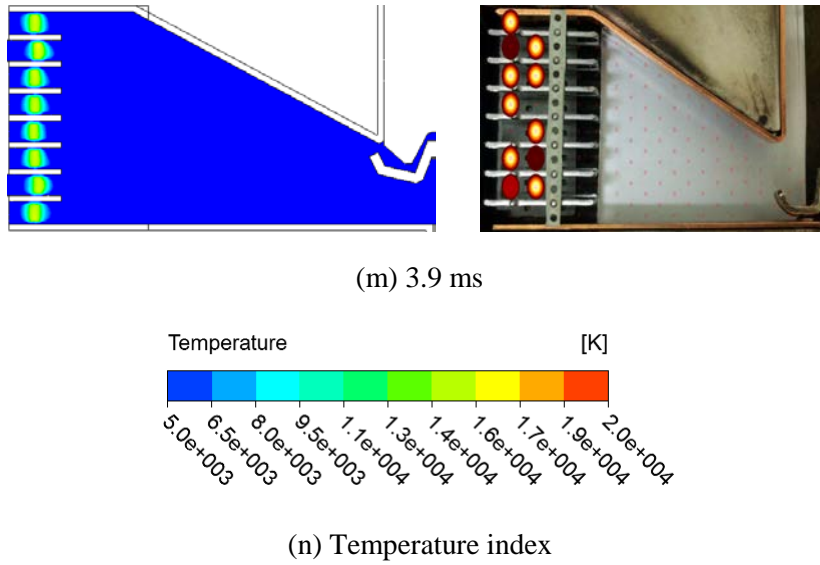


Figure 136 Simulated temperature distribution in the half model and measured arc image data (dynamic threshold mode) in the quenching chamber of the FTA.

### 5.2.3 SIMULATION RESULTS WITH CURRENT LIMITATION

We simulate arc behaviour with the consideration of the external circuit (current limitation) and validate arc modelling by showing an agreement of the voltage waveforms of the simulation and experiment. Table 21 shows the simulation condition for arc modelling. Except consideration of the external circuit, other conditions are the same with Table 19. The experimental condition is the same with Table 20.

Table 21 Simulation condition for arc modelling with current limitation.

Consideration	Condition description
Current limitation	- Considering the external circuit as explained in 5.1.3
Arc root formation (V-J curve)	- Same with Table 19
Lorentz force	
Contact motion	
Radiation loss	



Figure 137 shows the waveforms obtained from the experiment and simulation considering current limitation (the experimental data are the same with data in previous section (5.2.2)). Arc modelling starts to consider the current limitation from 0.25 ms. Before 1.5 ms, the simulated arc voltage is more or less similar with the experimental result; therefore, the experimental and simulated current are in a good agreement. However, it is seen that the modelled arc voltage is lower than the experimentally observed value between 1.5 ms and 2.5ms, leading to the less rate of change of the simulated current than experimentally observed. The higher current is calculated near 2.5 ms than the measured one due to this lower arc voltage. The situation is reversed after 2.5ms where the modelled arc voltage is greater than experimentally observed, resulting in a more rapid onset of the current zero point in the simulated case. The simulated arc motion is shown in Appendix B. Overall, it can be said that arc modelling gives good prediction of switching current and voltage waveforms. The arcing time and exit arc voltage have a 5.5 % error (simulated value: 3.78 ms, measured value: 4.00 ms) and a 2.1% error (simulated value: 325 V, measured value: 332 V), respectively.

In the simulation with current limitation, the capacitor voltage corresponds to the system voltage in (46). Figure 138 presents the simulated voltage of the capacitor bank from 0.25 ms to the arc extinction. The capacitor voltage is calculated by (54)

$$U_{cap}(t_{n+1}) = U_{cap}(t_n) - \Delta t \frac{I(t_n)}{C} \quad (54)$$

where,  $U_{cap}$  is the voltage of the capacitor bank and  $C$  is the capacitance.

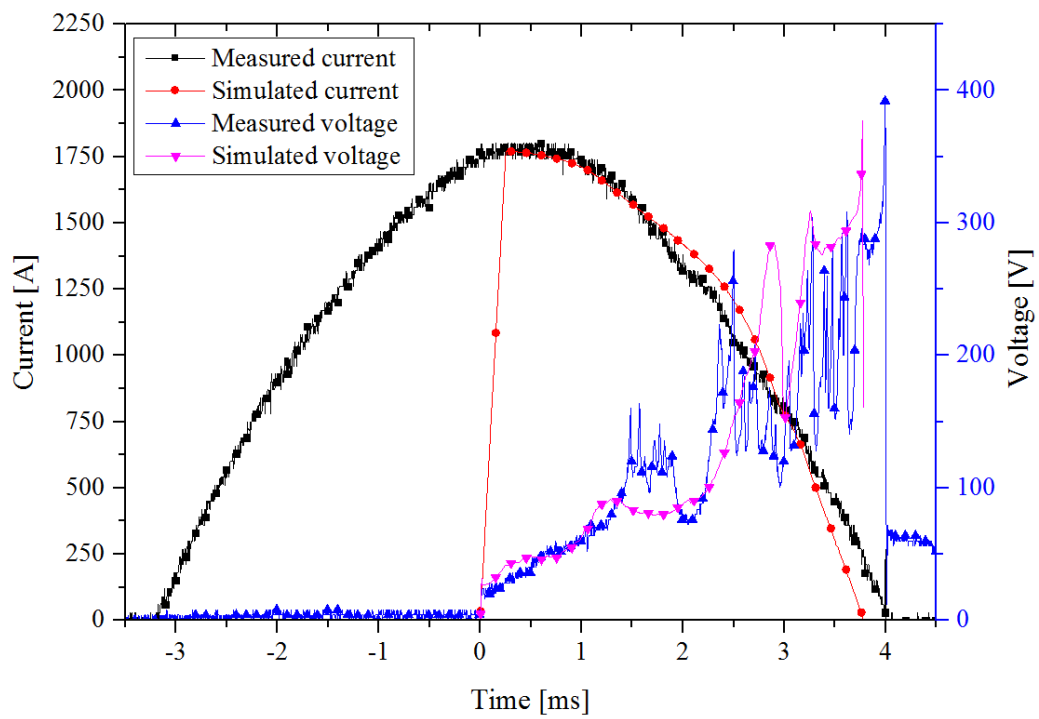


Figure 137 Comparison between experimental data and simulation results with current limitation.

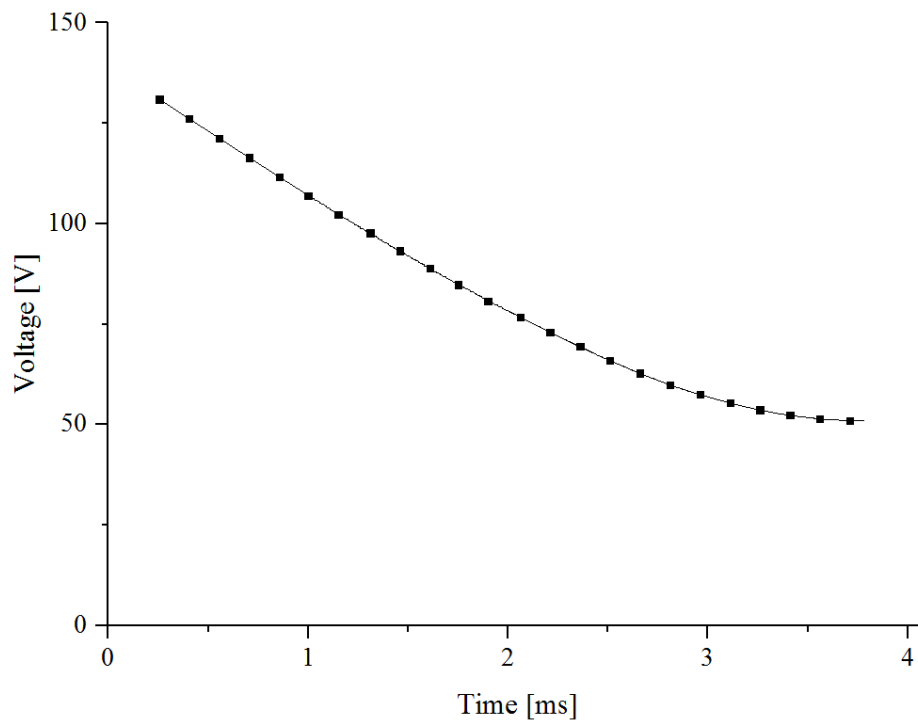


Figure 138 Simulated capacitor voltage.

#### 5.2.4 EFFECT OF VENT DISTRIBUTION ON ARC MOTION

It is observed that the well distributed vent contributes to an increase in arc motion velocity and improvement of switching performance in 4.2.2. In order to investigate the effect of vent distribution on the arc motion thoroughly, we simulate arc motion with different vent distribution and compare the results. The simulation condition is shown in Table 19. The current in Figure 127 is identically applied in the two simulation cases (2 apertures vent and 12 apertures vent model) without consideration of the external circuit. Table 22 shows the test conditions. Only vent distribution is different between two cases and other conditions are the same.

Figure 139 and Figure 140 show arc voltage waveforms and temperature distributions associated with the vent conditions. There is no difference between two cases in the arc motion and voltage waveforms from ignition to 0.5 ms. However, it can be seen that the arc of the 12 apertures model travels faster toward splitter plates from 0.5 ms and this arc enters quicker splitter plates than that of the 2 apertures model. Also, it is observed that there is no arc back motion in the case of 12 apertures. Between 2.45 ms and 2.75 ms, the arc voltage of the 2 apertures model is slightly higher than that of 12 apertures condition, which may be associated with the arc motion in a bottom part (see the A area of Figure 140 (f)). The wider bottom aperture of 2 vent model improves the gas flow in the bottom part of the arc and the bottom part of the arc moves towards splitter plates further than that of 12 apertures model, leading to the higher arc voltage. In general, the arc moves quicker towards splitter plates and the arc voltage is higher in the 12 apertures model when compared to the 2 apertures case.

Table 22 Experiment condition for arc imaging measurement.

Item	Condition description
Vent	- 12 apertures vent (23% open) as shown in Figure 85 (b) - 2 apertures vent (23% open) as shown in Figure 85 (a)
Charging voltage	Same with Table 20
Current	
Filter	

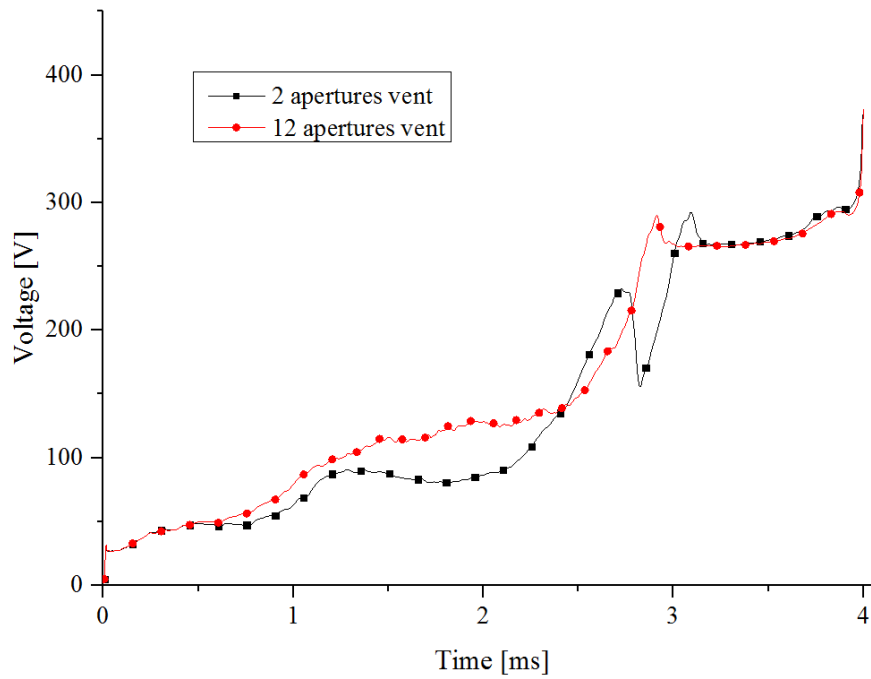
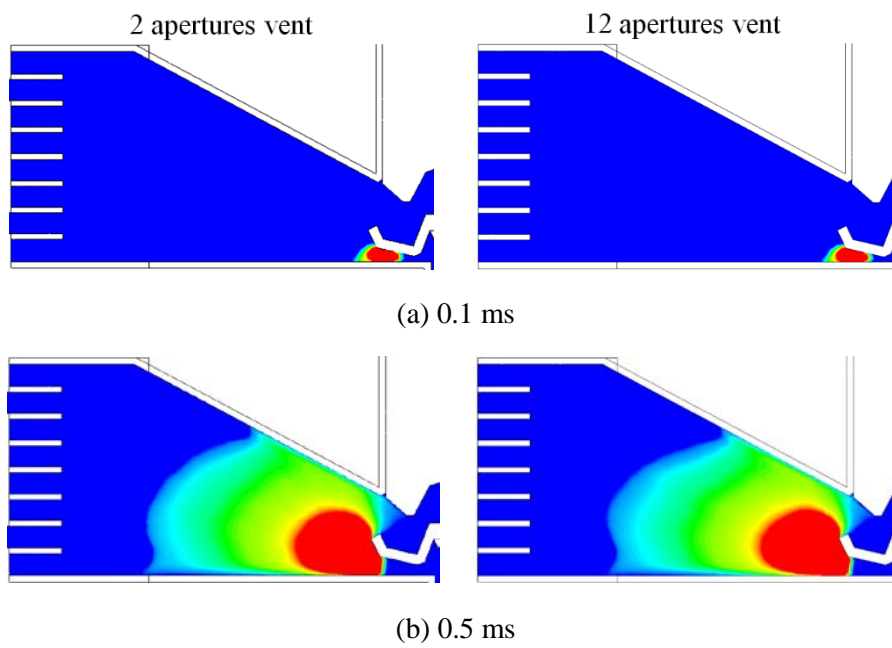
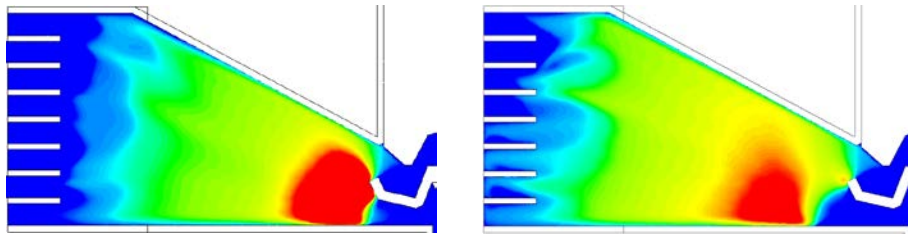
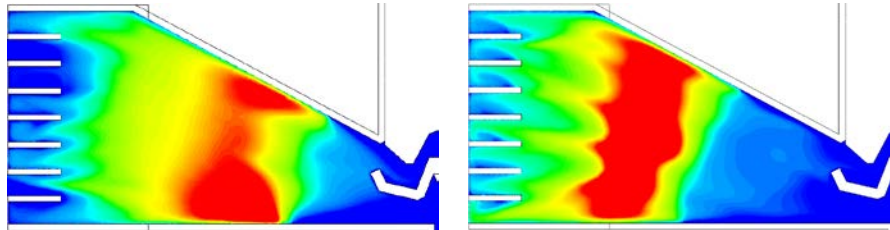


Figure 139 Comparison between simulation results depending on vent distribution; Figure 86 shows the detail vent condition.

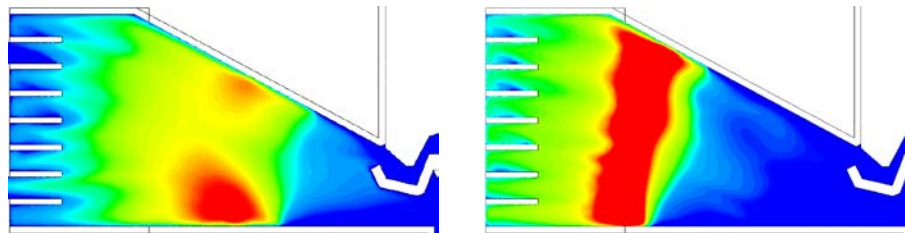




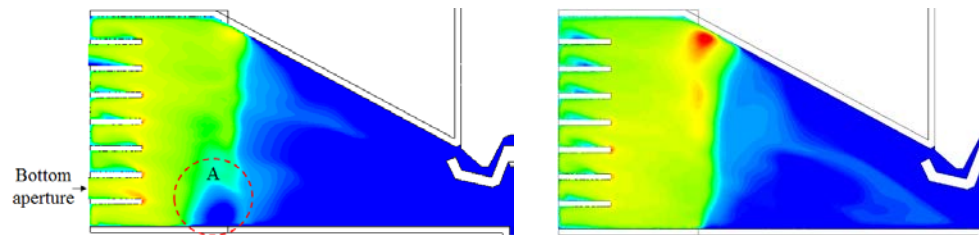
(c) 1.0 ms



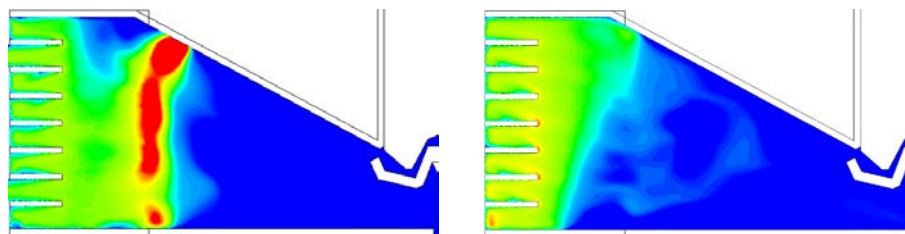
(d) 1.5 ms



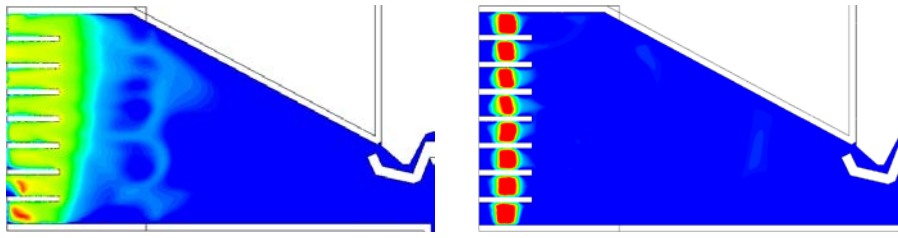
(e) 2.0 ms



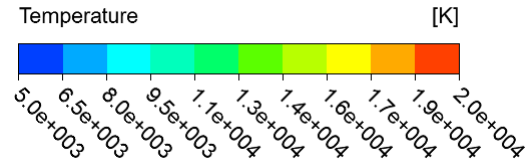
(f) 2.65 ms



(g) 2.8 ms



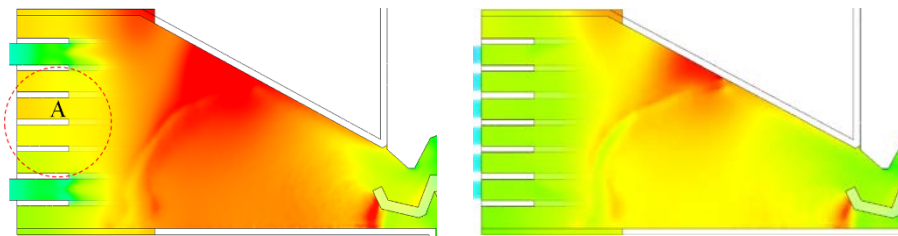
(h) 3.0 ms



(i) Temperature index

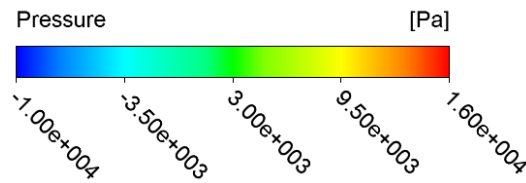
Figure 140 Comparison between simulated temperature distributions in the half model depending on vent distribution; left figures are the results of 2 apertures vent whereas right figures are the data of 12 apertures vent.

Figure 141 shows the relative pressure distributions in both cases at 0.5ms when both arc position and shape are similar. It is seen that there is a significant difference of the pressure distribution in the stack of splitter plates between the 2 apertures and 12 apertures model. The gas does not flow out through the vent in the A area of the 2 apertures (see Figure 141 (a)) and the pressure is relatively high compared to the case of 12 apertures. This blocking effect could be main reason of the difference of arc motion depending on the vent distribution.



(a) 2 apertures vent

(b) 12 apertures vent



(c) Pressure index

Figure 141 Comparison between simulated pressure distributions (volume rendering images) at 0.5 ms depending on vent distribution.

### 5.3 SUMMARY

The switching performance of LVSDs can be predicted by current limitation and the exit arc voltage that is the main parameter of the re-ignition evaluator (voltage ratio). We study the arc model to simulate the effect of current limitation and especially to calculate an accurate exit arc voltage. The model considers the influence of Lorentz force, contact motion and radiation losses. In order to consider the effect of arc root near the current zero, the V-J (voltage and current density) relationship in the arc root is modified based on the measured arc voltage and simulated current density.

We validate the arc model with the experimental data, especially the arc images measured by the AIS. It is observed that simulated arc motion (temperature distribution) has a similar trend with the measured arc images. Further, it is seen that the arc model gives the good prediction of the exit arc voltage and current limitation when compared to the measured data.

## CHAPTER 6: CONCLUSION

### 6.1 SUMMARY OF MAIN FINDINGS AND RESULTS

Nowadays, the present market trend for LVSDs is towards a compact product with high breaking capacity and DC switching devices. In order to produce competitive products meeting market demand with low development cost, it is essential to predict the switching performance, i.e. current limitation and re-ignition, and optimize the product prior to manufacturing real ones.

This research is concerned with prediction and improvement of switching performance of LVSDs. Through an extensive experimental study on the re-ignition phenomena and switching performance, the reliable evaluator for re-ignition and improved vent distribution have been proposed. In addition, numerical arc modelling has been built, based on the conventional MHD theory, which can be used to aid the design of LVSDs. Several conclusions are summarized as follows.

Firstly, an experimental investigation has been carried out regarding re-ignition evaluators that can predict the switching performance of LVSDs prior to empirical laboratory testing of real products. It is found that the voltage ratio (which is defined as the ratio of the recovery voltage to the exit arc voltage) is a reliable evaluator. Instantaneous re-ignition does not occur when the voltage ratio is positive or it lies in the range of 0 to -1.0. It can be used as a ‘strict’ global evaluator to predict re-ignition of the LVSD. Also, there is an experimentally observed ‘soft’ threshold of the voltage ratio at approximately -2.0, which distinguishes most of the successful interruptions from instantaneous re-ignitions. The rare cases of re-ignition when the ratio lies in the range of -1.0 to -2.0 are attributed to the arc attachment at the edges of splitter plates and re-ignition directly through an air gap without the arc root voltage (sheath voltage). Delayed re-ignition cannot be predicted by using either the exit arc voltage or voltage ratio; however, it was diagnosed with the result of failure in the LVSD operating mechanism. It should be the subject of mechanical design improvement, rather than optimisation of electrical arc dynamics.

Secondly, we have measured arc images in the quenching chamber and investigated arc motion in the splitter plates in detail. An array of total 109 optical fibres is placed in the FTA to allow observation of the arc motion in the overall chamber including the splitter plate region. It is found that the arc does not enter the splitter plates directly and it repeatedly moves backwards and forwards in the splitter plates. This arc back-and-forth-motion results in the fluctuation of arc voltage. The arc voltage drops when the arc comes out from the splitter plate; whereas, the arc voltage increases when the arc enters the plate region. Forming new arc roots on the surface of the splitter plate requires a certain



amount of energy to emit electrons from the cathode and to generate ions at the anode. During the arc splitting and root forming process in the plates, the hot gas remains in front of the splitter plates (the region behind the arc after the arc enters the splitter plates) and the conductance of the hot air behind the original arc column can be higher than that of the arc in the splitter plates. This leads to creating a new current path in front of the splitter plates and causes the instability of the arc position in the splitter plate region with the fluctuation of the arc voltage.

Thirdly, the investigation of the effect of vent condition on arc motion and switching performance has been empirically carried out. The vent condition has a significant influence on the arc motion and switching performance. It is observed that the arc moves further and more quickly if there is the larger vent opening area in the quenching chamber. In addition, it is seen that the well distributed vent helps increase the arc motion velocity and improve switching performance. This result is related to the blocking effect of vent apertures. From the simulation study, it is found that the partially choked vent with 2 apertures causes the blocking effect on the gas flow, leading to the arc back motion, whereas there is no arc back motion under the evenly distributed venting condition (12 apertures).

Fourthly, we have calculated the arc temperature from the relative spectrum intensity measured by the spectrometer and investigated the correlation between the temperature and the light intensity measured by the AIS. It is found that the light intensity is strongly related to the arc temperature; the higher temperature is evaluated when the greater light intensity is measured.

Fifthly, 3-D arc modelling has been implemented to predict switching performance (current limitation and re-ignition) of a LVSD. Arc modelling takes into account Lorentz force, plasma properties associated with temperature and pressure, contact motion, radiation loss, arc root voltage, and external circuit condition (current limitation). Especially, the V-J (voltage and current density) relationship in the arc root is modified, based on the measured arc voltage and simulated current density to calculate an accurate exit arc voltage (main parameter of the re-ignition evaluator) near the current zero. It is observed that the simulated results have a similar trend with the experimental data and it is able to predict arc motion, current limitation, exit arc voltage and arc temperature.

The results of this research can help predict and improve the switching performance of a LVSD. Especially, a LVSD designer can evaluate the performance of a particular chamber, modify it and find the improved design, based on the voltage ratio evaluator and arc modelling data.

## 6.2 FUTURE WORK

Arc modelling can be improved by including metal erosion and wall ablation phenomena. The electrodes, splitter plates and side wall can be heated up and vaporized when the arc current is high enough to generate sufficient energy. The vaporized material changes the properties of the original air plasma and has a significant influence on the arc behaviour during the switching process. Therefore, metal erosion and wall ablation phenomena need to be considered especially under a large short-circuit current.

In this research, the arc imaging measurement and modelling investigation have been carried out by using the FTA which is designed as the quenching chamber of the MCB, under the condition of the short-circuit current less than 2 kA. The MCCB and ACB have a more complex chamber structure and much higher breaking capacity than the MCB. This research can be benefitted from extending the experimental work and validation of arc modelling using more various kinds of LVSDs under more severe short-circuit conditions. For example, it is necessary to prove the effect of the vent condition on the arc motion in other types of LVSD. In addition, further validation works of arc modelling is required by using different types of LVSDs.

The calculation of the exit arc voltage has been improved through modifying the V-J curve, based on the experimental results in the case of a 1800 A peak current. However, the V-J curve could vary with the test condition, especially the current value. In the case of a larger current like several tens of kA, the hump region of the V-J curve can be narrower than the modified V-J curve as shown in Figure 130. A larger current makes the arc column and cathode surface hotter; hence less arc voltage is required to sustain the arc near the current zero point. It is necessary to investigate the calculation of the arc voltage near the current zero point, associated with the short-circuit current for the more general calculation of the exit arc voltage (which can be used for various kinds of test conditions).

## REFERENCES

- [1] D. Shin, I. O. Golosnoy, and J. W. McBride, “Numerical analysis of switching performance evaluators in low-voltage switching devices,” in *International Symposium on Electromagnetic Fields*, 2015.
- [2] D. Shin, I. O. Golosnoy, and J. W. McBride, “Arc modelling for switching performance evaluation in low-voltage switching devices,” in *International Conference on Electrical Contacts*, 2016, pp. 41–45.
- [3] J. W. McBride, D. Shin, and T. G. Bull, “A study of the motion of high current arcs in splitter plates using an arc imaging system,” in *International Conference on Electrical Contacts*, 2016, pp. 175–180.
- [4] D. Shin, I. O. Golosnoy, T. G. Bull, and J. W. McBride, “Experimental study on the influence of vent aperture size and distribution on arc motion and interruption in low-voltage switching devices,” in *International Conference on Electric Power Equipment - Switching Technology*, 2017, pp. 213–217.
- [5] D. Shin, I. O. Golosnoy, and J. W. McBride, “A study of arc modelling in low-voltage switching devices,” in *International Conference on the Computation of Electromagnetic Fields*, 2017.
- [6] D. Shin, I. O. Golosnoy, and J. W. McBride, “Experimental study of re-ignition evaluators in low voltage switching devices,” *IEEE Trans. Components Packag. Manuf. Technol.*, vol. PP, no. 99, 2018.
- [7] D. Shin, I. O. Golosnoy, and J. W. McBride, “Development of switching performance evaluator and arc modelling tool for low-voltage switching devices,” *COMPEL-Int. J. Comput. Math. Elect. Electron. Eng.*, 2018.
- [8] B. H. E. Limited, *Handbook of Switchgears*. New York: McGraw-Hill, 2007.
- [9] J. T. E. Browne, *Circuit Interruption Theory and Techniques*. New York: Marcel Dekker, Inc., 1984.
- [10] J. W. McBride, A. Balestrero, L. Ghezzi, G. Tribulato, and K. J. Cross, “Optical fiber imaging for high speed plasma motion diagnostics : Applied to low voltage circuit breakers,” *Rev. Sci. Instrum.*, vol. 81, no. 5, 2010.

- [11] R. Dai, D. Chen, X. Li, C. Niu, and W. Tong, "Study on the influence of different back-volume of arc chambers in the MCCB interruption," in *International Conference on Electrical Contacts*, 2008, pp. 561–565.
- [12] C. Niu, J. Ding, F. Yang, D. Dong, M. Rong, and D. Xu, "The influence of contact space on arc commutation process in air circuit breaker," *Plasma Sci. Technol.*, vol. 18, no. 5, pp. 460–464, 2016.
- [13] Q. Wang, X. Li, D. Chen, S. Member, and M. Rong, "Simulation of the venting configuration effects on arc plasma motion in low-voltage circuit breaker," *IEEE Trans. Plasma Sci.*, vol. 38, no. 9, pp. 2300–2305, 2010.
- [14] *Low-Voltage Switchgear and Controlgear-Part 2: Circuit Breakers, International Electrotechnical Commission, Edition 4.0, IEC Standard 60947-2*. 2006.
- [15] R. D. Garzon, *High voltage circuit breakers Design and Applications*. New York: Marcel Dekker, Inc., 2000.
- [16] HYUNDAI ELECTRIC & ENERGY SYSTEMS, "Low & medium voltage circuit breaker." [Online]. Available: <http://www.hyundai-elec.com/elec/en/biz/bizIndustrial3.jsp>. [Accessed: 01-Mar-2018].
- [17] J.-R. R. Ruiz, A. G. Espinosa, and L. Romeral, "A computer model for teaching the dynamic behavior of ac contactors," *IEEE Trans. Educ.*, vol. 53, no. 2, pp. 248–256, 2010.
- [18] Machine Design, "Engineering essentials: relays and contactors," 2014. [Online]. Available: <http://www.machinedesign.com/motion-control/engineering-essentials-relays-and-contactors>. [Accessed: 10-Feb-2018].
- [19] X. Li and D. Chen, "3-D finite element analysis and experimental investigation of electrodynamic repulsion force in molded case circuit breakers," *IEEE Trans. Components Packag. Technol.*, vol. 28, no. 4, pp. 877–883, 2005.
- [20] P. A. Jeffery, "The motion of short circuit arcs in low-voltage current limiting miniature circuit breakers," PhD thesis, University of Southampton, United Kingdom, 1999.
- [21] P. G. Slade, *Electrical Contacts Principles and Applications*. New York: CRC Press, 2014.
- [22] B. Barbu and F. Berger, "Sheath layer modeling for switching arcs," in *International Conference on Electrical Contacts*, 2014, pp. 575–580.

- [23] Y. Yokomizu, T. Matsumura, Y. Yokomizu, T. Matsumura, L. Sansonnens, J. Haidar, J. J. Lowke, and D. Uhrlandt, "Electrode sheath voltages for helium arcs between non-thermionic electrodes of iron, copper and titanium," *J. Phys. D. Appl. Phys.*, vol. 31, no. 7, pp. 880–883, 1998.
- [24] A. E. Guile, "Arc-electrode phenomena," *Proc. Inst. Electr. Eng.*, vol. 118, no. 9, pp. 1131–1154, 1971.
- [25] A. M. Howatson, *An introduction to gas discharges*, 2nd editio. Oxford: Pergamon Press Ltd., 1976.
- [26] A. Anders, *Cathodic arcs from fractal spots to energetic condensation*. New York: Springer Science+Business Media, 2008.
- [27] R. F. Ammerman, T. Gammon, P. K. Sen, and J. P. Nelson, "DC-arc models and incident-energy calculations," *IEEE Trans. Ind. Appl.*, vol. 46, no. 5, pp. 1810–1819, 2010.
- [28] J. Mentel, M. Ieee, J. Luhmann, and D. Nandelstadt, "Experimental investigation of electrodes for high pressure discharge lamps," in *Industry Applications Conference*, 2000, pp. 3293–3300.
- [29] J. Wendelstorf, "Ab initio modelling of thermal plasma gas discharges (electric arcs)," PhD thesis, TU Carolo-Wilhelmina, Germany, 2000.
- [30] P. G. Slade and E. Schulz-Gulde, "Spectroscopic analysis of high-current free-burning ac arcs between copper contacts in argon and air," *J. Appl. Phys.*, vol. 44, no. 1, pp. 157–162, 1973.
- [31] X. Li, D. Chen, H. Liu, Y. Chen, and Z. Li, "Imaging and spectrum diagnostics of air arc plasma characteristics," *IEEE Trans. Plasma Sci.*, vol. 32, no. 6, pp. 2243–2249, 2004.
- [32] M. Takeuchi and T. Kubono, "A spectroscopic detecting system for measuring the temperature distribution of silver breaking arc using a CCD color camera," *Instrum. Meas. IEEE Trans.*, vol. 48, no. 3, pp. 678–683, 1999.
- [33] B. Pauli, G. Mauthe, E. Ruoss, and G. Ecklin, "Development of a high current HVDC circuit breaker with fast fault clearing capability," *IEEE Trans. Power Deliv.*, vol. 3, no. 4, pp. 2072–2080, 1988.
- [34] J. Slepian, "Extinction of an A-C . Arc," *Trans. Am. Inst. Electr. Eng.*, vol. 47, no. 4, pp. 1398–1407, 1928.

- [35] J. Slepian, "Extinction of a long A-C. arc," *Trans. Am. Inst. Electr. Eng.*, vol. 49, no. 2, pp. 421–430, 1929.
- [36] H. Edels and F. Crawford, "Arc interruption. Part 2: Theory and experiment on gap recovery," *J. Inst. Electr. Eng.*, vol. 3, no. 26, pp. 88–93, 1957.
- [37] G. A. Farrall and J. D. Cobine, "Recovery strength measurements in crcs from atmospheric pressure to vacuum," *IEEE Trans. Power Appar. Syst.*, vol. PAS-86, no. 8, pp. 927–932, 1967.
- [38] J. W. McBride and P. M. Weaver, "Review of arcing phenomena in low voltage current limiting circuitbreakers," *Sci. Meas. Technol. IEE Proc.*, vol. 148, no. 1, pp. 1–7, 2001.
- [39] H. Stammberger, "Force calculations for the movable contact of circuit breakers," in *International Conference on Electrical Contacts*, 1998, pp. 369–374.
- [40] S. Ito, Y. Takato, Y. Kawase, and T. Ota, "Numerical analysis of electromagnetic forces in low voltage AC circuit breakers using 3-D finite element method taking into account eddy currents," *IEEE Trans. Magn.*, vol. 34, no. 5, pp. 5–8, 1998.
- [41] R. Ma, M. Rong, F. Yang, Y. Wu, H. Sun, D. Yuan, H. Wang, and C. Niu, "Investigation on arc behavior during crc motion in air DC circuit breaker," *IEEE Trans. Plasma Sci.*, vol. 41, no. 9, pp. 2551–2560, 2013.
- [42] C. Brdys, J. P. Toumazet, a Laurent, and J. L. Ponthenier, "Optical and magnetic diagnostics of the electric arc dynamics in a low voltage circuit breaker," *Meas. Sci. Technol.*, vol. 13, no. 7, pp. 1146–1153, 2002.
- [43] J. W. McBride and K. . Cross, "Studies of high current arcs using an optical fiber array based imaging system," in *International Conference on Electric Power Equipment - Switching Technology*, 2011, pp. 475–479.
- [44] X. Li, D. Chen, R. Dai, and Y. Geng, "Study of the influence of arc ignition position on arc motion in low-voltage circuit breaker," *IEEE Trans. Plasma Sci.*, vol. 35, no. 2 III, pp. 491–497, 2007.
- [45] P. M. Weaver, K. Pechrach, and J. W. McBride, "The energetics of gas flow and contact erosion during short circuit arcing," *IEEE Trans. Components Packag. Technol.*, vol. 27, no. 1, pp. 51–56, 2004.
- [46] J. W. McBride, K. Pechrach, and P. M. Weaver, "Arc root commutation from moving contacts

- in low voltage devices,” *IEEE Trans. Components Packag. Technol.*, vol. 24, no. 3, pp. 331–336, 2001.
- [47] K. Pechrach, “Arc root commutation from the contact region in low contact velocity circuit breakers,” PhD thesis, University of Southampton, United Kingdom, 2003.
  - [48] J. W. McBride, K. Pechrach, and P. M. Weaver, “Arc motion and gas flow in current limiting circuit breakers operating with a low contact switching velocity,” *IEEE Trans. Components Packag. Technol.*, vol. 25, no. 3, pp. 427–433, 2002.
  - [49] P. M. Weaver and J. W. McBride, “Magnetic and gas dynamic effects on arc motion in miniature circuit breakers,” *IEEE Trans. components, Packag. Manuf. Technol. Part A*, vol. 17, no. I, pp. 39–46, 1994.
  - [50] J. Slepian, “Theory of the Deion Circuit-Breaker,” *Trans. Am. Inst. Electr. Eng.*, vol. 48, pp. 523–527, 1929.
  - [51] K. Nakayama, Y. Yokomizu, T. Matsumura, E. Kanamori, and K. Kuwamura, “Mechanism of voltage rise of high-current arc at atmospheric pressure due to deion plates,” *Electr. Eng. Japan*, vol. 145, no. 3, pp. 17–24, 2003.
  - [52] W. Hauer, “Re – ignition phenomena in low – voltage circuit breakers,” PhD Thesis, Vienna University of Technology, Austria, 2012.
  - [53] D. Chen, R. Dai, and X. Li, “Experimental investigation on the arc motion with different configurations of quenching chamber in AC contactor,” *IEICE Trans. Electron.*, vol. E89–C, no. 8, pp. 1201–1205, 2006.
  - [54] W. Hauer and X. Zhou, “Re-ignition and post arc current phenomena in low voltage circuit breaker,” in *International Conference on Electrical Contacts*, 2014, pp. 398–403.
  - [55] L. Ghezzi and A. Balestrero, “Modeling and simulation of low voltage arcs,” PhD thesis, Technische Universiteit Delft, Netherland, 2010.
  - [56] Y. Enami and M. Sakata, “Simulation of arc in molded-case circuit breaker with metal vapor and moving electrode,” in *Electric Power Equipment - Switching Technology*, 2013.
  - [57] P. Freton and J. J. Gonzalez, “Overview of current research into low-voltage circuit breakers,” *Open Plasma Phys. J.*, vol. 2, pp. 105–119, 2009.

- [58] F. Yang, Y. Wu, M. Rong, H. Sun, A. B. Murphy, Z. Ren, and C. Niu, “Low-voltage circuit breaker arcs—simulation and measurements,” *J. Phys. D. Appl. Phys.*, vol. 46, p. 273001, 2013.
- [59] A. B. Thompson, G. Richardson, P. Dellar, M. McGuinness, and C. Budd, “Arc phenomena in low-voltage current limiting circuit breakers,” Study Group Report, University of Southampton, United Kingdom, 2010.
- [60] J. D. Anderson, *Computational Fluid Dynamics: The Basics with Applications*. New York: McGraw-Hill, 1995.
- [61] A. B. Murphy, “Transport coefficients of air, argon-air, nitrogen-air, and oxygen-air plasmas,” *Plasma Chem. Plasma Process.*, vol. 15, no. 2, pp. 279–307, 1995.
- [62] A. B. Murphy, “Transport coefficients of plasmas in mixtures of nitrogen and hydrogen,” *Chem. Phys.*, vol. 398, pp. 64–72, 2012.
- [63] B. Peyrou, L. Chemartin, P. Lalande, B. G. Chéron, P. Rivière, M.-Y. Perrin, and a Soufiani, “Radiative properties and radiative transfer in high pressure thermal air plasmas,” *J. Phys. D. Appl. Phys.*, vol. 45, p. 455203, 2012.
- [64] J. J. Lowke, “Simple theory of free-burning arcs,” *J. Phys. D Appl. Phys.*, vol. 12, pp. 1873–1886, 1979.
- [65] F. Karetta and M. Lindmayer, “Simulation of the gasdynamics and electromagnetic processes in low voltage switching arc,” *IEEE Trans. Compon. Packaging. Manuf. Technol.*, vol. 21, no. 1, pp. 96–103, 1998.
- [66] M. Lindmayer, E. Marzahn, A. Mutzke, T. Rüther, and M. Springstubbe, “The process of arc splitting between metal plates in low voltage arc chutes,” *IEEE Trans. Components Packag. Technol.*, vol. 29, no. 2, pp. 310–317, 2006.
- [67] M. Rong, F. Yang, Y. Wu, A. B. Murphy, W. Wang, and J. Guo, “Simulation of arc characteristics in miniature circuit breaker,” *IEEE Trans. Plasma Sci.*, vol. 38, no. 9, pp. 2306–2311, 2010.
- [68] A. Mutzke, T. Rüther, M. Lindmayer, and M. Kurrat, “Arc behavior in low-voltage arc chambers,” in *International Conference on Electrical Contacts*, 2008.
- [69] W. Hauer and X. Zhou, “Re-ignition and post arc current phenomena in low voltage circuit



- breaker,” in *International Conference on Electrical Contacts*, 2014, no. 9, pp. 398–403.
- [70] T. Onchi, M. Isozaki, and M. Wada, “Current limiting simulation for low voltage circuit breaker,” in *Proc. IECON*, 2003, pp. 631–636.
  - [71] TaiCaan Technologies, “Arc imager.” [Online]. Available: <http://www.taicaan.com/arc-imager/>. [Accessed: 23-Mar-2018].
  - [72] Farnell, “FDPF 4001 EH - Fiber Optic Cable, Polymer, Simplex, Plastic Optical.” [Online]. Available: [http://uk.farnell.com/fibre-data/fdpf-4001-eh/fibre-polymer-1-core-20m-reel/dp/1208838?st=Polymer Fibre Optic Cable](http://uk.farnell.com/fibre-data/fdpf-4001-eh/fibre-polymer-1-core-20m-reel/dp/1208838?st=Polymer+Fibre+Optic+Cable). [Accessed: 30-Mar-2018].
  - [73] Thorlab, “Neutral Density Filters.” [Online]. Available: [https://www.thorlabs.com/navigation.cfm?guide\\_id=2185](https://www.thorlabs.com/navigation.cfm?guide_id=2185). [Accessed: 30-Mar-2018].
  - [74] Ocean Optics, “Glossary.” [Online]. Available: <https://oceanoptics.com/glossary/>. [Accessed: 22-Nov-2017].
  - [75] Ocean Optics, “OCEAN FX Spectrometers.” [Online]. Available: <https://oceanoptics.com/product/ocean-fx/>. [Accessed: 22-Nov-2017].
  - [76] NIST, “NIST Atomic Spectra Database Lines Data.” [Online]. Available: [https://physics.nist.gov/cgi-bin/ASD/lines1.pl?spectra=Cu+I&limits\\_type=0&low\\_w=400&upp\\_w=600&unit=1&submit=Retrieve+Data&de=0&format=0&line\\_out=3&en\\_unit=1&output=0&bibrefs=1&page\\_size=15&show\\_obs\\_wl=1&show\\_calc\\_wl=1&unc\\_out=1&order\\_out=0&max\\_low\\_enrg=&show\\_av=2&max\\_upp\\_enrg=&tsb\\_value=0&min\\_str=&A\\_out=1&intens\\_out=on&max\\_str=&allowed\\_out=1&forbid\\_out=1&min\\_accu=&min\\_intens=&conf\\_out=on&term\\_out=on&enrg\\_out=on&J\\_out=on](https://physics.nist.gov/cgi-bin/ASD/lines1.pl?spectra=Cu+I&limits_type=0&low_w=400&upp_w=600&unit=1&submit=Retrieve+Data&de=0&format=0&line_out=3&en_unit=1&output=0&bibrefs=1&page_size=15&show_obs_wl=1&show_calc_wl=1&unc_out=1&order_out=0&max_low_enrg=&show_av=2&max_upp_enrg=&tsb_value=0&min_str=&A_out=1&intens_out=on&max_str=&allowed_out=1&forbid_out=1&min_accu=&min_intens=&conf_out=on&term_out=on&enrg_out=on&J_out=on). [Accessed: 10-Feb-2018].
  - [77] Ocean Optics, “Modular Spectrometers.” [Online]. Available: <https://oceanoptics.com/product-category/modular-spectrometers/>. [Accessed: 30-Mar-2018].
  - [78] R. Siegel and J. R. Howell, *Thermal radiation heat transfer*, 3rd editio. Washington: Hemisphere publishing corporation, 1992.
  - [79] Hamamatu, “Si PIN photodiode (S5971).” [Online]. Available: <https://www.hamamatsu.com/jp/en/product/category/3100/4001/4103/S5971/index.html>. [Accessed: 30-Mar-2018].

- [80] G. R. Jones, G. H. Freeman, M. T. C. Fang, G. R. Jones, M. T. C. Fang, C. W. Kimblin, H. Edels, and H. E. Lee, "Transient temperature distributions in cylindrical arc columns following abrupt current changes," *J. Phys. D Appl. Phys.*, vol. 4, pp. 236–245, 1971.
- [81] Q. Ma, M. Rong, Y. Wu, T. Xu, and Z. Sun, "Influence of copper vapor on low-voltage circuit breaker arcs during stationary and moving states," *Plasma Sci. Technol.*, vol. 10, no. 3, pp. 313–318, 2008.
- [82] A. Iturregi, "Modelization and analysis of the electric arc in low voltage," PhD thesis, Universidad del País Vasco Euskal Herriko Unibertsitatea, Spain, 2013.
- [83] Ansys, "CFX Documentation." [Online]. Available: [https://www.sharcnet.ca/Software/Ansys/15.0.7/en-us/help/ai\\_sinfo/cfx\\_intro.html](https://www.sharcnet.ca/Software/Ansys/15.0.7/en-us/help/ai_sinfo/cfx_intro.html). [Accessed: 03-Mar-2018].
- [84] ANSYS, "ANSYS Electronics Desktop." [Online]. Available: <https://www.ansys.com/products/electronics/ansys-electronics-desktop>. [Accessed: 10-Feb-2018].
- [85] K. E. Atkinson, *An introduction to numerical analysis*, 2nd ed. Jhon Wiley & Sons, 1989.
- [86] J. D. Irwin and R. M. Nelms, *Basic engineering circuit analysis*, 11th ed. Jhon Wiley & Sons, 2015.
- [87] C. Rumpler, A. Zacharias, and H. Stammberger, "Low – voltage circuit breaker arc simulation including contact arm motion," in *International Conference on Electrical Contacts*, 2014, pp. 290–294.
- [88] A. Iturregi, B. Barbu, E. Torres, F. Berger, and I. Zamora, "Electric arc in low-voltage circuit breakers : experiments and simulation," *IEEE Trans. Plasma Sci.*, vol. 45, no. 1, pp. 113–120, 2017.

# APPENDIX A: DETAILS OF ARC IMAGING MEASUREMENT

## A1 EXPERIMENT PROCESS

The experimental apparatus for the arc imaging measurement consists of the arc image system (AIS), capacitor discharge system (CDS), flexible test apparatus (FTA), digital storage oscilloscope (DSO), solenoid controller (SC) and computer. Figure 142 illustrates the general arrangement of the experimental apparatus for the arc imaging measurement. After setting the FTA and charging the CDS, a switching test can be conducted by a special program (FLEXGAV4.BAS). After running switching test, we need to discharge the voltage from the CDS and save the test results.

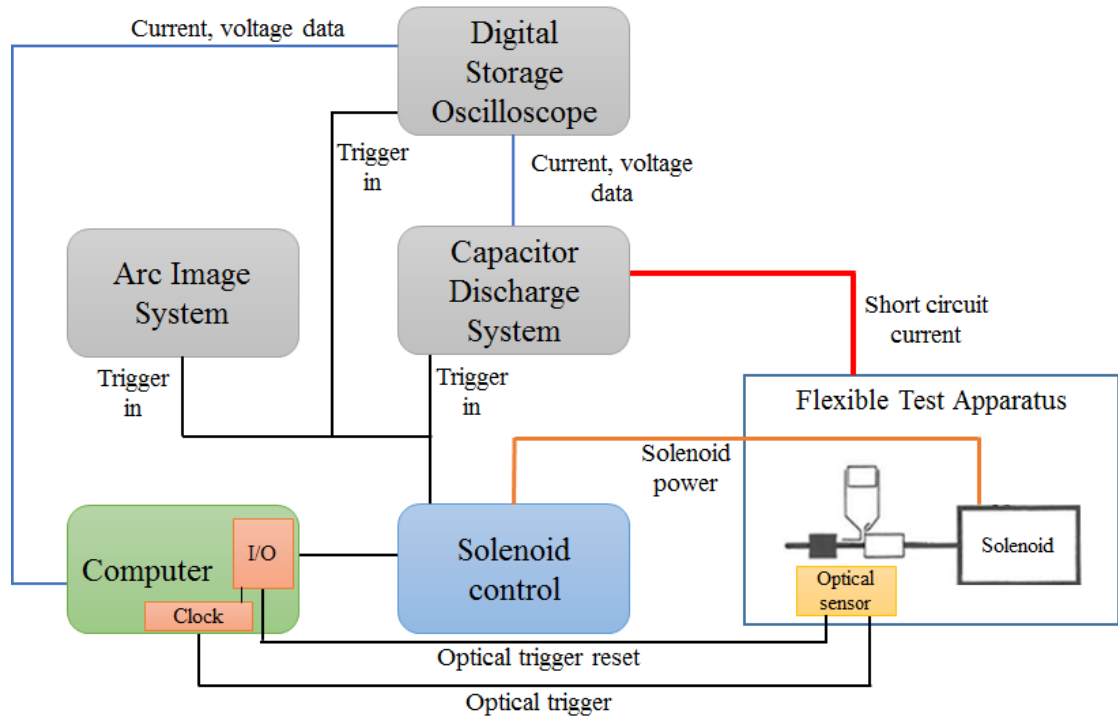


Figure 142 General arrangement of experimental apparatus for arc imaging test [20].

### A1.1 RESETTING FTA

Before running the arc test, we need to reset the FTA. While the shaft latch is lifted up, the solenoid hammer should be placed at the initial position (Figure 143). After then it is necessary to put the safety cover on the FTA in the case of an accident (Figure 144 (a)). The safety switch should be closed by

Figure 1 consists of two photographs. The left photograph shows a wooden frame housing a motor and a safety cover. A yellow warning label 'Electric shock risk' is visible. The right photograph is a close-up of the safety switch mechanism, which is a red button labeled 'Safety switch ON'.

(b) Safety switch

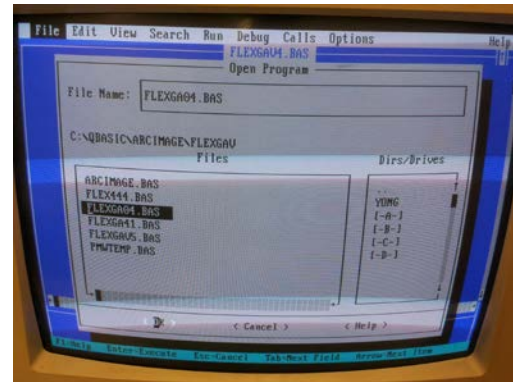
176

## A1.2 STARTING COMPUTER PROGRAM

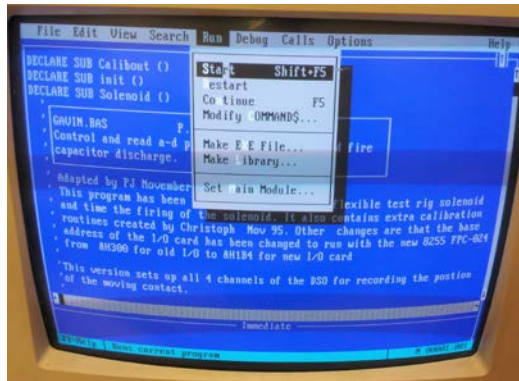
Before charging the CDS, we need to open the computer program. Figure 145 shows the computer program for the arc imaging test. If BLEXGA04.BAS is loaded in the initial state of the program (Figure 145 (b)), the control and data acquisition mode starts (Figure 145 (d)). In this mode, we can adjust the contact opening delay time ( $T_{cod}$ ), run the test and save the arc waveforms. In this research,  $T_{con}$  is set as 500  $\mu$ s.



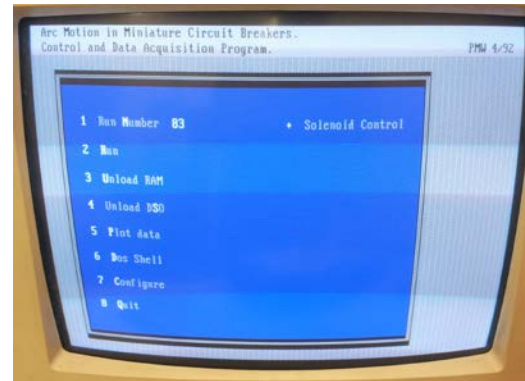
(a) Initial state



(b) Opening (loading) FLEXGA04.BAS



(c) Starting



(d) Control and data acquisition program

Figure 145 The computer program for the arc imaging test.

## A1.3 CHARGING VOLTAGE IN CDS

Figure 146 shows the front panel of the CDS. First of all, the switch 1, 2 and 3 should be turned on in order to charge the voltage in the CDS. And then, we can adjust the charging voltage by rotating dial after pushing the ON button (Figure 147 (a), (b)). The set voltage will be charged in the CDS

when we push the charging button (Figure 147 (c)), and the ready indicator will be turned on if the voltage charging is completed (Figure 147 (d)).

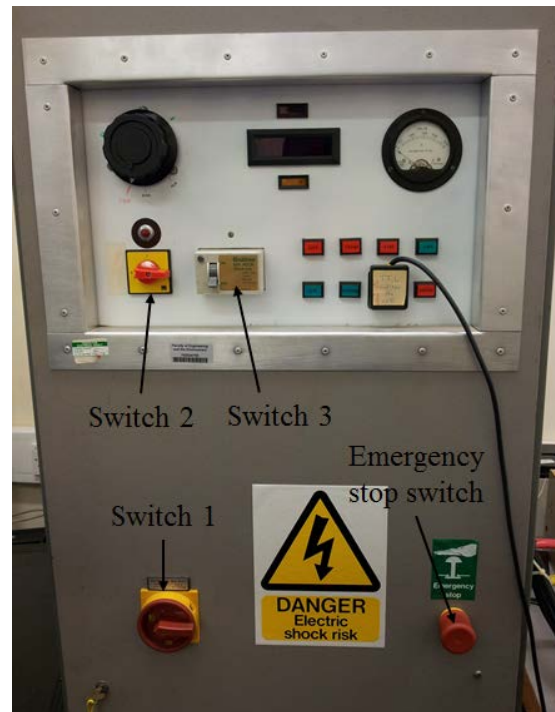


Figure 146 The front panel of the CDS.



(a) Pushing ON button



(b) Rotating the dial for setting voltage





(c) Pushing charging button



(d) Ready state

Figure 147 Procedure for voltage charging.

#### *A1.4 SETTING AIS FOR TRIGGER SIGNAL*

In order to measure the arc images by the AIS, the trigger waiting mode should be ready before running test. We can switch from the normal mode to the trigger waiting mode by clicking the button (Figure 148).

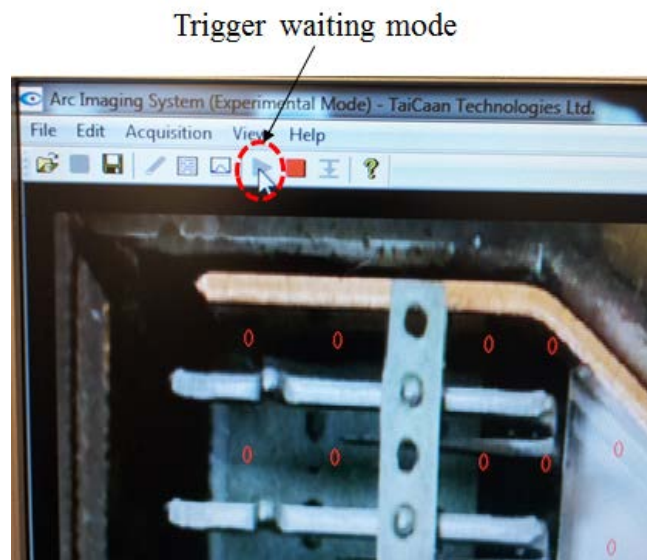
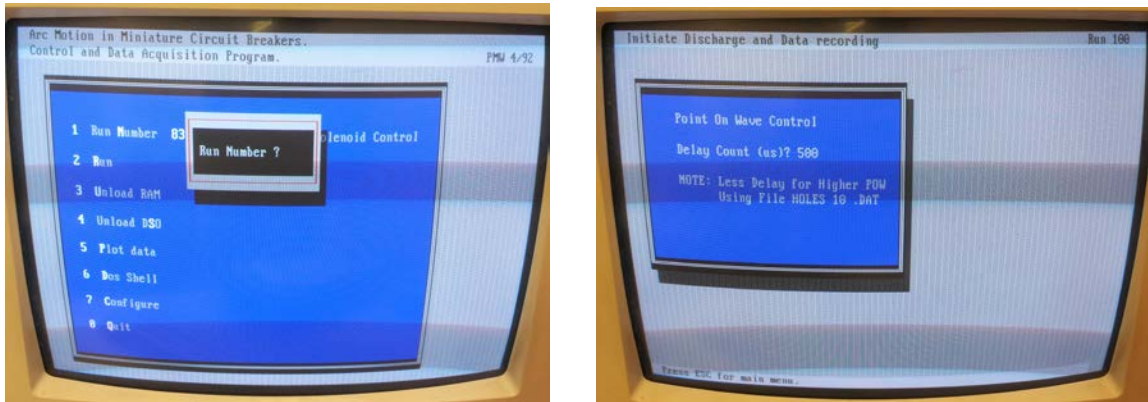


Figure 148 Clicking the button for the trigger waiting mode.

### A1.5 RUNNING TEST

Figure 149 shows how to set the test run number and contact delay time (500  $\mu$ s in these tests). The run number will be a name of the DSO file. The contact delay time means the period of time between the starting point of current and the moment of contact separation. After entering the contact delay time, we can run the test by pressing the enter button and space bar on a keyboard, sequentially.



(a) Entering the test run number      (b) Entering the contact opening delay time ( $T_{cod}$ )

Figure 149 Setting the test run number and contact opening delay time.

While the switching process runs, the DSO and AIS automatically measure the electrical waveforms and arc images, respectively. Figure 150 is the example of the DSO's waveforms.

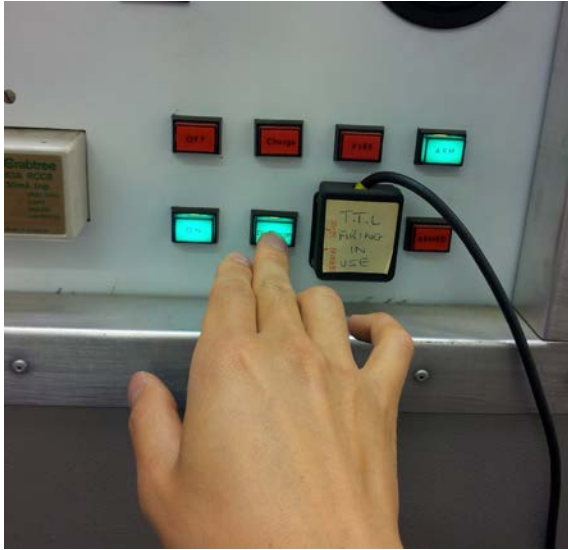


Figure 150 DSO waveforms.



### *A1.6 DISCHARGING VOLTAGE FROM CDS*

After running the test, the residual voltage in the CDS should be discharged for safety. First of all, we need to press the discharge button before touching the FTA or any conductor (Figure 151 (a)). After then, the CDS should be turned off by pushing the off button when the residual voltage is totally discharged (Figure 151 (b)).



(a) Pushing charging button



(b) Ready state

Figure 151 Procedure for discharging the residual voltage.

### *A1.7 SAVING EXPERIMENTAL DATA*

The DSO waveforms and arc image data are downloaded by the computer program and AIS, respectively. We can save the current and arc voltage waveforms by entering a “4” or “S” character on a keyboard (Figure 152). In terms of the arc image data, the optical fibre data can be downloaded by sequentially clicking the download and saving buttons as shown in Figure 153.

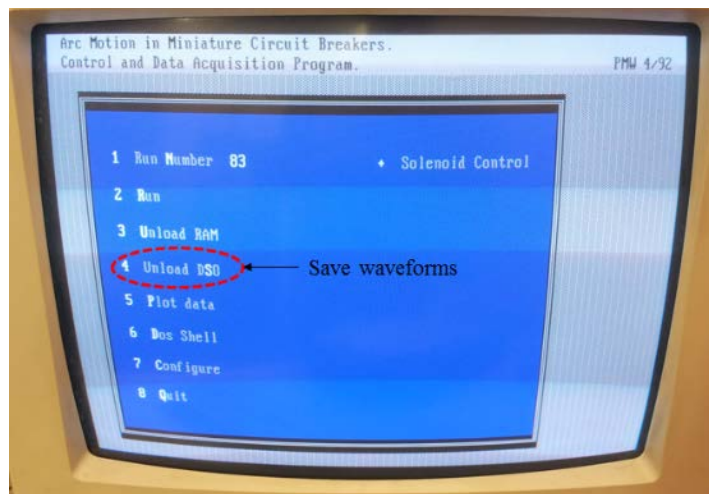
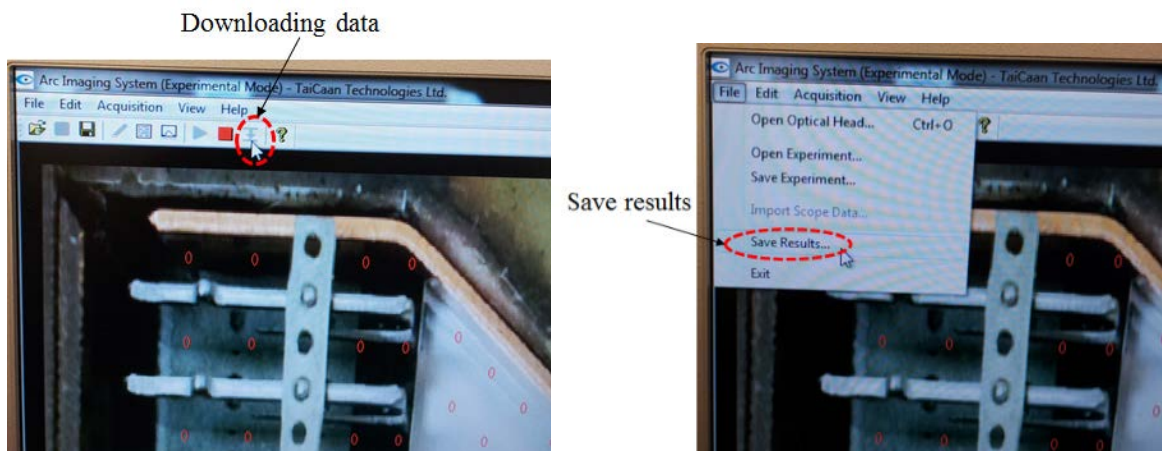


Figure 152 Saving DSO waveforms.



(a) Clicking the download button

(b) Clicking the button of save results

Figure 153 Saving the arc image data.

## A2 PREPARATIONS FOR FTA

There are some precautions to build up the flexible test apparatus (FTA) in order to measure arc images properly; those are about a stack of splitter plates and windows for optical fibres.

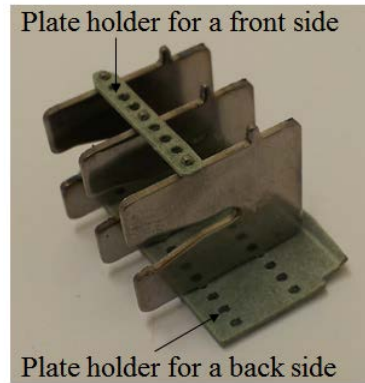
### A2.1 SPLITTER PLATES

The stack of iron plates has been made from the splitter plates of the commercial products (the Polestar MCB made by Crabtree Electrical Industries Ltd). Figure 154 shows the plate's stack which

has 3 iron plates. There are two kinds of plate holders which can support the splitter plates; one is a wide holder for a back side and the other is a narrow one for a front side (where the arc images are measured).



(a) An iron plate



(b) A stack of 3 splitter plates

Figure 154 An iron plate stack.

Figure 155 illustrates how to install the stack of splitter plates in the FTA. Two stack holders prevents the plate stack from moving and being disordered during the interruption operation.

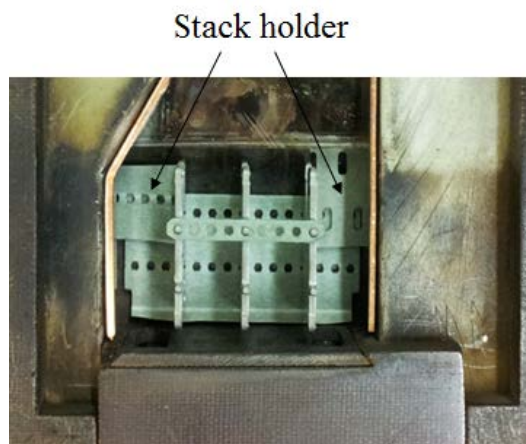


Figure 155 Installation of a stack of splitter plates.

## A2.2 FILTER AND GLASSES FOR OPTICAL FIBRES

There are 3 kinds of windows between the optical fibres and the arc plasma; a filter, outer glass and inner glass.

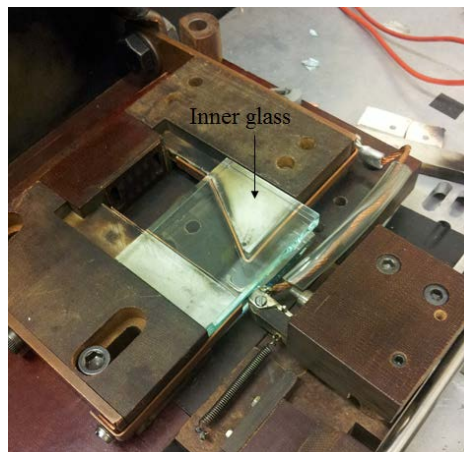
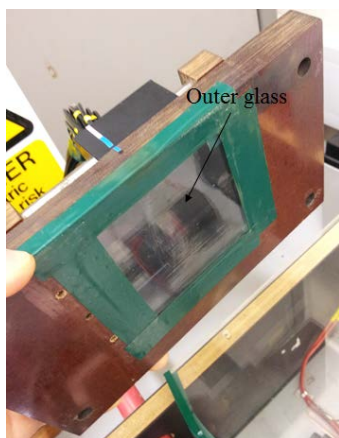
During a switching event, the arc is so bright that the light intensity measured by the fibres are easily saturated to highest value. In order to decrease the arc's brightness and avoid the saturated situation, the natural density (ND8) filter is placed in front of the fibre array block (Figure 1567).

The outer glass is put in front of the filter and it is fixed by an insulating tape (Figure 157 (a)). This outer glass made from quartz protects the filter and fibre array block from the thermal damage by the arc.

A pair of inner glasses is placed in both sides of the quenching chamber (Figure 157 (b)). It can be made from toughened or quartz glass.



Figure 156 Filter between a fibre array block and outer glass.



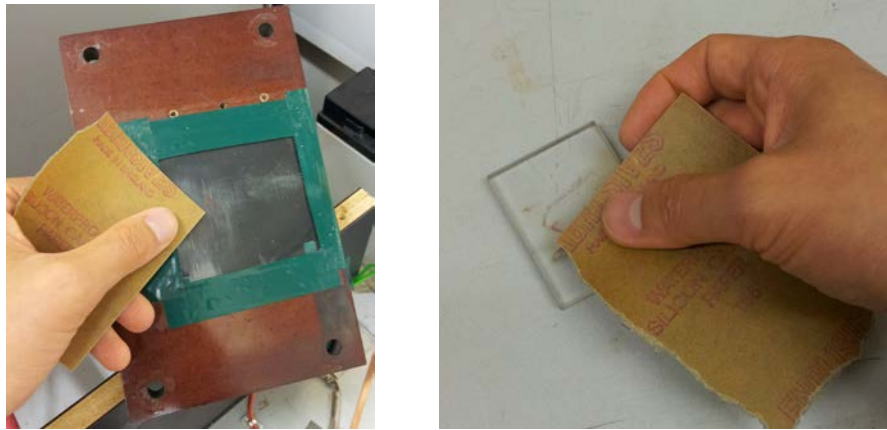
(a) An outer glass (quartz glass) (b) A pair of inner glasses (toughened or quartz glass)

Figure 157 Outer and inner glasses.

### A3 REARRANGEMENT OF FTA AFTER SWITCHING TEST

#### A3.1 CLEANING WINDOW GLASSES

The arc produces some soot in the outer and inner glasses. This soot can block the arc's light and the optical fibres cannot properly measure the arc images. Therefore, it is necessary to clean up soot after every switching test. We used a soft sand paper to clean glasses as shown in Figure 158.



(a) An outer glass

(b) A pair of inner glasses

Figure 158 Cleaning window glasses.

#### A3.2 ADJUSTING FIXED CONTACT AND ARC RUNNER

The fixed contact or arc runner can be bended by the high temperature of the arc like Figure 159. We need to check their condition after every test. If the fixed contact or arc runner is dislocated after a test, they should be rearranged in the same condition as before a test.

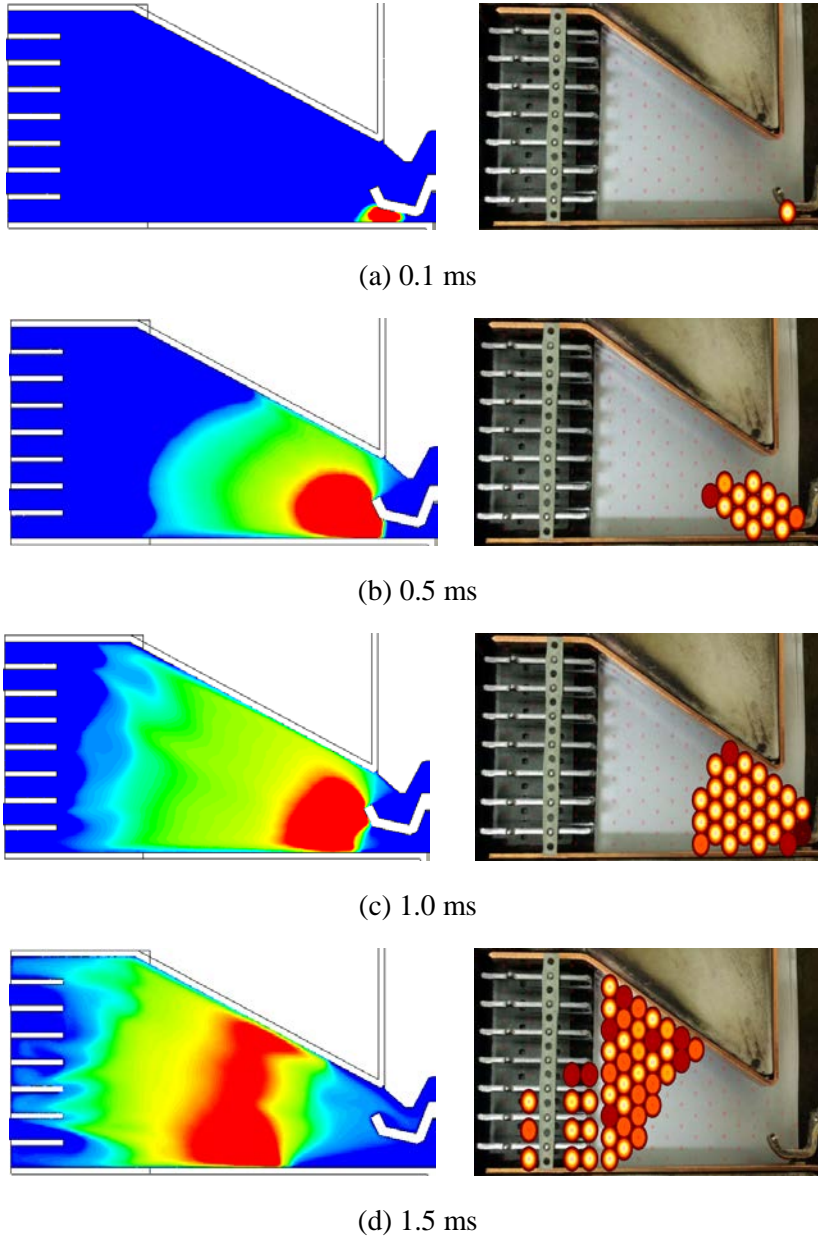


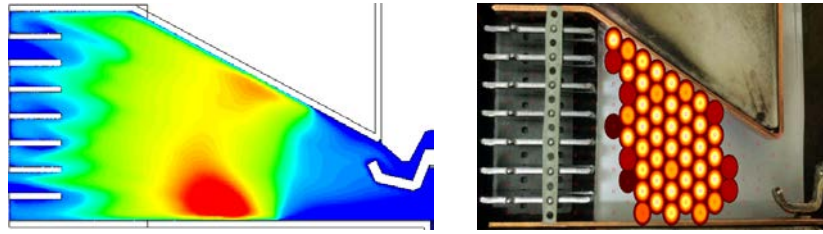
Figure 159 A bended fixed contact.



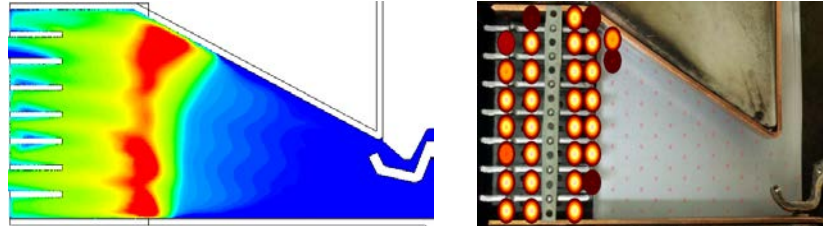
## APPENDIX B: ARC IMAGES WITH CONSIDERATION OF CURRENT LIMITATION

Figure 160 shows the simulated arc temperature distribution with the consideration of current limitation and arc motion (light intensity) recorded by the AIS. These data correspond with the waveforms in Figure 137.

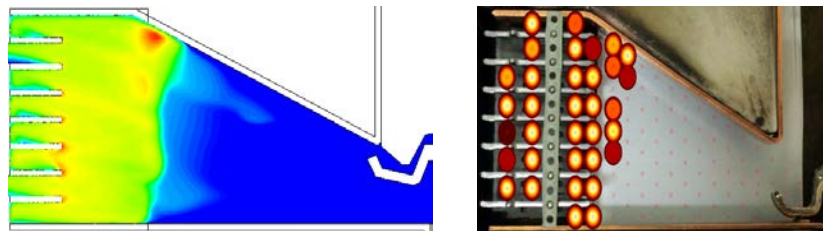




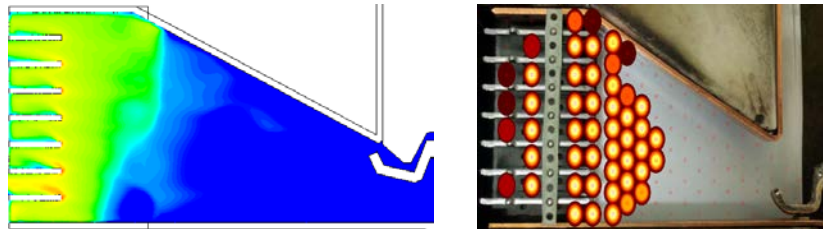
(e) 2.0 ms



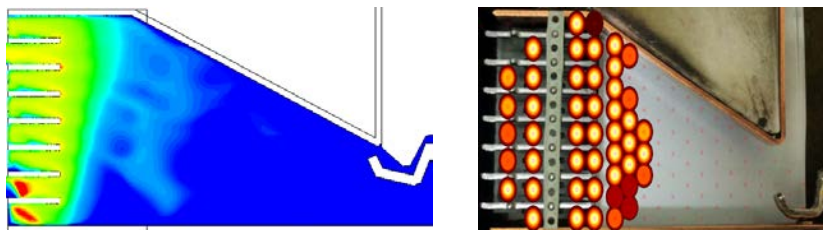
(f) 2.45 ms



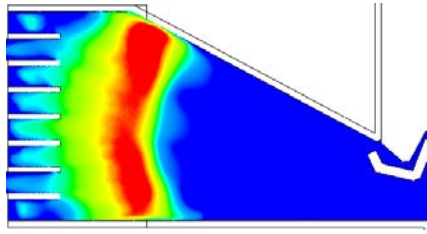
(g) 2.65 ms



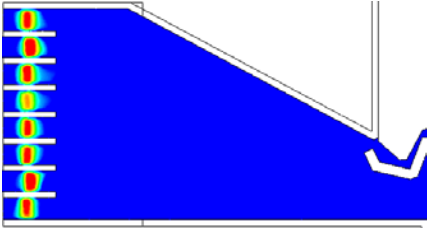
(h) 2.75 ms



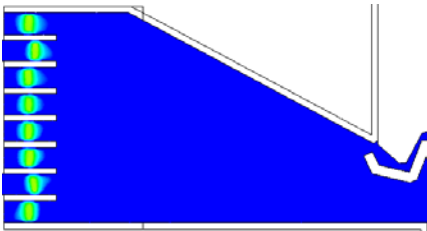
(i) 2.8 ms



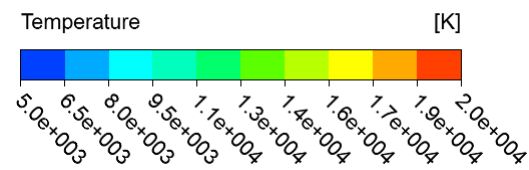
(j) 3.0 ms



(k) 3.5 ms



(l) 3.7 ms



(n) Temperature index

Figure 160 Simulated temperature distribution in the half model (with current limitation) and measured arc image data in the quenching chamber of the FTA; dynamic threshold mode and contour level of [10 %, 13 %, 16 %, 19 %, 22 %, 25 %, 28 %].



## APPENDIX C: PUBLISHED JOURNAL PAPER

1. D. Shin, I. O. Golosnoy, and J. W. McBride, “Experimental study of re-ignition evaluators in low voltage switching devices,” *IEEE Trans. Components Packag. Manuf. Technol.*, vol. PP, no. 99, 2018.
2. D. Shin, I. O. Golosnoy, and J. W. McBride, “Development of switching performance evaluator and arc modelling tool for low-voltage switching devices,” *COMPEL-Int. J. Comput. Math. Elect. Electron. Eng.*, to be published (Accepted).

# Experimental Study of Re-ignition Evaluators in Low Voltage Switching Devices

Dongkyu Shin, Igor O. Golosnoy, and John W. McBride

**Abstract**— The re-ignition of the arc during the interruption process deteriorates the switching performance of low voltage switching devices (LVSDs). Avoiding re-ignition is thus a key goal in the effective design of the quenching chamber. A reliable evaluator of re-ignition provides the opportunity to predict the switching performance of a LVSD during the design process and to refine the product prior to manufacture and empirical device testing. In this paper, re-ignition evaluators are investigated through the analysis of interruption test data for several types of LVSDs under the single-phase and three-phase circuit conditions. It is observed that the ratio of the recovery voltage to exit arc voltage, where exit arc voltage is defined as the value of the arc voltage immediately prior to the current zero point, is a reliable evaluator for the prediction of re-ignition in the switching tests of LVSDs. It is also noted that there are no occurrences of instantaneous re-ignition where this voltage ratio lies in the range of 1.0 to -1.0 and there is a threshold of the voltage ratio at approximately -2.0, which can distinguish the successful interruption and instantaneous re-ignition.

**Index Terms**—Exit arc voltage, low voltage switching device (LVSD), re-ignition evaluator, switching performance, voltage ratio.

## I. INTRODUCTION

LOW voltage switching devices (LVSDs) are widely utilized in power distribution networks to turn on and off circuits and to protect humans and other connected equipment against overload or short circuit accidents. The quenching chamber of a LVSD is the main volume for switching current and consists of a movable and fixed contact, splitter plate, side plate, magnetic yoke and vent as shown in Fig. 1. When the movable contact separates from the fixed contact, an arc is established in the contact gap which then moves towards the splitter plates by the combination of gas flow and Lorentz forces. After the arc enters the splitter plates, there is an increase in the arc voltage resulting from the multiple anodic and cathodic potential drops associated with the surface interactions with the splitter plates. Ideally, the arc is extinguished at the first current zero moment or sooner in the case of a current limiting device, however the arc can re-ignite after the current zero point.

D. Shin and I. O. Golosnoy are with the School of Electronics and Computer Science, University of Southampton, Southampton, SO17 1BJ, U.K. (e-mail: ds7g14@soton.ac.uk).

J. W. McBride is with the Faculty of Engineering and the Environment, University of Southampton, Southampton, SO17 1BJ, U.K. He is also with University of Southampton Malaysia Campus, Nusajaya, 79200, Johor, Malaysia.

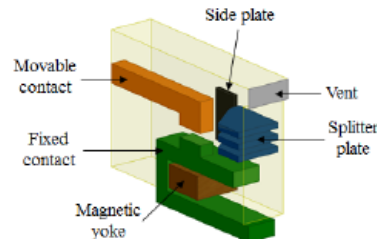


Fig. 1. Half symmetric geometry of a quenching chamber in an LVSD.

The present market trend for LVSDs is towards a more compact product with higher breaking capacity. In order to produce competitive products meeting this demand with low development costs in a short time, it is essential to predict the switching performance of a LVSD and to optimize a product prior to manufacturing a real device. One of the main factors in the deterioration of the switching performance is re-ignition after the first current zero point. Re-ignition in a LVSD interruption refers to the failure of the arc interruption at the first current zero point; hence the current continues its flow after the current zero point. Re-ignition may lead to longer arcing duration, severe contact erosion and side-wall damage of LVSDs during the interruption process. Avoiding re-ignition is therefore crucial when designing a quenching chamber. In practice a reliable evaluator is required to predict the re-ignition phenomena and to evaluate the switching performance of a particular device prior to empirical testing of real products.

It has been suggested that if the breakdown voltage is greater than the recovery voltage (applied voltage across the breaker at zero current point), there will be a successful interruption without re-ignition [1], [2]; however, the problem of determining the breakdown voltage of the arc plasma after the current zero point has not been fully addressed due to the changes at the breakdown characteristics of the gas-plasma mixture by complex recombination and cooling processes in the breakers. Some experimental studies have been undertaken regarding the breakdown voltage after the current zero point and evaluators of re-ignition in LVSDs in order to achieve the improved performance of switching devices. Shea measured the breakdown voltage depending on the vent area of a quenching chamber and reported that increasing the vent area enhances the breakdown voltage after current interruption [3]. Takahashi and Lindmayer compared the breakdown voltage of the double contacts ( $U_{Rd}$ ) with that of the single contact ( $U_{Rs}$ ) and observed that the ratio  $U_{Rd}/U_{Rs}$  is 1.7 – 1.8 for Ag alloy contact material, such as AgNi 90/10, AgCdO 90/10 and

AgSnO<sub>2</sub> 88/12 [4]. Chen *et al.* investigated the recovery characteristics of the breakdown voltage in four different chambers of the magnetic contactor in an attempt to understand the effect of the configuration of the quenching chamber [5]. More complex evaluators have been also suggested. Balestrero *et al.* presented the microscopic evaluators that can forecast re-ignition by obtaining the arc voltage or current through a sensitive current measuring device with a signal processing algorithm, for conditions under 10 kA [6], [7]. There were the current decay rate and the change in electric conductivity of the plasma in the microscopic evaluators, however implementation of these evaluators is not an easy task for a large scale evaluation campaign. Hauer *et al.* introduced the concept of the exit arc voltage, the arc voltage immediately prior to the current zero point, and proposed that the probability of re-ignition after the current zero moment is strongly dependent on the exit arc voltage [8], [9]. It was found that the evaluator of the exit arc voltage is a simple tool, however its reliability has not been rigorously tested. Shin *et al.* proposed an additional evaluator, the ratio of the system voltage to the exit arc voltage at the current zero point, through the switching test results of the miniature circuit breakers (MCBs) and molded case circuit breakers (MCCBs) [10]. Chen *et al.* studied the correlation between the arc motion and re-ignition in magnetic contactors by using optic fiber arc imaging technology and found that the better the arc entry into the splitter plates, the less likely the re-ignition [11].

The exit arc voltage could be the simplest evaluator for the industry engineers to evaluate re-ignition phenomena without the complex calculation of the breakdown voltage; however, it has some limitations regarding the test conditions conducted in previous studies and the accuracy of re-ignition evaluation. The previous experimental investigation was carried out under a single circuit condition using a single type of MCCB [8], [9]; hence the reliability of the exit arc voltage needs to be experimentally proved by various kinds of switching conditions. Also, there is no clear threshold value of the exit arc voltage to predict successful interruption. The objective of the work described in this paper is to investigate a more accurate and reliable evaluator for the prediction of re-ignition based on the switching data of various kinds of test conditions. The proposed evaluator, the voltage ratio, is an extension of the exit arc voltage technique. This paper presents the detailed comparison between the exit arc voltage and voltage ratio as a re-ignition evaluator. Further, it shows a clear threshold of the voltage ratio between the successful and failed interruption, which can aid in a LVSD design.

## II. EXPERIMENTAL METHODS AND WAVEFORM ANALYSIS

### A. Switching Test Circuits and Conditions

The experimental investigation is carried out with 10kA 20kA, 55kA and 100kA test circuits using either MCBs or MCCBs. Figure 2 shows diagrams of the interruption test circuits for single- and three-phase LVSDs. The short-circuit condition is adjusted by a transformer, resistor and reactor. Only R and T phases are utilized for the single-phase tests.

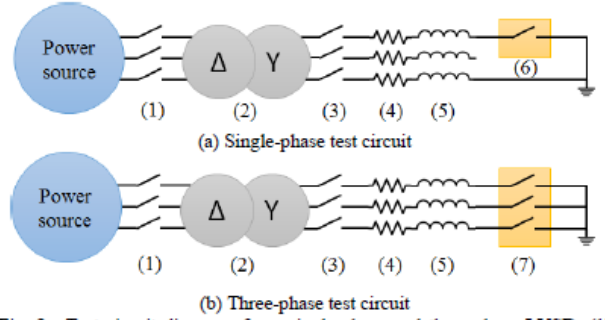


Fig. 2. Test circuit diagrams for a single-phase and three-phase LVSD: (1) back-up circuit breaker, (2) three-phase transformer, (3) making switch, (4) resistor, (5) reactor, (6) single-phase MCB, (7) three-phase MCB or MCCB.

A 13.8 kV commercial power line is used as the power source for the 10 kA and 20 kA switching tests, whereas a short-circuit generator provides the energy for the 55 kA and 100 kA tests. The current and voltage of each phase are recorded by an oscilloscope (10 MHz, Yokogawa DL750), a passive voltage probe (250MHz, Tektronix P5100) and a Rogowski current transducer (16MHz, PEM CWT). No any special filters are used to smooth the waveforms. The observed fluctuations in the waveforms are reflections of a physical phenomenon related to the back and forward motion of the arc at the splitter plates [12].

Table I shows the test condition of each switching case. A total of 110 interruption tests are conducted with previously unused switching devices under five different test circuits. Table II shows the quenching chamber features of the LVSDs used for given switching tests. When the circuit condition is repeated for the tests on the same LVSD type (for example, the switching cases of test number 1 – 26 in Table I), the venting condition varies and some components within the quenching chamber are replaced. This includes changing the geometry of the movable and fixed contact, splitter plate, side plate, magnetic yoke or gassing material. Therefore, there is no identical test condition among 110 switching cases presented in Table I. Testing a variety of circuit conditions and chamber configurations provides the broad switching results for the thorough investigation of re-ignition evaluators.

There are two types of the interruption operation in the switching tests: the open interruption and close-open interruption. The open interruption represents the switching test where short-circuit current starts to flow through a closed LVSD and the contacts automatically open due to short-circuit current. The close-open interruption is the switching test where a LVSD manually operates from the open state to the close state while the system voltage is applied across a device and then the contacts automatically open. The single-phase switching test is conducted through either the open or close-open interruption operation. However, the three-phase test is performed only through the close-open operation in order to obtain an accurate extrapolation of the system voltage at the current zero point. It is difficult to calculate the system voltage at the current zero point by the extrapolation method in a three-phase open interruption test due to distortions observed in the voltage waveforms after switching. The distortions may result from the



TABLE I  
SWITCHING TEST CONDITIONS

Number of phase	Voltage <sup>a</sup>	Prospective current	Power Factor <sup>b</sup>	Kind of LVSDs	Test number <sup>c</sup>
1	252 V	10 kA	0.45 <sup>d</sup>	63AF <sup>e</sup> MCB	1 - 26
3	483 V	10 kA	0.45 <sup>d</sup>		27 - 28
		20 kA	0.3	100AF MCCB	29 - 41
				125AF MCCB	42 - 48
				250AF MCCB	49 - 52
				800AF MCCB	53 - 56
		55 kA	0.2	125AF MCCB	57 - 65
				160AF MCCB	66 - 67
				250AF MCCB	68 - 69
				400AF MCCB	70 - 73
				800AF MCCB	74 - 78
		100 kA	0.2	160AF MCCB	79 - 86
				250AF MCCB	87 - 88
				400AF MCCB	89 - 91
				630AF MCCB	92 - 99
				800AF MCCB	100 - 110

<sup>a</sup> The voltage value refers to the phase voltage in single-phase tests and line-to-line voltage in three-phase tests.

<sup>b</sup> The power factor is selected according to IEC 60947-2 [13].

<sup>c</sup> The test number corresponds to the switching data in Fig. 6 and 7.

<sup>d</sup> According to IEC 60947-2, the power factor is 0.5 when short-circuit current is 10 kA.

<sup>e</sup> Ampere Frame(AF) represents the frame size rating of the LVSD.

step voltage applied to the circuit and associated travelling wave reflection at non-matching impedance points.

## B. Waveform Analysis

### 1) Switching results

There are three possible switching outcomes: 1) a successful interruption without re-ignition, 2) a failed interruption with instantaneous re-ignition or 3) a failed interruption with delayed re-ignition. All interruptions with re-ignition are regarded as failures in this paper. Figure 3 shows the current and voltage waveforms of a successful interruption and two kinds of re-ignition in the switching test of LVSDs. In the successful interruption, the arc is extinguished at the first current zero point without re-ignition (see Fig. 3 (a)). In the case of instantaneous re-ignition, the arc re-ignites and the current continues to flow immediately following the current zero point (see Fig. 3 (b)); however, delayed re-ignition has a pause without current flowing prior to arc re-ignition [8], [9] (see Fig. 3 (c)). It is believed that instantaneous re-ignition is related to a high temperature of the arc plasma, which keeps sufficient electrical conductivity of the residual plasma; whereas, delayed re-ignition relies on the dielectric breakdown which is mainly influenced by the recovery and breakdown

TABLE II  
QUENCHING CHAMBER FEATURES OF LVSDs

Kind of LVSDs <sup>a</sup>	Type of chamber <sup>b</sup>	Quantity of splitter plates	Parameters <sup>c</sup>
63AF MCB	Single	13	- Venting condition - Geometry of movable and fixed contact - Geometry of splitter plate - Geometry of side plate - Geometry and kind of gassing material <sup>d</sup>
100AF MCCB	Single	10	- Venting condition - Geometry of splitter plate - Geometry of gassing material
125AF MCCB	Single	10	- Venting condition - Geometry of splitter plate - Geometry of gassing material
160AF MCCB	Double	16	- Venting condition - Geometry of magnetic yoke - Geometry of gassing material
250AF MCCB	Double	16	- Venting condition - Geometry of magnetic yoke <sup>e</sup> - Geometry of side plate <sup>e</sup>
400AF MCCB	Double	18	- Geometry of splitter plate - Geometry of magnetic yoke
630AF MCCB	Double	18	- Geometry of movable contact - Geometry of splitter plate - Geometry of magnetic yoke
800AF MCCB	Double	18	- Geometry of movable contact - Geometry of splitter plate - Geometry of magnetic yoke

<sup>a</sup> Each kind of LVSDs has a different configuration of the quenching chamber. In general, the quantity of splitter plates is larger and the volume of a quenching chamber is bigger as the ampere frame (AF) becomes higher.

<sup>b</sup> There are two types of quenching chambers in LVSDs: one is a single contact chamber and the other is a double contact chamber.

<sup>c</sup> When the circuit condition is fixed for the tests on the same kind of the LVSD (for example, the switching cases of test number 1 – 26 in Table I), several design parameters (the venting condition and the geometry of a movable contact, fixed contact, splitter plate, side plate, magnetic yoke or gassing material) of the quenching chamber are changed.

<sup>d</sup> The polymer can be placed inside the quenching chamber to improve the switching performance. This polymer is called the gassing material.

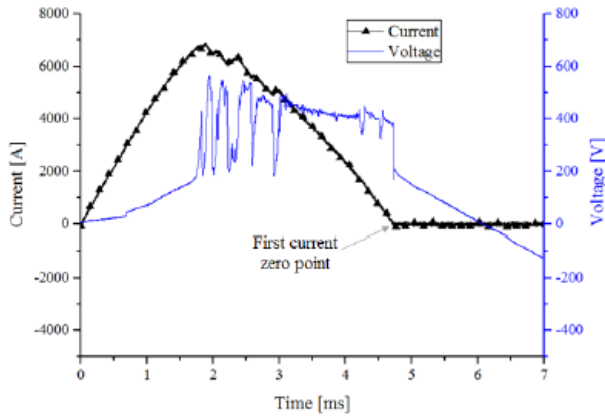
<sup>e</sup> The side plate and magnetic yoke (shown in Fig. 1) influence the magnetic field in the chamber and they help to increase Lorentz force on the arc.

voltage. Often delayed re-ignition is a consequence of the movable contact's back-motion in the quenching chamber of the LVSD.

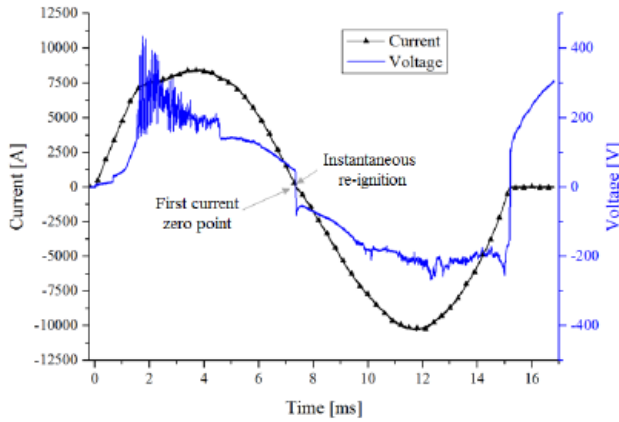
### 2) Exit arc voltage, re-ignition arc voltage and system voltage at the current zero point

To investigate re-ignition evaluators the following parameters are derived from the switching waveforms: the *exit arc voltage*, *re-ignition arc voltage* and *system voltage at the current zero point*. The exit arc voltage is now defined as the value of the arc voltage 20  $\mu$ s prior to the current zero point in either successful or failed interruptions, coinciding with the definition provided by Hauer *et al.* [8], [9]. The re-ignition arc voltage is the value of the arc voltage 20  $\mu$ s after the current zero point only when instantaneous re-ignition occurs. The system voltage at the current zero point is the value of the supplied voltage across a LVSD when the arc is extinguished or re-ignites.

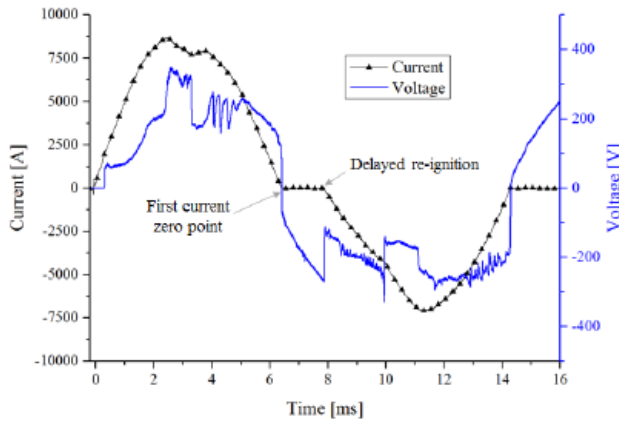
Figure 4 shows typical current and voltage waveforms during a three-phase interruption process of a MCCB where instantaneous re-ignition occurs in the R phase and the arc is



(a) Waveforms of successful interruption: the fluctuations of the arc voltage between 2 ms and 3 ms are related to the back and forward arc motion at the splitter plates [12].



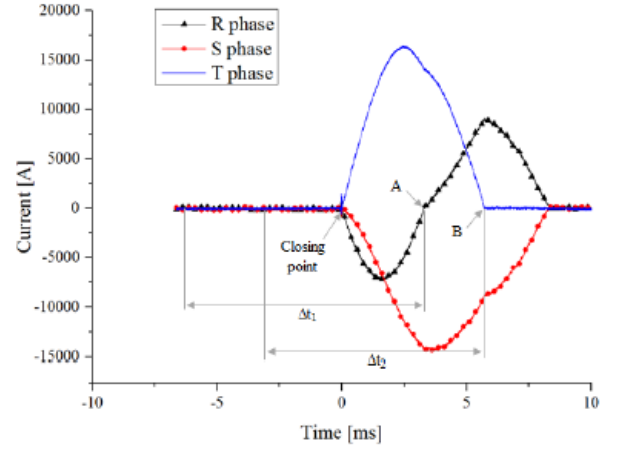
(b) Waveforms of instantaneous re-ignition.



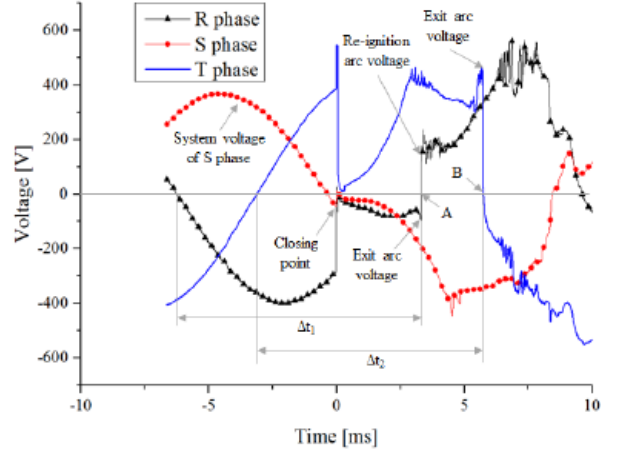
(c) Waveforms of delayed re-ignition.

Fig. 3. Current and voltage waveforms of a successful interruption and two kinds of re-ignition: these are the switching results of single-phase MCCBs under 252 V and 10 kA condition.

first extinguished in the T phase. The moving contacts of the device are manually closed to the fixed contacts at 0 ms and instantaneously begin to separate automatically due to the repulsion force caused by short-circuit current. It is observed that the arc voltage rises as the contact gap increases and, after passing the current zero point (A), the arc polarity reverses to



(a) Current waveforms.



(b) Voltage waveforms.

Fig. 4. Current and voltage waveforms of a three-phase MCCB switching test under 483 V and 20 kA condition: A is the first current zero point in R phase and B is the first current zero point in T phase.

match the current polarity in the R phase. After instantaneous re-ignition, the re-ignition arc voltage is recorded as a relatively high value when compared with the exit arc voltage, and finally the arc current is interrupted at the first current zero point (B) of the T phase. The exit and re-ignition arc voltage are directly measured from the arc voltage waveforms. The system voltages at the current zero points (A and B) are obtained through the extrapolation using the time period from the current zero point to the last zero moment of the system voltage prior to the arc ignition ( $\Delta t_1$  and  $\Delta t_2$ ).

In the case of the open interruption, the system voltage at the current zero point is computed by the extrapolation method based on the first zero point of the system voltage after the arc extinction.

If instantaneous re-ignition occurs, the data of the next current zero event are measured, which is either a successful interruption or delayed re-ignition.

### 3) Voltage ratio

Figure 5 shows the equivalent circuit diagram of the three-phase switching test and the circuit equation of the

R-phase based on Kirchhoff's voltage law can be expressed as [14],

$$U_{sys\_R}(t) = I_R(t)R_R + L_R \frac{dI_R(t)}{dt} + U_{arc\_R}(t) + U_N. \quad (1)$$

We can get (2), (3) and (4) since the three-phase power sources are synchronized.

$$U_{sys\_R}(t) + U_{sys\_S}(t) + U_{sys\_T}(t) = 0. \quad (2)$$

$$I_R(t) + I_S(t) + I_T(t) = 0. \quad (3)$$

$$\frac{dI_R(t)}{dt} + \frac{dI_S(t)}{dt} + \frac{dI_T(t)}{dt} = 0. \quad (4)$$

The voltage at the neutral point in the power source part can be calculated from (5) by using the three circuit equations of each phase and (2) - (4).

$$U_N = -\frac{U_{arc\_R}(t) + U_{arc\_S}(t) + U_{arc\_T}(t)}{3}. \quad (5)$$

It is assumed that the recovery voltage applied across each phase of the LVSD is composed of the system voltage and the neutral point voltage. Since the arc voltage becomes zero at the current zero point, the recovery voltage across the R phase can be written as

$$U_{rec\_R} = U_{sys\_R}(t) + \frac{U_{arc\_S}(t) + U_{arc\_T}(t)}{3}. \quad (6)$$

The voltage ratio is defined as the ratio of the recovery voltage to the exit arc voltage. For the three-phase and single-phase system, the voltage ratio can be formulated as (7) and (8), respectively,

$$Voltage\ ratio = \frac{U_{rec\_j}}{U_{exit\_j}}, \quad (7)$$

$$Voltage\ ratio = \frac{U_{sys}}{U_{exit}}, \quad (8)$$

where  $U_{exit}$  is the exit arc voltage and  $j$  is the index of the phase. In the single-phase test, only the system voltage is assumed as the recovery voltage.

#### 4) Polarity between the recovery voltage and exit arc voltage

When comparing the polarity of the recovery and exit arc voltage, there are two possible cases: the same polarity or opposing polarities. If there is a strong current limiting effect and a high exit arc voltage during the interruption process, the current drops to zero prior to the zero point of the system voltage and the same polarity case is observed.

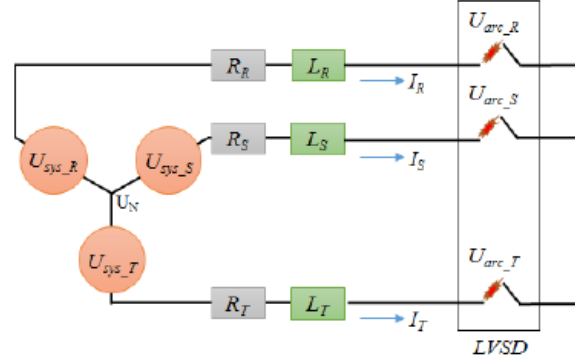


Fig. 5. Equivalent circuit diagram of a three-phase switching test:  $U_{sys}$  is the system voltage,  $I$  is short-circuit current,  $U_{arc}$  is the arc voltage,  $U_N$  is the voltage at the neutral point,  $R$  is the resistance,  $L$  is the inductance and the subscripts (R, S and T) represent each phase of the circuit.

### III. RESULTS AND DISCUSSION

The exit arc voltage, proposed by Hauer [8], [9], is the simplest evaluator to predict instantaneous re-ignition, which is easy to implement in an industrial design scenario; however, this evaluator does not consider the recovery voltage, which is the source of the breakdown (re-ignition) and its limitation in predicting successful interruption is observed in the switching test data (Fig. 6). Firstly, there are some successful interruption cases where the exit arc voltage is too small to forecast the success and therefore a failed interruption is expected according to the exit arc voltage. Secondly, there is no clear threshold to distinguish a successful and failed interruption in the evaluator of the exit arc voltage. To overcome the limitations of the exit arc voltage as a sole evaluator and to predict re-ignition more accurately, the voltage ratio is introduced in this study, as in (7) and (8).

#### A. Exit arc voltage as an Evaluator

Figure 6 presents the full data of the correlation between arc re-ignition occurrence and the absolute value of the exit arc voltage in 10 kA, 20kA, 55 kA and 100 kA switching tests. Since each point corresponds to a different test condition or device design, a large variation in the exit arc voltage is observed as expected. If the exit arc voltage exceeds 400V it is plotted as 400 V. There are 30 successful interruptions with the same polarities between the recovery and exit arc voltage, 74 successful ones with the opposing polarities, 31 instantaneous re-ignition events and 6 delayed re-ignition events in the switching data. In general, the absolute value of the exit arc voltage is low in the case of instantaneous re-ignition whereas a high value is observed in the successful interruption cases. But there are two limitations in the usage of the exit arc voltage as an evaluator for instantaneous re-ignition as presented in Fig. 6. The average value of the exit arc voltage of all instantaneous re-ignition events is 47 V, however two successful cases (A and B) are marked below this average, which is not explained by the evaluator of the exit arc voltage alone. Additionally, there is no clear threshold between successful and failed interruptions. Except A and B points, the minimum exit arc voltage in the



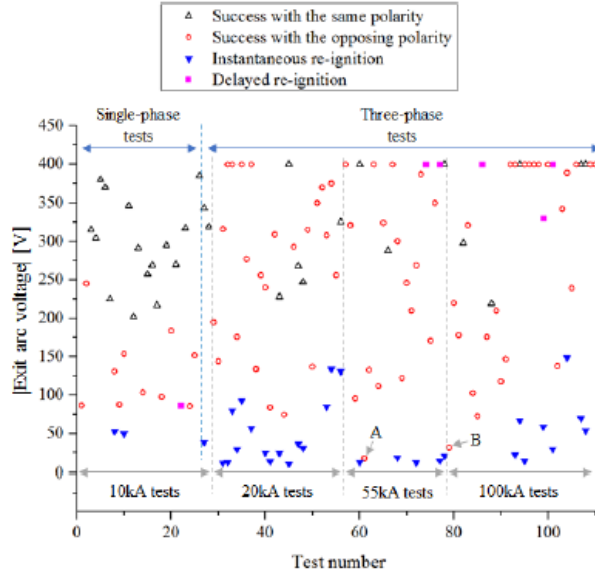


Fig. 6. Re-ignition occurrences depending on the exit arc voltage: the exit arc voltage is plotted as 400 V if it is greater than 400 V.

case of the successful interruption is 73 V, whereas the maximum value in the instantaneous re-ignition case is 149 V. There are 20 successful cases and 6 instantaneous re-ignitions in this overlapping region between 73 V and 149 V, which are not predicted by the exit arc voltage, accurately.

The delayed re-ignition phenomena cannot be predicted by the exit arc voltage. This may be attributed to a fault in the LVSD operating mechanism detected during the post-test examination of the device. As an example of the post-test examination, if the movable contact is not locked by the operating mechanism after opening, it can rebound and the contact gap will reduce, causing a failure.

#### B. Voltage Ratio as an Evaluator

Figure 7 uses the same test data as Fig. 6, but now shows the dependence of the re-ignition occurrence on the voltage ratio defined in (7) and (8). Values below a voltage ratio of -3.0 are plotted as -3.0. Three groups of the voltage ratio are observed: the first (region 1) is the positive ratio (in the case of the same polarity between the exit and system voltage), the second (region 2) is the range of 0 to -2.0 and the third (region 3) is less than -2.0. Omitting the cases of delayed re-ignition, all switching trials are successful in the range of the positive voltage ratio. There are 74 successful interruptions with the opposing polarity and 2 instantaneous re-ignition cases in the second region of 0 to -2.0 voltage ratio. Only instantaneous re-ignition events are seen in the range below -2.0. Particularly, both A and B successful interruptions are predicted by the voltage ratio, which is -0.52 and -1.37, respectively, but not by the exit arc voltage evaluator. Overall, it can be concluded that the voltage ratio is a more detailed and accurate evaluator to forecast the switching performance than the exit arc voltage.

Like the exit arc voltage, the voltage ratio evaluator cannot predict delayed re-ignition that is associated with the failure of the operating mechanism of the LVSD.

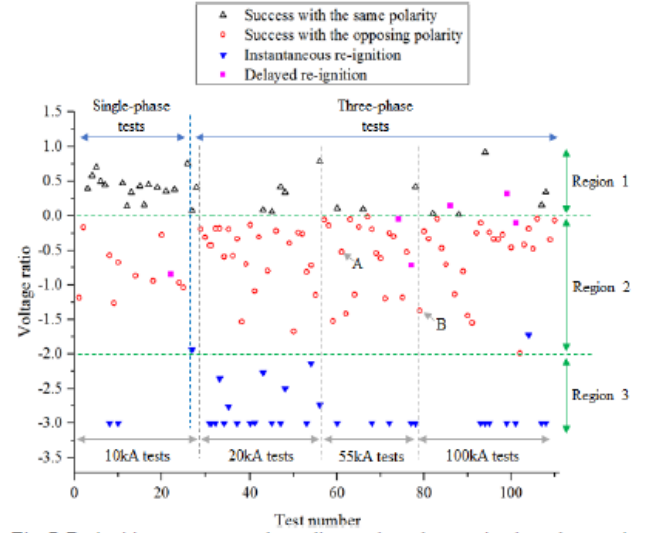


Fig. 7. Re-ignition occurrences depending on the voltage ratio; the voltage ratio is plotted as -3.0 if it is lower than -3.0.

#### C. Discussion

##### 1) The region of the positive voltage ratio

The successful operation with a positive voltage ratio can be explained by the inconsistency of the circuit equation near the current zero point. As the voltage drop across the external resistive load is negligible, the circuit equation near the current zero point in the single-phase test can be expressed as

$$U_{ex}(t) - U_{arc}(t) = L \frac{dI(t)}{dt}. \quad (9)$$

For the three-phase circuit, the voltage between the system voltage and the voltage at the neutral point is required in (9). If instantaneous re-ignition occurs in the range of the positive voltage ratio with the decreasing current where both system voltage and exit arc voltage are initially positive, the value of the left hand side in (9) prior to the current zero moment is negative due to a higher arc voltage compared to the system voltage; but it switches to positive immediately after the current zero moment due to a positive system voltage and the inversion of the arc voltage to negative. However, the value of the right hand side is still negative because the current continues to decrease after the current zero point. It indicates that such situations are not possible and the only solution is an open circuit, i.e. successful interruption.

##### 2) The region of the negative voltage ratio

The situation of the negative voltage ratio can be explained with the aid of the race theory presented by Slepian [1]. Instantaneous re-ignition occurs in the case of the recovery voltage (which is effectively an open circuit voltage across the gap in the device) being higher than the breakdown voltage immediately after the current zero point. As the value of the arc voltage is determined by the power input required to sustain the arc [2], the breakdown voltage should be greater than the arc voltage.

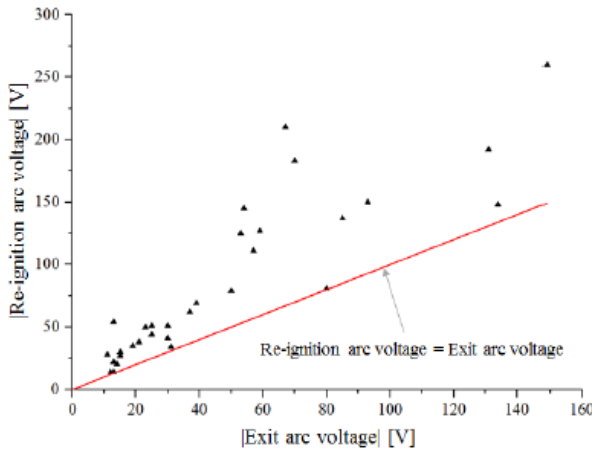


Fig. 8. Relationship between the absolute values of the re-ignition arc voltage and exit arc voltage; the absolute value of the re-ignition arc voltage is higher than that of the exit arc voltage in all cases.

It is observed from Fig. 8 that the absolute value of the re-ignition arc voltage (the arc voltage immediately after the current zero point) is greater than that of the exit arc voltage in all instantaneous re-ignition cases. From this test result, it is apparent that the exit arc voltage has a significant influence on the arc characteristics immediately after the current zero point. Further, Fig. 8 shows that a different test condition leads to very different re-ignition arc voltage which in turn indicates that the exit arc voltage itself is probably not the best evaluator.

It is in agreement with the theory, that there is no instantaneous re-ignition in the range of 0 to -1.0 voltage ratio, i.e. when the breakdown voltage is higher than the recovery voltage (note that the breakdown voltage is always higher than the exit arc voltage due to cooling effects). In practice, the threshold between successful and unsuccessful interruptions is observed at more relaxed conditions, when the voltage ratio of approximately -2.0 (see Fig. 7). There are two possible explanations for the observed threshold. The increase in the breakdown voltage due to plasma cooling and reduction in plasma conductivity is possible; therefore, a higher than the exit arc voltage is needed to support a colder arc. The other explanation can be a switching of cathodic and anodic sheaths over the splitter plate surfaces. This switch takes place just before re-ignition when the sufficient recovery voltage is applied to 1) compensate the voltage drop (which corresponds to the exit arc voltage) in the existing sheaths allowing electrons and ions to move in the opposite direction; 2) to create an additional voltage drop with opposite polarities accelerating electrons and ions for the ions generation at the anodic sheath and the electron emission from the cathode by ions bombardment. The magnitude of this additional voltage is equal to the exit arc voltage if we assume that the latter one is almost all due to the surface sheaths.

There are rare cases when re-ignition occurs at the ratio above -2.0. We believe that these cases correspond to situations when the arc is attached at the edges of some splitter plates prior to the current zero point and the arc re-ignites directly through an air gap skipping the edges. This re-ignition does not

require the sheath switch as the arc is established through the hot gas region in front of the splitter plates without creating an additional voltage drop in the cathode and anode sheath. In this case, the breakdown voltage can be less than 200% of the exit arc voltage, however, always greater than 100% of the exit arc voltage. The modelling can select the LVSD design to push the arc further towards splitter plates and this would allow to consider the relaxed re-ignition criterion, the voltage ratio  $> -2.0$ .

#### IV. CONCLUSION

In this paper, an experimental investigation has been carried out regarding re-ignition evaluators that can predict the switching performance of LVSDs prior to empirical laboratory testing of real products. The following conclusions can be drawn.

- 1) The voltage ratio (which is defined as the ratio of the recovery voltage to the exit arc voltage) is a reliable evaluator and provides more information than the exit arc voltage.
- 2) Instantaneous re-ignition does not occur when the voltage ratio is positive or it lies in the range of 0 to -1.0. It can be used as a 'strict' global evaluator to predict the switching performance of the LVSD. Also, there is an experimentally observed 'soft' threshold of the voltage ratio at approximately -2.0, which distinguishes most of the successful interruptions from instantaneous re-ignitions. The rare cases of re-ignition when the ratio lies in the range of -1.0 to -2.0 are attributed to the arc attachment at the edges of splitter plates and re-ignition directly through an air gap without the sheath voltage.
- 3) Delayed re-ignition cannot be predicted by using either the exit arc voltage or voltage ratio; however, it was diagnosed with the result of failure in the LVSD operating mechanism. It should be the subject of mechanical design improvement, rather than optimization of electrical arc dynamics.

#### REFERENCES

- [1] J. Slepian, "Extinction of an A-C. arc," *Trans. AIEE*, vol. 47, no. 4, pp. 1398-1407, 1928.
- [2] P. G. Slade, *Electrical Contacts Principles and Applications*. New York: CRC Press, 2014, pp. 553-616.
- [3] J. J. Shea, "Dielectric recovery characteristics of a high current arcing gap," *IEEE Trans. Compon. Packag. Technol.*, vol. 25, no. 3, pp. 402-408, Sep. 2002.
- [4] A. Takahashi and M. Lindmayer, "Reignition voltage of arcs on double-break contacts," *IEEE Trans. Compon., Hybrids, Manuf. Technol.*, vol. CHMT-9, no. 1, pp. 35-39, Mar. 1986.
- [5] D. Chen, X. Li and R. Dai, "Measurement of the dielectric recovery strength and reignition of AC contactors," *IEICE Trans. Electron.*, vol. E88-C, no. 8, pp. 1641-1646, Aug. 2005.
- [6] A. Balestrero, L. Ghezzi, M. Popov, and L. van der Sluis, "Current interruption in low-voltage circuit breakers," *IEEE Trans. Power Del.*, vol. 25, no. 1, pp. 206-211, Jan. 2010.
- [7] L. Ghezzi and A. Balestrero, "Modeling and simulation of low voltage arcs," Ph.D. dissertation, Tech. Univ. Delft, Delft, , Netherland, 2010.
- [8] W. Hauer and X. Zhou, "Re-ignition and post arc current phenomena in low voltage circuit breaker," in *Proc. ICEC*, 2014, pp. 398-403.
- [9] W. Hauer, "Re-ignition phenomena in low-voltage circuit breakers," Ph.D. dissertation, Vienna University of Technology, Austria, 2012.



- [10] D. Shin, I. O. Golosnoy, and J. W. McBride, "Arc modelling for switching performance evaluation in low-voltage switching devices," in *Proc. ICEC*, 2016, pp. 41–45.
- [11] D. Chen, R. Dai, and X. Li, "Experimental investigation on the arc motion with different configurations of quenching chamber in AC contactor," *IEICE Trans. Electron.*, vol. E89-C, no. 8, pp. 1201–1205, Aug. 2006.
- [12] J. W. McBride, D. Shin and T. Bull, "A study of the motion of high current arcs in splitter plates using an arc imaging system," in *Proc. ICEC*, 2016, pp. 175–180.
- [13] *Low-Voltage Switchgear and Controlgear-Part 2: Circuit Breakers*, International Electrotechnical Commission, Edition 4.0, IEC Standard 60947-2, 2006.
- [14] T. Onchi, M. Isozaki, and M. Wada, "Current limiting simulation for low voltage circuit breaker," in *Proc. IECON*, 2003, pp. 631–636.



**Dongkyu Shin** received the B.Eng. degree in electrical engineering from Hanyang University, South Korea, in 2004, the M.Eng. degree in electrical engineering from Seoul National University, South Korea, in 2006, and is currently pursuing the Ph.D. degree at the Electronics and Electrical Engineering Research Group, University of Southampton, U.K.



**Igor O. Golosnoy** received his M.Sc. degree in applied mathematics and physics from Moscow Institute of Physics and Technology, Russia in 1992 and the Ph.D. degree in mathematics and physics from the Institute for Mathematical Modelling, Moscow, Russia in 1995. Now he is an associate professor at the Electronics and Electrical Engineering Research Group, Faculty of Physical Sciences & Engineering, University of Southampton. His research interests include numerical modelling of various coupled electrical, thermal and mechanical phenomena in gas discharges and optical emission spectroscopy of plasmas.



**John W. McBride** is the CEO of the University of Southampton–Malaysia Campus, Johor Bahru, Malaysia, and a member of the Electromechanical Research Group with the University of Southampton, Southampton, U.K. Previously he was the Associate Dean of Research with the Faculty of Engineering and the Environment, and the Chair of the Electro-Mechanical Research Group. He is an Expert in electrical contact physics and surface characterization. He has authored over 200 papers, and holds three patents.

# Development of Switching Performance Evaluator and Arc Modelling Tool for Low-Voltage Switching Devices

## Abstract

### Purpose

The main objective of this study is to investigate a reliable evaluator of arc re-ignition and to develop a numerical tool for accurate prediction of arc behaviour of low-voltage switching devices (LVSDs) prior to empirical laboratory testing of real products.

### Design/methodology/approach

Two types of interruption tests have been carried out in the investigation of re-ignition evaluators. Arc modelling tool coupled with the load circuit has been developed to predict arc characteristics based on conventional magnetohydrodynamics theory, with special attention given to Lorentz force acting on the arc column and surface phenomena on the splitter plate. The model assumptions have been validated by experimental observation of arc motion and current and voltage waveforms.

### Findings

It is found that the exit-voltage across the switching device and the ratio of system to exit-voltage at the current zero point are reliable evaluators for prediction of re-ignition. Where the voltage ratio is positive, instantaneous re-ignition does not occur. Further, the probability of re-ignition is very low if the voltage ratio is in the range of -1.3 to 0.

### Originality/value

It is observed that the voltage ratio can be considered as a reliable global evaluator of re-ignition, which can be used for various types of LVSD test conditions. In addition, it is shown that arc modelling allows a good prediction of the current and voltage waveforms, arc motion as well as the exit-voltage, which can be used to obtain the evaluator of re-ignition.

## 1. Introduction

Low-voltage switching devices (LVSDs) are essential to turn on and off electric current and to protect humans and other connected equipment against overload or short circuit accidents in the power distribution network. A quenching chamber of an LVSD is the main volume for switching current and it consists of a movable and fixed contact, magnetic yoke, arc runner, vent and splitter plates (see Figure 1). When the movable contact separates from the fixed contact, an arc is established between the contacts and it moves towards the splitter plates by gas flow and Lorentz force. Concurrently, there is a dramatic increase in the arc voltage due to the multiple anodic and cathodic potential drops in surfaces of the plates. Ideally, the arc is extinguished at the first current zero moment, however the arc can re-ignite beyond this point. During this breaking process, the arc parameters have a great influence on interruption performance of the LVSD (Freton and Gonzalez, 2009).

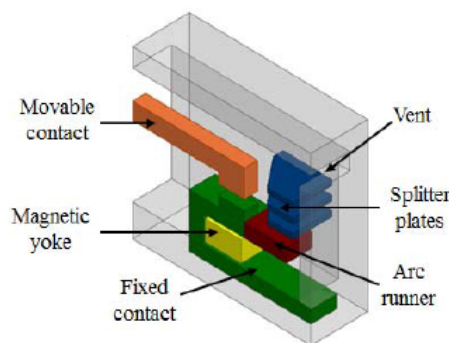


Figure 1. Half symmetric schematic structure of a quenching chamber in an LVSD.

There has been several reports on correlations between the experimentally observed behaviour of the arc and predicted performance of LVSDs. McBride *et al.* carried out experimental studies of the influence of contact opening velocity and material, wall material and venting condition on the arc motion in a miniature circuit breaker using a fibre optic imaging system, pressure gauges and spectrograph (McBride *et al.*, 2002). Balestrero

*et al.* introduced several ‘microscopic evaluators’ that can predict re-ignition by measuring the current or arc voltage over a 10  $\mu$ s time period near the current zero event, when ion recombination and non-equilibrium phenomena dominate (Balestrero *et al.*, 2010). Hauer *et al.* found that the probability of re-ignition after the current zero event is heavily dependent on the ‘exit-voltage’ (the arc voltage immediately prior to the current zero event) and Shin *et al.* backed Hauer’s findings by showing the test results of different types of LVSDs (Hauer and Zhou, 2014, Shin *et al.*, 2015, 2016).

Arcs are nonlinear phenomena and their characteristics are strongly dependent on the dimensions, temperature, pressure and attachment points of the arc. For the reliable prediction of the switching performance, the arc behaviour should be accurately simulated. Karetta *et al.* analysed the arc motion with a 3-D magnetohydrodynamics (MHD) model incorporating heat conduction, gas and current flows and magnetic force (Karetta and Lindmayer, 1998). Lindmayer *et al.* extended MHD arc modelling for the arc root formation by introducing the nonlinear relationship between the potential drop and current density in the arc root region of the splitter plates (Lindmayer *et al.*, 2006). Rong and Ma *et al.* conducted numerical analysis on the influence of metal erosion and wall ablation on plasma properties and arc behaviour in an LVSD (Rong *et al.*, 2009, Ma *et al.*, 2009).

Although the technology available for the design and analysis of LVSDs has been notably developed thanks to the previous experimental and numerical studies, there are still limitations in the prediction of the switching performance and optimization of LVSDs. The experimental approach is expensive and time-consuming. Moreover, it is difficult to experimentally obtain internal arc parameters such as current density and temperature that are useful in improving the design. Most previous numerical methods have focused on the behaviour of the arc plasma prior to the current zero moment without evaluating the probability of re-ignition following the current zero moment, even though avoiding re-ignition is a key goal when designing the quenching chamber.

This paper presents a reliable evaluator of switching performance, which can help judge the probability of re-ignition and a numerical tool for accurate prediction of arc behaviour in the LVSDs.

## 2. Experiments on arc re-ignition

It is considered that an interruption trial is successful without re-ignition if the breakdown voltage in the switch is greater than recovery voltage (Slade, 2014, Slepian, 1928); however, the evaluator is required for a re-ignition prediction for designing LVSDs because of the complexity in accurately calculating the breakdown voltage of the arc plasma in an LVSD after the current zero moment. It changes with time and depends on geometry due to complex recombination processes taking place inside the switch. In this paper, the re-ignition evaluator has been obtained prior to the current zero point without complex calculation of the breakdown voltage and it is used as a parameter which can judge the arc phenomena (re-ignition) after the current zero point.

### 2.1 Experimental method and explanation of switching circuit

The experimental investigation was carried out through two types of interruption tests (see Table I). The first is a low power test for a single-pole miniature circuit breaker (MCB) and the second is a high power one for a three-pole moulded case circuit breaker (MCCB). Figure 2 shows test circuits for the interruption tests of single-pole and three-pole LVSDs. The current and voltage waveforms were recorded by an oscilloscope during switching tests. All tests were conducted with a previously unused switching device and every device has a different quenching chamber design (vent size and position, splitter plate’s geometry, *etc.*) or contact opening velocity.

Table I. Two types of interruption tests.

Test sample	Number of pole	Voltage [V]	Prospective current [A]	Power factor	Frequency [Hz]
MCB	1	252 (phase voltage)	10000	0.45	60
MCCB	3	483 (line-to-line voltage)	20000	0.3	60

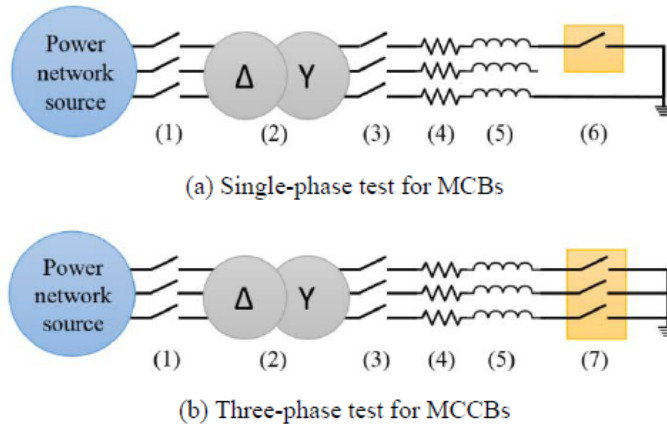


Figure 2. Test circuits for a single-phase and three-phase test: (1) back-up circuit breaker, (2) three-phase transformer, (3) making switch, (4) resistor, (5) reactor, (6) test MCB, (7) test MCCB.

Figure 3 shows the equivalent circuit during the interruption process. During switching operation of the LVSD, the arc current is significantly reduced due to the arc voltage when compared to the prospective current that is determined by the resistance ( $R$ ), reactor ( $L$ ) and system voltage ( $U_s$ ). This current limitation is explained by equation (1). The arc voltage is gradually raised up as the arc moves towards the splitter plates after the ignition between contacts. The arc voltage plays a role as a resistor to prevent the arc from increasing rapidly. Further, when the arc voltage is higher than the system voltage the rate of change of the current ( $dI/dt$ ) becomes negative and it leads to the early current zero point.

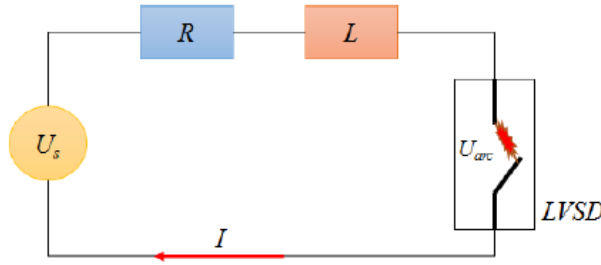


Figure 3. Equivalent circuit during interruption process;  $U_s$  is the system voltage,  $I$  is the current,  $R$  is the resistance,  $L$  is the inductance and  $U_{arc}$  is the arc voltage.

$$U_s(t) = I(t)R + L \frac{dI(t)}{dt} + U_{arc}(t) . \quad (1)$$

## 2.2 Experimental results and discussion

Figure 4 shows the voltage and current waveforms for both a successful and a failed interruption of an MCB. A successful interruption means that the short circuit current is interrupted at the first current zero point, whereas a failed one indicates there is re-ignition after the current zero point. During a successful interruption, the arc voltage waveform is relatively high and remains so up until the current zero point when compared to the voltage waveform of a failed interruption. If the LVSD fails to interrupt the short circuit current at the first current zero moment, a large current continues to flow until at least the next current zero point resulting in severe damage to the device.



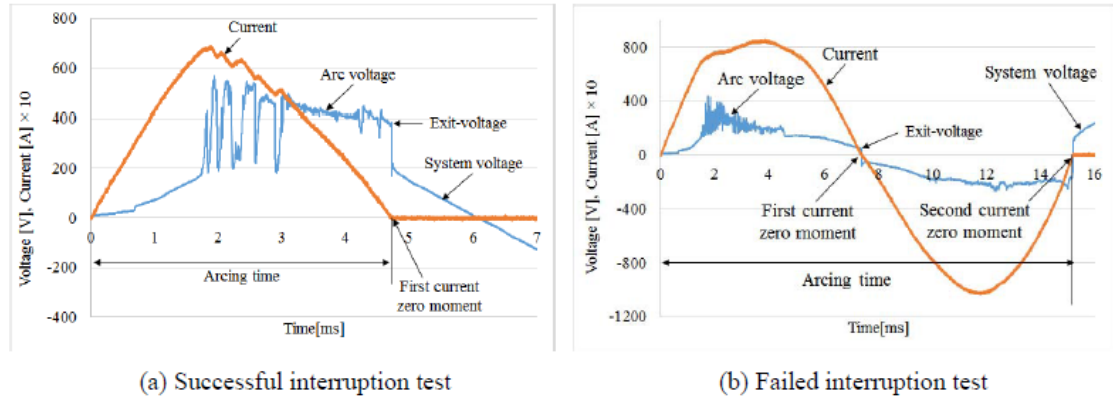


Figure 4. Voltage and current waveforms during interruption operation of MCBs.

Table II shows some switching test results of MCBs. System voltage means the value of system voltage at the current zero moment and re-ignition voltage is the value of arc voltage immediately after the current zero point when re-ignition happens. There are two possible cases of polarity: the exit-voltage and system voltage may have the same polarities (test number 3) or opposing polarities (test number 1, 8 and 22). In addition, re-ignition can be further classified as one of two types [4]: ‘instantaneous’ re-ignition, which occurs immediately after the current zero event causing the short circuit current continues to flow in reverse polarity and ‘delayed’ re-ignition, where there is a pause between the current zero moment and re-ignition (Hauer and Zhou, 2014).

Table II. Some test results of MCBs.

Test number	Exit-voltage [V]	System voltage [V]	Re-ignition Voltage [V] (immediately after the current zero point)	Polarities	Remark
1	87	-103	-	Different	Success
3	315	123	-	Same	Success
8	53	-198	-125	Different	Instantaneous fail
22*	87	-73 (-265 at delayed re-ignition point)	-115	Different	Delayed fail

\*The delayed re-ignition occurs at the moment of 1.49 ms after the first current zero point. Note that the re-ignition voltage (the arc voltage immediately after the current zero point) is different from the exit-voltage due to plasma cooling and expansion.

### 2.2.1 Exit-voltage as a re-ignition evaluator

Figure 5 presents the relationship between occurrence of arc re-ignition and the exit-voltage at the first current zero moment in the MCB and MCCB tests. It can be seen there are different thresholds of the exit-voltage that distinguish successful interruptions from failed interruptions, which are around 80 V for MCB tests and about 133 V for MCCB tests. These test results illustrate that re-ignition is strongly correlated to the exit-voltage but the threshold value varies with the test condition.

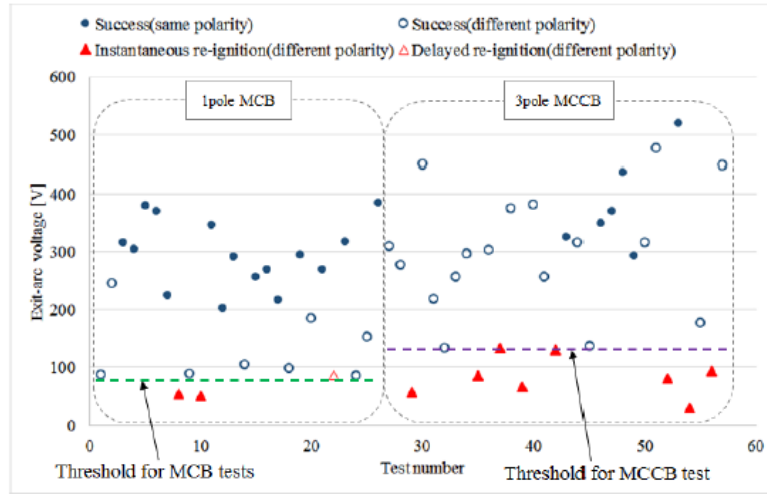


Figure 5. Relationship between interruption performance and exit-arc voltage of MCBs and MCCBs.

### 2.2.2 Voltage ratio as a re-ignition evaluator

In order to investigate a reliable evaluator for predicting re-ignition, the concept of the voltage ratio is introduced. The voltage ratio is calculated from the exit-voltage and the system voltage near the current zero, given in equation (2)

$$\text{Voltage ratio} = U_s(t_0) / U_{exit} \quad (2)$$

where  $t_0$  is the instant of the first current zero,  $U_s$  is the system voltage and  $U_{exit}$  is the exit-voltage.

Figure 6 shows the dependence of interruption performance of MCBs and MCCBs on the voltage ratio at the first current zero moment. It can be seen that the switching trials are always successful in the case of the same polarity (positive voltage ratio). Of the 26 trials where the voltage ratio is in the range of -1.3 to 0, there is only a single delayed re-ignition, not predicted by the exit-voltage or voltage ratio evaluators. This anomaly may be attributed to a fault in the operating mechanism detected during the post-test examination of the device.

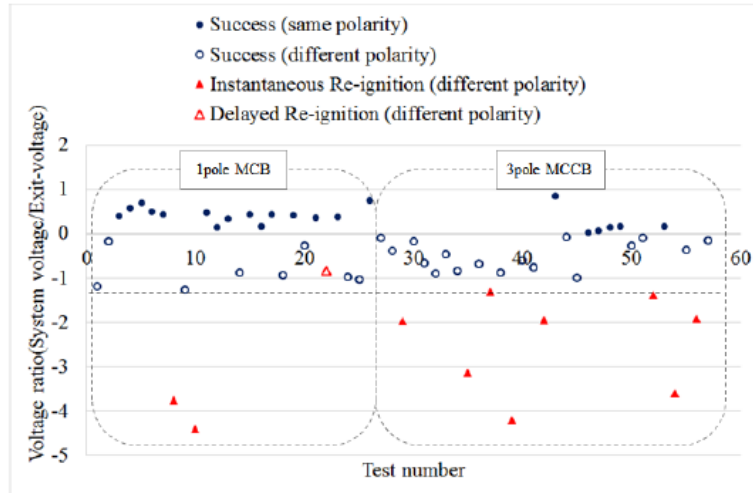


Figure 6. Relationship between the interruption performance and the voltage ratio of MCBs and MCCBs.

It is interesting to note that the interruption test is always successful if the voltage ratio is positive (the exit-voltage has the same polarity as the system voltage). This situation happens only when the arc moves quickly towards the splitter plates and a high arc voltage is generated. This result can be explained by Figure 3 and equation (1). Solving (1) at an instant  $t$  near the current zero point, the voltage drop across the external resistive load, the first term of the right hand side, is negligible and the circuit equation can be written as

$$U_s(t) - U_{arc}(t) = L \frac{dI(t)}{dt} \quad (3)$$

If instantaneous re-ignition can occur in the same polarity case (with decreasing current) where both system voltage and exit-voltage are initially positive, the value of the left hand side in (3) prior to the current zero moment is negative, but switches to positive immediately after the current zero moment due to the inversion of the arc voltage to negative. However, the value of the right hand side is still negative because the current continues to decrease after the current zero moment. It indicates that such situations are not possible and the only solution is an open circuit, i.e. successful interruption.

On the other hand, when the system voltage is negative but the exit-voltage is positive (in the case of different polarity), it may support the negative e.m.f. ( $L \frac{dI(t)}{dt}$ ) and provide a sufficient power for re-ignition to occur. After the current zero point, both the system and arc voltages are negative. In order to support any current flow and negative e.m.f., the absolute value of the system voltage should be higher than that of the re-ignition voltage (arc voltage immediately after the current zero point). Figure 7 fits with this explanation by showing the ratio of the system voltage to the re-ignition voltage when instantaneous re-ignition happens. Furthermore, a linear trend is observed between the absolute values of the re-ignition voltage and exit-voltage (Figure 8), which means that the exit-voltage considerably affects the arc characteristics (re-ignition voltage) after the current zero moment. This is the reason why the voltage ratio can also be a re-ignition evaluator in the case of different polarity and the re-ignition probability is very rare if the voltage ratio lies between around -1.3 and 0.

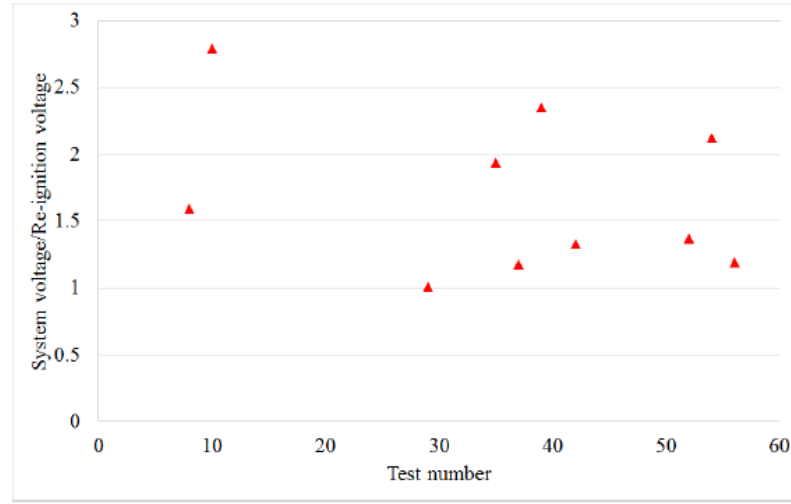


Figure 7. Ratio of the system voltage to re-ignition voltage for non-successful interruption tests.

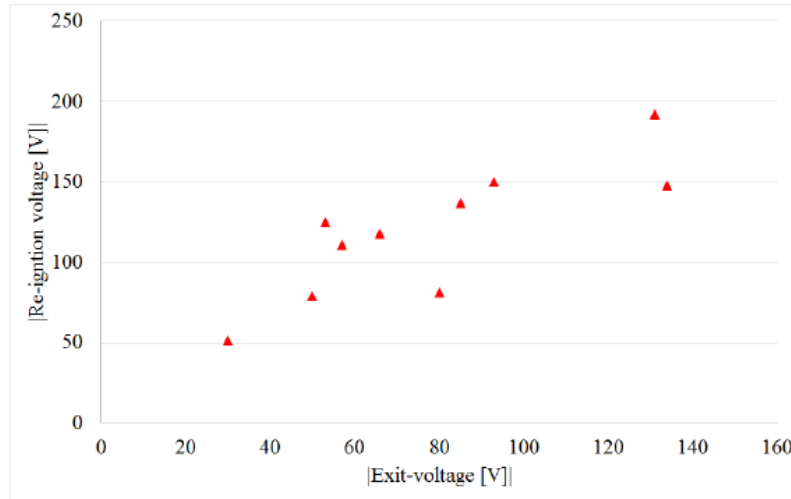


Figure 8. Relationship between the absolute values of the re-ignition voltage and exit-voltage for non-successful interruption tests: re-ignition voltage is higher than exit-voltage due to increased plasma resistance (cooling and expansion effects), and the error median between the absolute values of the re-ignition voltage and exit-voltage is 61.3 %.

### 3. Numerical model and simulation results

Prior to MHD computation of the arc plasma, Lorentz force is calculated by finite element method (FEM) and used as an input parameter (the external magnetic flux density). The effect of the arc root region is modelled using the contact resistance on the surface of the plate. To validate the model, the simulated motion is compared with experimentally measured arc motion by using a high speed optical arc imaging system (AIS) connected to a switching test apparatus described below.

#### 3.1 Arc image measurement for validation of arc model

The flexible test apparatus (FTA) in Figure 9 is designed as the structure of an MCB and it is used to record the arc motion under controlled test conditions (McBride *et al.*, 2002, 2016). There are 109 fibres distributed in the quenching chamber including 32 fibres between the splitter plates, which have 1 MHz sampling rate. The optic fibres are slotted into the holes in the fibre array block. The photosensors of the AIS have a spectral response range from 320 nm to 1060 nm and it enables the tracking of the arc motion through the light intensity and position in the chamber during an interruption operation. A half cycle wave of a short circuit current is provided by a capacitor bank and its magnitude is changed by adjusting a charging voltage of a capacitor.

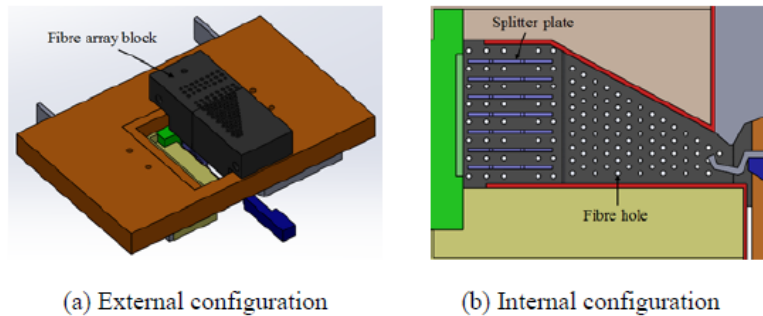


Figure 9. The flexible test apparatus for the arc image measurement.

#### 3.2 Calculation of Lorentz force

Lorentz force is calculated by a commercial FEM software depending on the current (from 0 A to 2000 A) and arc position (from the ignition region to splitter plates). Figure 10 shows the analysis geometry of Lorentz force. Figure 11 presents some results of Lorentz force acting towards the splitter plates depending on the current and arc column position (these data are used to obtain the external magnetic flux density that varies with the current and arc position).

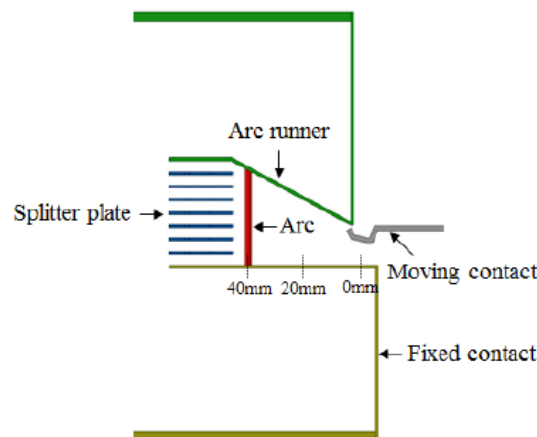


Figure 10. The Analysis model of Lorentz force.



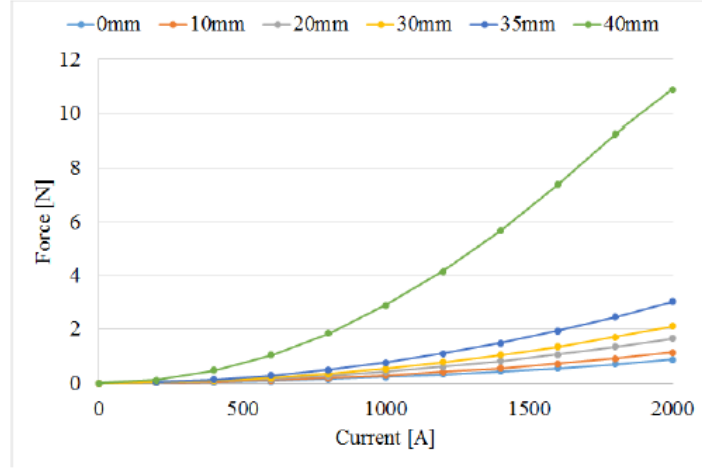


Figure 11. Lorentz force acting towards the splitter plates depending on the current and arc position.

To consider the influence of Lorentz force on the arc motion, the external magnetic flux density  $B_{ex}$  is computed by (4), and (5)

$$F_{Lo} = IB_{ex}L, \quad (4)$$

$$B_{ex} = F_{Lo}/(IL), \quad (5)$$

where  $F_{Lo}$  is Lorentz force (data in Figure 11),  $I$  is the current, and  $L$  is the arc length at the specific position (the arc column is assumed to be perpendicular to the fixed contact in the quenching chamber). In the arc model (MHD computation),  $B_{ex}$  is used as the input parameter, which is the function of the arc position and current.

### 3.3 Assumptions and simplifications for arc model

To reduce the complexity and computation load of the arc model in an LVSD, the following assumptions and simplifications have been adopted.

- The arc column is considered to be in a state of local thermodynamic equilibrium (LTE).
- The arc initial state is modelled as a hot channel in a small gap between contacts which has a homogeneous temperature distribution (1mm radius and 10,000 K temperature) (Ma *et al.*, 2009).
- The arc gas motion is regarded as a laminar flow.
- Metal erosion and wall ablation are not taken into account.
- Lorentz force generated by nonlinear ferromagnetic material and current path in a quenching chamber is calculated by FEM prior to the arc simulation using the external magnetic flux density as a input parameter applied to the fluid domain in the arc model.

### 3.4 MHD equations in arc column

The arc column is electrically neutral gas media. It is a mixture of electrons and heavy particles (ions, atoms and molecules) staying in thermal equilibrium at high temperature. If the assumption of LTE holds in the arc column, the arc can be treated as a single fluid and the mass, momentum and energy conservation equations can describe the relation between the velocity, pressure, temperature in the arc column as given below (Karetta and Lindmayer, 1998, Yang *et al.* 2013),

$$\frac{\partial \rho}{\partial t} + \nabla \cdot (\rho \vec{V}) = 0, \quad (6)$$

$$\frac{\partial (\rho v_i)}{\partial t} + \nabla \cdot (\rho v_i \vec{V}) = -\nabla p + \nabla \cdot (\eta \nabla v_i) + (\vec{J} \times \vec{B})_i, \quad (7)$$

$$\frac{\partial(\rho H)}{\partial t} + \nabla \cdot (\rho H \vec{V}) = \nabla \cdot \left( \frac{\lambda}{c_p} \nabla H \right) + \frac{\partial p}{\partial t} + \sigma E^2 + S_{rad} + S_\eta. \quad (8)$$

In the equations (6)-(8),  $\rho$  is the density,  $t$  is the time,  $\vec{V}$  is the velocity,  $v_i$  is the velocity component in  $i$  direction,  $p$  is the pressure,  $\eta$  is the dynamic viscosity,  $\vec{J}$  is the current density,  $\vec{B}$  is the magnetic flux density,  $H$  is the dynamic plasma enthalpy expressed by  $h + \vec{V}^2/2$ ,  $h$  is the static enthalpy determined by  $\int c_p dT$ ,  $\lambda$  is the thermal conductivity,  $c_p$  is the specific heat capacity,  $S_{rad}$  is the radiation energy losses and  $S_\eta$  is the heat generation due to viscous dissipation. These are standard fluid dynamics equations with an addition of the Lorentz force in momentum equation (7) and ohmic Joule heat plus the radiative losses in the energy equation (8).

The electric field  $\vec{E}$ , which determines the ohmic heating source in the energy equation, is calculated from Gauss's law, (9) and (10),

$$\nabla \cdot (\sigma \nabla \Phi) = 0, \quad (9)$$

$$\vec{E} = -\nabla \Phi, \quad (10)$$

where  $\sigma$  is the plasma electrical conductivity and  $\Phi$  is the electric scalar potential.

The simplified net emission coefficient method is employed in this work to calculate the radiation energy loss  $S_{rad}$ , and the net emission coefficients are computed from (11),

$$\varepsilon = C_1 (\exp(C_2 T) - \exp(C_2 T_r)) , \quad (11)$$

where  $C_1$  and  $C_2$  are the constant coefficients 300 W/m<sup>3</sup> and 0.0011 K<sup>-1</sup> respectively,  $T_r$  is the ambient temperature and  $T$  is the arc temperature (Barbu *et al.*, 2012).

### 3.5 Modelling domains and boundary conditions

Figure 12 shows the domains and boundaries for the FTA's arc model. The fluid component is the internal air volume of the FTA and it modelled by MHD theory with the external magnetic flux density, whereas the metal solid parts are considered as domains including only the electric and heat transfer phenomena. The current density calculated by the load circuit equation (2) is applied to the current-in boundary while there is 0 V electric potential at the current-out surface. The opening condition is set as atmospheric pressure and temperature (1 atm, 300 K). The simulation includes the temperature and pressure dependant properties of air (density, electrical conductivity, thermal conductivity, the specific heat capacity and viscosity) (Murphy, 1995, 2012).

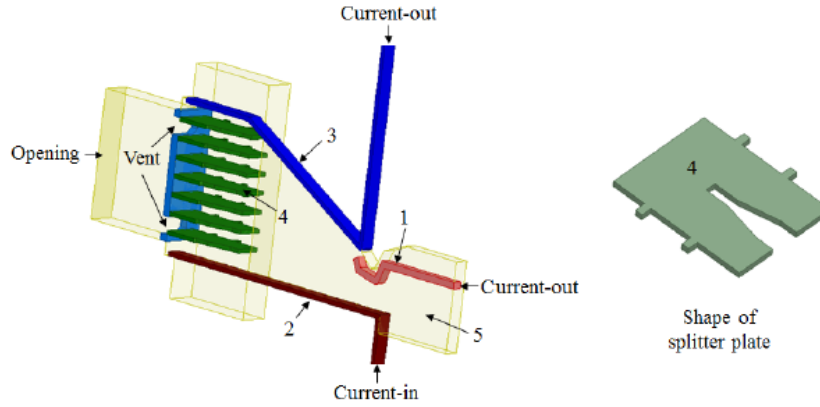


Figure 12. Domains and boundaries for arc simulation of MCB: (1) moving contact (copper), (2) fixed contact (copper), (3) arc runner (copper), (4) splitter plate (iron), (5) chamber volume (air).

### 3.6 Numerical model for arc root

The arc root is considered as a thin layer between the arc column and the metal surface of the cathode or anode. Before entering the splitter plates, the arc gradually bends and stretches around the plates generating the high voltage necessary to form arc roots on the splitter plates. After arc root formation, the voltage drops in the arc roots on the cathode and anode are relatively high when compared to that in the arc column. This arc root formation determines the exit-voltage and plays an important role in the switching performance of LVSDs. In

order to consider the arc root formation, further consideration is required as LTE condition does not hold in the arc root region and ordinary MHD theory cannot simulate the arc root phenomena.

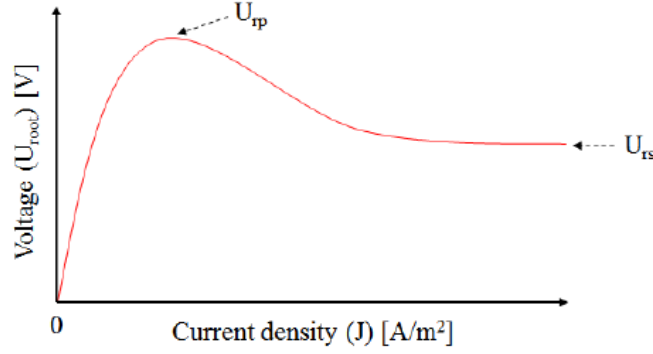


Figure 13. Relationship between potential drop and current density in the arc root.

In order to take into account the arc root formation, the empirical relationship (Lindmayer *et al.*, 2006) between the potential drop and current density is modelled in the simulation tool (see Figure 13). The contact resistance,  $CR_{root}$ , considering the effect of the arc root region is adopted on the surface of the splitter plate and it is obtained from (12),

$$CR_{root}(J) = \frac{U_{root}(J)}{J}, \quad (12)$$

where  $U_{root}$  is the potential drop in the anodic and cathodic arc roots.  $U_{rs}$  is selected to be 12.25 V that is a half of both anodic and cathodic drops on the surface of the plate (Nakayama *et al.*, 2003), and the peak voltage  $U_p$  across the root is  $2U_{rs}$ .

### 3.7 Implementation of arc simulation

The arc modelling process constitutes procedures of arc ignition, MHD computation including the external magnetic flux density, calculation of the external load circuit and contact motion (see Figure 14). After arc ignition, the arc voltage is calculated taking into account the external circuit and contact motion until the first current zero point. This modelling has been implemented in the Ansys CFX commercial software package widely used in previous studies (Lindmayer *et al.*, 2006, Barbu *et al.*, 2012).

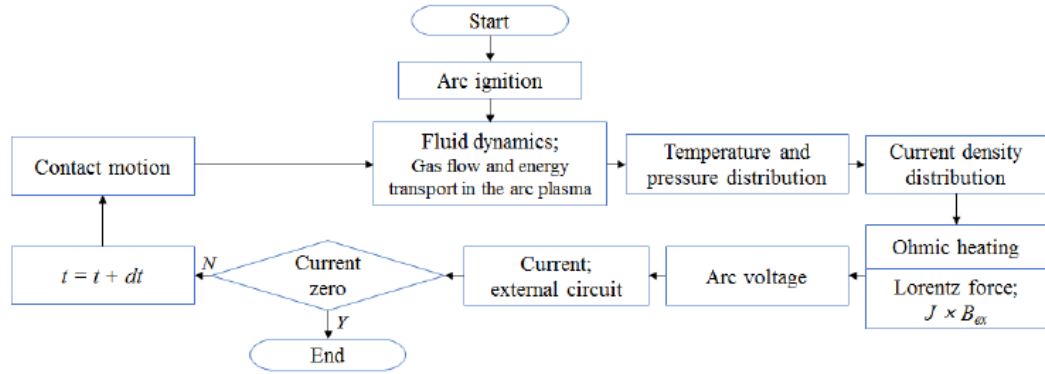


Figure 14. Diagram of the arc modelling process.

### 3.8 Validation of arc simulation

Figure 15 shows the waveform comparisons between experimental and simulated results of the FTA. Figure 16 presents the arc motion data recorded by the arc imaging system and the predicted arc temperature distribution in the quenching chamber, with corresponding voltage and current waveforms in Figure 15. In general, it can be said that the computed waveforms and arc motion have the similar trend with the experimental data. Furthermore, it is worth that this arc model can gives the similar value of the exit-voltage compared to the measured one (simulated value: 252 V, measured value: 280 V)

In Figure 15, the simulated arc voltage is too high at the beginning of the calculation because the thin hot conductive channel is placed between contacts for the ignition modelling but the arc voltage quickly reverses to a low value as the arc develops. As the arc moves towards splitter plates and elongates, the voltage begins to rise. Before 1.5 ms, the rate of change of the simulated current is higher than experimentally observed. This is due to the modelled arc voltage being greater than the experimentally observed value. This is reversed after 1.5ms where the modelled arc voltage is greater than experimentally observed leading to a more rapid onset of the current zero point in the simulated case.

In Figure 16, following arc ignition, the arc travels towards the splitter plates. When the arc enters the splitter plates, a high value of arc voltage is generated by the effects of arc root formation. It can be seen that the simulated arc moves faster after 1.65 ms and reaches the splitter plates more rapidly than experimentally observed. This higher velocity motion leads to a higher arc voltage than measured voltage after 1.5 ms (see Figure 15). In addition, arc back motion is observed at around 2.25ms in both simulated and measured data but its effect in the simulation is reduced when compared with the real arc (the arc moves slightly back and the drop of the arc voltage is small in the simulation compared to the experimental data).

Some discrepancies between the simulation and experiment may be expected from the use of a simplified model of Lorentz force, radiation cooling effect and the absence of metal erosion (which is important when the arc interacts with the plates).

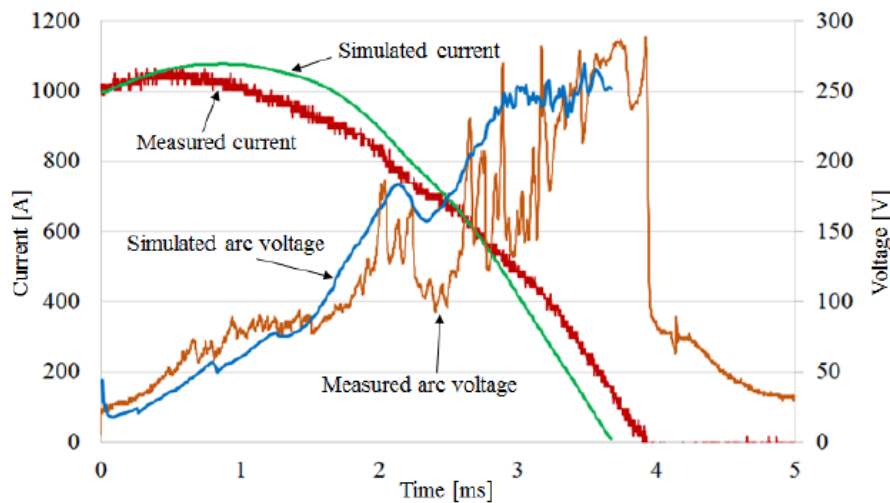
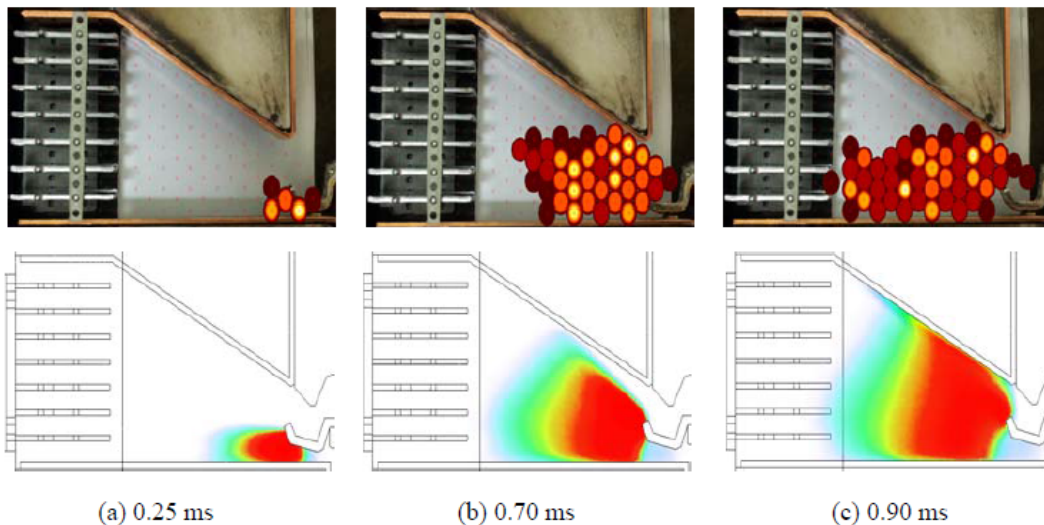


Figure 15. Comparisons between experimental and simulated results of the FTA.





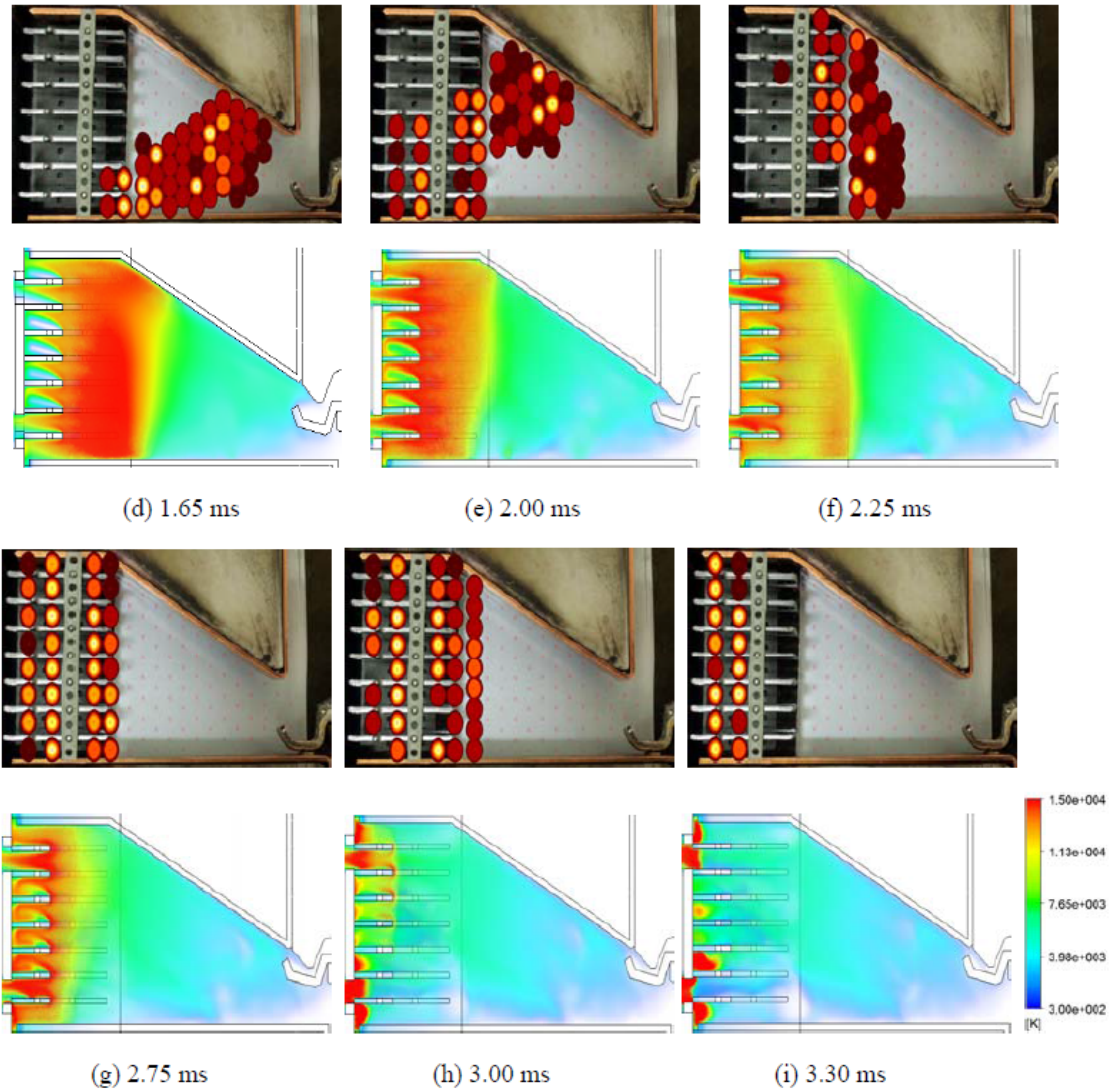


Figure 16. Arc images measured by the AIS and simulated temperature distribution (volume rendering in the half model) in the quenching chamber of the FTA.

#### 4. Conclusions

The experimental and numerical investigations on the arc behaviour and re-ignition evaluators of LVSDs have been studied in this paper. The following conclusions can be drawn:

- It is found that the ratio of the system voltage to exit-voltage is a reliable evaluator. If the voltage ratio is positive, instantaneous re-ignition never happens. In the case of the negative voltage ratio, if it lies in a range between -1.3 and 0.0, the re-ignition probability is very low because in such cases the voltage source does not have enough power to support the arc. This voltage ratio can be used for more accurate prediction of re-ignition in the LVSDs without complex calculation of the breakdown voltage.
- The model shows a good agreement with the experimental data. The arc modelling tool can predict the arc voltage and arc current as well as arc motion. Also, the exit voltage is simulated as a similar value with the measured one, which is an important parameter to obtain the evaluator of re-ignition.
- To make better predictions of arc behaviour and evaluation of switching performance, the arc modelling needs to be modified by including the metal erosion effect and improving Lorentz force and radiation cooling calculation.. This advanced fully coupled simulation is a part of ongoing research.

## References

- Balestrero, A., Ghezzi, L., Popov, M. and Sluis, L. (2010), "Current interruption in low-voltage circuit breakers", *IEEE Transactions on Power Delivery*, Vol. 25, No. 1, pp. 206-211.
- Barbu, B., Iturregi, A., Berger, F. and Torres, E. (2012), "Numerical analysis of the electric arc simulation using Ansys CFX", *Proceedings of the 26th International Conference on Electrical Contacts*, Beijing, China, 2012, pp. 311-316.
- Freton, P. and Gonzalez, J. J. (2009), "Overview of current research into low-voltage circuit breakers", *The Open Plasma Physics Journal*, 2, pp.105-119.
- Hauer, W. and Zhou, X. (2014), "Re-ignition and post arc current phenomena in low voltage circuit breaker", *Proceedings of the 27th International Conference on Electrical Contacts*, Dresden, Germany, 2014, pp. 398-403.
- Karetta, F. and Lindmayer, M. (1998), "Simulation of the gasdynamics and electromagnetic processes in low voltage switching arc", *IEEE Transactions on Components, Packaging, and Manufacturing Technology*, Vol. 21, No. 1, pp. 96-103.
- Lindmayer, M., Marzahn, E., Mutzke, A., R  ther, T. and Springstubbe, M. (2006), "The process of arc splitting between metal plates in low voltage arc chutes", *IEEE Transactions on Components and Packaging Technologies*, Vol. 29, No. C, pp. 310-317.
- Ma, Q., Rong, M., Murphy, A. B., Wu, Y. and Xu, T. (2009), "Simulation study of the influence of wall ablation on arc behaviour in a low-voltage circuit breaker", *IEEE Transactions on Plasma Science*, Vol. 37, No. 1, pp. 261-269.
- McBride, J. W., Pechrach, K. and Weaver, P. M. (2002), "Arc motion and gas flow in current limiting circuit breakers operating with a low contact switching velocity", *IEEE Transactions on Components and Packaging Technologies*, Vol. 25, No. 3, pp. 427-433.
- Mcbride, J. W., D. Shin, and T. Bull (2016), "A study of the motion of high current arcs in splitter plates using an arc imaging system", *Proceedings of the 28th International Conference on Electrical Contacts*, Edinburgh, GB, 2016, pp. 175-180.
- Murphy, A. B. (1995), "Transport coefficients of air, argon-air, nitrogen-air and oxygen-air plasmas", *Plasma Chemistry and Plasma Processing*, Vol. 15, pp. 279-307.
- Murphy, A. B. (2012), "Transport coefficients of plasmas in mixtures of nitrogen and hydrogen", *Chemical Physics*, Vol. 398, pp. 64-72.
- Nakayama, K., Yokomizu, Y., Matsumura, T., Kanamori, E. and Kuwamura, K. (2003), "Mechanism of voltage rise of high-current arc at atmospheric pressure due to deion plates", *Electrical Engineering in Japan*, Vol. 145, No. 3, pp. 17-24.
- Rong, M., Ma, Q., Wu, Y., Xu, T. and Murphy, A. B. (2009), "The influence of electrode erosion on the air arc in a low-voltage circuit breaker", *Journal of Applied Physics*, 106, 023308.
- Shin, D., Golosnoy, I. O. and McBride, J. W. (2015), "Numerical analysis of switching performance evaluators in low-voltage switching devices", in *International Symposium on Electromagnetic Fields in Mechatronics, Electrical and Electronic Engineering*, Valencia, Spain, 2015.
- Shin, D., Golosnoy, I. O. and McBride, J. W. (2016), "Arc modelling for switching performance evaluation in low-voltage switching devices", *Proceedings of the 28th International Conference on Electrical Contacts*, Edinburgh, GB, 2016, pp. 41-46.
- Slade, P. G. (2014), *Electrical Contacts Principles and Applications*, CRC Press, New York.
- Slepian, J. (1928), "Extinction of an A-C. arc", *Transactions of the American Institute of Electrical Engineers*, Vol. 47, No. 4, pp. 1398 - 1407.
- Yang, F., Wu, Y., Rong, M., Sun, H., Murphy, A. B., Ren, Z. and Niu, C. (2013), "Low-voltage circuit breaker arcs - simulation and measurements", *Journal of Physics D: Applied Physics*, Vol. 46, No. 27, 273001.